Molecular MRI using exogenous enzymatic sensors and endogenous chemical exchange contrast

Alexander John Taylor, MPhys

Thesis submitted to the University of Nottingham
for the degree of Doctor of Philosophy

Supervisors: Dr H. Faas, Professor N. Thomas
and Professor D. Auer
Internal assessor: Professor Richard Bowtell
July 2016

Contents

Abstract **1**

Declaration **2**

Acknowledgements **3**

Thesis overview **4**

1 Nuclear Magnetic Resonance and Magnetic Resonance Imaging

1.1 Origins of the NMR signal 6
1.1.1 Gyromagnetic ratios and Zeeman splitting 8
1.1.2 Boltzmann distribution and bulk magnetisation . . 10
1.1.3 The Bloch equation 12
1.1.4 Signal acquisition and relaxation phenomena 13
1.2 Magnetic Resonance Imaging 21
1.2.1 Slice selection 21
1.2.2 Frequency encoding 23
1.2.3 Phase encoding 24
1.2.4 Sequence types: gradient and spin echo 26
1.3 Contrast: paramagnetic relaxation 28
1.3.1 Alterative nuclei: ^{19}F as a contrast agent 32

2 Contrast agents and molecular imaging: biomarkers and imaging strategies

2.1 Outline 34
2.2 Introduction to current contrast agents (CAs) in MRI 35
2.2.1 T_1 agents: gadolinium contrast agents 35
2.2.2 T_2 agents: iron oxide contrast agents 37

2.2.3 The need for an alternative: towards molecular imaging using MRI . . . 39
2.3 Molecular contrast agents for MRI . . . 39
2.3.1 Detection of enzymes . . . 41
2.3.2 pH measurement . . . 43
2.3.3 Cell tracking . . . 44
2.4 ^{19}F contrast agents . . . 44
2.4.1 Molecular, gene expression and enzyme targeted probes . . . 45
2.4.2 Partial oxygen pressure measurement . . . 48
2.4.3 pH and ion sensitive probes . . . 50
2.4.4 Cell labelling . . . 53
2.5 Discussion . . . 56

3 Sensitivity considerations for ^{19}F MR signal detection
3.1 Introduction . . . 58
3.2 Theoretical sensitivity for MR . . . 60
3.2.1 Theoretical SNR for a ^{19}F MR experiment . . . 60
3.2.2 Noise and signal loss in MRI experiments . . . 63
3.2.3 Application to imaging sequences . . . 65
3.3 Materials and Methods . . . 65
3.3.1 Sample synthesis and preparation . . . 66
3.3.2 MR spectroscopy and imaging . . . 67
3.3.3 SNR determination . . . 67
3.4 Results . . . 68
3.4.1 Determining the gauge factor . . . 68
3.4.2 Minimum detectable limits . . . 69
3.4.3 Experimental detection limits . . . 71
3.4.4 Comparing the SNR measured by MRS and MRI . . . 72
3.4.5 Alternative T_2^* measurement . . . 74
3.5 Discussion . . . 74
3.5.1 Spectroscopy and imaging gauge factors . . . 74
3.5.2 Line broadening, T_2^* estimations and potential pitfalls . . . 75
3.5.3 Validation of detection limits . . . 76

3.5.4 Towards *in vivo* and limitations of the study 77
3.5.5 Summary and applications 78

4 Characterisation and development of a ^{19}F MRI sensor for enzyme detection

4.1 Introduction 80
4.2 Matrix metalloproteinases (MMPs): background, detection and a novel sensor 82
4.2.1 MMPs 82
4.2.2 MMP role in the hallmarks of cancer 83
4.2.3 Methods for MMP detection 86
4.2.4 ^{19}F MMP sensor 91
4.3 MMP sensor characterisation 93
4.3.1 Methods and image processing 93
4.3.2 Results: Timecourse and T_1 experiments 97
4.3.3 Probe imaging studies 102
4.3.4 Discussion of MMP probe results 104
4.4 Towards pre–clinical implementation 107
4.4.1 Sequence parameters and sample preparation . . . 108
4.4.2 ^{19}F surface coil construction and testing 108
4.4.3 *In vivo* MRI feasibility 112
4.4.4 Discussion of detection limits at 7 T 114
4.5 Outlook: Signal enhancement strategies 115

5 Alternative techniques for molecular imaging: chemical exchange saturation transfer (CEST)

5.1 Outline 118
5.2 Introduction 119
5.3 Theory and CEST methods review 121
5.3.1 Mathematical model 122
5.3.2 Applications of CEST 124
5.3.3 CEST methods 126
5.3.4 Bloch–McConnell equations 130
5.4 Optimising the CEST experiment: parameter simulation . . 133
5.4.1 Simulation parameters for two and three pool model 135

5.4.2 Field strength and pool model simulations 135
5.4.3 Optimal amide proton transfer (APT) parameters . 137
5.5 CEST setup optimisation: *in vitro* experiments 141
5.5.1 Material and methods 141
5.5.2 CEST sequences: Bruker 7 T and Varian 9.4 T 144
5.5.3 Detecting metabolites using the CEST effect 146
5.6 Discussion 153

6 CEST imaging in a cancer cell model and machine learning application
6.1 Outline 155
6.2 Introduction 156
6.3 Pattern recognition theory 159
6.3.1 Feature generation and selection 160
6.3.2 Classifiers: type, design and evaluation 163
6.4 Medulloblastoma cell imaging 169
6.4.1 Tumour cell model 169
6.4.2 Methods: experimental and post–processing parameters 170
6.4.3 CEST results 175
6.4.4 SVM applied to CEST data: ten day incubation samples 181
6.5 Discussion 189
6.5.1 CEST experiment results 189
6.5.2 SVM analysis results 192
6.5.3 Limitations and future work 193

7 Discussion
7.1 Summary 195
7.2 Exogenous contrast results 195
7.3 Endogenous contrast results 196
7.4 Future work 196
7.5 Concluding remarks 200

Glossary **201**

References **204**

Abstract

Molecular magnetic resonance imaging (MRI) methods have the potential to provide detailed information regarding cellular and molecular processes at small scales within the human body. Nuclear signals from chemical samples can be probed using specialised MRI techniques, to highlight molecular contrast from particular enzymes or metabolites. The aim of the work described in this thesis is to investigate both exogenous and endogenous contrast mechanisms using fluorine MRI and chemical exchange saturation transfer (CEST) respectively, in order to detect molecular changes *in vitro*.

Initial theoretical work investigates the factors which affect fluorine MRI signals and provides a theoretical framework to determine the sensitivity of such experiments. A novel paramagnetic fluorine sensor to detect enzyme activity is then characterised using high field nuclear magnetic resonance (NMR), showing 60 to 70–fold increases in T_1 relaxation values upon enzyme interaction. The effects on the fluorine lineshape from varying sample temperature and solvent were investigated. The possibility of imaging is demonstrated, but further investigations using the theoretical framework found pre–clinical implementation of the sensor is limited by the achievable experimental sensitivity.

Efforts then focussed on CEST molecular methods, which are not limited by sensitivity. A protocol is developed to target amide protons in an *in vitro* cancer cell model, with parameters optimised following simulation of the expected contrast. Analysis of CEST results were aided through use of a support vector machine (SVM) to distinguish group differences between cancer cells and control samples. A linear classifier was found to be suitable to discriminate between samples.

Declaration

I declare that the work presented in this thesis is my own original work based on research undertaken during my PhD study period at the University of Nottingham, in the Radiological Sciences group based in the School of Medicine (Division of Clinical Neuroscience).
In Chapter 3, I performed all the experimental work and analysed all the data independently. In Chapter 4, NMR facility manager Dr Huw Williams ran the 600 MHz acquisitions and Dr James Krupa synthesised all sensor compounds. I was responsible for designing the experiment and analysing all data ouput. I also built the fluorine surface coil and performed all 7 T Bruker investigations. For CEST experiments, all acquisitions and analysis were performed by myself. Ms Aishah Nasir incubated the cell samples. Adaptations to any software developed by other researchers is acknowledged in the text.

Relevant journal publications arising from work in this thesis:

- **A. J. Taylor**, J. Granwehr, C. Lesbats, J. L. Krupa, J. S. Six, G. E. Pavlovskaya, N. R. Thomas, D. P. Auer, T. Meersmann, H. M. Faas. *Probe–specific procedure to estimate sensitivity and detection limits for ^{19}F magnetic resonance imaging (MRI)*, PLoS One, submitted November 2015 (accepted with minor corrections)

- **A. J. Taylor**†, J. L. Krupa†, H. M. Faas, S. R. Johnson, T. Meersmann, H. E. L. Williams, N. R. Thomas. *In vitro matrix metalloproteinase (MMP) detection using a ^{19}F "on/off" MRI probe*, Chemistry – A European Journal, 2016 (in process of re–submission)
  † – joint first author

Acknowledgements

I have been very lucky during the course of my PhD to work with such a range and variety of people from different backgrounds and disciplines.

I would like to begin by acknowledging the help and support provided by my supervisors, Dr Henryk Faas, Prof. Neil Thomas and Prof. Dorothee Auer. I am grateful for their guidance and advice over the past few years.

At the Sir Peter Mansfield Centre and there are several people who helped me greatly there. I wish to thank Prof. Thomas Meersmann for his constructive comments and all his group members for their hands–on help (Dr Nicola Rogers, Clémentine Lesbats, Dr Joseph Six and Dr David Lilburn). The time Dr Josef Granwehr spent discussing ideas with me helped develop my project and his effort was really appreciated. Thank you also to Dr Paul Glover and Dr Aleksandra Sulikowska who advised me on building the fluorine surface coil.

At the Queen's Medical Centre, I would like to thank all of the Radiological sciences group for their advice and support. I am grateful to Ryan Hegarty for helping me with spectroscopy related issues and to Dr Maria Yanez Lopez for her advice on CEST, Matlab programming and the Varian 9.4 T. I appreciate the help provided by Aishah Nasir for the cell work.

Dr Malcolm Prior and Dr Huw Williams helped develop my skills on Bruker systems and I am very grateful for the useful discussions we had. I would like to thank Dr James Krupa, Dr Francesco Zamberlan and Matthew Stevenson for synthesising the chemical sensors.

Finally, I would like to thank Fiona for being there for me throughout my PhD.

Thesis overview

Chapter 1 provides the relevant background knowledge for NMR and MRI understanding. Analytic formulae for a sample's magnetisation are described, which will provide an introduction for later SNR studies. The mechanism of paramagnetic relaxation is briefly described, whose contrast effect in MRI is used extensively in this thesis.

In Chapter 2, the use of exogenous contrast agents in MRI is described with particular emphasis on molecular agents. The current literature pertaining to fluorine contrast agents is reviewed, in order to assess the novel sensor described in later chapters.

The sensitivity of a fluorine experiment is an important factor in designing such an experiment, and a thorough analysis of the factors affecting sensitivity is presented in Chapter 3. In this chapter an expression is formulated for the sensitivity achievable in a fluorine experiment, accounting for experimental and sample parameters and effects. This is used to assess the sensitivity for an example fluorine experiment, which could be used to predict the sensitivity of future fluorine experiments.

Chapter 4 takes a novel enzymatic sensor for the detection of matrix metalloproteinase (MMP) molecules and characterises its MR contrast and properties. The sensitivity of the probe is highlighted as the greatest problem facing translation to a pre–clinical set–up.

Chapter 5 changes focus to endogenous contrast mechanisms and in particular chemical exchange saturation transfer (CEST) contrast. A description of the mechanism behind CEST is given, with relevant technical and theoretical considerations discussed. Simulations and experiments are presented which will inform later CEST experiments performed on a 9.4

T Varian scanner.

In Chapter 6 an optimised CEST experiment is performed, using the optimisation parameters in Chapter 5, on a cancer cell line *in vitro*. A machine learning approach is applied to the resulting CEST spectra, in an attempt to classify data from the cancer cell sample and a control sample.

The results of both exogenous and endogenous studies are summarised in Chapter 7 and the future direction of the presented work is outlined.

CHAPTER 1

Nuclear Magnetic Resonance and Magnetic Resonance Imaging

For nuclear magnetic resonance (NMR) based experiments which exploit certain quantum properties of molecules, such as quantum coherence, it is not possible to explain or predict the observed NMR signals using a purely classical physics formalism. However, for most applications within the field of MRI it is suitable to use a classical description to describe the magnetisation experimentally observed. It is this classical description which forms the focus of this chapter. The purpose of this chapter is to provide the background physics specifically necessary to understand the original research presented in subsequent chapters. In particular the physical nature of magnetisation is described, which forms the basis of our sensitivity investigations in Chapter 3. The mechanism and formulations involved in relaxation theory, which is drawn on in Chapter 2 and 4, is also highlighted.

1.1 Origins of the NMR signal

The origin of the NMR phenomenon and the associated imaging techniques developed since its discovery, derive from the quantum mechanical concept of "intrinsic spin" or "spin". Spin is a vector quantity and was introduced initially in the mathematical framework of quantum mechanics (QM) to describe the energy states of the electron; in fact, the con-

cept of a spin operator for an electron is a direct consequence of the solution of the relativistic Dirac equation and deeply conceptually rooted in QM [1]. The intrinsic spin can be related to the total angular momentum, $\boldsymbol{J}$, such that the magnitude, $|\boldsymbol{J}|$, is given by

$$|\boldsymbol{J}| = \hbar\sqrt{S(S+1)} \quad . \tag{1.1.1}$$

Here $\hbar = h/2\pi$, where h is Planck's constant and $h = 6.63 \times 10^{-34}$ J s^{-1}. For an atomic nucleus, the total angular momentum may be viewed as a single summation of the composite protons and neutrons. Convention gives the nuclear spin as I , rather than as a constituent particle spin of S. Eq. 1.1.1 holds for $\boldsymbol{I}$ as well as $\boldsymbol{S}$.

Certain quantities such as spin and orbital angular momentum are observable quantities, and measurement of a given QM property (an observable) will yield a set of discrete values; these values are eigenvalues of the QM operator acting on a quantum state's eigenvector [1]. Measurement of a nucleus' angular momentum in the z spatial direction under the influence of an external magnetic field will consequently give a number of finite possible values, such that the angular momentum observed is quantised. The quantum rule that $m_z = -I, I+1, ..., I-1, I$ defines these eigenvalues, where m_z is the associated intrinsic spin quantum number and there are $2I+1$ possible different states such a measurement of $\boldsymbol{J}$ can take. A measurement of J_z, the projection of $\boldsymbol{J}$ in the z–direction, yields

$$J_z = \hbar m_z \quad . \tag{1.1.2}$$

For hydrogen and fluorine (both nuclei used in the experiments described in this thesis), $I = 1/2$ such that $\langle J_z \rangle$ can take one of two possible states; $J_z = +\hbar/2$ ("spin up" state) and $J_z = -\hbar/2$ ("spin down" state). These states are defined for spins which are parallel and anti–parallel to an external magnetic field respectively.

Element	**Symbol**	**Spin**	**Gyromagnetic ratio** γ_X [10^6 rad s^{-1} T^{-1}]	**Abundance** %
Hydrogen	^{1}H	1/2	267.522	99.99
Carbon	^{13}F	1/2	67.283	1.07
Fluorine	^{19}F	1/2	251.815	100
Phosphorus	^{31}P	1/2	108.394	100
Xenon	^{131}Xe	3/2	22.091	21.18
Oxygen	^{17}O	5/2	–36.281	0.038
Gadolinium	^{155}Gd	3/2	–8.213	14.80

Table 1.1: **Selected elements and their associated NMR properties**, taken from [2]. Notable points in this table include the proximity of fluorine's gyromagnetic ratio to the proton value, as well as the comparably low ratios for other nuclei (^{13}C, ^{131}Xe).

1.1.1 Gyromagnetic ratios and Zeeman splitting

The magnetic moment of a proton or particle, $\boldsymbol{\mu}$, is directly proportional to the angular momentum,

$$\boldsymbol{\mu} = \gamma \mathbf{J} \quad , \tag{1.1.3}$$

where γ is the proportionality factor or gyromagnetic ratio (this constant is specific for a given nuclei). For protons and many other nuclei $I = 1/2$, but several other values exist for different combinations of protons and neutrons in nuclei (see Table 1.1 for additional examples).

The energy of a particle, E, with a magnetic moment interacting with an external magnetic field, $\boldsymbol{B_0}$, is given by

$$E = -\boldsymbol{\mu}.\boldsymbol{B_0} \quad . \tag{1.1.4}$$

Nuclei at room temperature are thermally distributed between the two spin states, with spins aligned along the direction of the $\boldsymbol{B_0}$ field in the lower energy state. This spin alignment is known as Zeeman splitting in which the spin population is split by the external magnetic field, see Fig. 1.1. Conventionally the $\boldsymbol{B_0}$ field is applied in the z direction such that $\boldsymbol{B_0} = B_0\hat{\boldsymbol{z}}$, where $\hat{\boldsymbol{z}}$ denotes the principal z axis, in an orthogonal xyz basis set in Euclidean space.

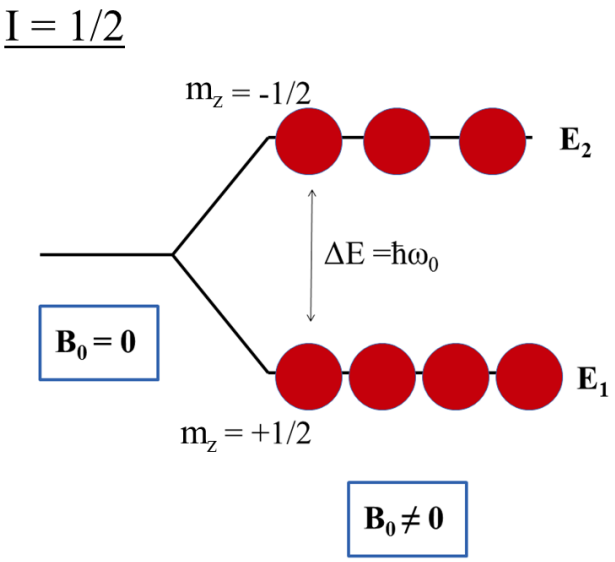


Figure 1.1: Zeeman splitting under the influence of an external magnetic field. Spin states are indistinguishable without the applied magnetic field, which on application, splits the spin population into two levels with different energies.

Combining Eq. 1.1.4 with the expression for the energy of a specific spin state in the z direction, using Eq. 1.1.2 and 1.1.3, we obtain,

$$\mathbf{E} = -\boldsymbol{\mu}.\boldsymbol{B_0} = -\gamma J_z B_0 = -m_z \gamma \hbar B_0 \quad . \tag{1.1.5}$$

In the case of spin 1/2 Zeeman splitting in an external magnetic field, the energy difference between the two states is:

$$\Delta E = E_2 - E_1 = -\gamma\hbar(-1/2)B_0 + \gamma\hbar(1/2)B_0 = \gamma\hbar B_0 \tag{1.1.6}$$

where the values of m_z are the allowed spin quantum number associated with a spin 1/2 particle denoting the two energy states. From the Zeeman diagram, the energy expression is substituted into Eqn. 1.1.6, and the energy difference between the two states can be written as:

$$\Delta E = h\nu = \hbar\omega_0 = \hbar\gamma B_0 \quad . \tag{1.1.7}$$

This allows one to calculate the energy needed to be transferred into the system in order to interact with the nuclei and to allow a transition into the higher spin energy state:

$$\omega_0 = \gamma \mathrm{B}_0 \quad . \tag{1.1.8}$$

The frequency, ω_0, is the characteristic frequency for a particular nucleus transition, also known as the *Larmor equation*.

1.1.2 Boltzmann distribution and bulk magnetisation

The total magnetisation of a sample, $\mathbf{M}$, is the sum of all the individual magnetic moments of a sample:

$$\mathbf{M} = \sum_{i=1}^{N_s} \boldsymbol{\mu}_i \tag{1.1.9}$$

where N_s is the number of spins in a sample and $\boldsymbol{\mu}_i$ is the magnetic moment of a single spin in a large spin ensemble of N_s spins. If no external magnetic field is present, the net sum of magnetic moments is equal to zero, since there is no preferential direction for the magnetic moment vectors. In the presence of an external magnetic field, the population of spins is distributed between the Zeeman–split discrete energy levels. According to the Maxwell–Boltzmann distribution, the population distribution is given below,

$$P = \frac{N}{Z} e^{-\frac{E_{m_z}}{k_B T_s}} \quad , \tag{1.1.10}$$

where Z is the partition function, k_B is the Boltzmann constant ($k_B = 1.38 \times 10^{-23}\,\mathrm{J\,K^{-1}}$), T_s is the sample temperature [K], N is the number of spins per unit volume, E_{m_z} is the energy of a particle in a state defined by the quantum number m_z (defined explicitly in Eq. 1.1.5). Z is a feature which normalises E_{m_z} ;

$$Z = \sum_{m_z=-I}^{m_z=I} e^{-\frac{E_{m_z}}{k_B T}} \quad . \tag{1.1.11}$$

where n covers all values of I. Using Eq. 1.1.9 the summation of the individual magnetic moments can be replaced by a weighted sum of the magnetisation in each separate state,

$$\mathbf{M} = \sum_{i=1}^{N_s} \boldsymbol{\mu}_i = \sum \langle \mu \rangle \, P \quad , \tag{1.1.12}$$

where $\langle \mu \rangle$ represents a possible spin state of magnetic moments. A general expression for the total magnetisation, M_{tot}, of a nuclei with spin J

is then given by,

$$M_{tot} = \frac{N\gamma\hbar}{Z} \sum_{m_z=-I}^{I} m_z \times \exp\Big(\frac{m_z\gamma\hbar B_0}{k_B T_s}\Big) \quad (1.1.13)$$

$$= \frac{N\gamma\hbar}{2}\left[(2I+1)\coth\left(\frac{(2I+1)\gamma\hbar B_0}{2k_B T_s}\right) - \coth\Big(\frac{\gamma\hbar B_0}{2k_B T_s}\Big)\right]. \quad (1.1.14)$$

At room temperature, the thermal energy, $k_B T_s$, is far greater than the magnetic energy, $m_z\gamma\hbar B_0$. In magnetic resonance experiments, the following orders of magnitude are representative of typical experimentally encountered energy values: $k_B T_s \sim 10^{-21}$ J and $m_z\gamma\hbar B_0 \sim 10^{-26}$ J. This leads to the high temperature approximation in Eq. 1.1.14,

$$\frac{I\gamma\hbar B_0}{kT_s} \ll 1 \quad . \quad (1.1.15)$$

Upon series expansion of the coth terms in Eq. 1.1.14,

$$\coth x = \frac{1}{x} + \frac{x}{3} - \frac{1}{45}x^3 + \frac{2}{945}x^5 - ... \quad . \quad (1.1.16)$$

Combining with Eq. 1.1.15 such that non-linear order terms are neglected and substituting into Eq. 1.1.14, we arrive at Curie's law, which describes the magnetisation's dependence upon temperature:

$$M_{tot} = I(I+1)\frac{N(\gamma\hbar)^2 B_0}{3k_B T_s} \quad . \quad (1.1.17)$$

In our case of a spin 1/2 particle, such as ^{1}H or ^{19}F, the total magnetisation available, M_0 is,

$$M_0 = \left(\frac{\gamma\hbar}{2}\right)^2 \frac{N}{k_B T_s} B_0 \quad . \quad (1.1.18)$$

The total magnetisation of a sample is an important quantity in determining the available signal for MR experiments and the above expression shows the relatively few parameters which affect M_0. The magnetisation has a square dependence upon the gyromagnetic ratio, illustrating a further benefit of using hydrogen and fluorine as MR nuclei; table 1.1 shows these nuclei to have some of the highest gyromagnetic ratio values. The number of spins per unit volume is linearly proportional to M_0 and inversely proportional to the sample temperature but these sample parameters are not often easily adapted to enhance magnetisation in conventional MR imaging.

1.1.3 The Bloch equation

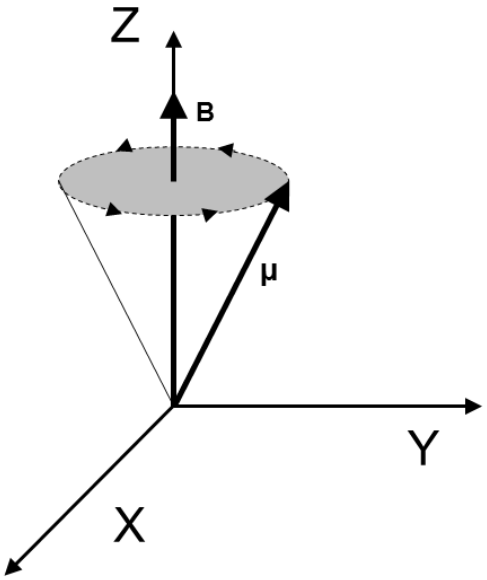


Figure 1.2: Magnetic moment precession around the z–axis. Under an external magnetic field, the magnetic moment of a particle will undergo gyroscopic rotation around an axis, with the direction of motion being determined using the cross product of the two vectors.

Quantum mechanics necessarily provides the spin and energy level description of a spin 1/2 particle in an external magnetic field, but classical dynamics accurately describes the changing magnetisation vector dynamics.

Each classically rotating object has an associated angular momentum, and analogously the angular momentum arising from a particle's nuclear spin produces a magnetic moment, $\boldsymbol{\mu}$ (shown already). In an external magnetic field, the magnetic moment will experience a torque, $\boldsymbol{\tau}$, given by:

$$\boldsymbol{\tau} = \boldsymbol{\mu} \times \boldsymbol{B} \quad . \tag{1.1.19}$$

The torque is defined as the rate of change of the angular momentum, $\boldsymbol{L}$:

$$\boldsymbol{\tau} = \frac{\mathrm{d}\mathbf{L}}{\mathrm{d}t} \quad . \tag{1.1.20}$$

Combining this with Eq. 1.1.19 and substituting for $\boldsymbol{M}$ we have:

$$\frac{\mathrm{d}\mathbf{L}}{\mathrm{d}t} = \mathbf{M} \times \mathbf{B} \quad . \tag{1.1.21}$$

This equation is combined with $\boldsymbol{M} = \gamma \boldsymbol{L}$, and allowing time dependent magnetisation and magnetic field vectors gives the Bloch equation:

$$\frac{\mathrm{d}\mathbf{M}(t)}{\mathrm{d}t} = \gamma(\mathbf{M}(t) \times \mathbf{B}(t)) \tag{1.1.22}$$

$$= \gamma((M_y B_z - M_z B_y)\mathbf{i} - (M_x B_z - M_z B_x)\mathbf{j} + (M_x B_y - M_y B_x)\mathbf{k}) \tag{1.1.23}$$

Here, $M_{x,y,z}$ and $B_{x,y,z}$ denote the magnetisation and magnetic field values in the x, y and z direction respectively. This equation shows there are three coupled linear differential equations, one for each orthogonal co–ordinate, in the general Bloch equation. Solution of this equation allows the depiction of a sample's magnetisation as a function of time, which forms the basis of understanding the spin system's dynamics after peturbation.

These initial equations show that under application of an external magnetic field, the magnetic moment (or indeed the magnetisation vector) will precess at a rate of ω_0 around the z axis. Fig. 1.2 illustrates the precessional motion of the magnetic moment.

1.1.4 Signal acquisition and relaxation phenomena

Rotating reference frame and radio frequency (R.F.) excitation

To an observer in the stationary laboratory frame, the magnetisation vector will precess under a B_0 field at a frequency of ω_0. An alternative reference frame can be formulated which rotates at the precessional rate, such that the magnetisation vector appears stationary in the xy plane and is unchanged in the z direction ($z = z'$). The transformations occurs only in the x and y direction [3], where $x \rightarrow x' = x\cos(\omega_0 t) - y\sin(\omega_0 t)$ and $y \rightarrow y' = x\sin(\omega_0 t) + y\cos(\omega_0 t)$, with x' and y' the transformed co–ordinates.

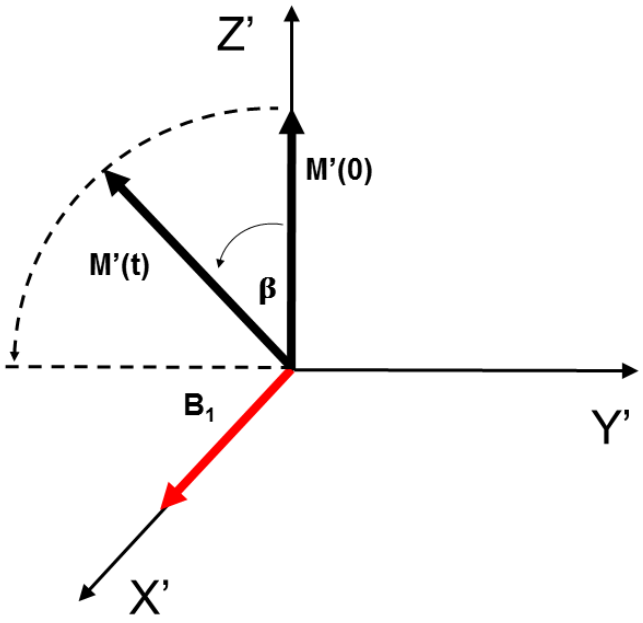


Figure 1.3: Magnetisation relaxation in the rotating reference frame. Upon B_1 interaction, the magnetisation is "flipped" into the $x'y'$ plane. The flip angle, β, is the angle between the z' axis and the magnetisation vector after B_1 pulse application. Note, in the laboratory frame (non–rotating reference frame), the magnetisation vector's path includes a precessional rotation in the new xy plane around the z' axis at a frequency of ω_0.

All NMR experiments utilise a R.F pulse (in the form of a $\boldsymbol{B_1}$ magnetic field pulse) to interact with a spin system, perturbing the magnetisation vector from its equilibrium state. This input of energy is distributed between the excited spins and external environment, such that the spin magnetisation returns to the initial state. The return of the magnetisation vector to the initial state can be described as two separate decay process in the transverse (xy) and longitudinal (z) plane; this process is known as relaxation. The $\boldsymbol{B_1}$ field can be described as an excitation in the xy plane of frequency ω_0,

$$\boldsymbol{B_1} = B_1\hat{\boldsymbol{x}}\cos(\omega_0 t) - B_1\hat{\boldsymbol{y}}\sin(\omega_0 t) \quad . \tag{1.1.24}$$

In the rotating frame, $\boldsymbol{B_1} = B_1\hat{\boldsymbol{x}}'$. The Bloch equation can be shown to be

modified by the combined B_0 and $\boldsymbol{B_1}$ fields, such that

$$\frac{\mathrm{d}\mathbf{M}'}{\mathrm{d}t} = \gamma \mathbf{M}' \times \mathbf{B_{1eff}} \quad , \tag{1.1.25}$$

where $\boldsymbol{B_{1_{eff}}} = (B_0 - \omega/\gamma)\hat{\boldsymbol{z}} + B_1\hat{\boldsymbol{x}}'$ and $\boldsymbol{M'}$ is the magnetisation vector in the rotating reference frame. This B_1 pulse causes the magnetisation to precess around the $\boldsymbol{B_1}$ field in the rotating reference frame and a creates tipping of the magnetisation from the z' axis into the $x'y'$ plane. The angle at which the magnetisation vector is tipped by is known as the flip angle, β. The duration, t, and the power of the B_1 pulse determine β, given by

$$\beta = \gamma B_1 t \quad , \tag{1.1.26}$$

for a non–modulated (amplitude) B_1 field. Fig. 1.3 shows the direction of the magnetisation at $t = 0$, and after the application of a $\boldsymbol{B_1}$ pulse. In the non–rotating frame the $\boldsymbol{B_1}$ field would cause a rotating magnetisation vector which reaches the same flip angle after precession around the z axis. A $\beta = 90^\circ$ or ($\pi/2$ in radians) pulse would transfer the magnetisation completely into the $x'y'$ plane, and a $\beta = 180^\circ$ transfers the magnetisation completely onto the $-z'$ axis.

Transverse relaxation: T_2

As the magnetisation vector interacts with a B_1 pulse and the longitudinal magnetisation component relaxes back to its equilibrium value, the transverse magnetisation components in the xy plane decay to zero. This decay is described by the following equations,

$$M_x(t) = M_x(0)\cos(\omega t)\exp\left(-\frac{t}{T_2}\right) \tag{1.1.27}$$

$$M_y(t) = M_x(0)\sin(\omega t)\exp\left(-\frac{t}{T_2}\right) \quad . \tag{1.1.28}$$

Defining $\boldsymbol{M_T(t)} = M_x\hat{\mathbf{x}} + M_y\hat{\mathbf{y}}$,

$$\frac{\mathrm{d}\boldsymbol{M_T(t)}}{\mathrm{d}t} = -\frac{\boldsymbol{M_T(t)}}{T_2} \quad , \tag{1.1.29}$$

which is integrated to give

$$\boldsymbol{M_T(t)} = \boldsymbol{M_T(0)}\exp\left(-\frac{t}{T_2}\right) \quad , \tag{1.1.30}$$

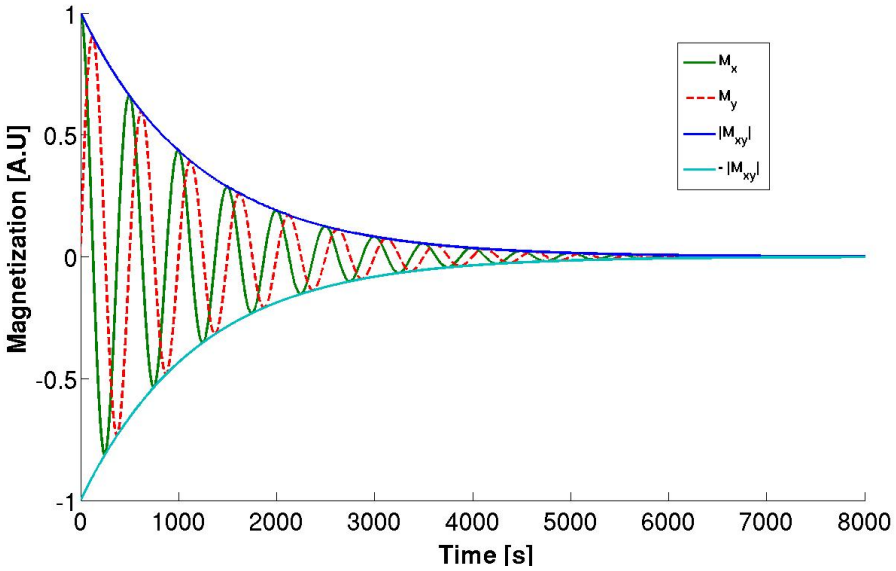


Figure 1.4: Transverse magnetisation components and their characteristic decay over time. The x and y components of T_2 relaxation have a $\pi/2$ phase difference. In this example, $T_2 = 1200$ ms.

where T_2 is the spin–spin transverse relaxation value or time constant. This decay is shown for the transverse component of the magnetisation and the individual x and y components in Fig. 1.4. The oscillation of the x and y components are enveloped by the exponential transverse decay with a characteristic decay time, T_2.

The energy acquired after B_1 application is conserved through energy transfer between spins in the sample. During this process, spins acquire different ω as spin–spin interactions create different local magnetic fields. This causes dephasing of the sample spins and consequently a reduction in the transverse magnetisation.

In practise, the transverse signal decays at a rate faster than T_2. This is because the transverse relaxation is not only affected through spin–spin interactions, but also the local magnetic inhomogeneities in the B_0 field. This realistic decay rate, T_2^*, is a combination of T_2 spin–spin effects and magnetic field effects:

$$\frac{1}{T_2^*} = \frac{1}{T_2} + \gamma \Delta B \quad . \tag{1.1.31}$$

Here, ΔB is the deviation in the local magnetic field from the B_0 value, which increases the rate of relaxation through inducing a faster spin de-

phasing.

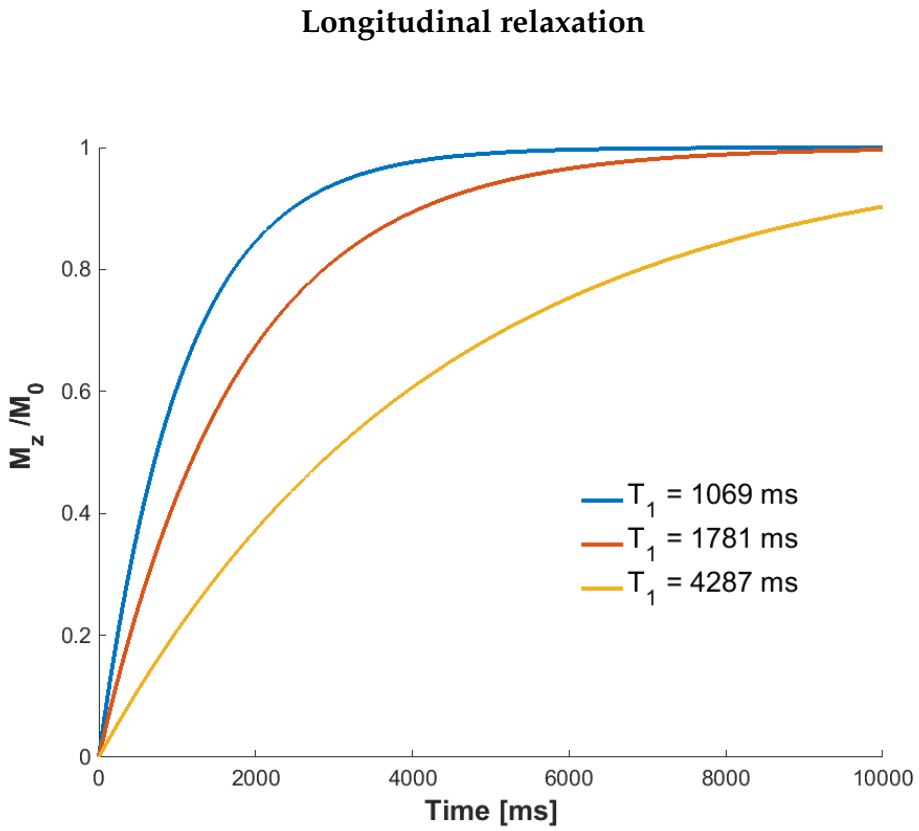


Figure 1.5: Longitudinal decay at 9.4 T in a mouse brain. The different longitudinal relaxation values of different regions in a mouse brain at 9.4 T are plotted, showing longer T_1 components taking longer to reach equilibrium magnetisation values. The regions used were $T_1 = 4287$ ms in the lateral ventricle, $T_1 = 1069$ ms in the posterior pituitary, and $T_1 = 1781$ ms in the corpus callosum. Values were taken from [4].

After a perturbation, the longitudinal component of the magnetisation will tend to relax back to the minimal energy state. A number of processes facilitate this spin–lattice relaxation (essentially an energy exchange process with the environment) including interactions between the spin system and molecular rotations and movement. This can be described by a first order differential equation, in which the magnetisation exponentially decays back to M_0, with a characteristic longitudinal decay constant, T_1,

$$\frac{\mathrm{d}M_{\mathrm{T}}(t)}{\mathrm{d}t} = -\frac{M_{\mathrm{Z}}(t) - M_0}{T_1} \quad . \tag{1.1.32}$$

This equation is solved by integration, yielding

$$M_z(t) = M_0 + \big(M_z(0) - M_0\big)\exp\bigg(-\frac{t}{T_1}\bigg). \tag{1.1.33}$$

Fig. 1.5 shows the effect different T_1 values have on the rate at which the magnetisation decays back to the equilibrium value.

Bloch equation including relaxation

Including the relaxation effects, the complete Bloch equation (eq. 1.1.23) becomes:

$$\frac{\mathrm{d}\mathbf{M}(t)}{\mathrm{d}t} = \gamma(\mathbf{M}(t) \times \mathbf{B}(t)) - \mathbf{R}(\mathbf{M}(t) - M_0) \quad . \tag{1.1.34}$$

Here, $\mathbf{R}$ is a relaxation matrix including the T_2 and T_1 contributions. The individual components of the magnetisation are:

$$\frac{\mathrm{d}M_x(t)}{\mathrm{d}t} = \gamma((M_y(t)B_z - M_z(t)B_y) - \frac{M_x(t)}{T_2} \tag{1.1.35}$$

$$\frac{\mathrm{d}M_y(t)}{\mathrm{d}t} = \gamma((M_z(t)B_x - M_x(t)B_z) - \frac{M_y(t)}{T_2} \tag{1.1.36}$$

$$\frac{\mathrm{d}M_z(t)}{\mathrm{d}t} = \gamma((M_x(t)B_y - M_y(t)B_x) - \frac{M_z(t) - M_0}{T_1} \tag{1.1.37}$$

In the simplest scenario, we consider a "single–pulse" experiment in which a $\boldsymbol{B_1}$ pulse is briefly applied to the spin system, using a flip angle of $\beta = 90°$, with the resulting spin dynamics predicted using the solution of the Bloch equation. The time dependent magnetisation is described below, with Fig. 1.6 showing the relaxation process,

$$\mathbf{M}(\mathbf{t}) = M_0\bigg(\big(e^{-t/T_2}\cos(\omega_0 t)\big)\hat{\boldsymbol{x}} + \big(e^{-t/T_2}\sin(\omega_0 t)\big)\hat{\boldsymbol{y}} + \big(1 - e^{-t/T_1}\big)\hat{\boldsymbol{z}}\bigg) \quad . \tag{1.1.38}$$

The dynamics of this excitation show a precession around the z axis as the peturbed magnetisation relaxes back to the equilibrium M_0 value. As the magnetisation relaxes, a changing electromagnetic (EM) field is generated by the changing magnetisation. This in turn generates a current (through Faraday induction) in a conducting coil in the xy plane, placed near the irradiated sample. The detection of this 90 ° pulse decay, is known as detection of the free induction decay (FID).

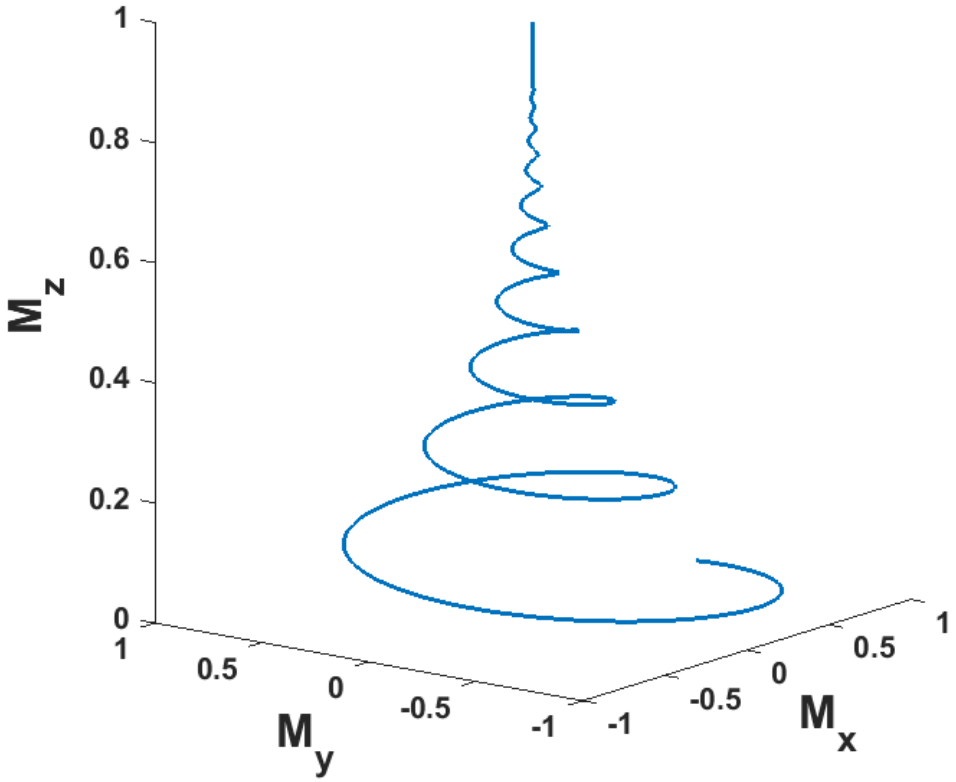


Figure 1.6: T_1 and T_2 full relaxation after $\beta = 90°$ excitation. The transverse component decays back to zero as the longitudinal component relaxes back to the equilibrium value. The parameters used in this simulation are $T_1 = 2500$ ms and $T_2 = 900$ ms, with a total durations of 10,000 ms.

Fourier transformation: application to free induction decay (FID)

The signal acquired in typical NMR experiments rarely has a single frequency contributing to a perfect exponential signal decay. In reality, the temporal signal consists of a number of frequencies which are convoluted to form a single spectrum. Since the frequency indicates the proton environment of the associated signal, deconvolution of the composite frequencies is necessary. This is achieved using a Fourier Transformation (a mathematical technique to change between a time and frequency

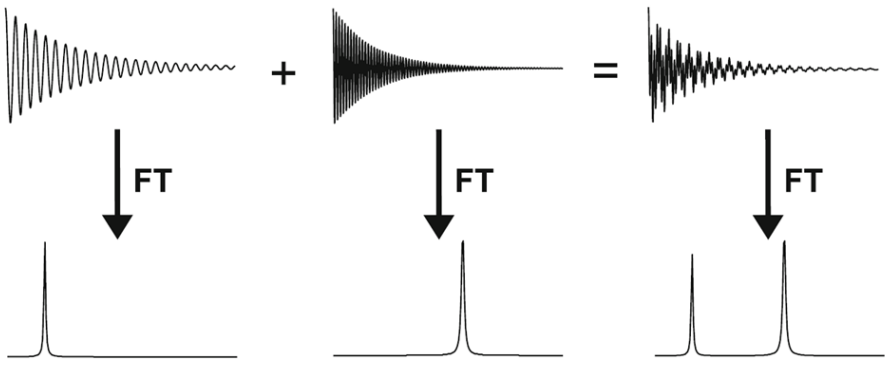


Figure 1.7: Fourier transformation of temporal frequencies into the spectral domain from [5]. The addition of two separate frequencies in the temporal domain leads to a convoluted FID signal. Fourier transformation of the signal shows two clear contributing frequencies in the frequency domain.

domain). The general form of the Fourier Transform (FT) is given by:

$$F(k) = \sqrt{\frac{1}{2\pi}} \int_{-\infty}^{+\infty} e^{-i2\pi kt} f(t) dt \tag{1.1.39}$$

where $f(t)$ is the function defining the NMR signal in the time domain and $F(k)$ it the Fourier transformed counter–part in the frequency (k) domain. The ideal example of a single frequency exponential decay from a simple FID experiment, can be Fourier transformed, following the Bloch equations which account for the transverse exponential relaxation. This resulting shape has both real and imaginary parts, to account for amplitude and signal phase, where the real part defines a Lorentzian lineshape after FT application. Fig. 1.7 gives an example of a FT application between the time and frequency domain.

Chemical shift

Alluded to above, a major advantage of using NMR is the specificity of signals to particular molecules or bonds. The electron cloud distributed around a nuclei will affect the frequency observed in an NMR exper-

iment. The effective magnetic field, B_{eff}, experienced by a species depends upon the shielding factor, σ, such that $B_{\text{eff}} = B_0(1-\sigma)$. The chemical shift, δ, is defined as:

$$\delta = \frac{\omega_{\text{eff}} - \omega_{TMS}}{\omega_{TMS}} \times 10^6 \tag{1.1.40}$$

where TMS is tetramethylsilane, commonly used as a reference standard to define 0 parts per million (ppm) in a frequency spectrum for ^{1}H experiments. In this thesis, convention is alternated between a ppm and frequency description depending on the most appropriate measure.

1.2 Magnetic Resonance Imaging

In imaging, additional magnetic field gradients (produced by gradient coils) are used in conjunction with the main magnetic field and act to change the magnetic field strength at a given point in the scanner; the change in magnetic field strength is linear with the distance from the centre of the coil,

$$\boldsymbol{G}(\boldsymbol{t}) = \frac{\mathrm{d}B_z}{\mathrm{d}x}\boldsymbol{x} + \frac{\mathrm{d}B_z}{\mathrm{d}y}\boldsymbol{y} + \frac{\mathrm{d}B_z}{\mathrm{d}z}\boldsymbol{z} = G_x x + G_y y + G_z z = \mathbf{G}.\mathbf{r} \quad , \tag{1.2.1}$$

where

$$G_x = \frac{\partial B_z}{\partial x} \quad G_y = \frac{\partial B_z}{\partial y} \quad G_z = \frac{\partial B_z}{\partial z} \quad , \tag{1.2.2}$$

with B_z being the scalar field and $\boldsymbol{G}(\boldsymbol{t})$ a general gradient vector. Using the relation between magnetic field and frequency in Eq. 1.1.8, the general frequency of the spins at a point $q(x,y,z)$ is shown to depend on the magnetic fields as follows:

$$\omega = \omega_0 + \Delta\omega = \gamma(B_0 + G_x x + G_y y + G_z z) \quad , \tag{1.2.3}$$

and with radial co–ordinates this is $\omega = \gamma(B_0 + \mathbf{G}.\mathbf{r})$. A higher magnetic field causes a higher resonant frequency, which is generated due to the spatial dependence of the magnetic field upon distance.

1.2.1 Slice selection

MRI is generally required to be selective in the thickness of the two dimensional (2–D) images acquired. The slice thickness is a compromise

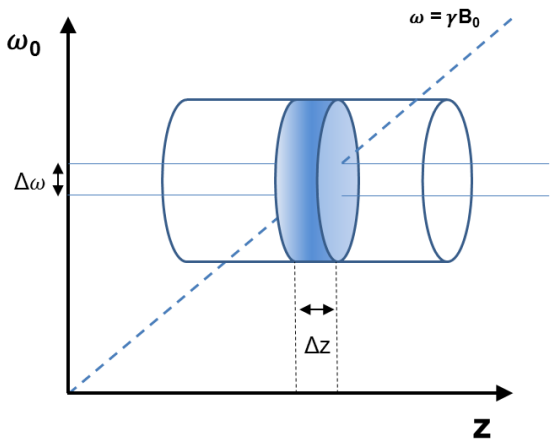


Figure 1.8: Slice selection achieved with varying magnetic field strength. A slice selective gradient applied across an object will vary the resonant frequency of the spins linearly with spatial distance in the direction of the applied gradient. The points at which the dashed line intersects the cylindrical object define the limits of the slice selection, and consequently the frequencies being excited. The steeper the dashed line (i.e. the stronger the field gradient), the smaller the slice thickness will be, since the resonant frequency will be increased.

between various factors: too thick and the detail of the image is lost as the signal is acquired over structurally different regions; too thin and not enough signal will be acquired leading to an image with low signal intensity. The solution to obtaining optimal 2–D slice thickness in MRI is to use R.F. pulses which are slice selective. Pulses are used which vary B_1 over the duration of the applied pulse. Such pulses use a flip angle, θ, given by

$$\theta = \int_0^T \gamma B_1(t) \mathrm{d}t \quad . \tag{1.2.4}$$

A FT of the pulse shape will produce a slice of the same shape, relative to the selection direction [6],

$$\text{slice width} = \frac{2\pi \times \text{R.F. bandwidth}}{\gamma G_z} = \frac{\Delta\omega}{\gamma G_z} \tag{1.2.5}$$

where the slice thickness is equivalent to Δz in Fig. 1.8. The gradient is applied for a time, t, and then a reverse slice gradient with opposing polarity refocuses the spins to their original phase. The area of the refocussing gradient applied in the slice encoding direction (in a time vs. gradient strength plot) must equal one half of the original slice selective gradient for complete rephasing.

1.2.2 Frequency encoding

Slice selection provides the signal in a given slice, and the process is characterised by the application of an excitation pulse to excite the slice whilst under a gradient (normally in the z direction). However, to produce an image, 2–D spatial information must be encoded into the acquisition part of the sequence. This is achieved by encoding the frequency of the sample spins in one direction, during the acquisition of the signal, by applying a field gradient in that particular direction (normally known as the x direction or the "read" direction) [5]. In the x–direction, the distance is linearly related to the strength of the gradient applied [6]:

$$f(x) = \frac{\gamma}{2\pi}(B_0 + x.G_x) \quad . \tag{1.2.6}$$

This equation shows that a higher signal frequency is produced the further a sampled point is from $x = 0$. The signal, $S(t)$, under the influence of an x–gradient is given by

$$S(t) = \int \rho(x) e^{i\omega t} \mathrm{d}x \quad , \tag{1.2.7}$$

where $\rho(x)$ is the density of the spins, as a function of x. In the x direction, $x = \omega/\gamma G_x$, where x can be re–arranged for ω in Eq. 1.2.7 such that,

$$S(t) = \int \rho(x) e^{ix\gamma G_x t} \mathrm{d}x \quad . \tag{1.2.8}$$

An alternative variable for the frequency can be defined as k_x such that,

$$k_x = -\gamma G_x \Delta t \quad , \tag{1.2.9}$$

where Δt is the separation between points sampled in the time domain. Convention defines the number of points sampled in the x direction as

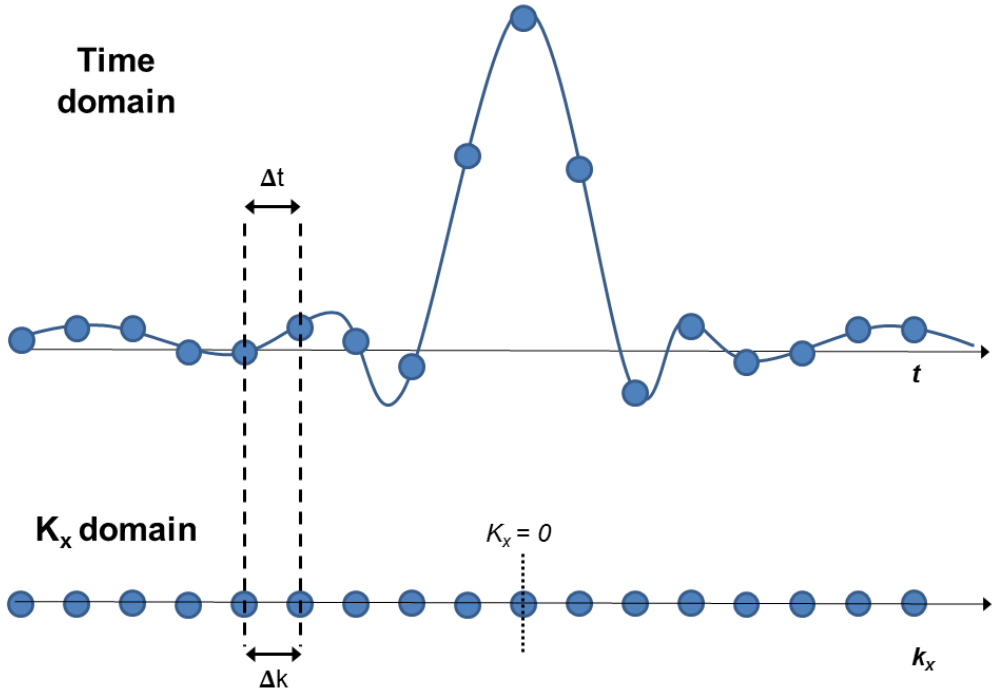


Figure 1.9: Relationship between sampling in the time and k–space domain. The distance between sampling points in the time domain is Δt which is the equivalent of Δk in the k_x domain.

N_x, such that the total sampling time, T, is given by $T = N_x \Delta t$ (demonstrated in Fig. 1.9) . The use of the alternative variable, k, better known through the concept of k–space [7], can be generalised as

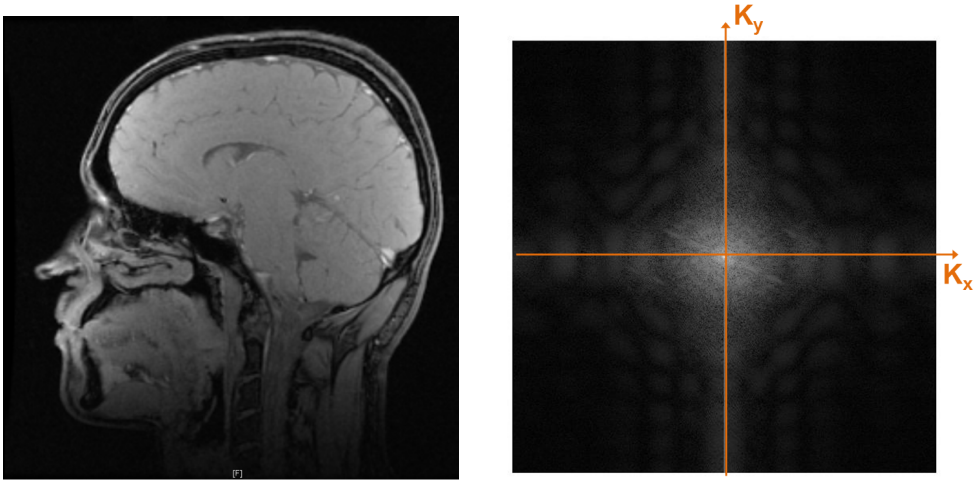
$$\boldsymbol{k}(t) = \gamma \int_0^t \boldsymbol{G}(t')\mathrm{d}t' \quad , \tag{1.2.10}$$

where $\boldsymbol{G}$ is the vector gradient of the magnetic flux and $\boldsymbol{k}$ is the scanning trajectory in the k–space plane. The signal in Eq. 1.2.8 can now be stated as,

$$S(x) = \int \rho(x) e^{-ixk_x} \mathrm{d}x \quad . \tag{1.2.11}$$

1.2.3 Phase encoding

To provide a 2–D or three dimensional (3–D) image, phase encoding must be used determine the phase of an MR signal. A gradient applied in the y–direction, G_y, will produce a change in the phase of the nuclei;



(a) **(b)**

Figure 1.10: Effect of FT on MR image. (a) An MR intensity image has a FT applied, **(b)** giving the corresponding k–space image.

a nuclei further away from the zero point will precess faster, and a nuclei closer to the zero point will precess slower. The quantity of phase shifting induced by a gradient in the phase direction, G_y, is given by:

$$k_y = -\gamma y G_y t \quad . \tag{1.2.12}$$

where k_y is the phase shift in the phase encoding (y) direction. Analogous to Eq. 1.2.8, the signal, $S(t)$ obtained under a phase gradient is given by,

$$S(t) = \int \rho(y) e^{i\gamma y \int G(t)\mathrm{d}t} \mathrm{d}y \quad , \tag{1.2.13}$$

where $\rho(y)$ is the density of spins, as a function of y. Since the gradient strength is varied to induce different phase shift quantities, the integral of the phase gradient is required. A single phase gradient is applied to modulate a single phase, and for N_y sampling points in the y direction N_y separate gradients must be applied.

Including the contribution of phase encoding to the signal, Eq. 1.2.11 can be adapted to include this second dimension,

$$S(x,y) = \int \int \rho(x,y) e^{-(ik_x x)} e^{-(ik_y y)} dx dy \quad , \tag{1.2.14}$$

such that the signal intensity depends on the frequency and phase of the signal acquired and the expressions for k_y and k_x are used.

The signal intensity in k–space is now related to the proton density in the Cartesian (x, y, z) co–ordinate system. By performing a Fourier transform of $S(k_x, k_y)$, $\rho(x, y)$ can be obtained. This FT method forms the basis of image production in MRI, where k space is sampled and then Fourier transformed to produce the proton density at a given point,

$$\rho(x,y) = FT^{-1}[S(k_x,k_y)] = \int\int S(k_x,k_y)e^{-(ik_x x + ik_y y)}dk_x dk_y \quad . \quad (1.2.15)$$

This illustrates the key concept in k–space which is that the trajectory in which the points in k–space are traversed or sampled is determined by the nature in which the read and phase encoding gradients are applied. Consequently, the field of view (FOV) obtained in an MR image is related to the sampling rate of the k–space geometry [3],

$$\mathrm{FOV_x} = \frac{1}{\Delta k_x} = \frac{2\pi}{\gamma G_x \Delta t} \quad (1.2.16)$$

$$\mathrm{FOV_y} = \frac{1}{\Delta k_y} = \frac{2\pi}{\gamma \Delta G_y t_{ph}} \quad , \quad (1.2.17)$$

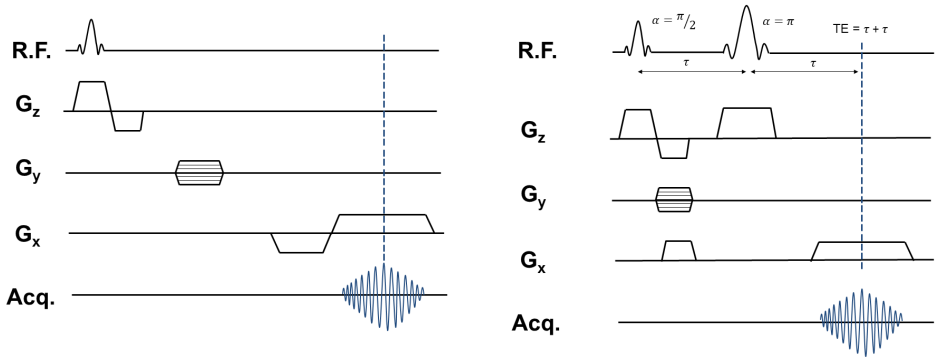
where $\mathrm{FOV_x}$ and $\mathrm{FOV_y}$ are the field of view length in the x and y directions respectively, ΔG_y is the phase encoding gradient step size and t_{ph} is the duration of the phase encoding. Fig. 1.10 shows an image which has been processed from the intensities sampled in the corresponding k–space domain.

1.2.4 Sequence types: gradient and spin echo

Two main categories of pulse sequence exist in MRI: spin echo (SE) and gradient echo (GE) sequences. Fig. 1.11 shows the pulse sequence representation with contributions from the read (G_x), phase (G_y) and slice encoding (G_z) gradients and the position of the acquired signal.

Gradient echo

A gradient echo imaging sequence uses the application of magnetic gradients in the read direction to refocus the proton signal after excitation.The process begins in an identical way to spin echo experiments, in which a R.F. pulse is applied to transfer the magnetisation into a non–equilibrium state. The slice selective gradients are applied, and the phase



(a) **(b)**

Figure 1.11: Pulse sequence diagram of gradient and spin echo methods. The application of magnetic gradients in the read, phase and slice selective directions are demonstrated for the gradient and spin echo methods. The acquisition of signal (Acq.) is shown, along with the timing of applied R.F. pulses.

gradients select the line of k–space to acquire signal from. The defining feature of the gradient echo scan is the way in which the read gradient is applied. A negative read gradient is applied for a period of time, τ, which causes the spins to dephase in the xy plane. This is immediately followed by a positive gradient of the same strength applied for a time 2τ. This positive gradient acts to refocus the spins, producing a maximum measurable signal at a time τ into the duration of the positive gradient application. The echo time for a gradient echo sequence is defined as the time between the middle of the R.F. pulse and the middle of the frequency encoding (data acquisition) gradient. The signal available, S, is given by,

$$S = \rho \frac{(1 - e^{-\frac{T_R}{T_1}})}{1 - e^{-\frac{T_R}{T_1}} \cos(\alpha)} e^{-\frac{TE}{T_2^*}} \sin\alpha \quad . \tag{1.2.18}$$

where the maximum signal intensity achievable for a gradient echo scan with a repetition time T_R, is achieved by choosing an optimal flip angle, α, value. This flip angle is known as the Ernst angle, in which α is maximised for optimal signal intensity in Eq. 1.2.18:

$$\alpha = \cos^{-1}(e^{-\frac{T_R}{T_1}}) \quad . \tag{1.2.19}$$

Spin echo

The idea of refocussing is also applied in spin echo methods. A $\pi/2$ pulse is applied to a sample, with slice and phase selective gradients applied, initiating dephasing of the spins. After a time, τ, a second pulse with a flip angle of π is applied. The second pulse inverts the dephasing spins, causing a refocussing of the signal at a time 2τ after the initial pulse. In SE experiments the echo time, TE, is defined as $TE = 2\tau$. The signal intensity of a spin echo sequence depends on the transverse signal decay after excitation and the time between pulses (repetition time, TR) which determines how much signal can relax back to equilibrium. This signal is given by,

$$S = \rho(1 - e^{-\frac{TR}{T_1}})e^{-\frac{TE}{T_2}} \quad . \tag{1.2.20}$$

1.3 Contrast: paramagnetic relaxation

Inner and outer sphere model

Molecular interactions between nuclei cause relaxation effects and in MRI, the paramagnetic relaxation induced by gadolinium (Gd(III)) is used in the majority of MR scans with a contrast agent [9]. The T_1 relaxation of a solvent (normally water) in the presence of paramagnetic Gd(III), depends on both diamagnetic and paramagnetic contributions [10]:

$$\frac{1}{T_{i,obs}} = \frac{1}{T_{i,d}} + \frac{1}{T_{i,p}} \quad i = 1, 2. \tag{1.3.1}$$

where $T_{i,obs}$ is the observed T_1 or T_2 value and T_i, d and T_i, p are the diamagnetic and paramagnetic contributions to the longitudinal or transverse relaxation values respectively. The contribution of the paramagnetic effect is linearly proportional to the Gd(III) concentration:

$$\frac{1}{T_{i,obs}} = \frac{1}{T_{i,d}} + c_i[Gd(III)] \quad i = 1, 2. \tag{1.3.2}$$

Here, c_i is the concentration of gadolinium. The paramagnetic mechanism of relaxation is caused by the dipole–dipole interactions between

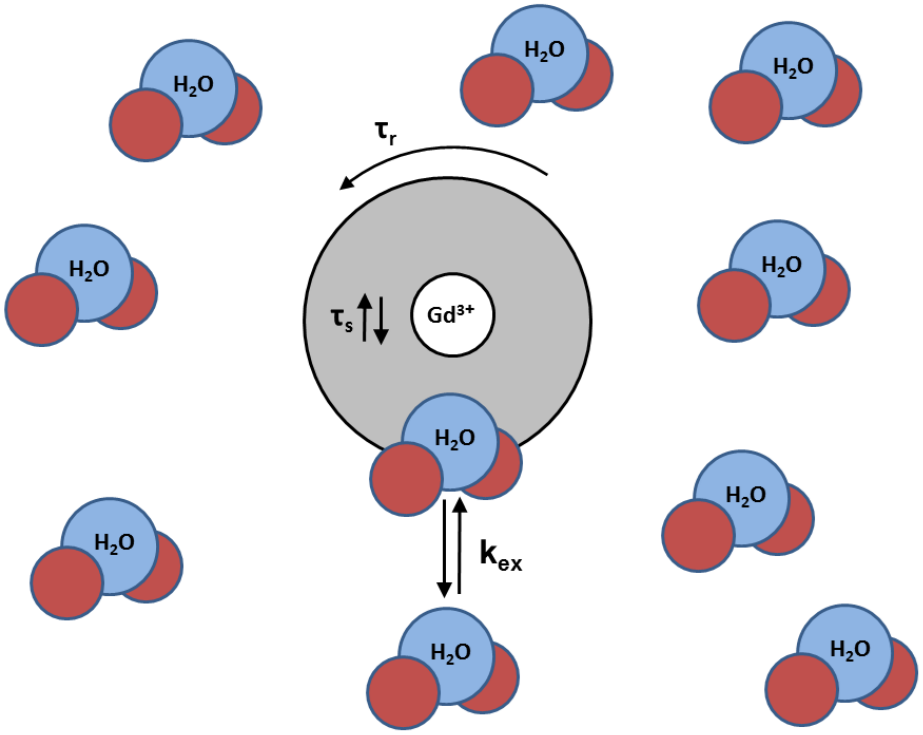


Figure 1.12: Paramagnetic relaxation effect of gadolinium on surrounding water . Here, τ_r is the rotational correlation time of the gadolinium molecule, k_{ex} is the exchange rate and τ_s represents the longitudinal and transverse relaxation times of the paramagnetic electrons [8].

proton spins and the paramagnetic electron spins, which in turn is comprised of two separate relaxation contributions. The first contribution is termed the inner sphere (IS) contribution and this represents the direct proximal dipole interactions between nearby water protons and the gadolinium electrons. These inner sphere protons are said to be bound to the gadolinium chelate. The paramagnetic relaxation also affects the bulk water as a whole. The diffusive, random motion of the paramagnetic centre induces transient relaxation in the bulk water and is known as the outer sphere (OS) contribution. The contributions of the IS and OS relaxivities to the overall paramagnetic contribution are illustrated in Fig. 1.12 and mathematically defined as,

$$\frac{1}{T_{i,p}} = \left(\frac{1}{T_{i,p}}\right)^{IS} + \left(\frac{1}{T_{i,p}}\right)^{OS} \quad i = 1, 2. \tag{1.3.3}$$

Several mechanisms contribute to the IS relaxation. When the magnetic moments of two nuclei interact, fluctuations in the magnetic field can arise which is known as dipole–dipole interactions or dipolar coupling. The theory of this interaction was outlined first by Solomon in the 1950's [11]. Interactions between a nucleus and the electron can also affect the magnetic field, and this interaction is known as a scalar interaction. Additional relaxation effects arise through quadrupolar magnetic moments from non–spin 1/2 particles, but a discussion of this is beyond the scope of this thesis.

Other effects which induce relaxation include chemical shift anisotropy (CSA), where the chemical shift of a nucleus is affected by neighbouring electron cloud orientations. Spin–rotation relaxation, which arises from electron cloud movement in a molecule, is also particularly important for quickly rotating small molecules in a non–viscous lattice.

In paramagnetic systems, electron spin and nuclear spin population energy level differences induce a magnetic moment for systems adhering to the Boltzmann distribution, which is known as Curie relaxation. The relaxation due to a paramagnetic species is dominated by dipole–dipole interactions and scalar interactions, where Curie contributions are assumed to be small.

Modified Solomon–Bloembergen equations

The T_1 and T_2 relaxation rates of the bulk water in the inner sphere are given by

$$\left(\frac{1}{T_1}\right)^{IS} = \frac{1}{55.5}\frac{cq}{T_{1m}+\tau_m} \tag{1.3.4}$$

and

$$\left(\frac{1}{T_2}\right)^{IS} = \frac{cq}{55.5\tau_m}\frac{T_{2m}^{-2}+\tau_m^{-1}T_{2m}^{-1}+\Delta\omega_m^2}{(\tau_m^{-1}+T_{2m}^{-1})^2+\Delta\omega_m^2} \tag{1.3.5}$$

respectively. In these equations, T_{1m} and T_{2m} are the longitudinal and transverse relaxation rates for protons in the bound water respectively, τ_m $(= 1/k_{ex})$ is the lifetime of the water molecule in the inner sphere of the gadolinium chelate, $\Delta\omega_m$ is the chemical shift difference in frequency between bound and bulk water, c is the molal concentration and q is the number of water molecules bound to the gadolinium chelate (in the

inner sphere).

The bound proton relaxation times are composed of the scalar contact and dipole–dipole contributions, such that

$$\frac{1}{T_{im}} = \frac{1}{T_i^{DD}} + \frac{1}{T_i^{sc}} \quad i = 1, 2 \quad , \tag{1.3.6}$$

where T_{im} is affected solely by the dipole and scalar contact contributions. The dipole–dipole contributions in this above equation are given explicitly by the Bloembergen–Pound–Purcell (BPP) theory [12]:

$$\frac{1}{T_1^{DD}} = \frac{2}{15}\frac{\gamma_I^2 g^2}{r_{GdH}^6}\mu_B^2 S(S+1)\left(\frac{\mu_0}{4\pi}\right)^2\left[7\frac{\tau_{c2}}{1+\omega_s^2\tau_{c2}^2} + 3\frac{\tau_{c1}}{1+\omega_I^2\tau_{c1}^2}\right] \tag{1.3.7}$$

$$\frac{1}{T_2^{DD}} = \frac{1}{15}\frac{\gamma_I^2 g^2}{r_{GdH}^6}\mu_B^2 S(S+1)\left(\frac{\mu_0}{4\pi}\right)^2\left[13\frac{\tau_{c2}}{1+\omega_s^2\tau_{c2}^2} + 3\frac{\tau_{c1}}{1+\omega_I^2\tau_{c1}^2} + 4\tau_{c1}\right] \quad . \tag{1.3.8}$$

In these equations, r_{GdH} is the distance between the gadolinium and hydrogen atoms, g is the electron g factor, μ_B is Bohr's magneton, ω_S and ω_I are the nuclear and electron Larmor frequencies. The correlation times, τ_{ci} and τ_{ei} are given for i = 1, 2 :

$$\frac{1}{\tau_{ci}} = \frac{1}{\tau_R} + \frac{1}{T_{ie}} + \frac{1}{\tau_m} \tag{1.3.9}$$

$$\frac{1}{\tau_{ei}} = \frac{1}{T_{ie}} + \frac{1}{\tau_m} \tag{1.3.10}$$

where τ_R is the rotational correlation time and T_{1e} and T_{2e} are the metal ion longitudinal and transverse electron spin relaxation times.
The scalar contact contribution to T_1 and T_2 is given by:

$$\frac{1}{T_1^{SC}} = \frac{2S(S+1)}{3}\left(\frac{A}{\hbar}\right)^2\left(\frac{\tau_{e2}}{1+\omega_s^2\tau_{e2}^2}\right) \tag{1.3.11}$$

$$\frac{1}{T_2^{SC}} = \frac{S(S+1)}{3}\left(\frac{A}{\hbar}\right)^2\left(\frac{\tau_{e2}}{1+\omega_s^2\tau_{e2}^2} + \tau_{e1}\right) \quad . \tag{1.3.12}$$

where $(A/\hbar)$ is the hyperfine or scalar coupling constant.

1.3.1 Alterative nuclei: ^{19}F as a contrast agent

The first use of fluorine MRI is generally attributed to Holland et al. in 1977 at Nottingham University [13], shortly after the development of proton MRI. There are several similarities between fluorine and hydrogen, rendering them useful in MRI. Both fluorine and hydrogen have an intrinsic spin of 1/2, allowing the splitting of energy levels in the presence of an external magnetic field, a necessary feature for MRI compatible nuclei.

The gyromagnetic ratio of an atom also plays a role in determining the suitability that a nuclei has for MRI imaging. Fluorine has a gyromagnetic ratio of 40.053 MHz T^{-1} which is close to the value of 42.576 MHz T^{-1} for hydrogen, using Table 1.1. The majority of the literature quotes the sensitivity as being proportional to the cube of the gyromagnetic ratio and this leads to the fact that fluorine has 83 % of the sensitivity of hydrogen for MRI; an alternative proportionality relation gives the sensitivity as dependent upon the gyromagnetic ratio to the power of $\frac{11}{4}$, assuming the quality factor, Q, scales with the square root of the resonant frequency [14], leading to an 84.5 % sensitivity of fluorine compared to hydrogen. The quality factor is discussed in Chapter 3, and is a measure of the sensitivity of an MRI coil.

Regardless of the particular definition used, compared to the ratios for other spin 1/2 nuclei 6.4 % for ^{31}P and 1.6 % of ^{13}C, it is clear that fluorine's gyromagnetic ratio is very favourable in terms of sensitivity for magnetic resonance experiments. ^{19}F is also 100 % naturally abundant which means that one can be certain of the molecular weight of any fluorine atoms used in MRI experiments, i.e. monoisotopic. This certainty is useful for precise measurements in spectroscopic experiments, where the signal observed comes from a single chemical isotope.

Another prominent feature of fluorine is that it exhibits a very large chemical shift (around 300 ppm) under the influence of an external magnetic field. This is due to the seven electrons in the fluorine outer shell which are loosely held by the central nucleus, compared to the single electron held by a hydrogen atom. Consequently, the fluorine atom is

very sensitive to the environment it is placed in.

Most importantly, there is no background fluorine present *in vivo* meaning ^{19}F MRI has excellent specificity, a key attribute for molecular targeting. Put simply, if a fluorinated contrast agent is administered into a system then only the fluorine associated with the contrast agent will be detected. This "hotspot" method has the obvious advantage over conventional proton MR, where it is more difficult to distinguish the origin of a signal due to the large quantities of ^{1}H nuclei present in water. There are small amounts of fluorine present in the body, bound in the teeth and bones, but this is present in such small quantities and with very short T_2^* values that only very specialised techniques can detect it.

CHAPTER 2

Contrast agents and molecular imaging: biomarkers and imaging strategies

2.1 Outline

This chapter will cover the emerging need for exogenous molecular biomarkers in medicine, as well as highlighting the role contrast agents currently play in this field. There is a growing need in medicine to understand processes and function in the body at a molecular and cellular level rather than rely on larger scale features such as shape and size to predict outcomes in disease. Conventional and more clinically routine MR imaging methods use anatomical scans as a diagnostic tool but recent advances in the field of MR aim to use molecular information to gain a better understanding of different pathophysiologies. Later chapters explore a novel endogenous contrast mechanism (CEST), whilst Chapters 2 to 4 focus on exogenous contrast.

2.2 Introduction to current contrast agents (CAs) in MRI

MRI scans are used ubiquitously in modern healthcare systems as a diagnostic tool and over a third of clinical MR examinations use a contrast agent [15]. Currently, there are eleven MR CAs administered by intravenous (i.v.) injection, with a few commercially ingestible agents also available [16]. Clinical contrast agents tend to be classified as T_2 (iron oxide) or T_1 (gadolinium) contrast agents, with appropriate MR scans tailored accordingly to the individual relaxation parameter. These contrast agents will affect both T_1 and T_2 values, as shown in Chapter 1, but the definition refers to the parameter which is greatest affected by a particular agent.

2.2.1 T_1 agents: gadolinium contrast agents

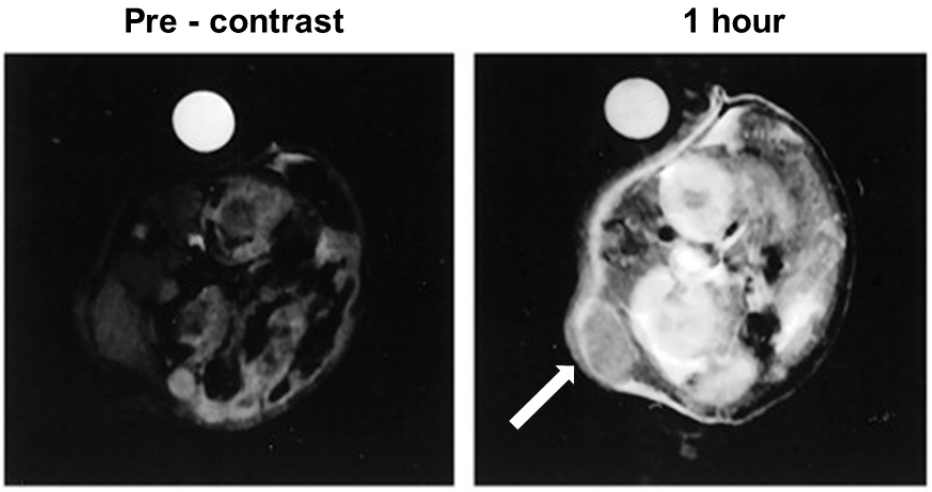


Figure 2.1: Tumour enhancement with gadolinium based contrast agent from Artemov et al. [17]. A T_1 weighted image of mouse model of a HER–2/neu expressing tumor before and one hour after injection of gadolinium CA is shown. The CA binds to herceptin in the tumour increasing the local CA concentration there. In a T_1 sequence, the intensity is increased due to the increased relaxation of tissue near to the CA; the white arrow indicates the location of the tumour.

Paramagnetic contrast agents which are based on Gd^{III} have 7 unpaired electrons ([Xe] $4f^7$), which have a positive magnetic susceptibility creating a reduction in T_1 and T_2 times of surrounding media. Gd^{III} must be encased or chelated since a free gadolinium ion produces a toxic effect *in vivo*. The first Gd^{III} CA for clinical use was gadolinium(III) diethylene–tetra–amine–penta–acetic acid (Gd–DTPA) in 1987, approved for cancer patients to detect brain tumours [16] with manifold applications demonstrated since.

Widest use has been for the anatomical and functional delineation of solid brain tumours, in which the CA passes through the disrupted blood brain barrier (BBB), and accumulates at the tumour site to cause MR contrast. In particular, dynamic contrast enhanced (DCE) MRI has been developed to measure quantitative parameters, such as permeability and other pharmokinetic parameters, showing good ability to assess cancer treatment effectiveness [18]. Fig. 2.1 shows the intensity enhancement visible one hour after gadolinium CA administration in a mouse tumour model.

MR angiography (MRA) has been clinically used for many years to image blood vessels, initially by measuring signal differences between flowing blood and static tissue, known as the time–of–flight (TOF) method [19]. The advent of contrast agents has allowed contrast–enhanced MRA via a bolus injection to reduce the blood T_1 for blood vessel imaging; reduction of T_1 is typically of the order of 10^2 ms [20].

Problems for gadolinium contrast agents are the confusion between background signals and contrast agent induced signals. Paramagnetic species such as oxygen or iron compounds in the body produce a similar appearance to contrast agents, and a high concentration is needed to provide sufficient contrast [15]. Gadolinium is also toxic, with the stability of gadolinium chelates being affected by hydroxyl groups [21]. The hydroxyl groups reduce the capability of the chelate to bind the gadolinium and acidic conditions increase the probability of gadolinium being released in solution. Biological systems cannot differentiate between large metal ions such as calcium and gadolinium due to their similar size, and consequently gadolinium is mistakenly uptaken cellularly. In high

enough doses, this leads to a condition known as Nephrogenic Systemic Fibrosis (NSF), which is a disease of fibrosis of the internal organs. This was an issue for early contrast agents, such as Gd–DPTA, which were given to patients with poor kidney function who within a month developed symptoms of NSF [22]; the cause of this was not recognised at the time. In patients with compromised kidney function, the clearance of the compound takes an extended period of time during which the gadolinium can "leak" out of the chelate; this dissociation is caused by acidic conditions in the environment as well as the presence of endogenous metals ions such as calcium and zinc. More recently, long term retention of gadolinium has been shown in subjects who have not had a history of kidney disease, although the implications of this are not yet known [23].

Around 1 in 6 people in the US suffer from chronic kidney disease (CKD) [24] and would therefore be ineligible for imaging using conventional gadolinium CA scans. This group of patients often suffer from other comorbidities and would be most at need of diagnostic MR techniques to assess organ function and guide therapeutic decisions, which provides the need for a gadolinium alternative MR contrast agent [25].

2.2.2 T_2 agents: iron oxide contrast agents

Iron oxide based compounds used for MR purposes tend to be referred to as super paramagnetic iron oxide (SPIO) compounds. SPIOs are composed of a Fe_3O_4 (magnetite) or γ Fe_2O_3 (maghemite) central structure, encased in a hydrophilic coating, typically ranging in size from 10^{-9} up to 10^{-6} m, depending on the end application [26]. The primary mechanism of relaxation for this category of contrast agent is from the paramagnetic iron oxide (in a similar manner to other paramagnetic ions such as Mn^{2+}, Gd^{3+} etc.). In SPIOs, the whole crystallite material's magnetic moment will tend to align with an external magnetic field, in contrast with purely paramagnetic materials in which only individual atoms align. This is the key difference between SPIOs and gadolinium contrast agents. The SPIO contrast is generated in proton–rich solutions, such as water and *in vivo*, by the dipole–dipole interaction between the magnetic

moment of the paramagnetic electrons and the magnetic moment of the solution proton in a similar way to Gd^{III} paramagnetism [27]. This large magnetic effect produces dark spots in areas of SPIO accumulation in MR images.

Applications using SPIOs have included targeting cancer and for imaging of the liver and spleen. Combidex® has been used in the detection of lymph node metastases, with the first application shown in prostate cancer patients in 2003 [28]. SPIOs are small enough to be retained in lymph nodes but not to permeate the metastases. Thus, lymph nodes appear black on an MRI scan whilst tumour tissue is white; lymph nodes without metastases are completely black and those with metastases are an inhomogeneous combination of the two. Bowel imaging has proved possible with oral SPIO contrast agents such as Lumirem® [29]. Lumirem has a high relaxivity (72 $mmol^{-1}$ L s^{-1}) and is coated in an insoluble matrix which does not degrade during transit through the bowel. Other agents such as Endorem® accumulate in the liver and spleen (80 % and 10 % respectively [29]). Peak concentrations were found in the liver two hours after i.v. administration in a iron deficient rat model [30].

As the MR signal to identify SPIOs is ^1H based, background signals *in vivo* can also confound MR results using this technique. Additionally, information on the viability of labelled cells for molecular imaging applications is limited. Once labelled, the position of a SPIO compound may be inferred but whether the cells are alive or dead, or any other physiological information, is not available [31]. A recent study reiterated the utility of SPIO particles for tracking stem cells in rats, but suggested that the long term fate of cells was unclear due to uncertainty around monitoring cell proliferation and migration [32]. Confusion with signal from endogenous molecules has been shown by Van den Boss et al. [33] to interfere with the signal from iron oxide labelled cells in a pig model of myocardial infarction.

2.2.3 The need for an alternative: towards molecular imaging using MRI

Molecular imaging represents a paradigm shift in the information generated from imaging modalities and has seen a revolution in imaging in the past two decades. Traditionally, imaging has used morphological observations to inform biological theories, yet molecular and cellular imaging may provide functional information to improve our biological understanding

Molecular imaging has allowed scientists to establish important biomedical goals, of which several are relevant to the work described in this thesis. These include: the non–invasive *in vivo* imaging of specific molecular or cellular processes; the tracking of specific cells or cell populations; and the monitoring of disease progression at a molecular level [34]. Developing in parallel with biotechnology advances, imaging modalities have an increased "arsenal" of technologies and methodologies to target cellular and molecular processes [35].

2.3 Molecular contrast agents for MRI

In 1997, Moat et al. [36] developed what is considered as the first demonstration of a "smart" or molecular contrast agent (these terms are used interchangeably in the literature and I follow this convention). This class of contrast agent typically changes the MR detectable signal to reflect changes in the molecular environment. This CA was designed to be sensitive to β–galactosidase with a mechanism based on an increased water accessibility to the inner co–ordination sphere, where a blocking group is removed from the chelate to increase q upon enzyme contact. Later, this mechanism was demonstrated *in vivo* to indicate reporter gene expression [37] (see Fig. 2.2).

With smart MR probes, we are generally interested in observing changes in a particular parameter space to generate observable MR contrast. Based on the categorisation given by Hingorani et al. [38] in a recent review pa-

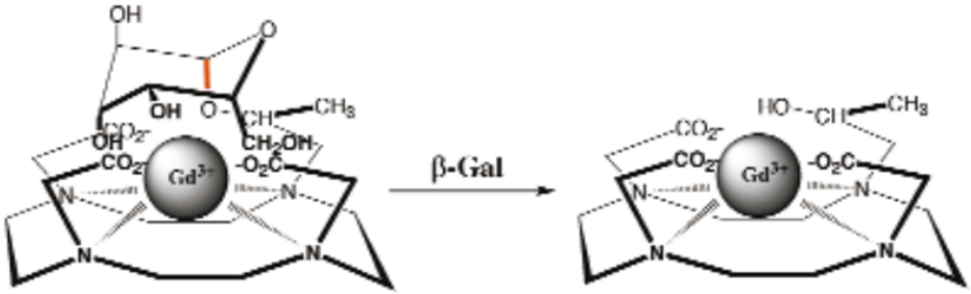


Figure 2.2: Molecular interactions change q number in MR probe from [37]. The chelated gadolinium has one of its water binding sites blocked by a sugar moiety. Upon enzyme addition this sugar is removed, increasing the q value and hence the relaxivity.

per, six key changes which can be applied to observe molecular activity are outlined below:

- **Water accessibility** – Changing a molecule's q number, will allow a larger bulk water relaxation when the exchange site contains a magnetically influencing ion such as paramagnetic gadolinium.
- **Ligand proximity** – Composite molecules may have nuclei which are magnetically affected by the proximity of certain elements. Modulation of this distance, often through molecular cleavage, produces a change in the MR signal.
- **Rotational tumbling time** – Factors such as the size of a molecular will affect its rotational dynamics in solution. Generally, a slower rotational tumbling time will reduce T_1, from the BPP equations in Chapter 1.
- **Aggregation state and superparamagnetism** – SPIO particles generate a strong T_2^* contrast. If molecules cluster, the T_2 is reduced due to the increased proximity of spins.
- **Chemical exchange rate with water** – Selective saturation techniques can highlight the magnetic transfer of protons, which is the key feature of the CEST technique.

- **Electron shielding and chemical shift** – Chemical interactions may alter the MR contributing nuclei environment, which can lead to a change in the chemical shift or the addition/removal of MR peaks.

The following section highlights current responsive molecular MR probes based on these categories.

2.3.1 Detection of enzymes

Enzyme activity is responsible for the majority of cellular and molecular activity in the body, yet many enzymes are produced in an inactivated form. Activation can occur given appropriate molecular signalling and it is the activation state of such enzymes, rather than the mere presence, which is one of the goals of modern responsive MR agents.

Tumbling time mechanisms

MR sensors have been developed which change their tumbling time, upon enzymatic contact. Gadolinium based sensors which are hydrolysed by β–galactosidase exhibit changing r_1 ($r_1 = 1/T_1$) relaxivity due to protein binding from the increased reactivity after hydrolyisis [39]. Other gadolinium chelates have been constructed to form macrocyclic nanoparticles upon cleavage of ligands by the enzyme furin [40].

CEST agents: PARACEST, DIACEST

The first demonstration of a paramagnetic CEST agent as an MRI agent was given by Zhang et al. and showed a large ($\sim$ 60 ppm) ppm difference between the water bound to an europium compound and the bulk water [41]. Enzymatic targets have been of particular interest for paramagnetic chemical exchange saturation transfer (PARACEST) applications. Yoo and colleagues developed a PARACEST agent to detect urokinase plasminogen activator (uPA), a protease biomarker of pancreatic cancer and an important matrix metalloproteinase (MMP) activator. A synthesised lanthanide–DOTA (tetra–azacyclo–dodecane–tetra–acetic acid) complex gave a 10 % CEST effect upon uPA addition [42]. It has also been shown that a chemical shift in the CEST effect from a PARACEST agent can be used to indicate the presence of transglutami-

nase [43]. Work demonstrating that chemical reactions can create "CEST active bonds", used the creation of an amine group onto a PARACEST agent to highlight esterase interaction [44].

HYPER–CEST

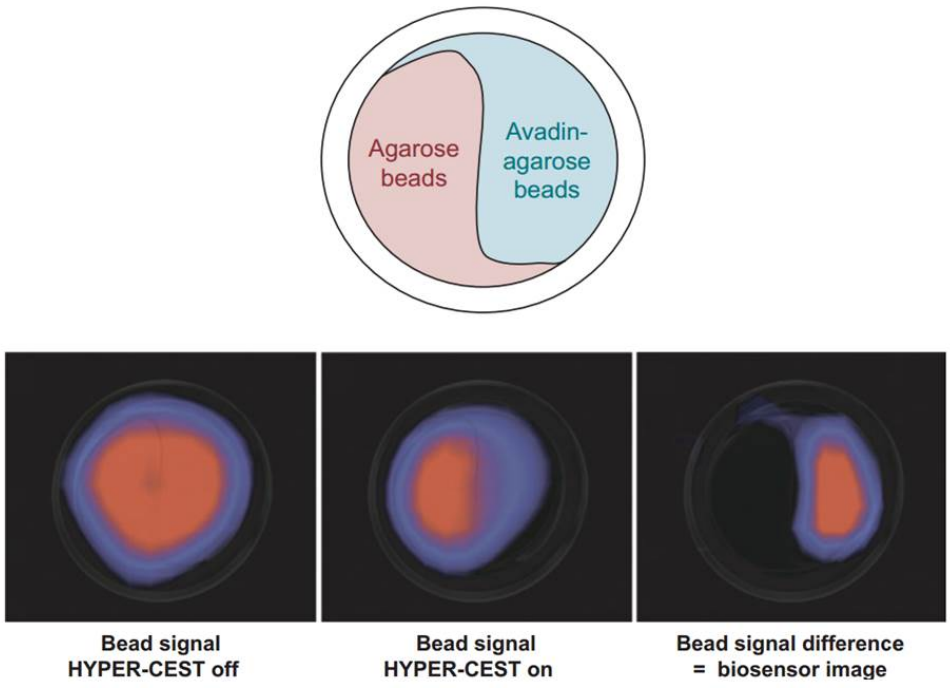


Figure 2.3: Molecular specificity of the HYPER–CEST method taken from [45]. The bead signal can be selectively saturated and subtracted from a non–selective image to produce an avadin–specific molecular signal.

CEST applications have been widened with the incorporation of hyperpolarised methods, combining both novel methods in a technique named HYPER–CEST. This technique is similar to CEST but uses hyperpolarised xenon along with a cryptophane cage which can "trap" xenon and change the chemical shift of the gaseous xenon. Early examples of this work investigated avidin–functionalised agarose beads [45], using a HYPER–CEST xenon method, which allowed delineation of the avadin–environment xenon, free xenon and xenon in the biosensor (see Fig. 2.3).

Ion sensors

MRI probes have also been used to detect ions, in particular, biologically important ions which are used in cellular signalling and protein construction [46]. Zinc ions have been detected with chelated gadolinium probes which bind zinc, and in doing so release additional water binding sites to increase q. Binding to zinc was found to increase the relaxivity by a factor of two for a probe synthesised by Major et al. [47]. A similar mechanism was used to demonstrate the ability to detect calcium ions, noting a r_1 change in relaxivity of 5.76 $\mathrm{mM}^{-1}\ \mathrm{s}^{-1}$ to 3.57 $\mathrm{mM}^{-1}\ \mathrm{s}^{-1}$ after calcium addition [48].

2.3.2 pH measurement

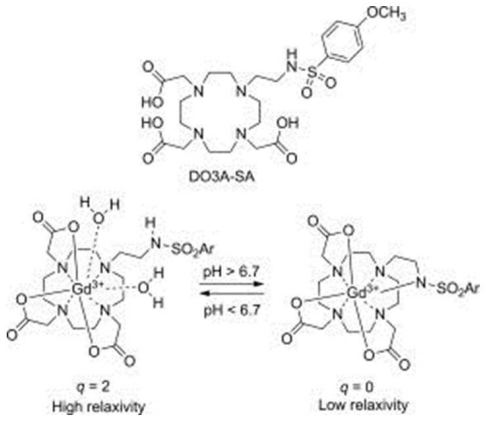


Figure 2.4: Chemical structure dependent pH alterations for Gd–DO3A molecule from [49]. The free ligand arm attaches fully to the chelate upon pH conditions above 6.7, changing the water accessibility from $q = 2$ to $q = 0$.

A change in the water accessibility, due to a change in protonation state is another method which has been used to measure pH. Probes have been developed which bind an attached ligand to a gadolinium chelate at a pH greater than 6.7 (see Fig. 2.4), reducing the q number and hence decreasing the relaxivity [49]. This probe is reversibly pH sensitive and will increase relaxivity in pH conditions less than 6.7; a two–fold relaxation enhancement was orchestrated using this technique.

Aime and colleagues [50] exploited the T_1/T_2 dependence on rotational

correlation time, τ_r, to measure pH. A modified gadolinium chelate is constructed such that increased pH causes a deprotonation effect, such that the molecules form helical structures. The structure tumbles more slowly than the protonated chelate molecule, and is sensitive to the pH environment. Investigations using gadolinium bound metallofullerenes, which aggregate at low pH, raised the possibility that such sensors could produce pH sensitive relaxivity measurements [51]. This was experimentally demonstrated by Toth et al. [52], in a study which showed a two–fold increase in relaxivity when the pH was changed from pH = 3 to pH = 8.

2.3.3 Cell tracking

Molecular applications using SPIOs have included a large research area in cell tracking, including a small number of clinical applications [53]. Cell tracking is not implemented with gadolinium based agents due to the long–term retention in labelled cells and the associated risks posed. The first clinical application of iron oxide labelled cells used SPIO labelled dendritic cells which were injected into melanoma patients, using a ferumoxide (Feridex, Bayer HealthCare) SPIO molecule [54]. Ferumoxides were approved by the FDA in 1996 and are known as Endorem outside of the US. The study found that ferumoxide–labeled cells injected into lymph nodes could be detected, as well as in nearby lymph nodes after migration. A later study showed detection was possible in the brain, in a study involving traumatic brain injury patients and the stereotactic injection of ferumoxide labelled neural stem cells [55].

2.4 ^{19}F contrast agents

^{19}F CAs can utilise many of the contrast generating mechanisms associated with ^{1}H agents, including aggregation, enzymatic cleavage, utilisation of the PRE, and change in chemical shift, amongst other effects. Applications have been found in many diverse areas, such as measuring oxygenation in cancer [56], catheter tracking [57] and monitoring of flu-

orinated drug distribution [58, 59], which reinforce the potential of ^{19}F MR methods for biomedical applications.

The wealth of available fluorine MR techniques to investigate different pathologies does however make categorisation of fluorine CAs difficult. Past definitions have separated agents into two broad categories: "passive" and "active" [60]. The term passive contrast agent refers to molecules which are injected or administered into a system, *in vivo* or *in vitro*, for which a continuous fluorine signal, relating intensity and position, can be established. These molecules do not interact significantly with the immediate chemical environment and are generally used as markers for cells or molecules by accumulating at specific sites. Active contrast agents rely on a specific mechanism or an interaction with a specific molecule to produce a change in the fluorine signal. Generally, this category of MRI probe have an enzyme cleavable ligand which is attached to a contrast inducing ion (namely chelated Gd^{III} [61]) to generate contrast, but other less common mechanisms have also been demonstrated. Other definitions exist for contrast agents, categorised by their application or target [62], for which there can be several different mechanisms for the same application, and it is this later definition which we will adopt.

The following sections highlight a number of different applications, for both active and passive contrast agents, using fluorine MRI. I aim to demonstrate that fluorine CAs play an important role, and have the potential to provide mechanisms for molecular biomarker detection and monitoring.

2.4.1 Molecular, gene expression and enzyme targeted probes

Several key molecules of biomedical interest have been detected and observed using ^{19}F MR methods. Amyloid β plaques were detected *in vivo* using an i.v. injection of a fluorinated amyloidophilic sensor which selectively labels these plaques, and allowed ^{19}F MRI to visualise location and distribution [63]. The activity of glutathione (GSH) transferases (GST) using a ^{19}F sensor was first demonstrated by Ito et

al. [64] in cell cultures of *E.coli*, through a change in NMR signal. More recently, using a self–assembly nanoparticle system at 14.1 T, a fluorine signal was found to reduce upon GTH interaction [65]. Other molecular self–assembly mechanisms include those developed by Takaoka et al. [66] to target carbonic anhydrase. The group constructed a fluorinated benzene derivative with six magnetically identical fluorine atoms attached to a benzene–sulfonamide moiety via a hydrophobic linker. The ligand moiety is specifically chosen to target human carbonic anhydrase. In solution, this molecule will combine with other molecules into a larger molecular mass ensemble, of the order of hundreds of nanometers, which has a broad ^{19}F linewidth. The molecules are then disassembled and activated by individual protein interactions with the carbonic anhydrase. The individual molecules have a relative low molecular mass now, such that the NMR signal is increased and intensity can be visualised. A SNR of 60.1 was recorded on individual activation by addition of carbonic anhydrase compared with a negligible signal without.

Other molecular sensors applied in cells include an "On/Off" type mechanism in which a molecular linker is cleavable by β–lactamase, leading to the production of visible fluorine signals [67]. The probe was developed from a mechanism outlined by Mizukami et al. [68] in 2011 which used the β-galactosidase enzyme to study cellular gene expression. The previous method was modified due to the poor ability of the ^{19}F probe to permeate the cell; the new method uses β–lactamase which is a reporter protein found on the exterior of cell membranes. β–galactosidase is one of the most popular molecular targets for current molecular fluorine probes, whose reporter gene is *LacZ*.

Gene expression probes for β–galactosidase were developed over a decade ago for use in ^{1}H MRI in which access to water was regulated (changing q) in order to measure a changeable NMR signal [36, 37]. Other groups have previously used ^{19}F NMR to also detect β–galactosidase activity in human cancer cells *in vitro* [69], and more recently *in vivo*; a sensor design published by Yu et al. [70] exhibits a chemical shift in fluorine signal and a quenched T_2 proton signal due to a ferromagnetic iron core interaction to detect β–galactosidase. Other gene expression targets have been

cytosine deaminase (CD), which is a microbial gene investigated for its prodrug gene therapy potential. A study by Stegman and colleagues [71], showed that conversion of the antifungal agent 5–fluorocytosine (5–FC) to the antimetabolite 5–fluorouracil (5–FU) could be observed in a mouse tumour model after 5–FC intraperitoneal (i.p.) administration, using ^{19}F magnetic resonance spectroscopy (MRS).

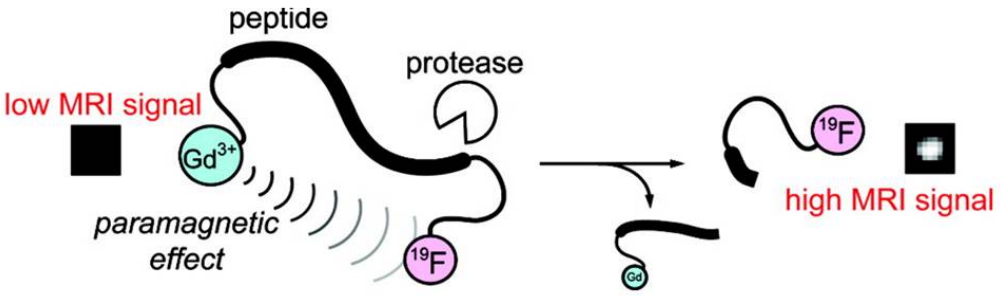


Figure 2.5: Mechanism of a ^{19}F enzymatic sensor using the PRE from [60]. A low MRI signal is produced in the uncleaved state of the sensor in which the fluorine moitey is bound closely to the paramagnetic gadolinium. Upon contact with a given protease, the peptide linker is cleaved and the distance between the fluorine and gadolinium is increased. This leads to an observable MR image, since an increase in the T_1 and T_2 has occurred.

Exciting work by Mizukami and colleagues in 2008 [60] demonstrated the paramagnetic relaxation enhancement (PRE) effect applied to fluorine MR *in vitro*, which monitored enzymatic activity using a fluorine sensor sensitive to caspase–3. The design makes use of the PRE in which the relaxation times of a fluorine atom can be greatly shortened when placed at close distances from a Gd^{3+} ion; typically at distances less than 70 nm, and connected via a peptide linker which is cleaved at the C–terminal peptide bond by a particular enzyme, thus changing the fluorine–Gd distance and hence relaxation properties. An example of this mechanism is shown in Fig. 2.5. This mechanism was successfully demonstrated in real–time at 11.7 T with a 1 mM sensor solution and the addition of Caspase–3, showing an increase in signal after 70 minutes. The measured T_2 time further confirmed successful cleavage; be-

fore caspase–3 addition the T_1 and T_2 values could not be measured (due to broad fluorine signal), and after, T_1 = 0.122 s and T_2 = 0.032 s [60].

Several groups, including our own, have sought to use the same technique for other enzymes. A dual ^{19}F and ^{1}H probe design based on a self–immolation mechanism was proposed by Keliris et al. in 2012 [72], in which β–galactosidase initiates a self–immolation reaction in the probe to change the Gd–fluorine distance and affect relaxation. More recently in late 2014, an MMP–2 sensor was published by Yue et al. [73]. This sensor was published during the characterisation of our own MMP probe, and reported an 8.5 fold increase and a 4.5 fold increase in T_1 and T_2, respectively.

2.4.2 Partial oxygen pressure measurement

One of the most successful applications of ^{19}F MRI has been within the field of oximetry, namely, mapping tumour oxygenation using perfluorocarbons (PFCs) and other fluorinated compounds. Low levels of oxygen in tumours lead to anticancer chemotherapy and radiotherapy resistance, and knowledge or mapping of the tumour micro–environment can inform treatment adaptation [74]. Oxygenation mapping measures the partial pressure of oxygen within biological systems by using the linear relationship between the longitudinal relaxation rate of fluorine (r_1) and the partial oxygen pressure (pO_2) [75]. PFCs in particular can carry a large quantity of dissolved oxygen and allow a fast gas exchange rate with surrounding tissue [76]; this method of oximetry can measure the tissue oxygen levels rather than the blood oxygen levels, as is the case with other ^{1}H methods.

PFC compounds used to measure oxygenation have included perfluorooctyl bromide (PFOB), perfluoro(15)–crown–5–ether (PFCE) and hexafluorobenzene (HFB) amongst others (see Fig 2.6). These compounds are nontoxic and stable *in vivo*, with clearance occurring biologically via circulation as well as through respiration [78]. ^{19}F pO_2 measurements have been compared with other oximetry methods in mouse tumour models including a fibre–optic probe method [79], showing an increased

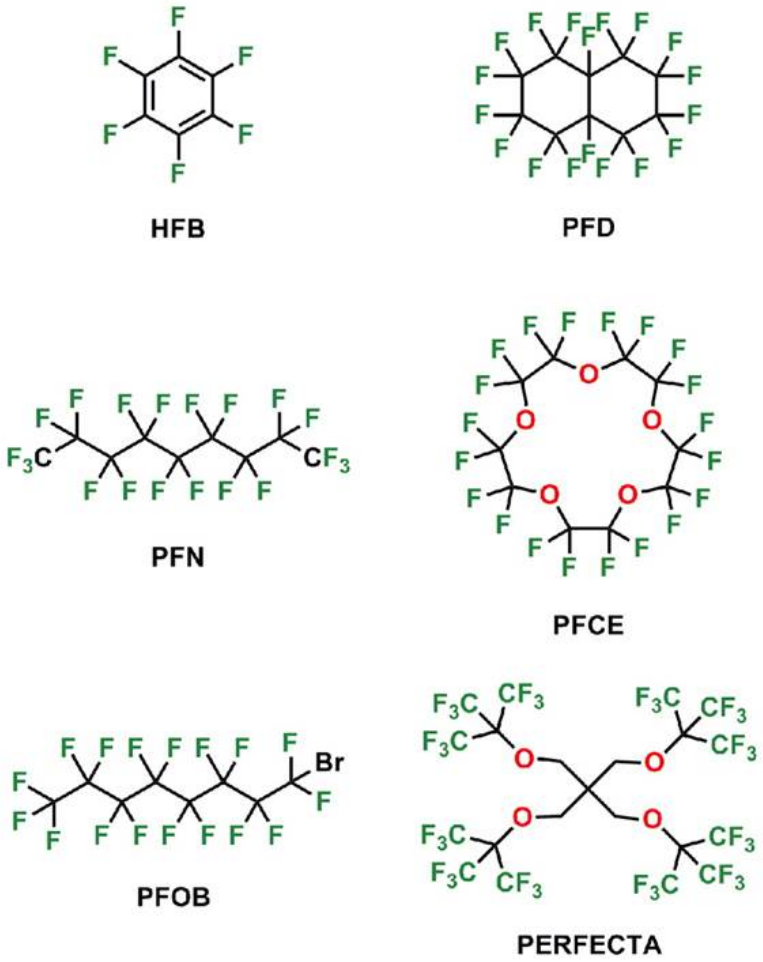


Figure 2.6: Chemical structures of commonly used PFCs from Tirotta et al. [77]. Compounds shown clockwise from top left are hexafluorobenzene (HFB), perfluorodecalin (PFD), perfluoro(15)–crown–5–ether (PFCE), tetra(perfluorotertbutyl)pentaerythritol (PERFECTA), perfluoroctyl bromide (PFOB), and perfluorononane (PFN).

sensitivity. Comparision with histology found a linear correlation between the two methods [80]. Fast T_1 methods have been developed by Mason and colleagues specifically for this application, such as fluorocarbon relaxometry using echo planar imaging for dynamic oxygen mapping (FREDOM) MRI, successfully measuring HFB signals in a rat tumour model [81]. The main obstacle this method faces is the heterogeneity of tumours and the uneven distribution of the PFC within it, with the greatest signal occurring in the most highly perfused areas [82].

Compounds which undergo a chemical change to indicate pO_2 conditions have been mostly fluoronitromidazoles, which have been used to detect hypoxia. This group of compounds undergo a reductive reaction by cellular components which liberate highly reactive fluorinated molecules; under hypoxic conditions these molecules will remain in the tissue, but can be cleared out upon oxygenation. In particular, the nitromidazole hypoxia marker SR4554 has even been trialled in man as part of a phase I clinical study [83]. SR4554 was developed by Aboagye et al. [84] and has been shown to allow monitoring of tumour hypoxia non–invasively in pre–clinical rodent models [85]. Clinical application allowed detection of the retained fluorine signal, but was limited by the dose tolerated by patients [86].

2.4.3 pH and ion sensititive probes

pH sensors

Originally investigated by Deutsch et al. [88] in the late eighties, the possibility to measure pH changes using fluorine MR chemical shifts has been demonstrated almost exclusively *in vitro*. The interest in pH measurements stems from the Warburg effect, meaning most tumours exhibit more acidic pH conditions than normally observed in the body [89], and detection of such changes this could lead to an earlier diagnosis. The Warburg effect itself is the observation that cancer cells exhibit increased glycolisis in the presence of oxygen, producing lactic acid, which has an acidic pH.

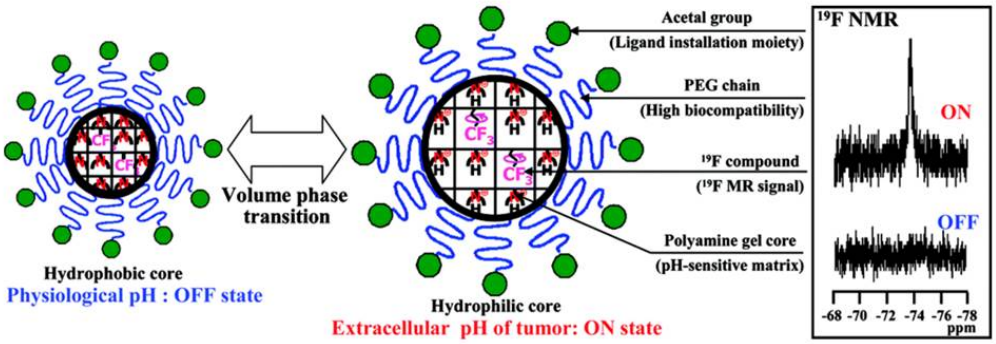


Figure 2.7: "On–off" regulation mechanism in response to local pH from [87]. A sensor concentration of 55 μM allowed sufficient signal in the "On" state to identify a pH of 6.5, after a volume transition was induced.

Early work focussed on fluoroalanines [90], and aimed to measure intra– and extra–cellular pH, finding the two equal for a pH range of 6.7 – 7.3 in human lympocyte cells, with a changing extracellular pH outside of this region [91]. A chemical shift of up to 2 ppm is exhibited by fluoroalanines, based on the protonation of the amine group [62], with later work investigating aromatic fluroinated compounds which have larger chemical shifts ($\sim 10^1$ ppm) [92].

Other approaches have used sensor accumulation in tissue to measure pH. In a paper by Oishi et al. [87], a method for measuring pH is based upon accumulation and structural alteration of a fluorinated gel probe *in vitro* at tumour representative pH ($\sim$ 6.5). This accumulation in the tumour tissue which allows a detectable signal measurement is called the enhanced permeability and retention (EPR) effect. The accumulation of certain sized molecules occur more in tumours than normal tissue, which is attributable to the quick angiogenesis and growth of tumours, as well as poor lymphatic drainage. The design of the sensor allowed a core hydrophillic–hydrophobic (volume) transitional increase to take place in the presence of a more acidic pH environment. When the volume transition occurs, there is greater volume for fluorine molecules to move around in, which gives rise to a larger T_2 value and hence a stronger fluorine signal (see Fig. 2.7). A fluorine signal sensitive to pH

values between 6.5 and 7 is produced (a typical pH range for tumours), indicating a promising mechanism for *in vivo* work. Subsequent sensors were synthesised, using a similar volumetric change mechanism to measure pH, in which protonation of an ammonium group linked to a fluorine source leads to molecular dispersion and ^{19}F signal increase [93]. This later work was able to distinguish pH environments as low as 4.5, at 0.25 pH unit intervals.

Ion specific probes

Early examples of chelated probes which directly targeted biological ions were detailed by Smith et al. [94] almost three decades ago, with most ion reporter probes undergoing a binding–dependent chemical shift for detection purposes [62]. A large range of other metal ions have been detected *in vitro* using changing chemical shifts, including K^+ [95], Na^{2+} (using a 5FBAPTA molecule [96]) and Zn^+ [97]. Jiang et al. [98] synthesised a fluorinated chelator whose fluorine chemical shift and relaxation times vary depending on the metal ion which is chelated, allowing detection of lanthanide series metals, Cu^{3+} and Ca^{2+} ions amongst others.

Recent trends have been to utilise gadolinium or other paramagnetic lanthanide ions for additional ^{19}F probe sensitivity. Harvey et al. described the concept behind increased ^{19}F sensitivity by inclusion of a paramagnetic ion [99], later applying this to detect calcium and citrate levels, measuring a doubling of the longitudinal relaxivity upon addition of 1 mM of calcium chloride [100]. Kadjane and colleagues [101] developed dual $^{1}H/^{19}F$ probes to detect Ca^{2+} which showed an 82% change in longitudinal relaxation per Gd^{3+} ion. Imaging was performed using the sensors to determine minimum concentrations needed ($\sim$ 1.2 mM), with the potential to replace the fluorine source to provide a three–fold increase in sensitivity.

2.4.4 Cell labelling

Cell labelling is one of the most popular and active research areas within MRI, with cellular therapeutics offering promise for treating disease through the implantation of cells *in vivo*. Tracking labelled cells with ^{19}F imaging offers benefits over traditional proton MRI tracking methods, in which monitoring cells after administration is currently challenging; contrast agents for ^{1}H MR create signals which are difficult to identify and distinguish from other background sources in the body, whereas with fluorine there is no endogenous signal present in biological systems. Fluorinated cell labels tend to be simple, highly fluorinated structures such as traditional PFCs, but other more complex fluorine compounds have been developed for a range of translational uses, including clinical, such as the patented and commercially available Celsense compounds [102].

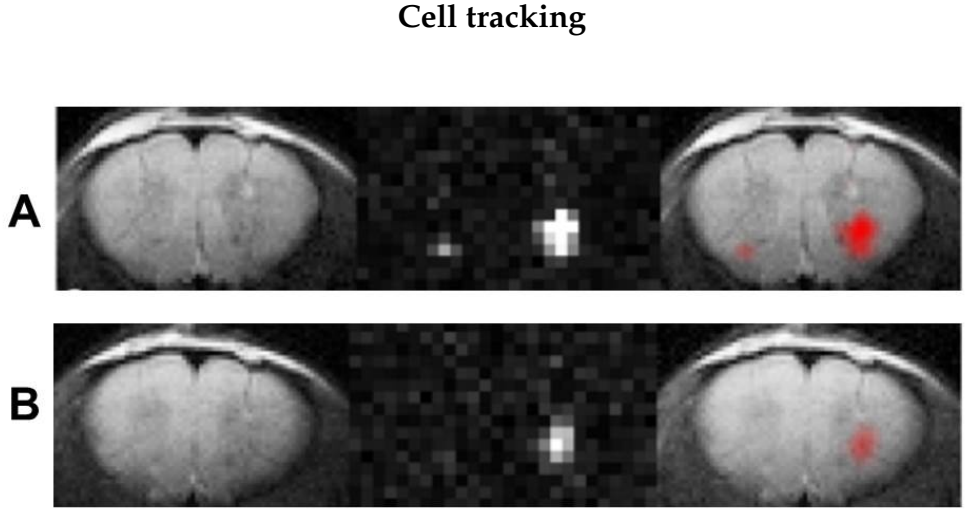


Figure 2.8: "Hotspot" ^{19}F imaging of implanted stem cells bilaterally in mice striatum from Boehm–Sturm et al. [103]. Proton, fluorine and merged images are shown in the left, centre and right of the figure respectively. A clear signal is seen two days **(A)** after implantation, with a reduction noticeable after six days **(B)**.

Initial experiments of fluorine tracking with dendritic cells were first reported in 2005 [104], as an early method of tracking immunotherapeutic cells with later immune cell studies also tracking T cells in rats [105].

Partlow et al. [106] used PFC nanoparticles to label mononuclear cells and track the migration of the cells on implantation in tumour bearing mice. Attention was given to quantification of cell numbers in this study, and to determine the sensitivity with fluorine MRI; cell numbers greater than 2000 were detected with a SNR $\geq$ 3.5. Ahrens and colleagues in particular have emphasised the importance of quantification of the fluorine signal, pioneering the use of spin–density ^{19}F images to quantify cell loading and detection limits of PFC labelled cells [105].

In 2011, Boehm–Sturm et al. [103] used fluorine MRI and labelled stem cells, implanted into mice brains, to track migratory stem cell effects (see Fig. 2.8). A perfluoropolyether (PFPE) cell emulsion was used to label stem cells implanted into mouse striatums, with a noticeable signal from labelled cells being observed a week after injection. Furthermore, a linear relationship between the SNR and the number of cells was assumed, allowing an estimate of the minimum number of detectable cells which was found to be of the order of 10^3 cells [107]. Later work by Tennstaedt et al. [108] used a multi–modal read–out, combining bioluminescence imaging and ^{19}F MR. To validate the loss of ^{19}F signal over a period of several days, correlation with bioluminescence signal indicated a migration of cells away from the original implantation site.

Other studies by Bible and colleagues have tracked transplanted human neural stem cells in a rat stroke model [109] and a mouse stem cell graft model at 9.4 T has also been performed [110]. Recently, mesenchymal stem cells were tracked for a variety of mouse models (immune competent and immune compromised) [111] with the latest research in the field aiming to translate pre–clinical advances to clinical applications [112].

Whilst current cell tracking methods using ^{19}F MR have the ability to track fluorine labels, no information can be extracted regarding the viability of the cell, if it is alive or dead, or even if the label is still within the original cell. *Ex vivo* analysis can determine the exact location of the label [113], but non–invasive *in vivo* verification would be preferable.

Inflammation applications

PFCs have found numerous applications for monitoring and detecting inflammation using ^{19}F MRI. In biological systems, the intravenous introduction of emulsified PFCs causes the circulating monocyte–macrophage system to uptake the solution as part of an innate immune response. The ^{19}F labelled macrophages will then tend to accumulate at sites of inflammation, providing a measurable signal once sufficient cells have aggregated. This provides a possible mechanism for tracking of this macrophage population [114]. After accumulation, clearance occurs through the reticuloendothelial system, as evidenced by Weise et al. [115]. Using a model of neuroinflammation by insult to the peripheral nervous system, the group was able to show fluorine uptake in lungs, spleen and liver.

^{19}F literature tends to categorise this collection of fluorine applications as "inflammation" rather than "cell tracking". Cell tracking applications generally introduce cells after labelling occurs outside the biological system, whereas inflammation applications generally allow the fluorinated emulsion to be taken up upon introduction to a biological system.

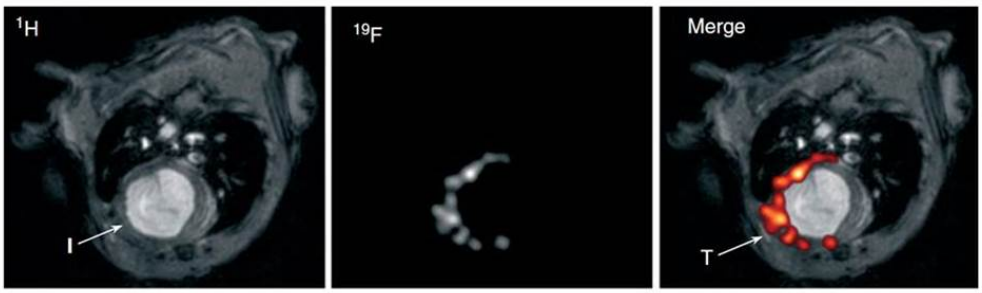


Figure 2.9: Myocardial infarction detection with ^{19}F MRI from Floegel et al [116]. A anatomical proton image **(left)** shows the infarcted region (I), with a fluorine image **(centre)** showing areas of accumulation from labelled macrophages. In the merged proton/fluorine image **(right)**, the fluorine signal is apparent in not only the infarcted region, but also the point of surgery in the thorax (T), used to induce the infarction.

One of the first reports of the *in vivo* application of PFC labeled immune cells to detect inflammation was a murine model of acute cardiac ischaemia [116], in which PFCs were found to infiltrate areas of infarction and were detectable with ^{19}F MRI (see Fig. 2.9). The PFC signal increased over time and was localisable to monocytes/macrophages using histological analysis. Signal accumulation has been observed in animal models of inflammatory bowel disease [117], pneumonia [118] (correlation between lung inflammation and fluorine signal), and experimental allergic encephalomyelitis (EAE) [119]. Recent studies on EAE (an animal model of MS) have shown that the *in situ* method of PFC labelling can be used as a marker of disease burden [120]. Another application by Hertlein et al. [121] showed that i.v. introduction of a PFC (Celsense, VS1000H) in a murine thigh infection model of *Staphylococcus aureus* allowed abscess delineation. Injected PFC emulsions have also be used to correlate the fluorine signal intensity with allograft rejection status (higher signal indicated more severe rejection) in rats [122], which was also shown by Floegel et al. [123] in a mouse heart transplant model.

2.5 Discussion

The range and breadth of applications of ^{19}F MR methods demonstrated in this section is great, using many of the mechanisms and techniques developed for ^{1}H MRI as well as fluorine specific imaging benefits; the lack of background signal has allowed for "hotspot" type imaging methods to be used to good effect. The area of fluorine CA research is exciting and expanding, with the first clinical applications being only recently reported [112]. It is clear that this is a promising technique, which has been developed only recently relative to other proton methods, and does not suffer from background issues unlike ^{1}H MRI.

Enzyme monitoring is an attractive target for potential MR probes, with only a small number of sensors synthesised for such a purpose. Few of these sensors have been comprehensively demonstrated *in vivo* to monitor enzyme activity, despite the validation of the various contrast mechanisms *in vitro*. Our aim in subsequent chapters is to use the ^{19}F MR

imaging modality along with a suitable contrast mechanism to monitor enzyme activity *in vitro,* working towards molecular application in *in vivo*.

CHAPTER 3

Sensitivity considerations for ^{19}F MR signal detection

3.1 Introduction

^{19} F MRI can provide important molecular information regarding a fluorinated sensor's chemical environment. In particular, ^{19}F is an ideal marker to study the transient fate of exogenous molecules by MRI. For most applications an important goal is therefore to maximise the sensitivity of the experiment, as well as ascertaining a minimum detectable concentration for the fluorine compound. The following chapter highlights the importance of understanding the theoretical factors which affect sensitivity and to this end, a theoretical method is described to estimate the sensitivity of ^{19}F MRI experiments. Theoretical understanding of fluorine sensitivity is crucial for choosing experimental parameters involved in testing novel fluorine molecular probes.

^{19}F MRI is an attractive modality for biomedical imaging applications including molecular sensing [72, 101] and cell tracking [62, 103], owing to the absence of a detectable fluorine background *in vivo*. While this offers high specificity, the low sensitivity due to the relatively small fluorine concentrations that can be achieved *in vivo* remains one of the main obstacles for the clinical application of fluorine MRI [124]. Therefore, knowledge of the potential sensitivity of a ^{19}F MRI experiment and influencing factors is particularly important for quantification in cell tracking

and labelling studies.

The fluorine signal is proportional to the number of ^{19}F spins, and quantification *in vivo* can be achieved by comparing the total signal of a sample with a reference standard of known concentration [104]. In cell tracking, a minimum detectable number of cells can then be extrapolated by measuring the peak signal–to–noise ratio (SNR) over a range of fluorine concentrations [106, 125]. To determine this limit beforehand, a range of images at different concentrations are taken and can be quantitatively used to inform experimental concentrations [126]. However, there is little in the literature which details a theoretical approach to fluorine sensitivity and minimum detectable concentration limits for a given SNR. Whilst a number of references in the literature provide an estimate of the sensitivity of a particular ^{19}F technique, these tend to be based on calculations taking into account *a priori* data, rather than a theoretical prediction based on available knowledge of parameters.

Efforts towards predicting the SNR for simple proton experiments have been well studied, firstly by Hoult et al. [127], with later studies incorporating specific factors related to *in vivo* imaging including electrical losses [128] and additional noise contributions [129, 130]. Several groups have developed theoretical models to describe the experimentally available SNR but have focused specifically on comparing SNRs at different field strengths (for ^{31}P) [131] or on different coil designs for SNR maximization [132]. Determining concentrations has been successfully demonstrated for metabolites in ^{1}H spectroscopy [133], although this method is not directly applicable to fluorine studies which use exogenous chemical reference standards rather than endogenous water for calibration purposes.

Based on a theoretical model using Hoult's principle of reciprocity [127], the aim of this chapter is to present a theoretical description of the factors affecting fluorine sensitivity and demonstrate an application in estimation of the number of ^{19}F spins detectable in an MRI experiment. Such an estimate could allow prediction of the minimum concentration required to achieve a target SNR for novel molecular fluorine probes, eliminating the need for another calibration experiment as long as the setup remains

unchanged. This could be especially useful to estimate the signal from a new contrast agent or fluorinated drug before synthesis [134].

3.2 Theoretical sensitivity for MR

3.2.1 Theoretical SNR for a ^{19}F MR experiment

The signal–to–noise ratio is defined as the ratio of the peak amplitude of the NMR signal divided by the root mean square noise. In the formulation described by Abragam [135] and adapted to pulsed magnetic resonance, where the receiver bandwidth is replaced by the bandwidth of a matched filter [136], the theoretically achievable SNR, Ψ, in a single pulse nuclear magnetic resonance experiment can be approximated by,

$$\Psi = K\eta_c M_0 \sqrt{\frac{\mu_0 Q \omega_{LC} V_c \pi T_2^*}{4 F k_B T_c}} \sin(\beta) \quad . \tag{3.2.1}$$

Here M_0 is the nuclear magnetization of the sample at thermal equilibrium, T_c is the temperature of the coil, V_c is the volume of the coil, F is the pre–amplifier noise figure (which is generally constant for a given nuclei frequency [137]), μ_0 is the permeability of free space, Q is the quality factor of the detection circuit, ω_{LC} is the frequency of the resonant circuit, and β is the flip angle associated with the excitation pulse. K is a numerical factor introduced by Hoult and Richards to account for the specific receiving coil geometry [127]. The quality factors for the following *in vitro* experiments will be similar and small differences are not significant due to the square root dependence. However, for *in vivo* situations the coil's loaded quality factor, Q_L, will be significantly different from the empty quality factor, Q_E; incorporation of these Q factors into the model for this case are described in the discussion section of this chapter.

The filling factor, η_c, is a measure of the fraction of the coil volume occupied by the sample. For an ideal solenoidal volume coil this can be approximated as,

$$\eta_c \approx \frac{V_s}{2V_c} \quad , \tag{3.2.2}$$

where V_s is the sample volume.

For spin 1/2 nuclei, such as ^{19}F, in the high temperature limit M_0 is given by the equation for the magnetisation stated in Chapter 1 (Eq. 1.1.18),

$$M_0 = \frac{N\gamma^2\hbar^2 B_0}{4k_B T_s} \quad , \tag{3.2.3}$$

where all terms are previously defined. The $\sin(\beta)$ term in Eq. 3.2.1 represents the contribution of the pulse sequence (in this case, a single–pulse experiment with detection of the FID) to the SNR. Eq. 3.2.1 assumes that a matched filter is applied, which can be implemented by multiplying the time–domain signal by an exponentially decaying window function with time constant T_2^* prior to Fourier transformation [136]. It is also possible to approximate $\omega_{LC} \approx |\omega_0|$, where $|\omega_0| = |\gamma B_0|$, implying that the resonant frequency of the circuit is tuned to the Larmor frequency of the ^{19}F signal. We further assumed that the coil temperature is similar to the sample temperature, $T_s \approx T_c$. Both terms can then be replaced with a general temperature, T. The number of contributing spins in a sample per unit volume, N, is defined as $N = N_s V_s^{-1}$, with the total number of contributing spins in a sample given by

$$N_s = cN_A n_e V_s \quad . \tag{3.2.4}$$

Here c is the concentration in units of mole/m^3, V_s is the sample volume, n_e the number of equivalent fluorine spins per molecule that contribute to a signal with identical chemical shift, and N_A is Avogadro's constant. Substitution in Eq. 3.2.1 provides an alternative expression for the SNR,

$$\Psi = \frac{cN_A n_e \gamma\hbar^2 V_s}{16}\sqrt{\frac{K^2\mu_0 Q\omega_0^3\pi T_2^*}{V_c F k_B^3 T^3}}\sin(\beta) \quad , \tag{3.2.5}$$

which can be used to determine the concentration from a measured SNR value. Rearranging this equation yields the concentration, c, needed to obtain a chosen SNR, Ψ,

$$c = \frac{16\Psi}{N_A n_e V_s \gamma\hbar^2}\sqrt{\frac{FV_c k_B^3 T^3}{K^2\mu_0 Q\omega_0^3\pi T_2^*}}\frac{1}{\sin(\beta)} \quad . \tag{3.2.6}$$

To formulate a practical equation which can be used to calculate a minimum concentration or SNR, a gauge factor, Λ, is introduced which is experimentally determined for each hardware setup. The gauge factor

has to be measured only once for a particular setup in order to calibrate the theoretical model to the experimental SNR, and is only valid for the specific coil used. Based on our idealized SNR equation, the gauge factor is

$$\Lambda = \sqrt{\frac{K^2 Q}{F V_c}} \quad . \tag{3.2.7}$$

In practice, the gauge factor also includes correction factors for experiments whose performance differs from the ideal situation in Eq. 3.2.1. These factors, which include the filling factor as a function of the coil geometry [127], only contribute a constant multiplicative factor for the MRI hardware setup and nucleus (i.e. a particular resonance frequency). To simplify the equations further all constant terms are combined into Π, which is independent of the sample and can be calculated without performing an experiment,

$$\Pi = \frac{16}{N_A \gamma \hbar^2} \sqrt{\frac{k_B^3 T^3}{\mu_0 \pi \omega_0^3}} \quad . \tag{3.2.8}$$

The minimum concentration to obtain a target SNR is then,

$$c = \frac{\Pi}{\Lambda} \frac{\Psi}{n_e V_s \sqrt{T_2^*}} \frac{1}{\sin(\beta)} \quad . \tag{3.2.9}$$

Factoring in additional NMR acquisition parameters (the repetition time, T_R, the longitudinal relaxation time, T_1, and the number of acquisitions, N_{acq}) yields the minimum concentration [136],

$$c = \frac{\Pi}{\Lambda} \frac{\Psi}{n_e V_s \sqrt{N_{acq} T_2^*}} \mathrm{SF} \frac{1}{\sin(\beta)} \quad , \tag{3.2.10}$$

where the saturation factor,

$$\mathrm{SF} = (1 - \cos(\beta)\exp(-T_R/T_1)) \times (1 - \exp(-T_R/T_1))^{-1}, \tag{3.2.11}$$

is introduced to account for incomplete relaxation (SF ≈ 1, if $T_R \geq 5 \times T_1$). For *in vivo* situations, β and T_R should be optimised to give the best SNR per unit time. Eq. 3.2.9 allows one to predict the minimum concentration of ^{19}F nuclei in a MRS experiment.

3.2.2 Noise and signal loss in MRI experiments

The model is defined in terms of the peak signal–to–noise rather than the integral value of a lineshape. The units of integration are a relative quantity which are only practical when comparing metabolite integrals in the same spectra, for example, in which there is a known concentration which can be ascribed to a given peak which then allows concentration quantification of another peak reference. However, from the point of view of minimum detectable quantities it is the SNR which we use to define this limit. SNRs take the full width half maximum (FWHM) value of the lineshape into account; broad lineshapes with large FWHM values will have a lower SNR than lineshapes with sharper and narrower FWHM values. For two samples of identical concentration but different lineshape, an integral measure would give the same value regardless of FWHM value.

For the *in vitro* experiments in this study, the dominant source of noise is assumed to be thermal electronic excitation (Johnson noise). *In vivo*, physiological noise is significant, as well as the thermal noise generated by the patient or in the detection circuit [129, 130]. For a given frequency and B_0 field strength, this noise contribution could be added in quadrature to the Johnson noise and included into the model. The noise term does not feature explicitly in the equations but one should be aware of the noise's field dependency when considering the gauge factor's applicability in different situations.

Rician noise effects

In MRI the images are usually presented in magnitude mode. The relevant noise amplitude, σ, is given by the variation of the signal amplitude as determined by a large number of repetitions of the experiment. As long as Ψ is not very large [138], measuring the off–resonant noise at positions in the spectrum or image that do not contain any signal provides a good estimate of σ with a much smaller number of repetitions. However, assuming a Gaussian noise distribution for off–resonant noise of magnitude data over–estimates the SNR and a Rician noise distribution

is more appropriate. In this analysis, the noise is estimated from off–resonant data. The theoretical model for $\Psi > 3$ is adapted by dividing the SNR with a factor of $\sqrt{2 - \pi/2}$ (approximated to 0.655) to account for a Rician noise distribution [139]. For $\Psi < 3$, this factor needs to be readjusted.

SNR dependence upon B_0 in different noise regimes

From Eq. 3.2.1 and the magnetisation expression given in Eq. 3.2.3, it can be seen that the signal emitted by a spin 1/2 sample will increase linearly with B_0, based purely on the contribution from the sample magnetization; this is the main motivation for the current trend of using higher magnetic field strengths in both clinical and research settings. However, the noise is related to the B_0 field as well and for reasons stated immediately above, it has been shown that there are two different field dependencies under different noise conditions [5]:

- For small samples where coil noise dominates: SNR $\propto {B_0}^{7/4}$
- For large *in vivo* experiments where sample noise dominates: SNR $\propto B_0$

In our situation we are interested in comparing and predicting quantities initially on the same set–up (B_0 is constant) so these general dependencies will not feature in the quantitative model. Translating detectable concentrations between wholly different set–ups (pre–clinical to clinical), for example, is not as straightforward as replacing the field strength or resonant frequency values in Eq. 3.2.5 and predicting new detection limits; ideally a measure of the noise is needed to extrapolate between set–ups.

3.2.3 Application to imaging sequences

Eq. 3.2.10 can be adapted for MR imaging. For a fast low angle shot (FLASH) gradient echo sequence [140] we obtain,

$$c = \frac{1}{0.655}\frac{\Pi}{\Lambda}\frac{\Psi}{n_e V_s \sqrt{N_{acq} T_2^*}} \mathrm{SF} \frac{1}{\sin(\beta) e^{-\frac{TE}{T_2}}} \quad , \tag{3.2.12}$$

where V_s now specifies the voxel size and N_s the number of spins that are required in a voxel to obtain a pre–selected Ψ. The pulse sequence contribution is reflected by simply adding relaxation terms, i.e. changing $\sin(\beta)$ to $\sin(\beta)e^{-\frac{TE}{T_2}}$; in this case a realistic fluorine acquisition sequence is chosen [103] but the model is not limited by the choice of pulse sequence. More generally, a numerical factor could be determined for a particular pulse sequence that provides the signal amplitude relative to a single–pulse experiment with subsequent acquisition of the FID. Notice that this factor could be larger than one, for example in the case of a multi–spin–echo sequence.

Instead of a minimum concentration, c, the minimum number of detectable spins required in a sample to achieve a certain SNR can be expressed as,

$$N_s = \frac{1}{0.655}\frac{\Pi N_A}{\Lambda}\frac{\Psi}{\sqrt{N_{acq} T_2^*}} \mathrm{SF} \frac{1}{\sin(\beta) e^{-\frac{TE}{T_2}}} \quad . \tag{3.2.13}$$

This is the most useful quantity to compare detection limits from different studies, since it is not volume dependent unlike concentration.

3.3 Materials and Methods

All experiments were performed on a 9.4 T vertical bore Bruker Avance III microimaging system (Bruker Corporation, Billerica, Massachusetts, USA) with a ^{19}F 25 mm volume coil tuned to the resonant frequencies of the specific compounds (approximately 376.5 MHz).

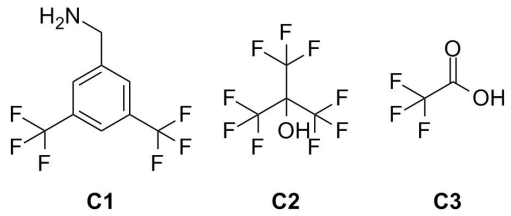


Figure 3.1: Chemical structures of compounds with variable number of fluorine spins per molecule. Compounds C1 (3,5–Bis(trifluoromethyl)benzylamine), six fluorine spins; C2 (perfluoro-tert-butyl alcohol), nine fluorine spins; C3 (trifluoroacetic acid), three fluorine spins.

3.3.1 Sample synthesis and preparation

Three basic fluorine compounds were used, all displaying a single fluorine peak in the NMR spectrum (Fig. 3.1). Two solutions were initially prepared: compound C1 contained 58 mM of 3,5–Bis(trifluoromethyl)benzylamine (Sigma Aldrich, UK), and compound C2 contained 322 mM of perfluoro-tert-butyl alcohol (Sigma Aldrich, UK), both using methanol as a solvent. All other solutions were made by dissolving anhydrous trifluoroacetic acid (TFA, C3 in Fig. 3.1) powder (Sigma Aldrich, UK) dissolved in distilled H_2O.

A line broadening effect on a compound's linewidth is likely to occur *in vivo*, where paramagnetic species or changing magnetic susceptibility affect fluorine molecules' linewidth. Such possible line broadening was replicated in the SNR experiments to verify the theoretical model's robustness in such cases. To induce line broadening, samples containing compound C3 were prepared by either: (a) adding a gadolinium based contrast agent, gadobenate dimeglumine (MultiHance, Bracco Imaging, SpA, Milan, Italy) which leads to line broadening due to paramagnetic relaxation; or by (b), introducing the solution into a porous medium that increases susceptibility broadening, consisting of a 5 mm NMR tube filled with 0.5 mm diameter solid glass beads (BioSpec Products, Bartlesville, OK). The beads introduce additional magnetic field gradients at the glass–liquid boundary.

3.3.2 MR spectroscopy and imaging

Thin walled 5 mm NMR tubes were prepared with 1 mL of each sample and placed into the magnet. The same position set–up and manual shimming procedures were performed for all samples. T_1 was measured using an inversion recovery (IR) sequence with eight logarithmically spaced time delays between 0.1 s and 20 s; for C1, T_1 = 1.59 $\pm$ 0.01 s, for C2, T_1 = 3.12 $\pm$ 0.01 s, and samples prepared from C3 had $T_1 \leq$ 4 s. The SNR was measured with a single 90° pulse–acquire sequence, where the pulse power and duration were calibrated manually. The following general parameters were used for MRS experiments: Gaussian excitation pulse duration = 67 μs, pulse power = 3 dB, flip angle = 90°, $TR = 30$ s, N_{acq} = 8, number of datapoints in time domain = 4×10^4, and receiver frequency bandwidth (BW) = 50 kHz.

One dimensional (1–D) spectra were Fourier transformed and phase corrected (Topspin 2.0, Bruker BioSpin GmbH, Ettlingen, Germany). The SNR was optimized according to the matched filter condition by applying a line broadening factor equal to the linewidth at full width half maximum (FWHM). T_2^* was calculated as,

$$T_2^* = (\pi \Delta \nu)^{-1}, \tag{3.3.1}$$

where $\Delta\nu$ is the linewidth at FWHM. The experimental SNR was determined by dividing the peak signal amplitude by the root mean square noise (determined from a region of the spectrum that does not show any fluorine signal) using Matlab (The Mathworks Inc, Natick, MA). The experimental error was calculated from six repeat measurements, where samples were repositioned into the magnet for each measurement. The gauge factor, Λ, was then calculated from Eq. 3.2.9 by dividing the experimental SNR by the term $n_e c V_s \sqrt{T_2^*} \sin(\beta) \Pi^{-1}$. The gauge factor error was calculated using error propagation in Eq. 3.2.9.

3.3.3 SNR determination

To determine the SNR, ^{19}F MR images were acquired with a fast low angle shot (FLASH) sequence (TE = 1.27 ms; matrix size (MTX) = 32 $\times$

32; FOV = 12 $\times$ 12 mm; slice thickness = 40 mm; BW = 50 kHz). Images were processed by zero–filling to a 64 $\times$ 64 matrix and applying a sine squared window function. The SNR was determined from the images by dividing the ratio of the average intensity in a region of interest (ROI) containing fluorine signal by the standard deviation of a noise ROI.

The SNRs for two sets of samples (C3 with gadolinium, as well as C3 in the glass bead medium) were measured with MR imaging and spectroscopy, keeping pulse power and pulse duration constant in both measurements. The sample volume in the glass bead medium was derived from the packing volume of the glass beads in the NMR tube, obtained experimentally by comparing liquid volumes between an empty tube and a tube containing the glass beads; 60 $\pm$ 10 % volume was occupied by the beads, compared with an ideal packing volume [141] of 74 %.

An alternative method of T_2^* estimation was used for the sample C3 in the glass bead medium using a proton multi gradient echo (MGE) sequence (N_{acq} = 32, T_R = 3 s, MTX = 32 $\times$ 32, FOV = 12 $\times$ 12 mm^2, slice thickness = 40 mm with 12 echo times ranging from 1.98 ms to 14 ms) using Paravision 5.1 (Bruker, Ettlingen, GmbH Germany) with a linear phase encoding scheme. The T_2^* measurement is made for protons using a range of echo times and fitting the intensity of the signal produced at each echo, using an exponentially decaying curve, where signal $\propto \exp^{-t/T_2^*}$, and where T_2^* here is the estimated T_2^* value of the sample. Using Eq. 1.1.31, $T_2^* \propto \gamma^{-1}$, such that $\gamma_F T_{2,F}^* = \gamma_P T_{2,P}^*$, where P and F denote proton and fluorine parameters respectively. This is rearranged to obtain an estimate of the fluorine T_2^* value, provided the proton T_2^* is estimated through the above T_2^* MGE method.

3.4 Results

3.4.1 Determining the gauge factor

To test the validity of the model for the minimum detectable ^{19}F concentrations (Eq. 3.2.9), spectra for a range of fluorine samples and of various

Sample	^{19}F conc.	Gd conc.	Linewidth	SNR	$\Lambda\ [m^{1.5}\times10^4]$
C1	58 mM	0 mM	3.6 Hz	700 ± 63	(4.6 ± 0.6)
C2	322 mM	0 mM	3.0 Hz	5524 ± 497	(4.1 ± 0.5)
	1000 mM	0 mM	7.5 Hz	3698 ± 348	(4.2 ± 0.3)
	800 mM	0 mM	7.3 Hz	2983 ± 274	(4.2 ± 0.4)
	600 mM	0 mM	7.0 Hz	2152 ± 196	(4.0 ± 0.4)
C3	400 mM	0 mM	7.2 Hz	1499 ± 139	(4.2 ± 0.4)
	200 mM	0 mM	7.1Hz	723 ± 63	(4.0 ± 0.5)
	100 mM	0 mM	8.2 Hz	$36\ 3 \pm 31$	(4.3 ± 0.6)
	900 mM	0 mM	7 Hz	2418 ± 270	(3.9 ± 0.5)
C3	900 mM	50 mM	36 Hz	1450 ± 143	(4.3 ± 0.5)
	900 mM	500 mM	339 Hz	666 ± 67	(5.5 ± 0.7)

Table 3.1: **SNR and gauge factor.** The gauge factor was calculated through the rearranged Eq. 3.2.9 using number of fluorine spins per molecule (n_e), ^{19}F sample concentrations and T_2^* obtained from the linewidth.

concentrations (compounds C1–C3) were compared and the data was processed with the appropriate line broadening factor (Table 3.1). The gauge factor, Λ, was calculated from Eq. 3.2.9. For simplicity, possible steady–state signal reduction (as described by factor SF) was avoided by choosing T_R times such that $T_R > 5 \times T_1$ for all compounds. Table 3.1 shows that even with different compound structures and an increase in linewidth by two orders of magnitude, the calculated gauge factors remained within $(3.9 – 5.5) \times 10^4$ m$^{1.5}$. The broadening effect on the fluorine line shape caused by the presence of gadolinium is shown for sample C3 in Fig. 3.2.

3.4.2 Minimum detectable limits

The minimum fluorine concentration was determined by extrapolation using a minimum detectable SNR of $\Psi_{\text{min}} = 3.5$; the exact value of this minimum SNR is arbitrary to an extent, and previous studies have used

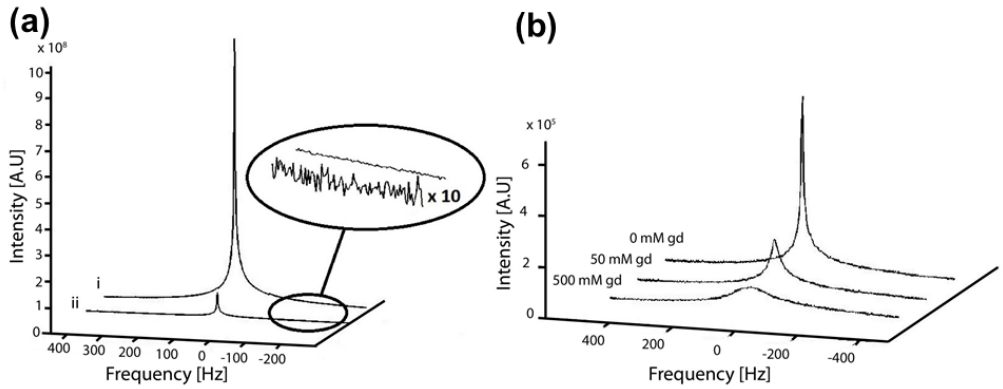


Figure 3.2: ^{19}F spectra with varying fluorine concentration and paramagnetic broadening. **(a)** Spectra of 1000 mM (i) and 100 mM (ii) concentrations of C3. The magnified section shows the scaled noise section. **(b)** Spectra of C3 (900 mM) with varying concentrations of gadolinium added. The origin of the spectra (0 Hz) in both **(a)** and **(b)** corresponds to a laboratory frame of reference of arbitrary chosen frequency.

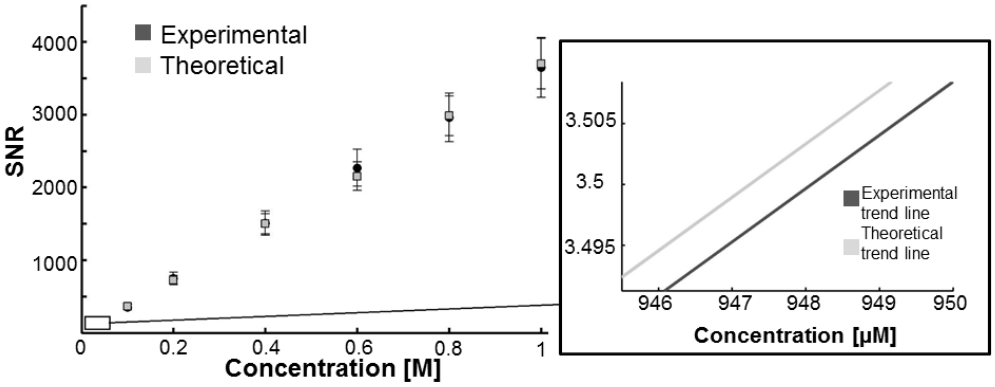


Figure 3.3: Minimum detectable concentrations in fluorine MRS. Experimental (solid circles) and derived SNRs (open squares) vs. concentration for compound C3. The derived SNR was obtained from an average gauge factor using Eq. 3.2.9. Lines of best fit were extrapolated to determine a minimum detectable concentration assuming a minimum required SNR of 3.5. (**Insert, right**) The fitting of the experimental (light grey line) and derived data (dark grey line) both resulted in a minimum detectable limit of 948 μM.

values of 3 or 3.5 [103, 106, 116]. First, an average gauge factor was determined from the average ratio of the experimental spectroscopic

SNR and the term $n_e c V_s \sqrt{T_2^*} \sin(\beta) \Pi^{-1}$ for a range of concentrations, using sample C3 without gadolinium (Table 3.1). From this gauge factor, Λ=$(4.2 \pm 1.1) \times 10^4$ m$^{1.5}$, a derived SNR was calculated. Using the spectroscopy data, two lines of best fit intersecting the origin were constructed using a linear least squares regression of the experimental and derived data; concentrations ranged from 100 to 1000 mM and r^2 = 0.99 was obtained for both lines. The intersection of the lines of best fit at Ψ_{min} were used to estimate a minimum concentration (Fig. 3.3); this was found to be 948 μM for both experimental and derived data.

3.4.3 Experimental detection limits

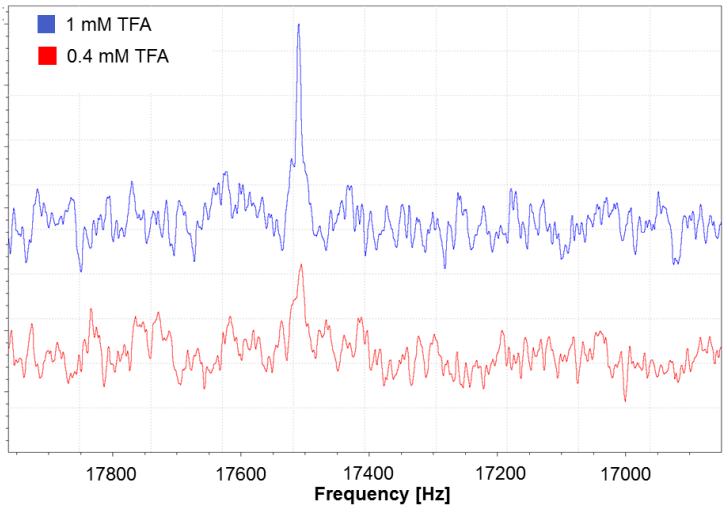


Figure 3.4: ^{19}F signals at low concentrations. 0.4 mM and 1 mM TFA spectra on the 9.4 T; whilst the 0.4 mM is difficult to disinguish from the background noise, the 1 mM sample is clearly visible. Line broadening of 5.1 Hz has been added to both spectra.

Using 0.4 mM and 1 mM of TFA, the SNRs of fluorine samples at low concentrations were measured close to the detection limit. Both SNR experiments used identical single–pulse sequences to all other SNR experiments, with two minor changes to the parameters: BW = 5 kHz and $N_{acq} = 8$ (for the 0.4 mM sample). The measured linewidth of the 1 mM peak was 5.1 Hz which produced an SNR of 5.8 after optimal line broad-

ening was applied. For the 0.4 mM peak, an SNR of 2.1 was observed prior to adding line broadening which made it difficult to accurately identify the FWHM (see Fig. 3.4); the same linewidth was used as the 1 mM for line broadening (LB), giving a final SNR of 3.8. For the 0.4 mM sample, 8 acquisitions ($N_{acq} = 8$) were needed to accumulate sufficient signal, with a single scan SNR calculated as $4.8/\sqrt{8} = 1.7$.

3.4.4 Comparing the SNR measured by MRS and MRI

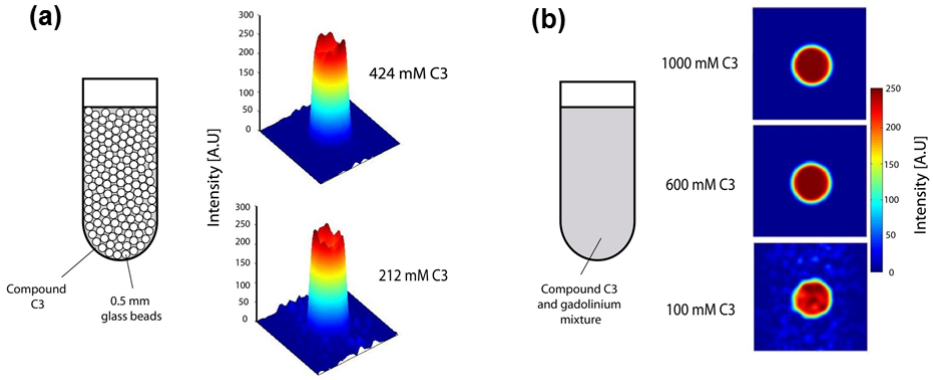


Figure 3.5: Paramagnetic and susceptibility broadening effect on ^{19}F MRI. (a) ^{19}F image intensity plots for C3 (424 mM and 212 mM) in a glass bead medium (sketch) inducing susceptibility line broadening. **(b)** ^{19}F images of C3 (1000 mM, 600 mM, 100 mM) with 50 mM gadolinium added to induce paramagnetic line broadening. Images were acquired with a gradient echo FLASH sequence (TE = 1.2 ms, T_R adapted to allow full relaxation, MTX = 64 × 64, FOV = 12 × 12 mm^2, N_{acq} = 1, and slice thickness = 40 mm).

To determine whether the gauge factor differed when measured by MR spectroscopy rather than MR imaging, the experimental imaging SNR values from MRI (Fig. 3.5) and MRS experiments were compared for the samples containing compound C3. To introduce paramagnetic broadening, gadolinium was added leading to a maximum broadened linewidth of 50 Hz (Table 3.2), while for susceptibility broadening, a glass bead medium was used which caused a linewidth of 419 Hz (Table 3.3).

	1000 mM	**600 mM**	**100 mM**
Linewidth [Hz]	29.3	29.5	49.6
$\mathbf{T_2^*}$ **[ms]**	10.9	10.8	6.4
MRS SNR	2667 ± 240	1888 ± 170	266 ± 24
MRI SNR	391 ± 109	240 ± 65	37 ± 4
$\mathbf{\Lambda_S}$ $[\times \mathbf{10^4\ m^{1.5}}]$	6.0 ± 1.1	7.1 ± 1.4	7.9 ± 1.7
$\mathbf{\Lambda_I}$ $[\times \mathbf{10^4\ m^{1.5}}]$	4.9 ± 0.5	5.0 ± 0.4	5.9 ± 0.5

Table 3.2: **Gauge factor under paramagnetic broadening.** Gauge factors derived from experimental SNR data from MR spectroscopy, Λ_S, and imaging, Λ_I, for sample C3 (1000 mM, 600 mM and 100 mM) with paramagnetic broadening from a constant gadolinium concentration (50 mM). The linewidth is the spectral linewidth at full width half maximum (FWHM). The model provides largely consistent gauge factors for both imaging and spectroscopy experiments separately.

	424 mM	**212 mM**
Linewidth [Hz]	419	396
$\mathbf{T_2^*}$ **[ms]**	0.77	0.80
MRS SNR	342 ± 31	162 ± 16
MRI SNR	28 ± 6	13 ± 3
$\mathbf{\Lambda_S}$ $[\mathbf{m^{1.5}} \times \mathbf{10^4}]$	6.8 ± 1.7	6.2 ± 1.6
$\mathbf{\Lambda_I}$ $[\mathbf{m^{1.5}} \times \mathbf{10^4}]$	7.5 ± 1.9	7.5 ± 2.1

Table 3.3: **Gauge factor under susceptibility broadening.** Gauge factors derived from experimental SNR data acquired with MR spectroscopy, Λ_S, and imaging, Λ_I, for sample C3 (424 mM and 212 mM) with susceptibility broadening through a glass bead medium. The broadening effect of the glass beads is demonstrated by the large linewidths and the sharply reduced SNR values.

3.4.5 Alternative T_2^* measurement

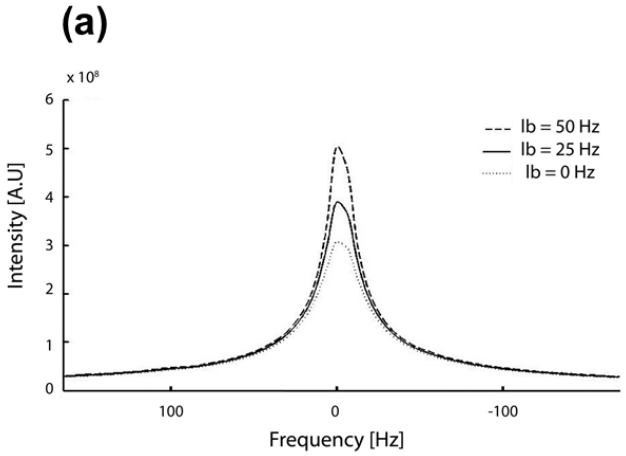
A series of proton T_2^* MGE images were used to estimate the fluorine T_2^* value, from a ROI, for the SNR in Eq. 3.2.12 (compound C3 at 424 mM concentration in Fig. 3.5); T_2^* was found to be 0.72 ± 0.21 ms. Assuming susceptibility line broadening is the dominant broadening mechanism in the glass bead sample, $\Delta\nu \propto \gamma$, such that $T_2^* \propto \gamma^{-1}$. From this, the fluorine relaxation value was estimated to be $T_2^* = 0.81 \pm 0.08$ ms. By comparison, the direct measurement of the fluorine linewidth yielded T_2^*= 0.77 ms (Table 3.3). Using the fluorine T_2^* estimate from the proton images, the fluorine linewidth was $\Delta\nu = 393 \pm 38$ Hz compared with 419 Hz from the actual fluorine sample spectrum.

3.5 Discussion

3.5.1 Spectroscopy and imaging gauge factors

The gauge factor was found to be largely independent of the measurement technique for the same specific coil, for spectroscopy or imaging, which means that spectroscopic measurements – rather than an imaging experiment – are sufficient to predict SNRs. Furthermore, signal processing in spectroscopy (line broadening) and imaging (sine squared window function) produced a similar SNR increase, in agreement with recent work by Jacoby et al. [142]. The gauge factor was confirmed to remain largely stable for a range of samples with different structures and fluorine concentrations. Even under the more "extreme" conditions studied (paramagnetic broadening with high concentrations of gadolinium and susceptibility broadening in a glass bead medium), the gauge factor varied by less than a factor of two. The signal decay in these cases is no longer mono–exponential, hence the matched filter condition assumed in this model is no longer met. This leads to a systematic error, which is the main reason for the discrepancy from the theoretically expected behaviour for the gadolinium–doped samples.

3.5.2 Line broadening, T_2^* estimations and potential pitfalls



(b)

LB value	Relative LB to FWHM LB	SNR
40 Hz	80 %	386
45 Hz	90 %	396
50 Hz	100 %	403
55 Hz	110 %	397
60 Hz	120 %	392

Figure 3.6: Effect of line broadening (LB/lb) on the SNR. (a) Line broadening with factors (25–50 Hz) applied to a sample spectrum of gadolinium doped sample C3, compared with the original spectrum. **(b)** The optimal line broadening factor was 50 Hz, corresponding to 100 % relative line broadening to FWHM. The SNR and FWHM values follow the expected relation SNR $\propto (T_2^*)^{0.5} \propto \text{FWHM}^{-0.5}$ (Eq. 5). The SNR was found to reduce to 96 % of the maximum value for a line broadening value set at 80 % of the value of the FWHM line broadening value. Since the spectrum is broadly symmetrical, a 20 % variation in line broadening corresponds to a reduction in SNR of 4 %.

The SNR is inversely proportional to the square root of the linewidth of the signal and therefore robust over a range of line broadening factors as illustrated in Fig. 3.6. This is important for *in vivo* situations where it is challenging to determine an exact T_2^* value, due to tissue heterogeneity. In non–proton experiments the receiver gain needs to be optimized to avoid signal clipping, since automatic receiver gain calibration is not always possible due to a low sample signal. This is particularly true when the actual receiver gain differs from the receiver gain settings [143, 144]. For the theoretical model to be accurate, the dwell time, Δt, between data points must be much smaller than T_2^*, otherwise additional systematic errors are introduced. As long as this condition is fulfilled, the

influence of the receiver bandwidth on the validity of the model is small. We have shown that the ^{19}F linewidth estimated from proton T_2^* images is in close agreement with actual ^{19}F linewidth measurements. When it is difficult to obtain a fluorine T_2^* measurement due to low sensitivity or in situations where a T_2^* value via a linewidth calculation from fluorine spectroscopy is not available, a proton T_2^* measurement can instead be used to determine the theoretical SNR.

3.5.3 Validation of detection limits

One of the most useful features of the model is the ability to predict minimum detectable limits. Experimental verification of the model at these low SNR regions experimentally was important, using the 1 mM and 0.4 mM samples. From the extrapolated limits, a minimum SNR of 3.5 should be produced for a concentration 0.948 mM, and from the experimental SNR data a SNR of 5.75 is observed for a 1 mM solution. Importantly, the linewidth of the two samples is different and since a sharper linewidth will produce a higher SNR, the two values must take account of this difference before a direct comparison can be made. Assuming all other parameters in the theoretical model except concentration and linewidth were the same between the predicted detection limit in Fig. 3.3 and the experimental 1 mM sample, one can deduce the SNR of the of the sample if linewidth and concentration were identical:

$$SNR_{new} \propto SNR_{5.75}\frac{c_{pre}}{c_{5.75}}\sqrt{\frac{\Delta\nu_{5.75}}{\Delta\nu_{pre}}} = 5.75 \times \frac{0.95}{1}\sqrt{\frac{5.1}{7.4}} = 4.5 \quad (3.5.1)$$

where the subscripts "5.75" and "*pre*" indicate parameters from the experimental sample and the extrapolated model based on high SNR data respectively. There is an approximate 20% difference between the new SNR and the minimum detectable predicted SNR of 3.5 which, when taking into account errors in concentration during the set–up, indicates that the model is robust in predictions at low SNRs. A rigorous analysis of Rician effects was not incorporated into the spectral analysis for these samples, since the main objective for this experiment was to establish whether the model had provided sensible detection limits (rather than

establish the minimum detectable concentration of TFA for our experimental setup).

A review article by Amiri et al. [145] compared several fluorine studies and calculated the minimum detectable fluorine per cm^3 for each, giving an overview of the different limits for different compounds. Detection limits are generally of the order of 10^0 mM, but direct comparison is difficult due to varying field strengths and coil and experimental set–ups.

3.5.4 Towards *in vivo* and limitations of the study

In vivo, loading a coil with a patient introduces signal losses in terms of both the Q factor and the SNR (due to additional noise contributions) [129]. Further adjustments for the theoretical model could account for this by using a phantom or calibration standard which has a similar Q factor to typical *in vivo* values when calculating the gauge factor. A pre–clinical study at 3 T used a $CuSO_4$ phantom in a solenoid coil to provide a Q factor of 89, compared with a Q factor of 84 when imaging a rat [146]. Due to the square root dependence of the Q factor on the SNR, small differences will have negligible impact on predictions using the model. If the Q factors for a loaded and unloaded coil can be measured, these can be factored into Eq. 3.2.5 [147], such that it becomes:

$$\Psi = \frac{cN_A n_e \gamma \hbar^2 V_s}{16} \sqrt{\frac{Q_L}{Q_E} \frac{K^2 \mu_0 \omega_0^3 \pi T_2^*}{V_c F k_B^3 T^3}} \sin(\beta) \quad . \tag{3.5.2}$$

Typical values of the Q factor for loaded and unloaded surface coils at 7 T in a pre–clinical scanner vary by a factor of around 4, so consideration of the reduced Q factor is important in these cases [148]. The *in vivo* sample thermal noise should be accounted for in the model, as stated previously, since the SNR would be reduced even if a similar Q factor for patient and sample was exhibited. This would require a measure of the noise by performing a single *in vivo* experiment and measuring the SNR; since the thermal noise is independent of the MR field strength, it would contribute a constant factor which could be subsumed into the equations.

Additional complications *in vivo* are the long T_1 times of fluorine compounds and use of the appropriate detection circuit. Typically used fluorinated molecules have a long T_1, of the order of seconds, which limits sensitivity and can be problematic for *in vivo* studies [149]. However, the use of paramagnetic substances to modulate the fluorine signal for improved sensitivity has been shown to be a promising approach to this issue [150]. Gauge factors calculated using solenoidal or surface coils will be different and it may be difficult to model the filling factor and detectable coil volume accurately. For surface coils this is especially true, and it is important to make sure the detection field is as homogenous as possible by using a B_1 map to ensure correct estimations which are not heavily spatially dependent [151].

In the presented theoretical method any temperature related effects have been excluded, since the samples were measured in identical conditions in a temperature controlled environment. However, the SNR is proportional to $T^{-1.5}$ where a factor of T^{-1} is contributed by the sample magnetization and a factor of $T^{-1/2}$ is caused by thermal noise. A fluorinated compound administered *in vivo* could result in a SNR decrease of up to 5% compared to a room temperature measurement if coil and sample are independently controlled. By heating the reference sample to the temperature of the environment of the desired fluorine experiment such a systematic error is avoidable.

3.5.5 Summary and applications

A simple theoretical method to determine an estimate of detection limits for a given ^{19}F MRI set–up based on cheap and readily obtainable reference standards has been demonstrated, allowing extrapolation to more expensive or valuable compounds. Known properties of potential sensors, such as number of fluorine atoms per molecule or possible T_1 value, could be used in the model to predict the sensitivity of a future set–up. The theoretical model outlined was validated over a range of experimental conditions and a gauge factor, constant for a given MRI setup, needed to be determined once. This theoretical model is not in-

tended to replace the use of a reference standard *in vivo*, but can provide sensitivity information prior to an experiment, without having to use fluorine probe material to estimate the detection limit. Additional factors for *in vivo* experiments need to be considered but the model should provide the starting point for sensitivity estimates. Although demonstrated for ^{19}F experiments, the presented approach is not limited to this nucleus. In principle, the same method could be applied to any nuclei of interest in magnetic resonance. Independent calibrations are required for every probe used on a particular spectrometer and, in case of broadband probes that are sometimes employed in microimaging, for nuclei with significantly different gyromagnetic ratios.

A possible application of predicting fluorine SNR and concentrations could be found in quantifying fluorine labelled cells. As previously mentioned, quantification of minimum detectable cell numbers in cell labelling studies rely on the assumption that all labelled fluorine is detectable in an MR acquisition [152]. In situations where fluorinated compounds interact with cells to produce short T_2 values, some fluorine signals are not visible and this can lead to under–estimation of the number of labelled cells [113, 153]. With the theoretical model, expected and actual fluorine content can be compared and differences could imply underlying biological processes occurring.

CHAPTER 4

Characterisation and development of a ^{19}F MRI sensor for enzyme detection

4.1 Introduction

Identifying biomarkers of pathological disease is one of the key goals in modern molecular imaging and medicine [154], with enzyme activity currently being investigated as a promising indicator of abnormal functioning in living systems. Matrix metalloproteinases (MMPs) in particular have been identified as a possible biomarker for tumour stage or cancer type [155], as well as indicators of disease severity in neuroinflammatory disease [156]. The ability to detect changes in MMP levels *in vivo* could allow for earlier diagnosis of cancers and neurodegenerative diseases and provide greater information for disease prognosis.

Several imaging methods have attempted to monitor and detect MMPs *in vivo* using near–infrared (NIR) optical imaging probes [157], as well indirect measurement of MMP inhibitors through ^{111}I PET compounds [158]. However, optical techniques have limited tissue penetration and current PET probes are at a very preliminary stage of investigation [159]. There is currently no established, non–invasive method available to monitor MMP activity *in vivo*.

As demonstrated from the literature in Chapter 2, fluorine MRI offers

a non–invasive imaging modality with high molecular specificity for a number of biomedically relevant molecules and compounds. In particular, the use of paramagnetic chelates to modulate fluorine signals in different molecular environments has been successfully demonstrated *in vitro* [60]. Based on a similar mechanism, Prof Neil Thomas and Dr James Krupa synthesised a MMP–sensitive sensor [160] and it was my task to characterise and investigate its MR properties.

Thus, the overarching aim of this chapter was to identify the presence of MMPs in a solution using a ^{19}F MR molecular sensor and characterise signal changes associated with the molecular detection. Furthermore, two observable characteristics of the sensor signal upon molecular detection were hypothesised: firstly, that an increase in the ^{19}F T_1 value of the sensor will be observed after exposure to MMPs, due to cleavage and an increased distance from the gadolinium moiety; secondly, that a sharpening of the fluorine lineshape will occur along with a decreased FWHM, since the broadening effect from the gadolinium is reduced. A secondary aim of this work was to investigate the possibility of translation to pre–clinical set–ups for *in vivo* experiments.

This chapter is organised as follows. Firstly, a description of the role of MMPs as a molecular target is outlined, with the composition and mechanism of the ^{19}F sensor explained. The method and results of high field experiments on the MMP sensor are described, with timecourse and T_1 experiments chosen to characterise the function of the sensor. Finally, a fluorine surface coil which I built is tested on a pre–clinical animal scanner to assess future prospects of applying the sensor to an *in vivo* study. The theoretical contributions to fluorine sensitivity detailed in Chapter 3 are utilised to extrapolate detection limits for the pre–clinical scanner. Conclusions and future prospects for the sensor are then discussed with potential changes highlighted.

4.2 Matrix metalloproteinases (MMPs): background, detection and a novel sensor

4.2.1 MMPs

MMP structure

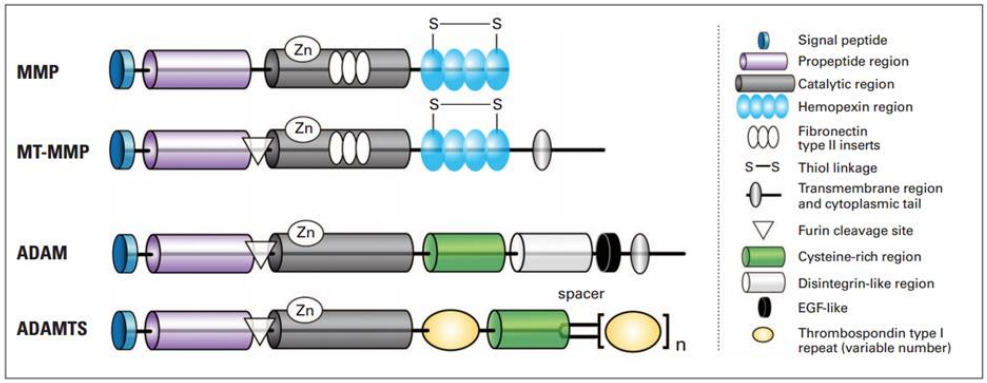


Figure 4.1: Structural diagram of MMPs and related proteases from [155]. MMPs consist of a signal peptide and catalytic, propeptide, and hemopexin regions. Other proteases such as the disintegrin and metalloproteinases (ADAMs), disintegrin and metalloproteinases with thrombospondin motif (ADAMTs) and membrane bound MMP (MT–MMP) subgroups have additional functional sections, including cysteine rich regions and cytoplasmic tails. These proteases provide a similar function to MMPs in terms of ECM modelling.

MMPs are a group of zinc dependent endopeptidases which are involved in a range of processes within the body, including normal growth and wound repair, and play a key role in the development of many different pathologies including cancers. The prefix of "matrix" relates to the principle role of this protease group which is the remodelling of extracellular matrix (ECM). The ECM refers to the collection of macromolecules which form a physical support network or matrix between cells and tissues, and provide a pathway for cell migration [161]. MMPs are generally found extracellularly, but certain MMPs have been found to be active in-

tracellularly, playing a role in cell apoptosis (MMP–1 [162]), and being present in cardiac myocytes (MMP–5 [163]). There are 23 MMPs present in humans and a similar structure is found for most MMPs, consisting of four distinct sections: a propeptide section; a hemopexin region; a catalytic region; and a signalling peptide (Fig. 4.1).

MMPs are produced in a latent form, as pre–proenzymes, which require activation. Firstly, the signalling peptide is removed to form the proMMP, referred to as a zymogen or inactive enzyme precursor. The signalling peptide is used to guide the enzyme within a cell's cytoplasm, with the proMMP preserving the enzyme until disruption or removal. The proMMP contains a cysteine bond, which whilst chelated to the zinc ion renders the MMP inactive. Upon removal of the bond, in a process known as the" cysteine switch", the MMP is activated; this switch can be activated by plasmins as well as other MMPs. The hemopexin (a heme binding protein) section of MMPs determines the substrate specificity to the particular MMPs which may cleave it. In the body, the regulation of activation and inhibition of MMPs is controlled in part by tissue inhibitors of metalloproteinases (TIMPS) [164], which themselves have been targeted as an indirect measure of MMP activity with molecular PET probes.

4.2.2 MMP role in the hallmarks of cancer

MMPs have been implicated as the leading mediators of cancer progression, responsible for the observable changes in the tumour microenvironment [166]. They have been identified to be involved in each of the characteristic hallmarks of cancer and are upregulated in every known type of cancer [167]. Examples include circulating MMP–7 levels which have been correlated with a poor prognostic outcome in bladder cancer as a molecular marker, with highest levels being found in a grade IV tumour [168]. A meta–analysis found that positive tumour derived MMP–2 levels in ovarian cancer patients were indicative of a lower survival rate compared to MMP–2 negative tumours [169]. Fig. 4.2 shows the myriad of MMPs involved in breast cancer, and the variety of origins

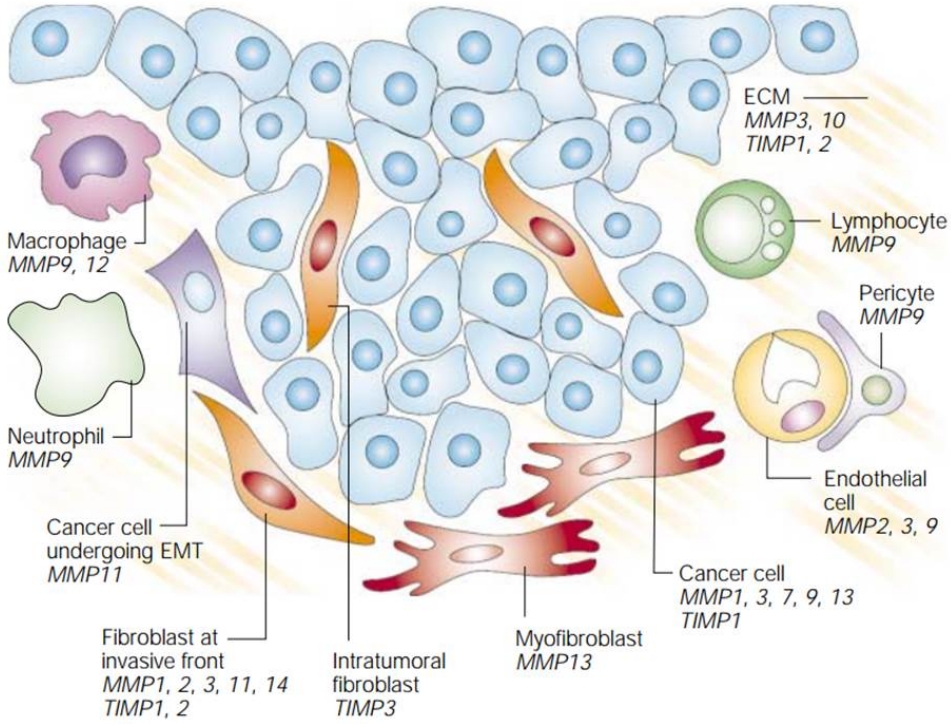


Figure 4.2: Diagrammatic representation of the cells and corresponding MMPs activated in breast cancer from [165]. MMPs are transported and regulated through several immune cells which respond to chemical signalling from the surrounding tumour site, such as inflammation areas.

of the the different MMPs.

Tumour invasion

The invasion of a tumour into tissue and blood vessels (intravasation) characterise the initial stages of cancer growth, requiring remodelling of the ECM, regulated by MMPs. Critically, this invasive behaviour includes the reordering of random collagen fibre arrays, and the bulk clearance of collagen fibres in the bound ECM layer with studies showing that MMP–14 actively facilitates this process [170].

Tumour vasculature – angiogenesis and vasculogenesis

Tumours require a blood supply to continue growth. A prominent feature of tumour progression is therefore the acquisition of blood vessels from existing vessels (angiogenesis) and the formation of new blood ves-

sels from endothelial cells (vasculogenesis). An important signalling protein in this process is the vascular endothelial growth factor (VEGF), whose bioavailability is dramatically increased by local MMP–9 activity. The presence of MMP–9 itself is due to local inflammation which attracts immune cells carrying the MMP. This begins the complex process of angiogenesis, which is often known as the "angiogenic switch" [171]. Studies have shown MMP–9 to be an important component in this switching, through the angiogenic changing of normal islet cells to produce VEGF in a transgenic mouse model [172]. MMP–2 has also been positively correlated with increased VEGF in gastric carcinoma samples, linked to an increased venous invasiveness and tumour vasculature [173].

Evading apoptosis

Apoptosis is the programmed death of cells, mediated by extracellular receptors, such as the Fas receptor (FasR), which tumours attempt to evade in order to increase cell numbers. MMP–7 has been shown to cleave FasR adhesion to doxorubicin treated cancer cells, reducing the intended apoptosis [174]. Doxorubicin is a chemotherapeutic drug which interacts with DNA to reduce cell replication. Mouse models of pancreatic acinar–to–ductal metaplasia showed that MMP–7 deficient mice displayed inhibited tumour cell growth [175].

Immune system circumvention

A depressed immune response is a common feature observed in cancer, in which the normal immune responder activity (T–lymphocytes, natural killer (NK) cells, neutrophils and macrophage activity) is reduced, allowing more aggressive cancer progression. T cells rely on interleukin–2 receptor α (IL–2 α) as an essential receptor for proliferation and it has been suggested MMP–9 and MMP–2 downregulate IL–2 α, mediating cleavage from cancer cells [176].

MMPs can also boost cancer cell resistance to NK cells, by cleaving the α1-proteinase inhibitor (αPI) to produce a reactive molecule which then modulates NK activity. MMP–1, –3, –8, –11 and –7 all effectively cleave αPI but MMP–7 is the most efficient protease to do so [177].

4.2.3 Methods for MMP detection

MRI

The first MRI responsive sensor for MMP–7 detection used a water accessibility mechanism [178], which is activated upon cleavage by the MMP. A mouse tumour model overexpressing MMP–7 and an identical tumour cell line with negligible MMP–7 levels were injected subcutaneously with several agents to investigate whether signal differences could be detected between MMP specific and unspecific sensors. Injected agents were a proteinase modulated contrast agent (PCA)–7, a scrambled version of PCA–7 (i.e. a peptide sequence which should not be cleaved by the MMP) and a Gd–DPTA compound. A small difference was observed between the scrambled and PCA–7 sensors, yet the distinction between MMP–7 positive and negative animal models was unclear due to large signal variability. The clearest measure presented in the study was obtained by taking the difference in slope of an intensity time–plot for each sensor, yielding a 15 % change between the PCA switch and the scrambled version. Later work by the same author used a similar solubility mechanism but targeted MMP–2 instead [179].

MMP–9 has been targeted *in vitro* using a different MRI approach. Iron oxide coated nanosensors with MMP ligands were modified to cluster together and affect T_2^* relaxation values after cleavage by the MMP. By measuring the signal intensity in a T_2^* weighted image acquired every 15 s after MMP addition, a signal decrease of 80% was observed at a sensor concentration of 300 nM [180]. An interesting approach developed by Silvio Aime's group uses a ratiometric approach to detect MMP–2, using the ratio of the T_2 and T_1 values of a chelated gadolinium to detect cleavage of an MMP substrate [61]. The chelated gadolinium is bound initially to a large molecular liposome system (around 80 nm in size) with reduced mobility and short relaxation values; upon MMP–2 addition, the gadolinium chelates are cleaved and dispersed, increasing relaxation. Approximately a four–fold increase could be observed using this effect between the cleaved and uncleaved states, due to the influence of the paramagnetic ion (see Chapter 2 for more details of this

mechanism).

^{19}F methods are particularly promising for detecting molecular changes, especially due to the low background signal encountered *in vivo*. An "On/Off" aggregation approach, which modulates T_2 significantly, allowed detection of a fluorine signal associated with MMP–2 cleavage [181]. Fluorine nanosensors were synthesised to self–assemble into a large aggregation structure which could be deconstructed and dispersed upon MMP contact. A measurable signal in both NMR and MRI demonstrated the mechanism. A ^{19}F MMP sensor was recently published using the same idea as our sensor, with a Gd^{III} chelate to quench the fluorine signal, modulated by cleavage of an MMP substrate between the chelate and fluorine source [73].

Other imaging modalities to monitor MMPs

FRET and optical imaging

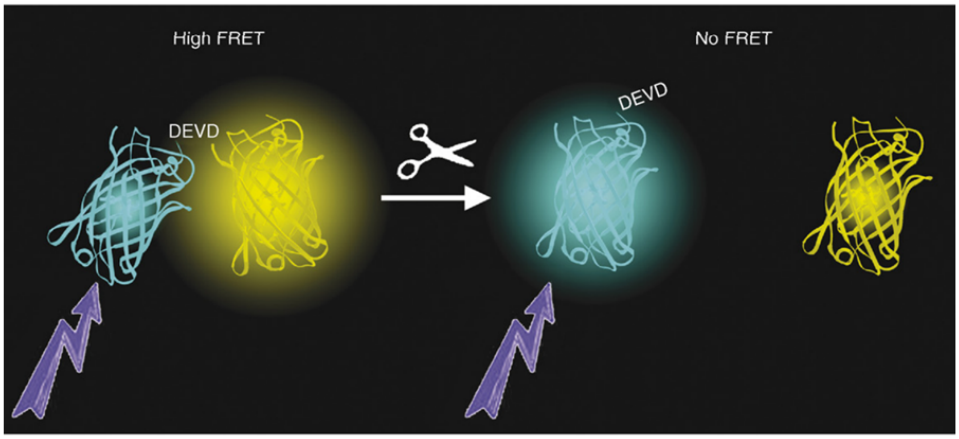


Figure 4.3: FRET principle demonstration for caspase–3 activity from [182]. The donor and acceptor are linked using a caspase–3 substrate, such that the distance between the two is small and allows a high FRET. Caspase activation will cleave the donor–acceptor linker and increase their distance, thus decreasing the FRET. This mechanism allows for the differentiation between an active and inactive caspase molecular environment.

The "On/Off" principle used in MRI contrast sensors is analogous to

a physical mechanism used for over 50 years in biochemistry, known as Förster Resonance Energy Transfer (FRET) [183]. In FRET, two fluorescent molecules in close proximity to each other interact by transference of virtual photons, from the excited molecule (the donor) to the other molecule (the acceptor). The efficiency of this transfer is dependent upon r^6, where r is the distance between the fluorescent molecules. Thus, if molecules are close to each other, the transfer efficiency is high. For FRET to occur, the emission spectrum of the donor molecules must overlap with the absorption spectrum of the acceptor. Irradiation of the donor then allows energy transfer from donor to acceptor, and the acceptor may then emit radiation at the acceptor frequency (Fig. 4.3).

FRET has been used to demonstrate MMP activity, using genetically encoded fluorescence indicators. Yang et al. [184] showed that MMP–2 cleavable acceptor and donor molecules attached to cellular surfaces exhibited different fluorescence intensities between MMP inhibitor and control samples. Later work in this area demonstrated the same principles applied to monitoring MMP–9 activity [185].

Optical imaging using fluorescent reporter probes has also been successful in detecting MMPs in certain *in vivo* studies. This form of optical imaging does not rely on a donor–acceptor set–up, but needs only a fluorescent probe which emits radiation at a given frequency; in the same way as ^{19}F MRI, this method uses the probe as a marker of uptake *in vivo*. Fig. 4.4 shows the application of an optical NIR study to detect tumours in a mouse cancer model. A study in 2001 by Tung et al. [157] showed it is feasible to image MMP–2 activity for an *in vivo* mouse tumour model, with a fluorescent imaging probe, showing an 850 % increase in signal intensity. The presence of MMP–7 has also been investigated using an optical probe, with a 60 % reduction in fluorescence intensity after addition of an MMP inhibitor [187].

Positron emission tomography (PET)

Positron emission tomography is a nuclear medicine technique which uses positron (β^+) emission to trace radionuclides *in vivo*. Upon emission, positrons travel short distances in the body before dissipating energy and finally interacting with electrons clouds from nearby atoms.

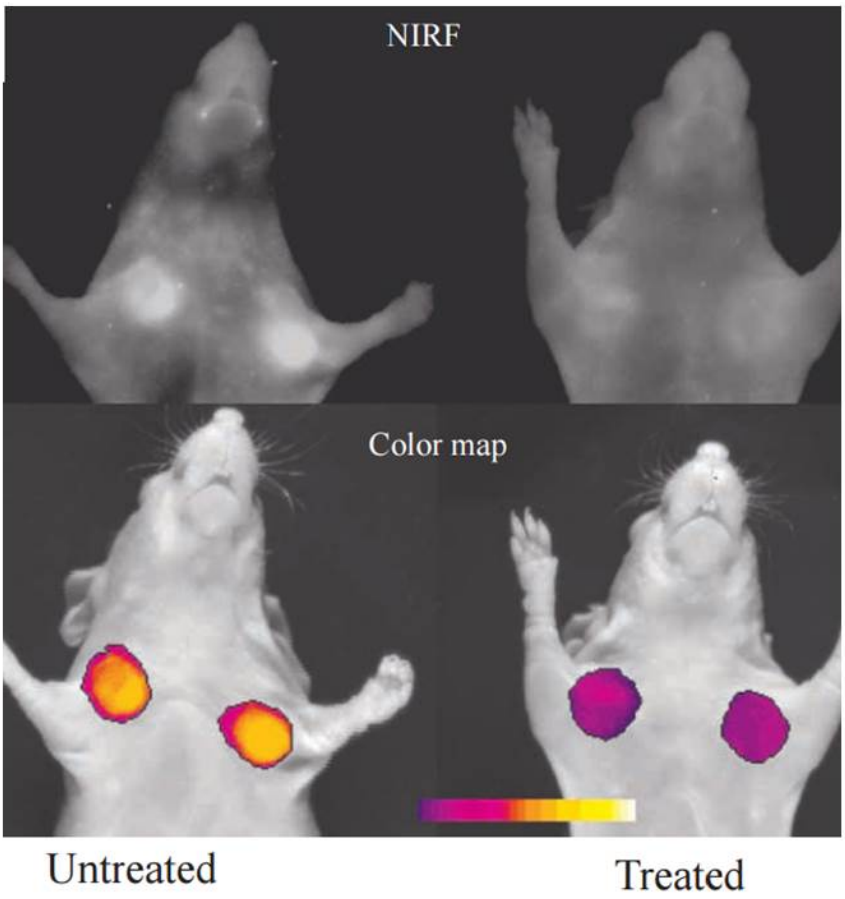


Figure 4.4: NIR imaging reveals differences in signal between MMP inhibitor treated and untreated tumour xenografts from [186]. The upper image shows the raw NIR image, in which the difference between treated and untreated models is more apparent in the scaled colourbar image below. A statistically significant intensity difference of 100 % was found between the two models.

This interaction results in annihilation of both electron and positron, producing two γ photons in opposite directions, each with an energy of 511 keV. A series of scintillation crystals positioned around the body detect the emitted radiation, using time–of–flight algorithms to determine the position of the emitted positron; Fig. 4.5 depicts this process.

For ionising MMP imaging, most approaches rely on being able to track MMP inhibitors (MMPIs), observing the location of the radiolabelled inhibitor rather than the MMP itself. PET studies have shown increased uptake in tumour tissues compared to other organs using an ^{18}F–labelled

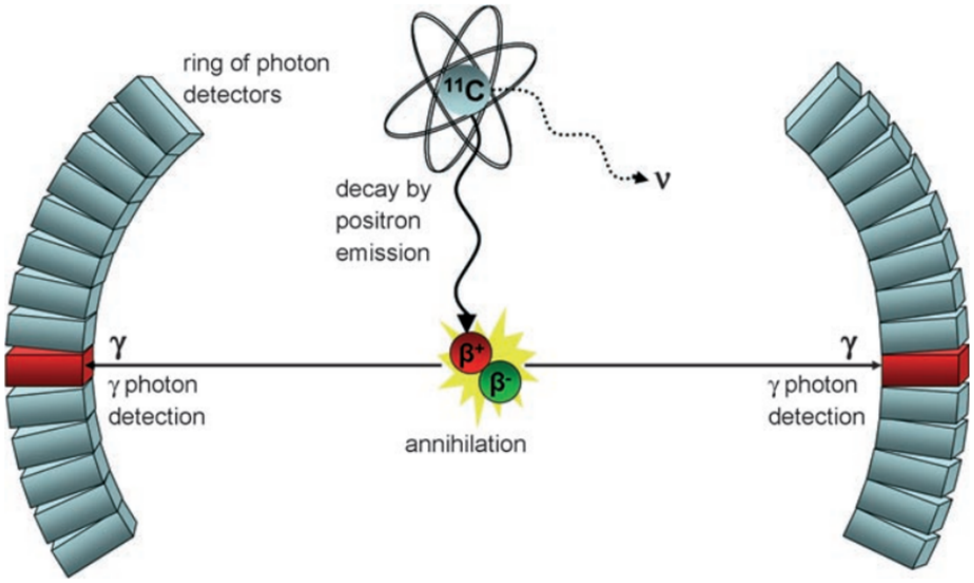


Figure 4.5: Principle and detection method of positron emission tomography from [188]. The radioactive nucleus emits the positron which then annihilates with an electron, producing two γ rays. The position at which annihilation occurred can be inferred using a ring of photon detectors around the radionuclide. A neutrino, ν, is also emitted but plays no part in the PET detection process.

MMP–2 inhibitor [189], indicating increased MMP–2 levels in such tissue. ^{11}C has also been utilised as a radioactive source to target MMP activity, with MMP–2 inhibitors being targeted as markers of MMP–2 activity [190].

Recent PET studies have been able to directly target MMPs, with Kondo et al. [191] using a MT–1 MMP ^{18}F PET imaging probe in a mouse tumour model. A cleavable PET probe with a PEG moiety, linked via a MMP substrate peptide, was designed to prevent the probe being taken up by cells . Upon contact with MT–1 MMPs, the PEG section is removed and the ^{18}F source may be uptaken by tumour cells. A high MT–1 MMP activity tumour xenograft on a mouse hind leg showed greater positron emission than a low activity tumour on the same animal.

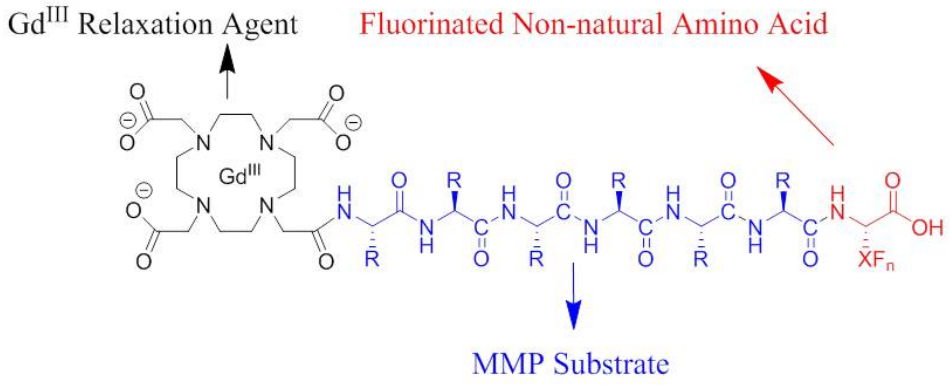


Figure 4.6: General chemical structure of our novel MMP sensors, from [160]. The three components are clearly shown: the gadolinium chelate which acts as the relaxation agent; a peptide sequence specific to MMPs; and a fluorinated amino acid source of signal.

4.2.4 ^{19}F MMP sensor

A large section of the work presented in this thesis is based on the characterisation of a MMP enzymatic sensor (see Fig. 4.6 for the general sensor structure), and the principle and components of this novel sensor are described below.

MMP sensor principle

Based on a similar mechanism to previous literature [60], a MMP sensor design was synthesised by Dr Krupa which consisted of three linked parts: a gadolinium chelate; a fluorine source; and a peptide linker. In the initial form, the fluorine signal is quenched or dampened due to the proximity of the paramagnetic gadolinium (known as the PRE effect). This state is termed the "Off" state. Upon MMP addition, the peptide sequence will be cleaved and the distance between the fluorine and gadolinium is increased, such that the relaxation is decreased. This mechanism is shown pictorially in Fig. 4.7.

MMP peptide sequence

The specificity of MMPs to a given MMP substrate is well established from earlier fluorescence work and a range of MMP substrates were

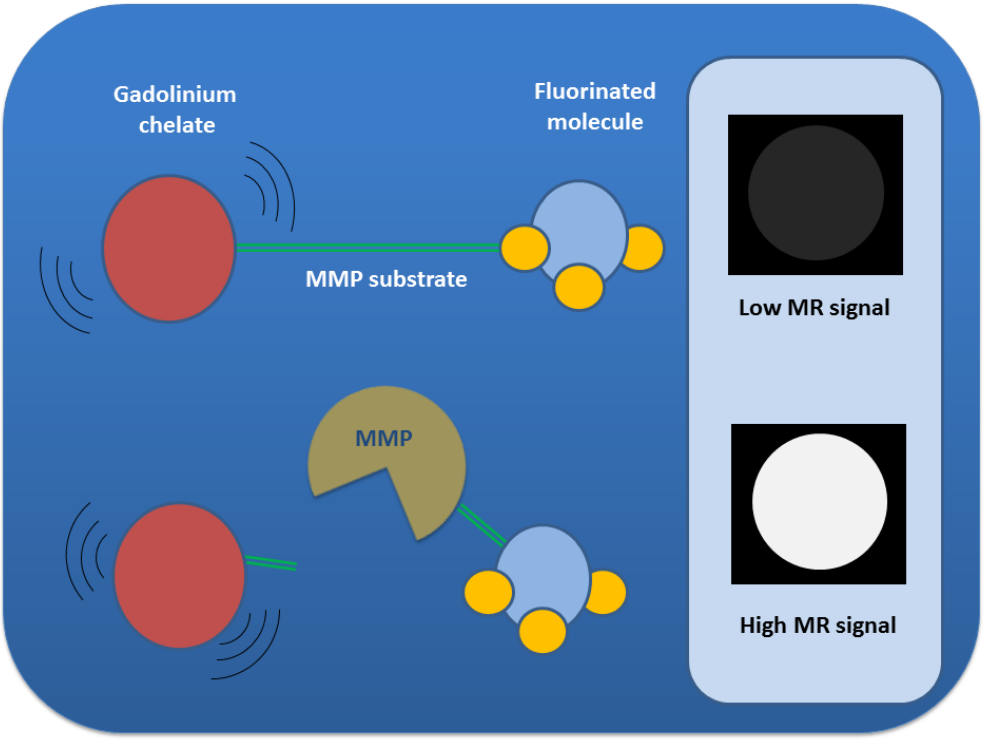


Figure 4.7: Mechanism of MMP fluorine sensor. In the bound state, the fluorine source is in close proximity to the gadolinium chelate. This causes a broad fluorine lineshape, due to the PRE, with a low signal intensity in an MR image. Upon contact with MMPs, the peptide linker is cleaved and the fluorine source is no longer bound to the chelate. This acts to increase the distance between the chelate and fluorine, reducing the PRE and decreasing the linewidth of the fluorine signal. The signal intensity is now greater than before MMP addition. The low MR signal state is often referred to as the "Off" image and the increased contrast after sensor cleavage is termed the "On" image.

therefore available, including: a generic MMP sequence [192] and an MMP–2 and –9 (2/9) sequence [193]. Additional sensors used in this work included substrates for MMP–7 [194] and MMP–1 [195]. These substrate sequences are composed of several amino acids and were synthesised using solid phase peptide synthesis (SPPS) techniques.

Gadolinium chelate and fluorine source

The paramagnetic agent used in our sensor is chelated gadolinium bound in a DOTA cage, based on a modification of a commercially available cy-

clen compound. The fluorine source used is based on a fluorinated benzylamine compound with six identical fluorine atoms; other fluorinated amino acids were investigated by Dr Krupa to improve the sensor's sensitivity but problems were found in attaching the three sections together.

4.3 MMP sensor characterisation

4.3.1 Methods and image processing

The next section of this chapter will detail the characterisation process taken for the fluorine sensor, beginning at initial incubation with MMPs, with later sections assessing the potential of translation to a pre-clinical approach. The literature review in section 4.2 helped inform the experimental procedure for probe characterisation, highlighting previous approaches and potential challenges. A high field strength was used for characterisation experiments consequently, since poor fluorine signal was reported in lower field strength studies. To study signal changes as a consequence of molecular changes, the standard procedure in fluorine studies is the acquisition of a range of timepoints and to compare SNR or intensity over a given timecourse [60, 73]. T_1 changes are indicative of molecular changes and experiments to measure T_1 values before and after MMP addition were also performed.

Sample preparation

For both of the main probes of interest, the MMP–generic and MMP–2/9 sensors (see Fig. 4.8), it was decided that MMP–9 would be used as the enzyme of choice to cleave each fluorinated sensor, since both amino acid chains would act as a substrate to the MMP.

Two types of NMR samples were prepared by Dr J Krupa, namely "D_2O" samples and "H_2O" samples: D_2O samples consisted of 100 % distilled deuterated water (D_2O) by solvent volume; H_2O samples were 90 % distilled water (H_2O) and 10 % D_2O by volume. The presence of deuterated water was needed to avoid ^{1}H spectra dominated by a water solvent

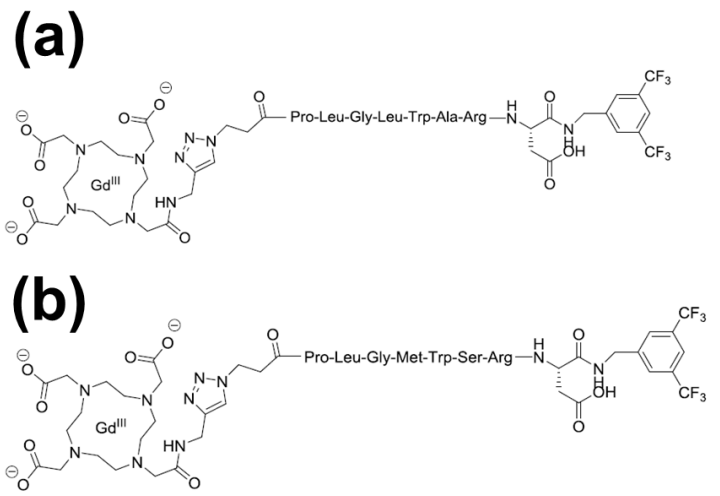


Figure 4.8: MMP–activatable ^{19}F MR sensors. **(a)** Sensor sensitive to all types of MMP (generic sensor); **(b)** Sensor sensitive only to MMP–2/9. The general structure of the sensors show a chelated gadolinium ion attached via a peptide chain, shown here with specific amino acids making up the linker, to a fluorinated amino acid.

signal as well as being used for shimming of the magnetic field.

To simulate a more realistic physiological temperature, some samples were heated and kept at 310 K for around 30 minutes prior to addition of MMP–9 and during the experiment; for samples scanned at temperatures of 298 K, no additional heating was required. Heating was generated using an in–built heating system inside the spectrometer.

Each sample had MMP–9 added to it at the beginning of each timecourse experiment, with the solution of MMP–9 being activated [160] and diluted to a concentration of 10 μg/mL prior to addition. The concentration of MMP in the NMR sample volume was always approximately 20 μM. After each use, the MMP–9 stock solution was stored at - 20°C for future use. MMP sensor concentration in prepared samples was 100 μM.

High resolution NMR spectrometry methods

Initial characterisation of the MMP sensors were performed on a high field NMR system, a 600 MHz Bruker Avance III spectrometer with a tuneable multi–frequency birdcage probe (^{1}H and ^{19}F tuneable). All samples used in this apparatus were contained within a thin–walled 5 mm NMR tube, with a volume of around 600 μL.

To study the fluorine lineshape and intensity after MMP cleavage, experiments were devised such that a fluorine spectrum is acquired at a number of discrete timepoints over a long timecourse, beginning at the points of MMP addition ($t = 0$). A 2–D timecourse experiment was devised in which a series of 1–D spectra were acquired over a period of time, using a simple pulse/acquire "zg" sequence, and then collated into a single dataset. The pulse sequence and parameters were set using the scanner's Topspin 3.0 software, with the following parameters for the timecourse experiment: resonant frequency = 564.65 MHz, N_{acq} = 32, BW = 250,000 Hz, TD (number of points in the time domain) = 277,762, dummy scans = 4, T_R (per scan per 1–D spectra) = 2.5 s, number of 1–D spectra acquired = 400. The maximum peak intensity in each 1–D spectrum was recorded and normalised to the maximum intensity achieved for all spectra in the timecourse. A simple exponential was fitted to the intensity data points following $y = 1 - ae^{-bt} + c$, where y is the signal intensity and a, b and c are fitted parameters.

For experiments measuring the T_1 of samples, a standard inversion recovery experiment ("T1ir") was modified for our specific MMP addition set–up: T_R = 2.5 s, N_{acq} = 288, BW = 16892 Hz or 29.9 ppm, TD = 16384, resonant frequency = 564.65 MHz and a variable delay list containing 16 or 24 inversion times from 1 ms to 8000 ms (depending on whether a post– or pre–cleavage experiment respectively). From the hypothesis stated earlier, it was anticipated that there would be two distinct types of T_1 values; previous literature of pre–protease cleavage values are around 10^0 to 10^2 ms, with post-cleavage values expected to be $\geq$ 350 ms [60, 196]. Consequently, the set of inversion times were adapted to adequately capture changes for post–cleavage samples, with a larger

parameter set for pre–cleavage samples.

Post–processing of T_1 data was performed by extracting the raw data from Topspin into Matlab and using a curve fitting tool ("cftool") to establish T_1 components from a fitted curve. The curve fitting tool in Matlab used a Levenberg–Marquardt algorithm (LMA), commonly used to solve non–linear least squares problems, to find the T_1 components from a T_1 inversion recovery experiment. For a single T_1 component, a single exponential was used to model the intensity as a function of time:

$$y = a(1 - be^{-t/T_{1a}} + c) \tag{4.3.1}$$

where a, b and c are variables in the fitting process, y is the intensity given in arbitrary units and T_{1a} is the T_1 value of a single component for a sample. For situations in which there are believed to be two separate T_1 components,

$$y = a(1 - be^{-t/T_{1a}} + (1 - b)e^{-t/T_{1b}} + c) \tag{4.3.2}$$

can be used, where T_{1b} is the T_1 value of the second component in a sample. It is important to note the form of the co–efficients for each exponential, which are b and $(1 - b)$ for the first and second exponential respectively. By constraining these co–efficients in this way, it is implied that the T_1 intensity observed is the linear sum of the two exponential components, i.e. $b + (1 - b) = 1$. In this model it is assumed that after MMP addition, $A + B \rightarrow A + B$ where A and B represent two distinct components i.e. there are no additional components present in this model. Fitting using the two component model does not require two components to be calculated but allows for up to two to be found depending on the optimal fit.

9.4 T MRI system and associated methods

Imaging was performed on a 9.4 T Bruker Avance III microimaging system with Paravision 5.1 imaging software and Topspin 2.0 spectral software (Bruker Corporation, Billerica, Massachusetts, USA). The same ^{19}F coil used in Chapter 3 for investigating the SNR was used, with a single NMR tube filled with 600 μL of MMP solution (concentration of sensor

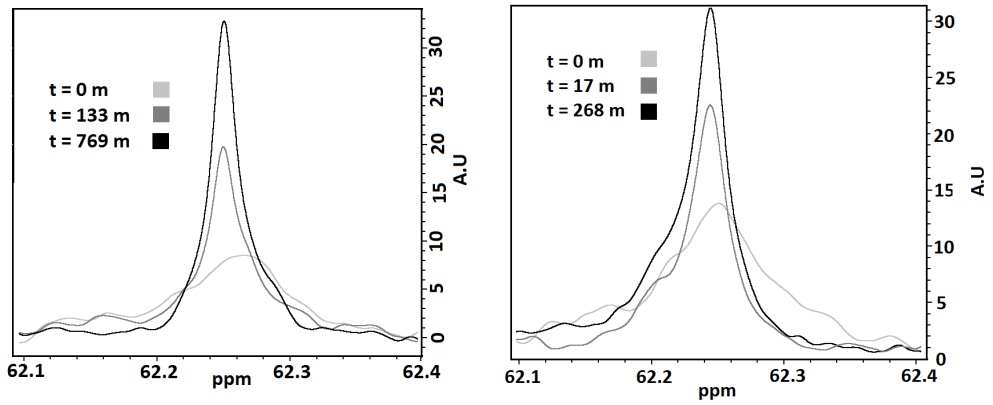


Figure 4.9: Changes in sensor lineshape after MMP addition. A series of 1–D spectra were acquired separately for the generic MMP **(a)** and the MMP–2/9 sensors **(b)**, with single spectral acquisitions every 1.5 minutes, to map spectral changes over time. A sharpening of the most prominent fluorine peaks is visible along with an increased intensity. Intensity values are in arbitrary units, with ppm values given relative to ppm downfield from 0 ppm (frequency $\sim$ 564.686388 MHz).

was 1 mM). After the fluorine signal from the MMP probe was identified on Topspin, a single image was acquired on Paravision over an extended period of time (due to the low signal and the requirement for a large number of averages).

The sequence used a FLASH scan with parameters: T_R = 15 s, TE = 10 ms, N_{acq} = 128, BW = 5 kHz, resonant frequency $\sim$ 376.522 MHz and FOV = 40 $\times$ 40 mm^2.

4.3.2 Results: Timecourse and T_1 experiments

Spectral lineshape acquisition

To observe the effect of MMP addition on the fluorine lineshape, a 1–D spectra was acquired every 1.5 minutes, comparing the changes in linewidth and intensity over 400 acquired spectra for the generic and 2/9 MMP sensors at 310 K, in a 90 % H_2O/10 % D_2O solution. The linewidths at the $t = 0$ were chosen as the minimum linewidth and once

the intensity had flattened out, the linewidth was at that point selected as the maximum linewidth of the 2–D acquisition, illustrated in Fig 4.9.

The MMP–2/9 sensor linewidth decreased from between 120 Hz and 50 Hz to 17.6 Hz, and from Eq. 3.3.1 this is a change from between 6.4 ms and 2.6 ms to 18 ms. For the generic MMP probe, the linewidth changed from between 138 Hz and 51 Hz to 13.4 Hz, giving an increase from between 2.3 ms and 6.3 ms up to 23.8 ms. The uncertainty in the initial linewidth is dependent upon which section of the spectra is used to measure the FWHM, an issue discussed later. Nevertheless, a clear sharpening effect on the linewidth was apparent, with an intensity (and consequently SNR) increase of at least a factor of two.

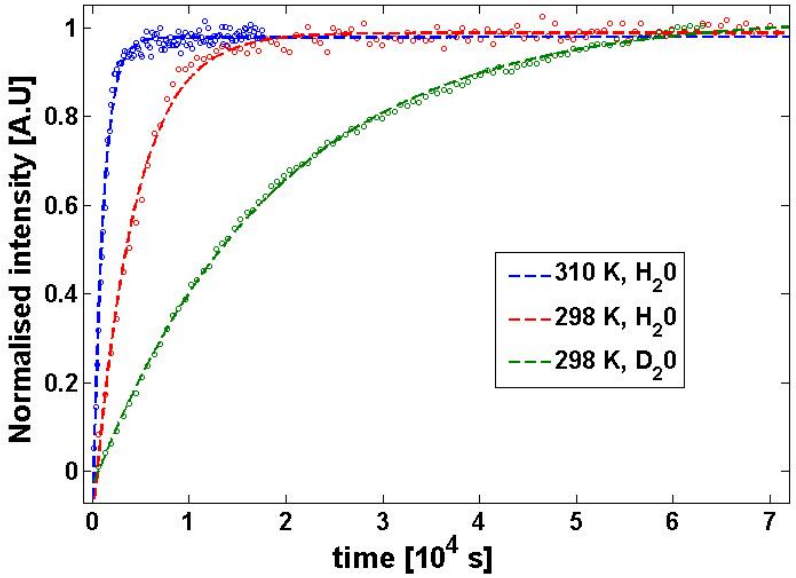


Figure 4.10: Temperature increases reaction rate for MMP–2/9 probe. The sensor was incubated in three different conditions (298 K in 100 % D_2O; 298 K in 90% H_2O and 10 % D2O; 310K in 90 % H_2O and 10 % D_2O), with MMP–9 added at $t = 0$. The sample at 310 K shows the steepest intensity curve initially, reaching the maximum value the quickest.

For both MMP–2/9 and generic MMP probes, a series of three separate samples were used to explore the effect of temperature and solvent on the temporal signal intensity after MMP addition: one sample was scanned at 310 K in 90 % H_2O; one sample was scanned at 298 K in 90 % H_2O; one sample was scanned at 298 K in 100 % D_2O. The tempera-

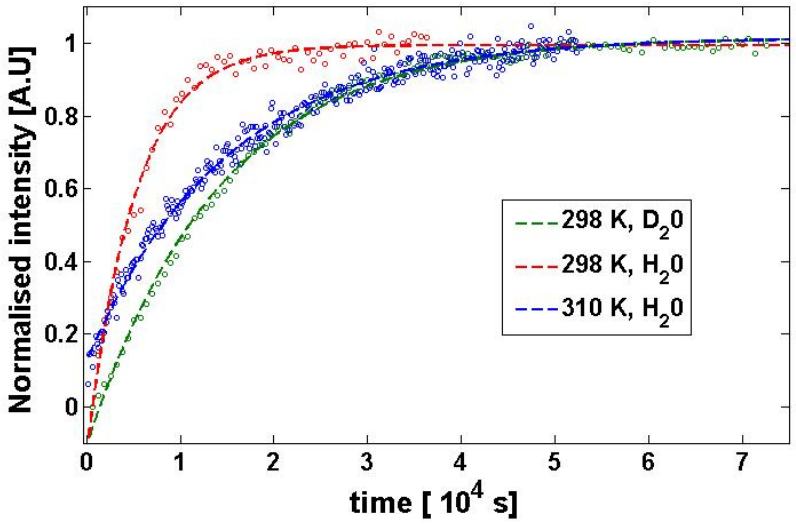


Figure 4.11: Reaction rate of generic MMP probe under different solvent and temperature conditions. The peak height intensities of the fluorine spectra are shown to increase over time, with the intensity gradient indicative of the reaction rate. Three sample conditions shown are: 298 K in 100 % D_2O; 298 K in 90 % H_2O and 10 % D2O; 310K in 90 % H_2O and 10 % D_2O. An unusually shallow gradient is noted for the 310 K sample, compared to relatively fast reaction rate for the 310 K sample in Fig. 4.10.

tures were chosen to be: the ambient temperature of the air in the NMR facility, 298 K; and a physiologically relevant temperature, 310 K (37 °C).

The effect of D_2O in the samples was found to decrease the rate of reaction or the steepness of intensity curve for both types of MMP probe (Fig. 4.10 and Fig. 4.11), compared to samples at the same temperature in 100 % H_2O. For the MMP–2/9 sensor, a higher temperature produced a faster reaction with an intensity plateau reached in under three hours. However, the generic MMP sample at 310 K produced an intensity curve which was not as quickly reacting as the 298 K 90 % H_2O sample, taking almost five times as long as the MMP–2/9 sensor to finish reacting.

Longitudinal relaxation

Prior to MMP addition, a T_1 IR experiment was performed for both MMP – 2/9 and generic samples at 310 K, as well as after MMP addition and

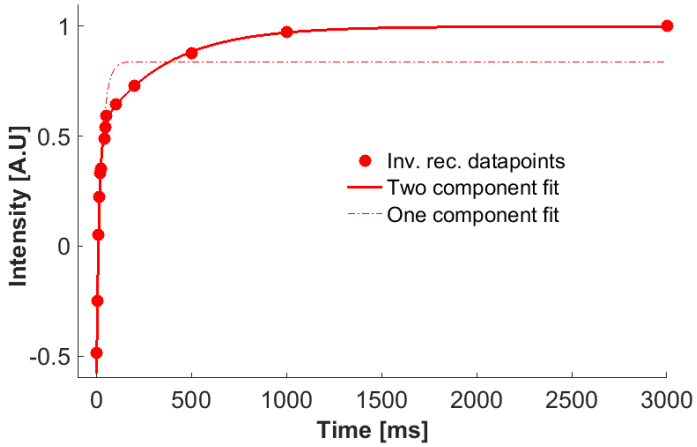


Figure 4.12: Justification of using multi component model for pre–cleaved T_1 data. IR timepoints taken from the pre–cleavage 310 K generic MMP sample, with fitting performed using one and two exponential component fits.

the timecourse experiments. It was found that the IR T_1 curves for the pre–cleaved samples were best modelled by fitting the two–component exponential model in Eq. 4.3.2 (Fig. 4.12 illustrates the appropriateness of the fitting clearly). The spectra shown in Fig. 4.9 are clearly convoluted with a mixture of lineshapes and it is reasonable that a single component fit is not the most appropriate here. In this case, the T_1 value is taken as the dominant value (the exponential component which contributes the majority of the T_1 data). In terms of T_1 values, $T_1 = 15.1$ ms and $T_1 = 12.8$ ms for the pre-cleavage MMP–2/9 and generic MMP sensors respectively. After cleavage, at least an order of magnitude increase is noted with values of $T_1 = 961$ ms and $T_1 = 960$ ms respectively, see Fig. 4.13.

Additional sensors: MMP–1 and MMP–7 substrates

Two additional substrates were tested in addition to the generic and 2/9 sensors, namely two sensors specific to MMP–1 and MMP–7. For the purposes of this chapter, we are interested in only the T_1 values pre– and post–cleavage and will not repeat the full lineshape analysis conducted for the initial two sensors. T_1 IR experiments were conducted in an identical manner to those in section 4.3.2 for the four additional probes. Ta-

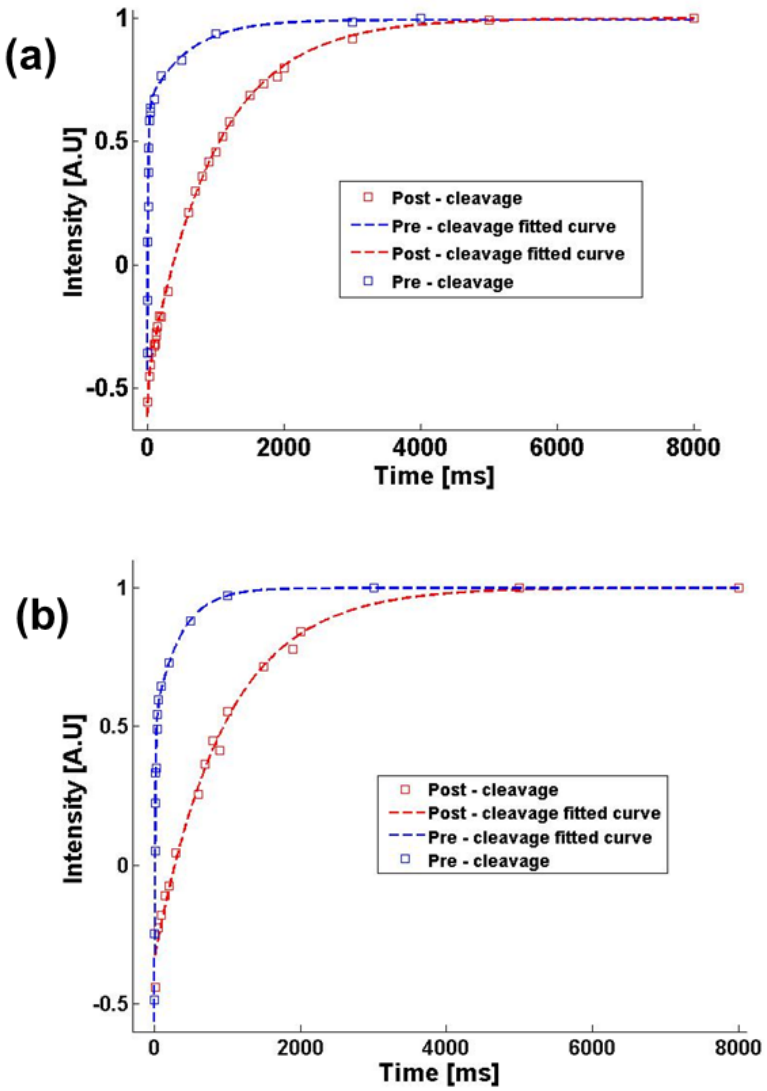


Figure 4.13: Longitudinal relaxation before and after MMP addition for MMP generic (a) and 2/9 (b) sensors. An IR experiment was performed for both MMP sensors, to measure fluorine T_1 relaxation times in a cleaved and uncleaved sensor. A steeper initial IR curve is observed in both cases for the uncleaved state, showing a distinct difference in T_1 relaxation after the sensors are cleaved.

ble 4.1 details the T_1 values for each component from the exponential fitting, along with the r^2 value of the fitting and the % composition to

the T_1 data which each component contributes. The composition is calculated from the exponential co–efficients (b and $(1-b)$ from the two component model in Eq. 4.3.2).

Both the MMP–7 and MMP–1 sensors were found to have dominating short T_1 values before cleavage ($\sim 10^1$ ms), with values up to 10^3 ms after cleavage; this is comparable to the MMP–2/9 and generic sensor results.

T_1 components for additional probes			
Probe state and type	**T_1 [ms]**	**Exp. weighting**	**r^2 value**
MMP–1 pre–cleavage	23 953	66 % 33 %	0.9977
MMP–1 post–cleavage	1038	N/A	0.9997
MMP–7 pre–cleavage	40 882	65 % 35%	0.9905
MMP–7 post–cleavage	1003	N/A	0.9980

Table 4.1: **Longitudinal relaxation components of additional MMP probes.** Both MMP–1 and MMP–7 sensors follow the previous trend of a dominating short (less than 50 ms) initial component before cleavage, with a longer ($\approx$ 1 s) single component after MMP cleavage. N/A indicates a single component fit was used and hence the two component curve composition analysis is not applicable.

4.3.3 Probe imaging studies

After the MMP sensors were characterised using the high field NMR system, a 9.4 T microimaging system was used to attempt to show the "On/Off" mechanism using imaging for the MMP–2/9 sensor. The imaging experiments were performed during development of the probes, with limited quantity of the probes available. The initial concentrations of the individual samples used on the 600 MHz spectrometer were below the detectable limit of the 9.4 T scanner and in order to increase the sample concentration to a detectable level, samples used for high field studies

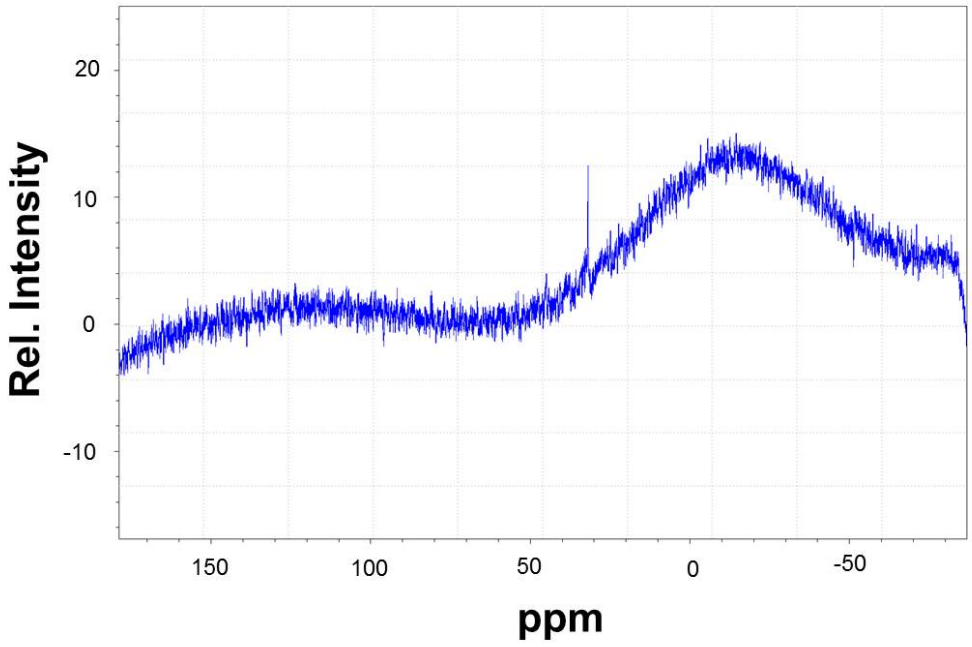
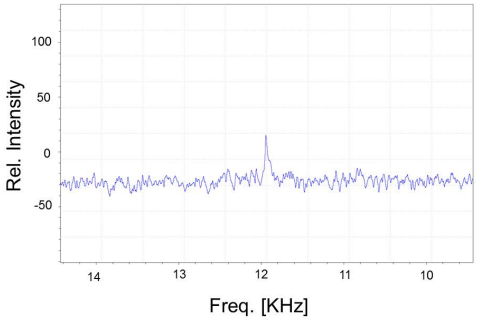


Figure 4.14: Fluorine background at 9.4 T using ^{19}F volume coil. Fluorinated glue used in the coil construction contributes a $\sim$ 100 ppm wide resonance to the fluorine spectra.

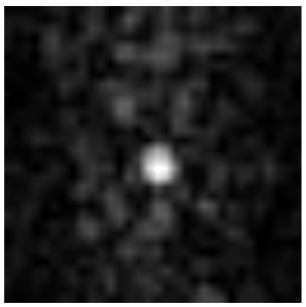
were combined to produce a single sample of 1 mM concentration. These samples had already had MMP added and had been cleaved, meaning that a before ("Off") image was not possible to obtain, but an after ("On") image to demonstrate feasibility of imaging the sensor was possible.

The fluorine detection coil unfortunately, but not uncommonly, contained a fluorinated glue which contributed a very wide (small T_2^*) background resonance which could not be removed with phase corrections (Fig. 4.14). However, this did not appear to significantly affect the signal from the MMP sensor.

A very weak NMR signal from the 1 mM MMP–2/9 solution was observed, shown in Fig. 4.15a, which was immediately imaged using a FLASH scan on Paravision software, using similar parameters to the ^{19}F experiments in Chapter 3, allowing full relaxation. Additional changes were: BW = 5 kHz and $N_{acq} = 128$. An overnight scan produced a faint but observable signal, indicating that the sensor can be imaged in the "On" state at 9.4 T (Fig. 4.15b).



(a)



(b)

Figure 4.15: MR imaging of cleaved MMP–2/9 sensor at 9.4 T. A spectrum was taken to identify the MMP–fluorine peak **(a)**, with a ^{19}F FLASH MR image also acquired, **(b)**. A large number of scans were required but a signal is visible.

4.3.4 Discussion of MMP probe results

We have demonstrated that there is a clear change in the observable fluorine MR parameters of both MMP–2/9 and generic MMP sensors, after addition of MMP–9. In particular for the MMP–2/9 sensor, a 60–fold increase in T_1 was observed after MMP addition, as well as a 3 to 7–fold decrease in linewidth (and consequently, a 3–7 fold increase in T_2^*).

Linewidth and T_2^* changes

Linewidth changes after MMP addition showed a measurable difference in value, with up to a seven–fold decrease being observed. The uncertainty in fluorine linewidth due to spectral convolution meant that the FWHM was difficult to accurately determine, with the lower estimate of a three–fold increase being based on the maximum possible FWHM. Other published probes noted a similar order of magnitude difference in intensity changes from the fluorine spectra [73]. Higher intensity changes are observed for probes with a reduced fluorine–Gd distance [60]. The change in T_2^* was used in this study as a proxy for change in T_2 times, which is a more commonly used parameter for such measurements. Our NMR study was limited in that T_2 measurements were

not available due to hardware constraints. However, the high field spectrometer was able to produce a very homogenous magnetic field and it is likely that the differences between T_2 and T_2^* in this study would be small.

Probe specificity

The specificity of the sensor substrate to the specific MMP is an important feature of molecular sensors. All sequences used for the MMP probes have been demonstrated to be specific only to the relevant MMPs (from previously published FRET literature [192–195]). This was confirmed using mass spectrometry (MS), to investigate if any cleavage products were formed from an MMP–2/9 sensor after incubation with MMP–12; the MS output was found to be identical for both before and after MMP addition (data not shown).

Paramagnetic relaxation effects

The change in T_1 times for all sensors exhibited the most significant parameter with which to measure the presence of MMPs, with a factor of 60 to 75 being observed (even higher than previously published probes). This is most likely due to the increased average distance between fluorine source and gadolinium chelate after cleavage, reducing the PRE effect.

The distance from the gadolinium moiety to the fluorinated amino acid was estimated to be around 20 Å, using ChemDraw software. However, the peptide sequence is a flexible linker which allows for rotation and coiling; it is likely that these dynamic effects occurred during experimental work. This explanation is the likely reason for the convoluted fluorine spectra observed pre–cleavage, with less convolution apparent after cleavage. It also provides physical justification of the use of a multiple T_1 model, in that if some fluorine molecules are coiled closer to the gadolinium than others, a stronger spin–spin interaction occurs and hence multiple T_1 components are evident.

Density functional theory (DFT) could be used to calculate more precise configurations which, in turn with additional relaxation measurements at different field strengths, could be used to calculate the fluorine–gadolinium distance. This data has been used in previous studies to optimise observed relaxation times through controlling the exact fluorine–lanthanide ion distance [197] and to estimate the reporter molecule to lanthanide distance itself [198]; future work using our probe may involve distance extension or reduction and optimisation using this method may be necessary.

Imaging of the sensor and hardware

The imaging of the probe represents very preliminary work, and as a result a number of sequence optimisations could be implemented. As it was not known what order of magnitude T_1 values would be observed, a T_R based on five times the value observed for TFA was taken. The complicating factor is the changing T_1 due to enzymatic cleavage, but this could be used advantageously to create a mechanism in which a brighter image is observed pre–cleavage (provided sufficient signal). For a short TR, as the T_1 increased a lower signal would be produced, compared to a faster relaxing pre–cleavage sample, as alluded to by Schmid et al. [199].

The FLASH sequence could be used more effectively to increase the imaging sensitivity. To do this, the repetition time must firstly be reduced as short as possible, which for a high field research scanner can be around 10^1 ms. The Ernst angle can then be calculated based on the ratio of the minimum TR and estimated T_1 of the fluorine sample; this angle is likely to be low since the TR/T_1 ratio is likely to be much less than 1. This would speed up the acquisition considerably, by at least a factor of a hundred; a modest TR of 100 ms for an optimised FLASH sequence would allow 200 acquisitions compared to a single acquisition using $TR = 20$ s for the exisiting scheme. The "Off" state of the probe would exhibit an increased signal compared to the cleaved state under this regime, where the shorter T_1 of the uncleaved state leads to less signal saturation during the rapid TR scheme. This would lead to a decreased signal intensity upon enzymatic cleavage of the sensor.

The most apparent disadvantage for imaging our sensor in terms of imaging hardware is the lack of an appropriate coil for 9.4 T imaging. The 25 mm volume coil did not efficiently enclose the sample, and from Chapter 3, will have had a reduced filling factor and hence, reduced available SNR. This may explain why Mizukami et al. [196] were able to use imaging in a timecourse experiment to observe intensity changes, since they used an 8 mm coil at 11.4 T, which will have a hugely increased SNR available. Additionally, due to the availability of the sample in small amounts, we were only able to acquire an image of the "On" state of the probe. The next step would be to demonstrate the mechanism by obtaining a "Off" image once more sensor material has been synthesised.

Chemical structure

An important benefit with our sensor compared to the ^{19}F MMP sensor by Yue et al. [73] is the type of gadolinium complex used, which is a relatively stable octadentate DOTA–type complex. The complex used by Yue et al. is a less kinetically inert heptadentate Gd-DO3A complex, in which the gadolinium is more likely to leech under acidic conditions. Yue et al. additionally included a polyethylene glycol (PEG) linker as part of their probe construction, in order to increase solubility. Our probe was found to be soluble in all concentrations of up to 1 mM but higher concentrations may require measures to increase solubility.

4.4 Towards pre–clinical implementation

Investigations into the possibility of translating the sensor towards an *in vivo* set–up were conducted on an animal pre–clinical 7 T scanner, with the aim of quantifying the sensitivity required for this translational imaging set–up. A surface coil for fluorine and proton imaging was constructed, with dual nuclei imaging tested, and the detection limits for the scanner computed using simple fluorinated compounds.

4.4.1 Sequence parameters and sample preparation

All experiments were performed on a 7 T Bruker Biospec Avance III 70/20 USR system (Bruker Biospin MRI GmbH, Ettlingen, Germany). Simple 1–D NMR experiments were performed to detect fluorine signal and to measure the SNR. For this, Topspin 2.0 software was used along with a pulse–acquire "zg" experiment. Imaging was performed using two main sequences, a rapid imaging with refocussed pulses (RARE) method and a FLASH method, using Paravision 5.1 software, also available on the Bruker scanner. Specific acquisition parameters are stated in the relevant text.

Two sets of samples were used for surface coil testing experiments: firstly, a set of three 1 mL fluorinated samples of different concentrations of fluorine; secondly, a single 3 mL glass tube with two fluorine species present. The three single 1 mL samples were prepared by making a stock solution of 10 mL H_2O and 0.1 mL of pure TFA (13 M concentration) and performing three dilutions: (1) taking 1 mL of stock solution; (2) taking 0.5 mL of stock solution and adding 0.5 mL of H_2O; (3) 0.2 mL of stock solution and 0.8 mL of H_2O. This produced a TFA concentration of 130 mM, 65 mM and 26 mM in samples respectively. The 3 mL sample was prepared by dissolving 10 mg of 3,5–Bis(trifluoromethyl)benzylamine (6FAA) powder with 0.15 mL of TFA and 0.1 mL DMSO, filled up to 3 mL volume using distilled H_2O. The two fluorine sources (TFA and 6FAA) have different concentrations (650 mM and 14 mM respectively) and different resonant frequencies.

4.4.2 ^{19}F surface coil construction and testing

A surface coil resonating at the 7 T fluorine frequency ($\approx$ 282.6 MHz) was constructed, by myself, at the electronics laboratory at the Sir Peter Mansfield Magnetic Resonance Centre. Surface coils generally allow a higher filling factor compared to volume coils and are therefore more sensitive; for our study a greater sensitivity will mean a lower detectable concentration which is important. The coil consisted of a printed circuit board (PCB) divided into three sections, with two variable capacitors

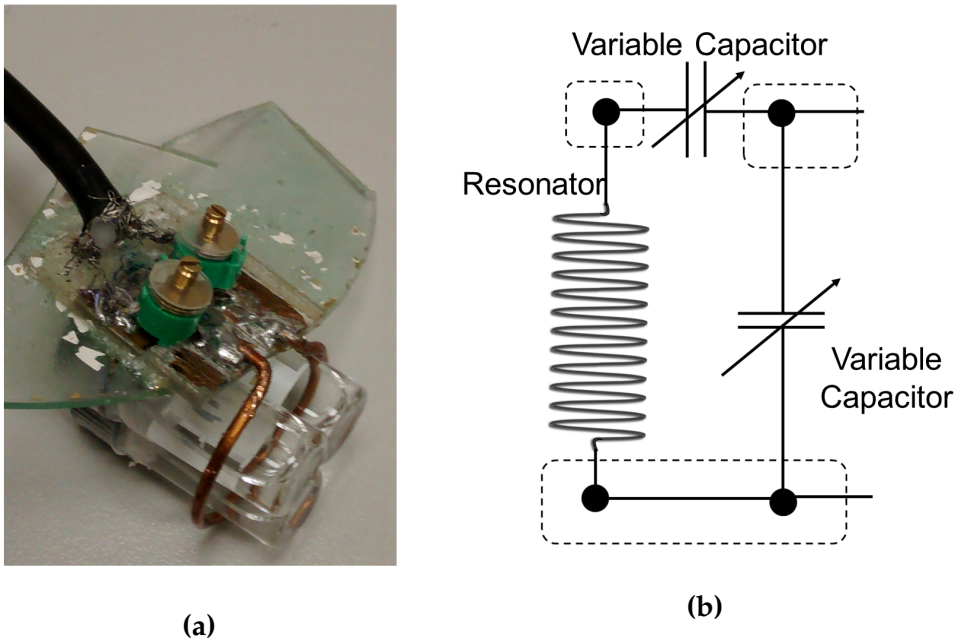


Figure 4.16: Custom–made ^{19}F surface coil. **(a)** Photograph of actual coil, showing three fluorinated samples positioned in the single loop coil, attached to a co–axial cable. The green variable capacitors are easily adjusted using a suitable screwdriver. **(b)** Electrical component diagram of surface coil with dashed lines indicating the separate electrical potential regions, divided into three parts on the circuit board.

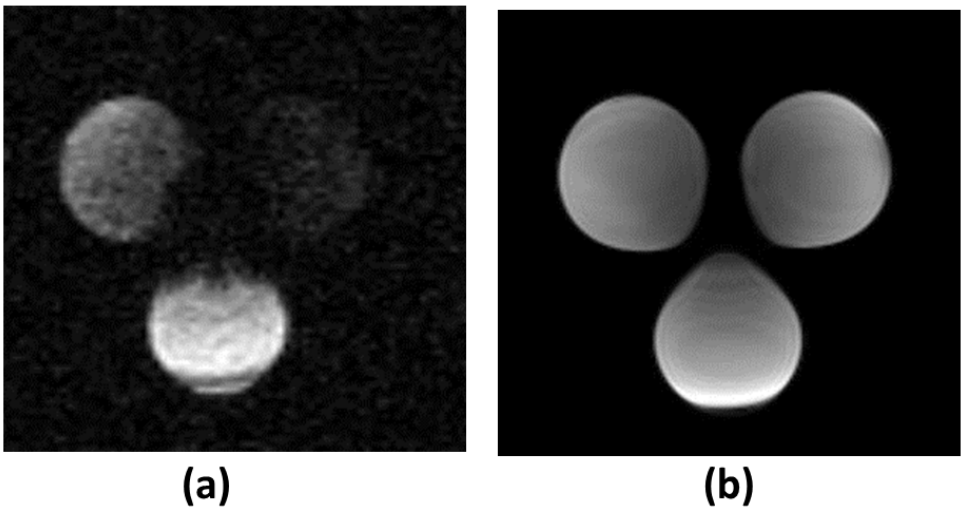
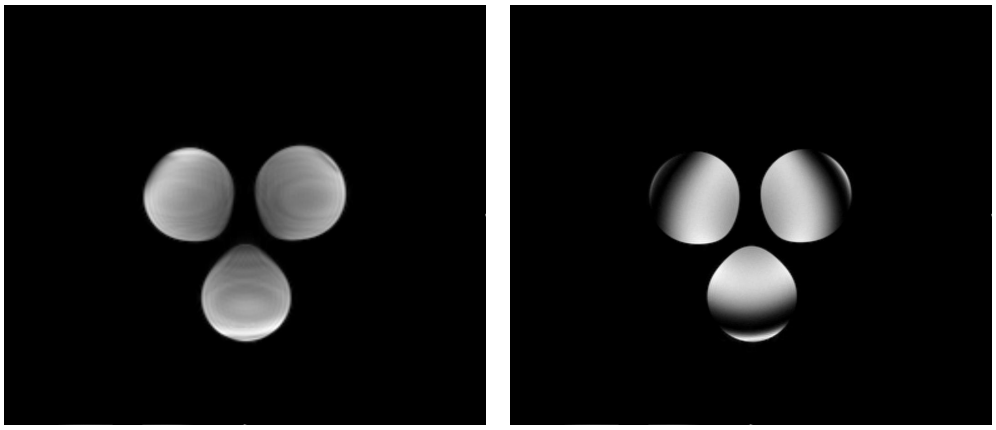


Figure 4.17: Sensitivity differences between ^{1}H and ^{19}F. A FLASH scan is used to acquire images for both nuclei where **(a)** is the fluorine image and **(b)** is the proton image. The fluorine concentration, clockwise starting from top left is 65 mM, 26 Mm and 130 mM. The water concentration in each sample is roughly constant. The proton image has a vastly greater intensity due to the much larger concentration of water compared to fluorine in the samples.

(range: 5 to 25 pF), connected to a 12 mm copper wire loop (acting as the resonator) in a series circuit, as shown in Fig. 4.16. Fortunately, the coil also had a tuneable H_2O resonance which allowed comparisons between the two nuclei.

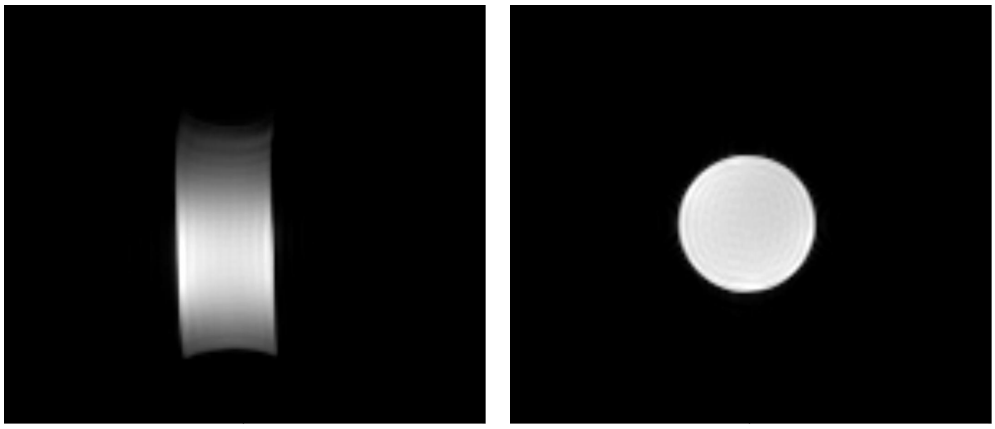
Initial experiments used the three 1 mL samples bound together and slotted inside the circular coil loop, to produce both fluorine and proton images (see Fig. 4.17). A FLASH scan was used for both images, with parameters: FOV = 40 $\times$ 40 mm^2, slice thickness = 1 mm, TE = 6 ms, flip angle = 70°, T_R = 15 s, N_{acq} = 8, MTX = 128 $\times$ 128. The proton scan depicts the three tubes with no discernible signal differences, as opposed to the fluorine image which correctly identifies the different concentrations between samples. Note that the FOV has been cropped to accurately show the two nuclei images side by side.

The differences between gradient and spin echo methods were found to be very apparent for proton measurements using the surface coil. The



(a) **(b)**

Figure 4.18: Two different ^{1}H imaging methods for the surface coil. (a) a gradient echo FLASH scan, **(b)** and a spin echo turbo–RARE method. The "ring" artefact in turbo–RARE method is due to excitation pulse angles different to precisely 90° and 180° achieved in the darker regions. Parameters for this sequence were: $N_{acq} = 1$, no. slices = 9, no. echos = 8, RARE factor = 8, effective echo time (TE_{eff}) = 36 ms, TR = 2.5 s, FOV = 45 × 52 mm, MTX = 384 × 384, slice thickness = 1mm. Similarly, the FLASH scan is susceptible to magnetic inhomogeneities, hence the inhomogeneous intensity across the samples. The FLASH scan used the following parameters: MTX = 256 × 192, no. slices = 9, slice thickness = 1, $N_{acq} = 8$, flip angle = 70°, $TR = 2.5$ s, TE = 6 ms, FOV = 45 × 52 mm.



(a) **(b)**

Figure 4.19: Detectable volume determination of surface coil using ^{1}H images. **(a)** A coronal and **(b)** axial FLASH proton image of the 3 mL sample. The axial image shows an accurate circular profile of the sample tube. The coronal image is relatively uniform, with signal loss at the top and bottom of the image where the detection region of the coil ends.

gradient echo method, such as FLASH, is susceptible to magnetic field distortions and inhomogeneities and this is clear in the spatial and intensity distortions in the FLASH image in Fig. 4.18a. For spin echo methods using a surface coil, which use a 90° and 180° pulse, perfect pulse calibration is impossible since the generated flip angle varies spatially. A banding type artefact may be produced, as in the case of the RARE scan [200] in Fig. 4.18b, which resulted from the banded region not receiving these exact pulses; this was in part due to B_1 inhomogeneity in which the pulse power emitted is not homogeneous across a sample.

4.4.3 *In vivo* MRI feasibility

The detectable volume of the coil was determined by placing the 3 mL sample to try and fill as much of the detectable volume as possible, extending at the top and bottom outside of the detectable region. Adiabatic pulses were used in order to reduce artefacts and to obtain an accurate distance measurement, with axial and coronal FLASH scans acquired, as shown in Fig. 4.19. Identical parameters to the previous section are used, aside from the adiabatic acquire pulses. The distance measurement tool

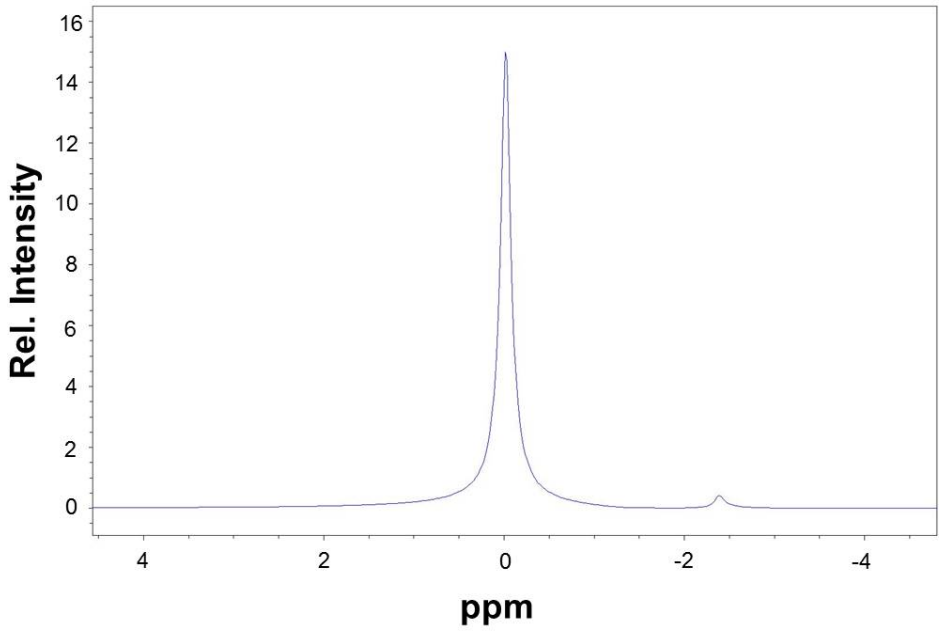


Figure 4.20: ^{19}F non–localised spectrum of fluorinated compounds using a surface coil. Compounds of known concentration produce fluorine signals which can be used to extrapolate detection limits for the set–up. 650 mM of trifluoroacetic acid (TFA, large peak) and 14 mM of 3,5–Bis(trifluoromethyl)benzylamine (6FAA, small peak to the right of centre) are the two compounds visible in this experiment.

in Paravision 5.1 software gave the following measurements: approximately 26 mm lengthways, with a circular cross–section of diameter of 11 mm, giving a total volume of 2.5 mL. This is the total available sample which can contribute a signal.

Fluorine spectroscopy was then performed on the 3 mL sample to calculate detectable limits; Fig. 4.20 shows an acquired spectrum from the sample with the two separate fluorine peaks visible. A "zg" sequence was used with N_{acq} = 8, BW = 10 ppm, TR = 20 s, pulse length = 58 μs, pulse power = 6 dB and TD = 1024, and the SNR was measured for both fluorine peaks present in the resulting spectrum. For TFA, $\text{SNR}_{TFA} = 2060/\sqrt{8} \approx 728$ at $c = 650$ mM, and for the 6FAA, $\text{SNR}_{6F} = 94/\sqrt{8} \approx 33$ at $c = 14$ mM. To calculate the concentration detection limit for this coil and scanner for each fluorine compound, the SNR measured is scaled to the minimum SNR, and the volume is corrected for the detectable volume available:

$$c_{6FAA_{min}} = \frac{\text{SNR}_{3.5}}{\text{SNR}_{TFA}} \times \frac{2.5}{3} \times c_{6FAA} = 1.2 \text{ mM} \tag{4.4.1}$$

$$c_{TFA_{min}} = \frac{\text{SNR}_{3.5}}{\text{SNR}_{TFA}} \times \frac{2.5}{3} \times c_{TFA} = 2.6 \text{ mM} \quad . \tag{4.4.2}$$

These are the minimum concentrations required for a sample of 2.5 mL to achieve an SNR of 3.5.

4.4.4 Discussion of detection limits at 7 T

The results of the detection limit study at 7 T using a surface coil show that a limit of around 1 mM is found for a compound containing six identical fluorine atoms; this is the same number as the MMP fluorine source. However, application of these detection limits to the MMP probe are affected by two further factors: fluorine linewidth and sample volume. The linewidth of the MMP sensor at 9.4 T was around 30 Hz (exact determination difficult due to very noisy spectra) and the linewidth of the compounds at 7 T were less than 5 Hz. Using the theoretical formulation in Chapter 3, this difference in linewidth will increase the detection limit by a factor of $\sqrt{6}$, to around 3 mM. The sample volume will also

affect the detection limit, since *in vivo* application to a mouse or rat disease model would require small injectable volumes. For volumes which could be injected i.v. to a mouse model, the volume will be of the order of 0.1 mL, since a mouse has a total blood volume of around 1 mL. Consequently, the minimum concentration would need to increase by a factor of (2.5 mL / 0.1 mL). This puts the minimum detectable concentration for the MMP probe to be around 75 mM. For a dynamic study, in which the fluorine signal is monitored over the course of an *in vivo* experiment (up to and including 4 hours max.), the concentration must be even higher to meet the SNR/time limit imposed in order to acquire every few minutes.

Exact *in vivo* minimal detectable limits are hard to quantify due to a compound's biodistribution, but previous studies have determined rough limits which agree with the conclusion that the MMP sensor is below the detectable limit for pre–clinical scanners. A human neck tumour metabolism study stated that in a 6 minute acquisition, the minimal detectable limit was a 30 μmol/g concentration per wet tissue from a 33 mL 5–FU chemotherapy administration on a 1.5 T scanner [201]. Other studies of a PFCE by Ruiz et al. [110] found a limit on a similar order of magnitude; 30 μmol/g wet weight in a 4 minute acquisition time in a volume of 60 μL. Importantly in these studies, the fluorine sources used are either very fluorinated (much more than the six fluorine per molecule we have) or use large volumes (the N_s is the detection limiting quantity for these studies), neither of which are possible adaptations which we can utilise for our sensor. It is clear from my investigations that the current fluorine source is insufficient to provide enough signal for translation to a pre–clinical set–up.

4.5 Outlook: Signal enhancement strategies

Clearly, a major goal for the application of current fluorine contrast agents is to increase sensitivity, with several advances in both chemistry and physics leading towards this.

Chemistry: increased amount of fluorine atoms

One approach is to increase the amount of fluorine attached to each molecule; Takaoka et al. [202] demonstrated the linear relationship between SNR and the number of fluorine spins of different synthesised molecules. This is supported by the standard equations for the SNR from a simple NMR pulse sequence (detailed in Chapter 3), where there is a directly proportional relationship between fluorine spins and the SNR. Commonly used PFCs such as PFCE produce a sevenfold increase in sensitivity compared to a molecule with just a CF_3 group. A molecule with 36 identical fluorine atoms named PERFECTA [77] was recently synthesised, which increases the sensitivity of a CF_3 group by a factor of twelve. A very highly fluorinated probe containing 540 identical fluorine atoms is the latest addition to this group of sensors [203]. It is not yet clear whether this structure is ideal for *in vivo* applications, as it has not been shown that the high fluorine content is enough to outweigh possible signal reductions from slow tumbling rate and other broadening effects related to the molecule.

However, for "active" enzymatic probes which consist of several individual molecules which are attached together, simply adding more fluorinated groups can be problematic. This is due to the increased electronegativity of a compound from the electronegative fluorine atoms. Consequently a CF_9 molecule is more difficult to attach in such an enzymatic sensor than a CF_3 group. Additionally, the larger a fluorinated structure present, the more the kinetics of the whole molecule will be affected. Factors such as the rotational tumbling time of the molecules will decrease for large structure since the molecule is less mobile, and hence the fluorine linewidth will broaden.

Physics: pulse acquisition methods

Zero echo time (ZTE) and radial *k*–space sampling

A technique for ultra–fast imaging of fluorinated compounds has led to the development of a signal enhancement strategy for ^{19}F MRI. In a recent publication, Schmid et al. [199] build on previous work by Chalmers

et al. [197, 204] and describe a GE imaging sequence which can be used to measure an increased signal from small fluorinated molecules in fluorine MRI, which have short T_1 values from paramagnetic relaxation effects. Radial sampling in *k*–space using a zero echo time method [205] is used to obtain a signal from the highly relaxed fluorine. With this approach in mind, it has been conjectured that this sampling method could be applied to measure the relaxed fluorine signal from a linked Gd-fluorine compound such as that used by Mizukami et al. [60].

Accelerated (compressed) sensing

Compressed sensing is a concept adapted from information theory and is based on the principle that an image can be compressed by recording a small number of parameters and then reconstructing the image fully, based on the given parameters. It was theorised that if a compression and reconstruction can take place, then some of the initial data should not be needed if the reconstruction relies on only a select number of points. This should allow a small amount of *k*–space to be sampled and then reconstructed without the need for full sampling of *k*–space, ultimately allowing a faster acquisition time. The data sampling technique as applied to MRI was detailed by Lustig et al. in 2007 [206] and has since gained popularity within a number of applications in MRI. Kampf et al. [207] used a compressed sensing method for chemical shift imaging and more recently Zhong et al. [208] have shown a method of compressed sensing applied to ^{19}F MRI. The Zhong group showed that an eight–fold reduction in imaging time for a PFC emulsion phantom using ^{19}F imaging scan can be achieved with little reduction in image quality. Fluorine imaging tends to detect sparse "hotspots", rather than structural information as is the case in proton MRI, and it is likely that the development of these sparse imaging methods will reduce acquisition times for fluorine MRI in the future.

CHAPTER 5

Alternative techniques for molecular imaging: chemical exchange saturation transfer (CEST)

5.1 Outline

The preceding chapters have demonstrated the application of an exciting molecular technique in ^{19}F MRI, yet it is clear that sensitivity is the greatest prohibitive consideration for this method. With this in mind, the remainder of this thesis is centred on a molecular MR technique which seeks to address the issue of sensitivity, namely chemical exchange saturation transfer (CEST).

In this chapter, the basic principles involved in CEST are introduced, before moving to the more theoretical aspects of the method. This chapter discusses the technical details involved in a CEST experiment, presenting results from experiments and optimised simulations. These results will inform later chapters.

The purpose of this chapter is to simulate the optimal experimental parameters for an amide proton transfer (APT) CEST experiment, and to test CEST sequences *in vitro* prior to a full CEST study. Simulating the CEST effect can help inform choosing experimental parameters for *in*

vitro experiments, highlighting important parameters and the nature of their effect on the CEST effect. Various experimental set–ups are investigated to ascertain potential issues, before performing an *in vitro* cell experiment in Chapter 6. In particular, initial experiments are performed using a fast imaging with steady–state precession (FISP) sequence on a Bruker 7 T scanner as well as cine and GE sequences on a Varian 9.4 T scanner to compare optimal conditions for APT experiments. Creatine (Cr) phantoms are tested using CEST sequences, since creatine is widely used in the CEST literature to replicate the exchange rate of APT CEST. In addition, myo–inositol (mI) phantoms are used to investigate metabolite effects near the water peak. Optimisation is performed only for APT simulations, to inform parameter choice in Chapter 6; otherwise generic saturation parameters are sufficient for observing CEST effects and these are stated in the text.

5.2 Introduction

CEST was originally developed by Ward and Balaban as a method to study pH changes using NMR [210]. The simplest physical interpretation of CEST was to assume two distinct chemical pools engaging in proton chemical exchange; the two exchanging pools being a bulk water pool (pool A) and a small pool of labile protons in solution (pool B). The protons are exchanged between these pools at an exchange rate of k_{ab}, for exchanges from pool A to B, and at a rate of k_{ba} in the reverse direction [209]. Exchange is measured through selective irradiation, saturating specific frequencies over a given ppm interval. Certain irradiated frequencies correspond to the resonant frequencies of specific proton bonds in the solute molecules (e.g. N–H bonds, O–H bonds etc.), in the same way that protons in metabolites resonate at different frequencies in a MRS spectrum. Saturation in this spin 1/2 case is defined as the forced equilibrium of spin states; full saturation is the equal population of the "up" and "down" spin states.

Upon saturation, the solute protons exchange chemically with the bulk water at a rate k_{ab}, transferring the R.F. saturation to the bulk water peak

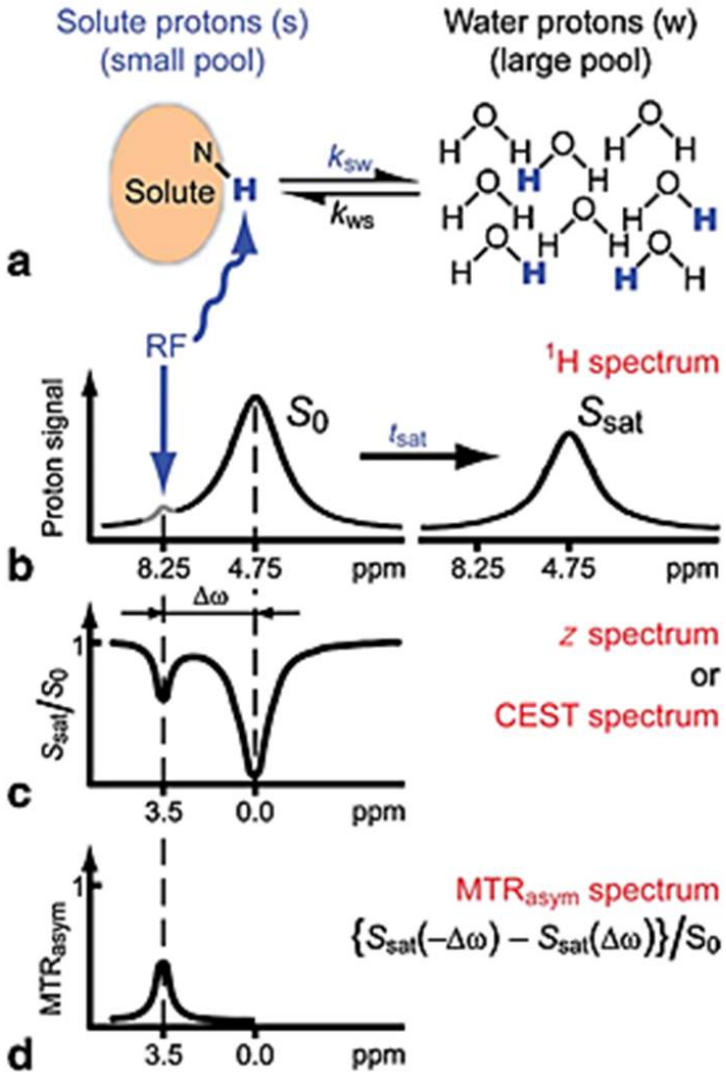


Figure 5.1: Chemical exchange saturation transfer process from [209]. **(a)** The solute protons exchange chemically with bulk water protons upon selective saturation. **(b)** Selectively saturated solute protons act to reduce the bulk water signal whilst being irradiated. Increased saturation time increases the CEST effect. **(c)** The intensity at each offset frequency can be plotted to form a Z–spectra. **(d)** The magnetisation asymmetry plot shows the normalised difference between positive and negative saturation offsets, either side of the water frequency at 0 ppm. Symbolically k_{sw} is equivalent to k_{ba} in the diagram.

which consequently reduces in intensity. CEST is a dynamic process in which saturated solute protons are replaced with unsaturated protons which continue to be replaced during the period of R.F. saturation, t_{sat}.

Provided the solute protons are saturated for a sufficient amount of time for this unsaturated proton replacement process to occur many times, a significant reduction in the water peak is observed.

Generally a CEST experiment will cycle through a range of frequencies around the water resonant frequency (labelled as 0 ppm in CEST and 4.75 ppm in spectroscopy). There is little or no reduction in water peak intensities if there is no chemical exchange at a given frequency. A measure of which frequencies produce the greatest water peak signal reduction can be given by measuring the saturated water peak at each saturation frequency, S_{sat}. The signal at the saturation frequency is then normalised by dividing by the water peak intensity without saturation, S_0, and plotting; this is known as the CEST spectrum or Z–spectrum (see Fig. 5.1). A number of processes contribute to the CEST spectrum (discussed below), with CEST contrast generally defined using a magnetisation transfer ratio (MTR) asymmetry spectrum [211]. The MTR asymmetry method assumes symmetrical non–CEST contributions to the Z–spectrum around 0 ppm. This implies the normalised difference between corresponding frequencies either side of 0 ppm will indicate CEST contrast. This gives the CEST effect at a frequency $\Delta\omega$ away from 0 ppm,

$$\mathrm{MTR}_{\mathrm{asym}}(\Delta\omega) = \mathrm{MTR}(\Delta\omega) - \mathrm{MTR}(-\Delta\omega) \quad . \tag{5.2.1}$$

The MT ratio is defined as $\mathrm{MTR} = 1 - S_{sat}/S_0$, such that:

$$\mathrm{MTR}_{\mathrm{asym}}(\Delta\omega) = (S_{sat}(-\Delta\omega) - S_{sat}(\Delta\omega))/S_0 \quad . \tag{5.2.2}$$

This equation shows that to determine the CEST effect at $\Delta\omega$ ppm, the difference in signal intensity between right and left sides of the Z–spectrum should be calculated and normalised with the intensity in the absence of saturation.

5.3 Theory and CEST methods review

The physical processes involved in the CEST effect have their origin in a variety of chemical interactions [212]: 1) Protons in water may directly exchange with the protons attached to molecules; 2) whole water

molecules may exchange completely with the water molecules attached to larger molecules; 3) through a combination of both water and proton exchange; 4) water molecules may change molecular environments or compartments; 5) compartmental water exchange coupled with proton exchange. Most endogenous CEST effects use a combination of the first three mechanisms, with exogenous CEST agents tending to utilise the latter two. Further investigation or review of these mechanisms is beyond the scope of this work, with the focus for the remainder of this theory section being the mathematical formulation of the CEST effect.

5.3.1 Mathematical model

From a two pool model of exchange, the pure proton exchange effect (PTR) can be simply and analytically formulated as [209]:

$$PTR = X_s.\alpha_{sat}.k_{ba}.T_{1a}(1 - e^{-t_{sat}/T_{1a}}) \quad , \tag{5.3.1}$$

where T_{1a} is the water pool's T_1 value and α_{sat} is the saturation efficiency. X_s is:

$$X_s = \frac{[\text{solute proton}]}{[\text{water proton}]} = \frac{k_{ab}}{k_{ba}} \quad , \tag{5.3.2}$$

where square brackets denote concentrations. Here we assume the solute pool is small compared to the water pool and no back exchange occurs, and that irradiation to the solute pool does not affect the water pool (i.e. no spillover effects in the steady state). The saturation efficiency, α_{sat}, can be given as [213]:

$$\alpha_{sat} \approx \frac{(\gamma B_1)^2}{(\gamma B_1)^2 + (k_{ab})^2} \quad . \tag{5.3.3}$$

For situations in which the saturated–state is reached, $\alpha_{sat} = 1$. The saturated–state signal is obtained after a long B_1 saturation time such that $t_{sat} \geq 5 \times T_1$, and the spin system is saturated [214]. This equation shows that the pulse power must be great enough to produce high α_{sat} values and that the power must also compete with the bulk water to solute exchange rate. From Eq. 5.3.1, if the exchanging spin system is saturated, additional pulse power or saturation time will not increase the observed pure CEST or PTR effect.

Confounding CEST signal effects: direction saturation, nuclear Overhauser effect and magnetisation transfer

The CEST contrast generated purely by proton exchange (PTR, discussed above) is the primary contributor to the CEST spectrum, but other chemical interactions also have an effect. Direction saturation (DS) or water spillover is the reduction in the water peak when the water pool is directly saturated around 0 ppm . This effect produces the broad, symmetrical shape observed in Fig. 5.1c. DS effects are symmetrical around 0 ppm, which is why the MTR asymmetry method is useful to remove or reduce this effect.

The nuclear Overhauser effect (NOE) is the transfer of spin magnetisation from the side chain of molecules to the water pool via cross–relaxation, discovered in NMR around 60 years ago by Overhauser [215]. The NOE has been hypothesised to play a significant role in the signal intensity contributions on the negative side of the CEST spectrum between 0 and -5 ppm [216], due to aliphatic and olefinic molecular contributions [217]. This is a potential problem for the MTR asymmetry method, where the MTR effect from subtraction at positive and negative frequencies is reduced.

Magnetisation transfer (MT) effects also confound the pure proton exchange effect in CEST. MT has been used as a contrast mechanism itself for a number of years to investigate signal contributions from macromolecules with very short T_2 values [218]. The MT effect originates from a very broad molecular MT pool in which protons are bound to large macromolecules and have limited mobility. With MT, a single R.F. pulse may be placed anywhere in a very large range of frequencies and still saturate the MT pool. Importantly, CEST contrast is frequency specific ($\sim$ 1 ppm and less) but consists of a large overlap of resonances, where different solute proton environments may correspond to the same saturation frequency.

The observed experimental saturation is therefore difficult to separate between the PTR effect and the other confounding factors. The equation for the total saturation of water at a given frequency, $\Delta\omega$, is adapted from

[212] if exogenous contrast agents are not present, and can be stated as,

$$\frac{S_{sat}(\Delta\omega)}{S_0} = PTR^{endo}(\Delta\omega) + MT(\Delta\omega) + DS(\Delta\omega) \tag{5.3.4}$$

where $PTR^{endo}(\Delta\omega)$ is the pure proton exchange signal from endogenous molecules. A common simplification is to assume MT and DS are symmetric around water, and hence using the asymmetry measure is reasonable to investigate the PTR effect, since $MTR_{asym} \sim PTR^{endo}$.

Effect of chemical exchange rate on CEST signal

The speed with which the exchange takes place greatly affects the CEST effect, and is dependent upon the particular exchanging moiety. In general to observe chemical exchange, the exchange rate, k, must be less than or equal to the difference in frequency between the two exchange sites, $\Delta\omega$. The exchanging groups in a two pool model will normally be bulk water protons at 0 ppm and the exchanging solute proton (for example, amides). Slow exchange regimes are characterised by the exchange rate being much less than the frequency difference, i.e. $k \ll \Delta\omega$. For intermediate exchange regimes, $k \sim \Delta\omega$. Typically, amide protons ($k \sim 10^0$ to 10^2 s^{-1}) are slowly exchanging with the water peak, amine protons ($k \sim 10^2$ to 10^3 s^{-1}) have slow to medium exchanging rates and hydroxyl protons ($k \geq 10^3$ s^{-1}) [219] have medium to fast exchanging rates. Eq. 5.3.1 shows that an increased exchange rate will increase the observable CEST contrast, hence a lower contrast can be expected with slower exchange rates.

5.3.2 Applications of CEST

In a similar manner to the MRS spectrum in which specific groups or molecular environments contribute to a specific resonance, proton exchanging groups in CEST have been assigned specific ppm resonances in the CEST spectrum, see Table. 5.1. However, unlike in MRS, there is a great deal of overlap between different exchanging groups and the CEST effect at a particular frequency is often a contribution of several exchang-

CEST resonance (ppm)	Contributing CEST group
0.6	myo–inositol (OH) [220]
1	glycosaminoglycans (OH) [221]
1	glycogen (OH) [222].
1.9	creatine (OH) [223]
2 – 3	amine (NH_2) [224]
3	glutamate [225]
3.2	glycosaminoglycans (NH) [221]
3.5	amide (APT / NH)

Table 5.1: **CEST resonances and functional groups.** OH, NH, NH_2 symbols in brackets refer to the hydroxyl, amide and amine contributing CEST group respectively.

ing moieties. Additionally, metabolites may contain several endogenous "CEST active" groups which contribute to the chemical exchange in solution with water and will appear to contribute at several different frequencies.

The resonance of interest in this work is the NH proton bond which contributes to the CEST signal at + 3.5 ppm (APT resonance frequency), first described by Zhou et al. [226]. APT contrast increases with field strength [227], as with other resonances, and is commonly used in cancer studies. Importantly, the separation between the APT and water resonant frequency is increased as the field strength increases, making observation of APT contributions more apparent. This metabolite therefore looks to be a good molecular target using CEST imaging for a cancer cell CEST experiment. A more detailed description of APT applications is given in Chapter 6.

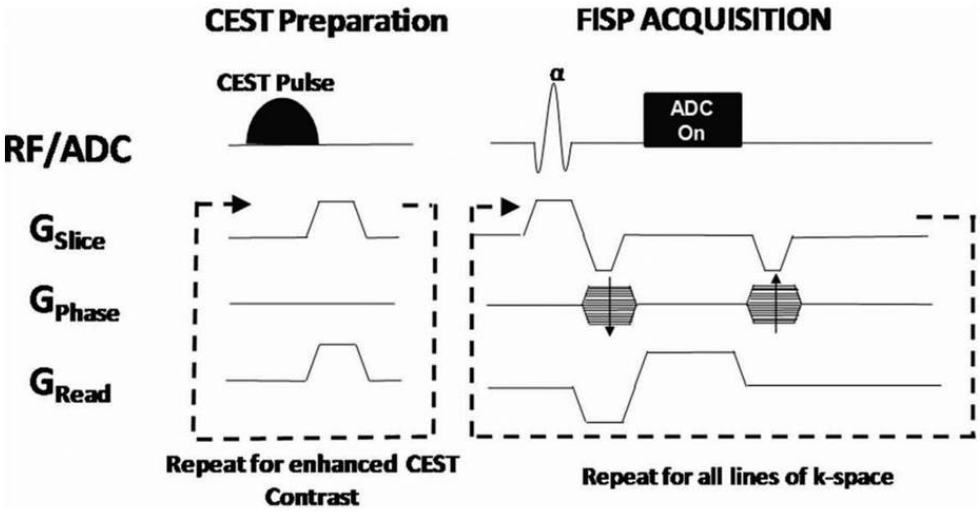


Figure 5.2: FISP sequence used in a CEST acquisition for Bruker 7 T experiments taken from [228]. The saturation module is separate to the steady state acquisition section of the FISP sequence. A centric encoding scheme is normally used in conjunction with the FISP sequence to decrease the acquisition time of the centre of *k*–space and to maximise the available signal detectable after excitation.

5.3.3 CEST methods

CEST acquisition sequences

A wide range of different sequences have been utilised in CEST experiments including; a FLASH sequence [229], gradient and spin echo sequences (GRASE) [230], and cine sequences [231]. One of the fastest CEST acquisitions to date has been using a Bruker FISP sequence [229], and this sequence is used in the presented *in vitro* experiments. Additionally, standard Varian GE and cine sequences are investigated in this thesis; the latter of the two is part of the fast gradient echo imaging family.

FISP sequences are also examples of fast GE imaging methods, which use short repetition times to reduce scanning time. The TrueFISP method used for Bruker CEST experiments achieves a steady–state magnetisation in which the residual transverse magnetisation is recycled after each T_R [232]. Application of an initial R.F. pulse of flip angle $\alpha/2$ prepares the

transverse magnetisation, followed quickly by a series of α pulses which generates a series of FIDs and spin echos to establish steady–state. This category of sequences are known as balanced steady–state in free precession (bSSFP) sequences, where the "balanced" prefix indicates the application of additional gradients to balance or refocus the magnetisation vector. Fig. 5.2 shows the general FISP pulse sequence used in previous CEST FISP literature.

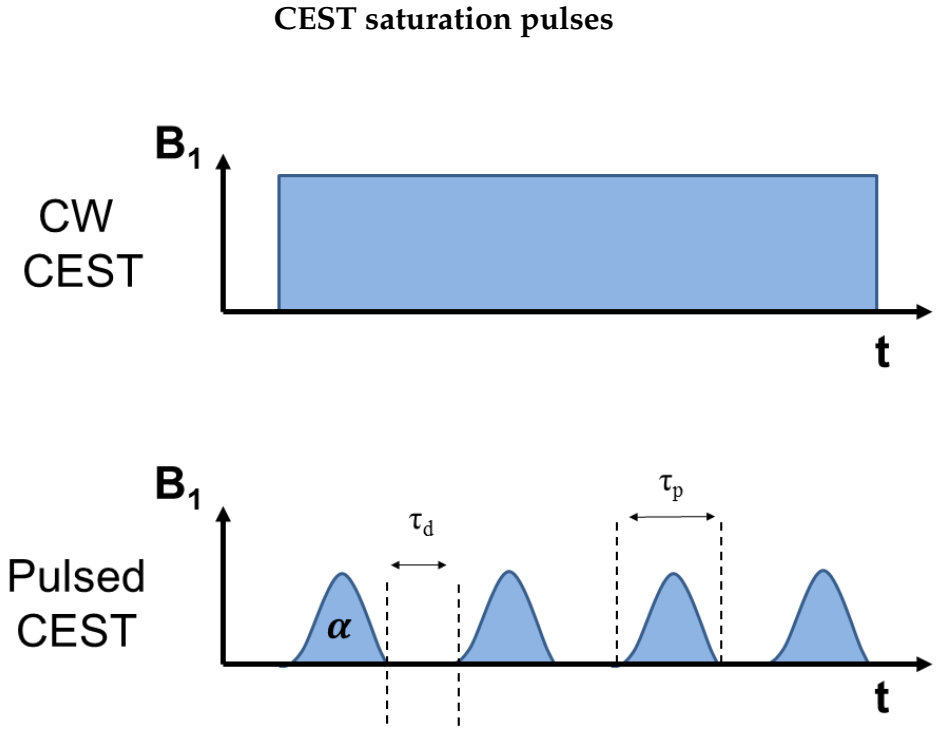


Figure 5.3: Basic CEST saturation schemes. Continuous wave (CW) and pulsed wave CEST sequence diagrams are compared, with pulsed wave CEST requiring definition of additional parameters to define the saturation scheme. The B_1 field for continuous wave is straightforward to calculate, yet pulsed CEST will be affected by the length of the gap between the pulses, τ_d, and the duration of individual pulses, τ_p.

Several schemes exist in CEST methods to induce chemical exchange with the two main categories of saturation being continuous wave (CW) and pulsed wave CEST schemes. Continuous wave refers to rectangular, hard pulses which have a constant B_1 value throughout their saturation

period, t_{sat}. Pulsed CEST is a series of pulse shapes such as Gaussian or sinc pulses, which are repeated over a time period, to form a pulse train. Pulsed CEST is often used on clinical systems due to the reduced specific absorption rate (SAR [J/kg]) compared with continuous irradiation.

For block pulses the saturation frequency, w_1 is given by [214]:

$$\omega_1 = \frac{B_1}{\gamma} \tag{5.3.5}$$

For pulsed CEST a series of soft pulses are used, with the flip angle, α, given by,

$$\alpha = \int B_1 \gamma \tau_p \quad . \tag{5.3.6}$$

The parameter called the duty cycle (DC) is commonly used to identify the fraction of time which consists of R.F. irradiation, where $DC = \tau_P/(\tau_p + \tau_d)$. A comparison between the pulsed and continuous wave set–ups are given in Fig. 5.3, with Gaussian pulse shapes used typically for pulsed CEST. Schmitt and colleagues' work [233] showed that other pulse shapes, such as sinc pulses, produced unwanted direct saturation effects when the CEST signal is Fourier transformed. In contrast to the saturation pulse, the readout pulse shape in the acquisition sequence has little effect on the saturation transfer, even with pulsed acquisition schemes [234].

Since B_1 is an important parameter in calculating the optimal acquisition conditions (see Eq. 5.3.3), one must calculate this value for pulsed CEST. The equations below details how one can calculate the mean square irradiation field (B_{avg_power}) for pulsed CEST [235]:

$$B_{avg_power} = \sqrt{\frac{1}{(\tau_p + \tau_d)} \int_0^{\tau_p} B_1^2 dt} \tag{5.3.7}$$

$$= \frac{\pi\theta}{180.\gamma.p_1} \sqrt{\frac{p_2}{(\tau_p + \tau_d).\tau_p}} \tag{5.3.8}$$

where p_1 is the ratio of average amplitude to the maximum amplitude of the irradiation pulse, p_2 is the ratio of the average of the square of the amplitude to the square of the maximum amplitude for the irradiation pulse. Tee and colleagues [236] showed in particular for slow exchang-

ing CEST pools that CW simulations are equivalent to pulsed CEST simulations where the average power definition is used.

Water shift saturation referencing (WASSR)

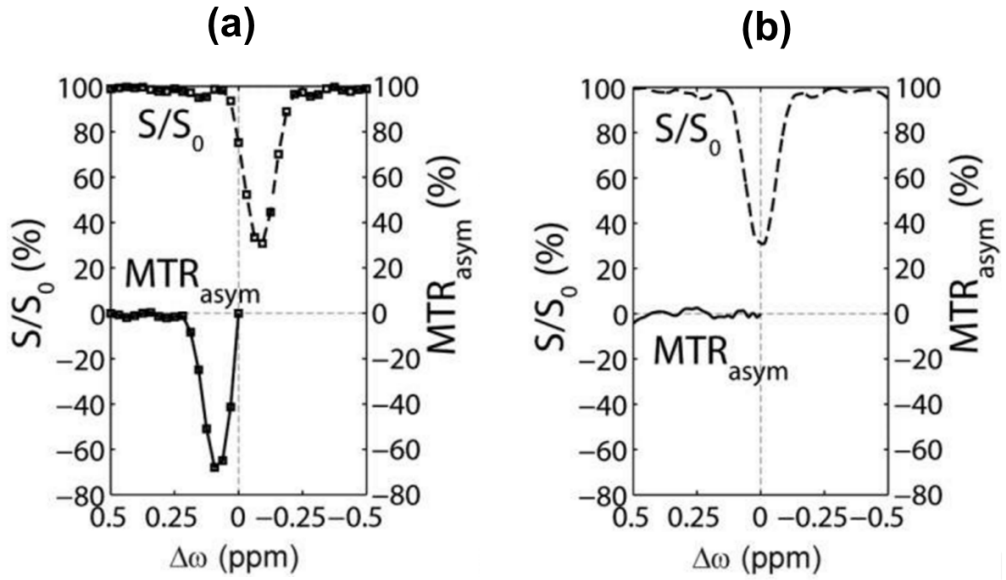


Figure 5.4: Effect of WASSR correction on WASSR data from [237]. **(a)** The raw WASSR data acquired close to the water peak can be used to fit the **(b)** corrected WASSR data, allowing accurate fitting of the minimum of the Z–spectrum around 0 ppm. The difference in erroneous CEST effect in the asymmetry curves is clear.

For situations in which OH groups attached to molecules contribute to the CEST spectrum, any CEST effect from these groups must compete with direct saturation effects due to the proximity of the water peak at 0 ppm. In particular, the MTR asymmetry analysis is sensitive to magnetic field inhomogeneities and it is important to correct for this. Kim et al. [237] demonstrated a fitting method which used low power saturation pulses to establish an absolute measure of the B_0 field close to the water frequency (by fitting the WASSR data) and then use this to "shift" the CEST acquired data, as shown in Fig. 5.4. The method measures the saturation at a large number of points surrounding the 0 ppm frequency in order to accurately plot the saturation profile of the water

peak. The minimum saturation intensity is then calculated using a maximum asymmetry method. The analysis is performed on a voxel–wise basis, with the CEST spectrum from each voxel being modified to fit the spectrum to 0 ppm, if the WASSR technique detects minimum intensities which are not centred at 0 ppm.

5.3.4 Bloch–McConnell equations

Two pool model

Following the mathematical formalism initially described by Woessner et al. [238], the Bloch equations established in Chapter 1 can be modified to include chemical exchange of magnetisation between two "pools" of magnetisation. These equations are known as the Bloch–McConnell (BC) equations. The equations describing this process are as follows:

$$\frac{\mathrm{d}M_x^a}{\mathrm{d}t} = -(\omega_a - \omega)M_y^a - k_{2a}M_x^a + C_bM_x^b \tag{5.3.9}$$

$$\frac{\mathrm{d}M_x^b}{\mathrm{d}t} = -(\omega_b - \omega)M_y^b - k_{2b}M_x^b + C_aM_x^a \tag{5.3.10}$$

$$\frac{\mathrm{d}M_y^a}{\mathrm{d}t} = (\omega_a - \omega)M_x^a - k_{2a}M_y^a + C_bM_y^b - \omega_1M_z^a \tag{5.3.11}$$

$$\frac{\mathrm{d}M_y^b}{\mathrm{d}t} = (\omega_b - \omega)M_x^b - k_{2b}M_y^b + C_aM_y^b - \omega_1M_z^b \tag{5.3.12}$$

$$\frac{\mathrm{d}M_z^a}{\mathrm{d}t} = \frac{M_0^a}{T_{1a}} - k_{1a}M_z^a + C_bM_z^b + \omega_1M_y^a \tag{5.3.13}$$

$$\frac{\mathrm{d}M_z^b}{\mathrm{d}t} = \frac{M_0^b}{T_{1b}} - k_{1b}M_z^b + C_aM_z^a + \omega_1M_y^b \tag{5.3.14}$$

where we follow the definition of the exchange relations to be:

$$k_{1a} = \frac{1}{T_{1a}} + C_a \tag{5.3.15}$$

$$k_{2a} = \frac{1}{T_{2a}} + C_a. \tag{5.3.16}$$

T_{1a} and T_{2a} represent the longitudinal relaxation time and the transverse relaxation time of pool A respectively, in a situation in which there is

no exchange. The symbol ω is the R.F. irradiation frequency, ω_a is the resonant frequency of pool A, and $B_1 = \omega_1/2\pi$ (in Hz). The transition rate , C_a, is given by,

$$C_a = \left(\frac{M_0^b}{M_0^a}\right) C_b = \left(\frac{M_0^b}{M_0^a}\right) \frac{1}{\tau_b} \tag{5.3.17}$$

with M_0^a and M_0^b denoting the thermal equilibrium Z magnetisations and τ_b being the lifetime of a proton in pool B. Identical definitions apply to pool B. Other magnetisation quantities are previously defined.

Three pool model

Allowing the effects of a third magnetisation pool (Pool C) to be included, provides a full set of equations for three pool modelling:

$$\frac{\mathrm{d}M_x^a}{\mathrm{d}t} = -(\omega_a - \omega)M_y^a - k_{2a}M_x^a + C_b M_x^b + C_c M_x^c \tag{5.3.18}$$
$$\frac{\mathrm{d}M_x^b}{\mathrm{d}t} = -(\omega_b - \omega)M_y^b - k_{2b}M_x^b + C_{ab} M_x^a \tag{5.3.19}$$
$$\frac{\mathrm{d}M_x^c}{\mathrm{d}t} = -(\omega_c - \omega)M_y^c - k_{2c}M_x^c + C_{ac} M_x^a \tag{5.3.20}$$
$$\frac{\mathrm{d}M_y^a}{\mathrm{d}t} = (\omega_a - \omega)M_x^a - k_{2a}M_y^a + C_b M_y^b + C_c M_y^c - \omega_1 M_z^a \tag{5.3.21}$$
$$\frac{\mathrm{d}M_y^b}{\mathrm{d}t} = (\omega_b - \omega)M_x^b - k_{2b}M_y^b + C_{ab} M_y^a - \omega_1 M_z^b \tag{5.3.22}$$
$$\frac{\mathrm{d}M_y^c}{\mathrm{d}t} = (\omega_c - \omega)M_x^c - k_{2c}M_y^c + C_{ac} M_y^a - \omega_1 M_z^c \tag{5.3.23}$$
$$\frac{\mathrm{d}M_z^a}{\mathrm{d}t} = \frac{M_0^a}{T_{1a}} - k_{1a}M_z^a + C_b M_z^b + C_c M_z^c + \omega_1 M_y^a \tag{5.3.24}$$
$$\frac{\mathrm{d}M_z^b}{\mathrm{d}t} = \frac{M_0^b}{T_{1b}} - k_{1b}M_z^b + C_{ab} M_z^a + \omega_1 M_y^b \tag{5.3.25}$$
$$\frac{\mathrm{d}M_z^c}{\mathrm{d}t} = \frac{M_0^c}{T_{1c}} - k_{1c}M_z^c + C_{ac} M_z^a + \omega_1 M_y^c \tag{5.3.26}$$

where C_{ab} is the exchange rate of pool A protons to pool B, and C_{ac} is similarly proton exchange from pool A to C such that $C_a = C_{ab} + C_{ac}$. There is no exchange assumed between pool B and pool C. Relating the pool magnetisations and the transition rates, $C_{ab}/C_b = M_0^b/M_0^a$.

Solution of BC equations and simulated saturation schemes

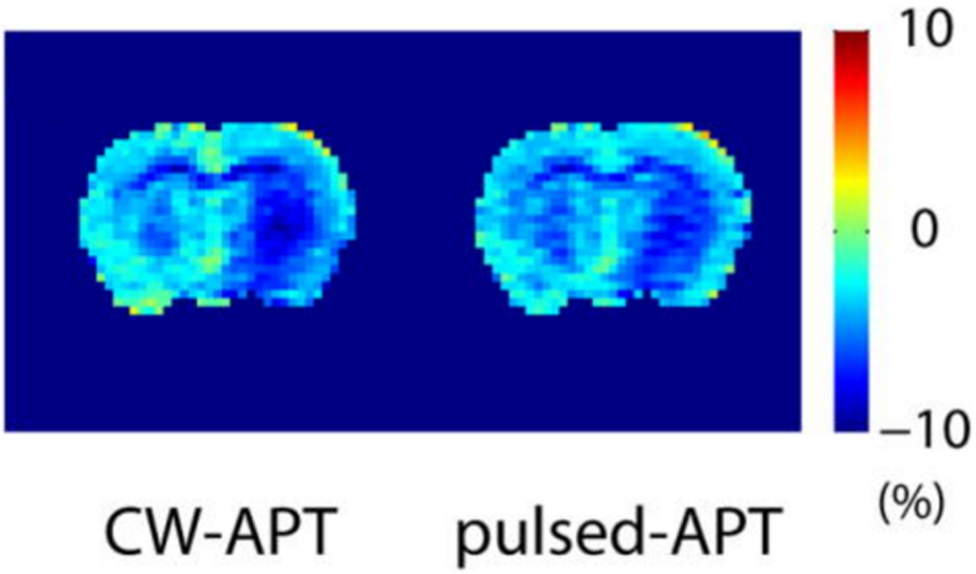


Figure 5.5: Pulsed and continous saturation schemes produce similar contrast for APT CEST from [239]. A mouse model of ischaemia is imaged using APT CEST, with continuous wave (CW) and pulsed saturation producing CEST effects within error of each other.

The sets of simultaneous equations for the two and three pool models can be pictured using a matrix format [240], such that,

$$\frac{\mathrm{d}\mathbf{M}}{\mathrm{d}t} = \mathbf{A} * \mathbf{M} \tag{5.3.27}$$

where $\mathbf{A}$ is (7 x 7) matrix (two pool) or (9 x 9) matrix (three pool) containing the exchange terms and the M/T_1 terms from the simultaneous equations and $\mathbf{M}$ is a (1 x 7) matrix or (1 x 9) matrix containing the individual $M_{x,y,z}$ magnetisation vector terms. Assuming full saturation, $\mathrm{d}\mathbf{M}/\mathrm{d}t = 0$. Woessner et al. [238] used a direct solution of the above matrix equation for the two and three pool models, with the "expm" (exponential matrix) function in Matlab:

$$\mathbf{M}(t) = e^{\mathbf{A}t}\mathbf{M}(0) \tag{5.3.28}$$

where $\mathbf{M}(0)$ is the initial magnetisation at $t = 0$. This equation shows that the time dependent magnetisation can be simulated by computing the initial magnetisation and the exponential of matrix $\mathbf{A}$. Murase et al.

Simulation parameters for two pool APT CEST at 9.4 T		
Hardware parameters	B_0	9.4 T
	coil	Volume transmit and receive
Relaxation times	T_{1a}	2.61 s[a]
	T_{2a}	0.27 s [b]
	T_{1b}	1 s [242]
	T_{2b}	15 ms [243]
Exchange rates	k_{ab}	28 Hz APT [244]
Concentration values	c	72 mM [245]

Table 5.2: **Two pool simulation parameters.** Parameters such as the relaxation values and exchange rate affect the CEST simulation contrast and are simulated to model expected effects *in vitro*.
[a] denotes parameters based on previous T_1 experimental work at 9.4 T (data not shown).
[b] denotes parameters based on my own experimental work, the methods of which are detailed as part of the CEST cell study in Chapter 6.

[240] used a different approach by calculating the eigenvectors of **A** in order to solve the equation. For pulsed CEST simulations, the saturation time can be taken as $t_{sat} = \tau_p + \tau_d$ [214]. For APT, Sun et al. [239] not only confirmed that continuous wave simulation is equivalent in terms of CEST contrast up to around 50 Hz, but that the two saturation regimes produce near identical results *in vivo* (Fig. 5.5).

5.4 Optimising the CEST experiment: parameter simulation

Simulations were performed using an in–house matlab code adapted from code originally written by Dr Yanez Lopez [241], based on the two and three pool model of chemical exchange [238].

Simulation parameters for three pool APT CEST at 9.4 T and 7 T		
Hardware parameters	B_0	9.4 T and 7 T
	coil	Volume transmit and receive
Relaxation times at 9.4 T	T_{1a}	2.61 s
	T_{2a}	0.27 s
	T_{1b}	1 s [242]
	T_{2b}	13 ms [243]
	T_{1c}	1 s [242]
	T_{2c}	15 μs [243]
Relaxation times at 7 T	T_{1a}	2.56 s
	T_{2a}	0.35 s
	T_{1b}	1 s [242]
	T_{2b}	20 ms [246]
	T_{1c}	1 s [242]
	T_{2c}	15 μs [243]
Exchange rates	k_{ab}	28 Hz [244]
	k_{ac}	48 Hz [235]
	k_{bc}	Assumed negligible
Concentration values	c	72 mM

Table 5.3: **Three pool simulation parameters for different field strengths.** A third additional pool models the broad MT pool which exchanges with the water pool. The MT pool has a similar exchange rate to the APT pool but with a much smaller T_2 value. Similar relaxation values are observed at both field strengths for the bulk water and the solute pools. Exchange rates are unaffected by field strength.

5.4.1 Simulation parameters for two and three pool model

The two pool model has been shown to be adequate for simulations of *in vitro* APT contrast [242], and parameters involved in my own two pool simulations are shown in Table. 5.2. Extending the simulation to three pools involves the introduction of a third pool, normally associated with the MT pool arising from semi–solid macromolecules with typically large linewidths and small T_2 values (see Table. 5.3). Simulation parameters such as the exchange rate were based on previous CEST literature values. Parameters such as the T_1 of the solute and MT are more difficult to acquire than T_{1a}, and do not significantly affect the simulated CEST contrast. For *in vivo* situations, the MT pool is asymmetric with respect to 0 ppm (thought to resonate at -2.34 ppm [246]). For agar and *in vitro* experiments the pool is centered at 0 ppm.

5.4.2 Field strength and pool model simulations

The effect of scanner field strength was simulated, to inform the decision between choosing to perform CEST experiments on the 7 T or 9.4 T system, shown in Fig. 5.6. As B_0 increases, T_1 increases and T_2 decreases, the total magnetisation available for chemical exchange increases and hence the CEST effect also increases. However, the separation of the solute protons from water at 0 ppm increases proportional to the magnetic field, such that the saturation effect at 3.5 ppm is more pronounced at the higher field; this is clear from Fig. 5.6 where the 7 T Z–spectra and asymmetry curve have a broader lineshape. Consequently, the CEST effect enhancement from choosing 9.4 T over 7 T is small, based on the simulated changes in T_1, T_2 and B_0. The exchange rates are not dependent upon the external magnetic field and remain constant for both 7 T and 9.4 T.

The number of pools used in the model simulation is important in order to accurately replicate effects occurring *in vivo* or *in vitro*. Fig. 5.7 demonstrates the differences between one, two and three pool models. To clearly illustrate the reduced S/S_0 values from the MT pool, parameters for the exchange rates are changed to $k_{ab} = 50$ Hz and $k_{ac} = 48$ Hz,

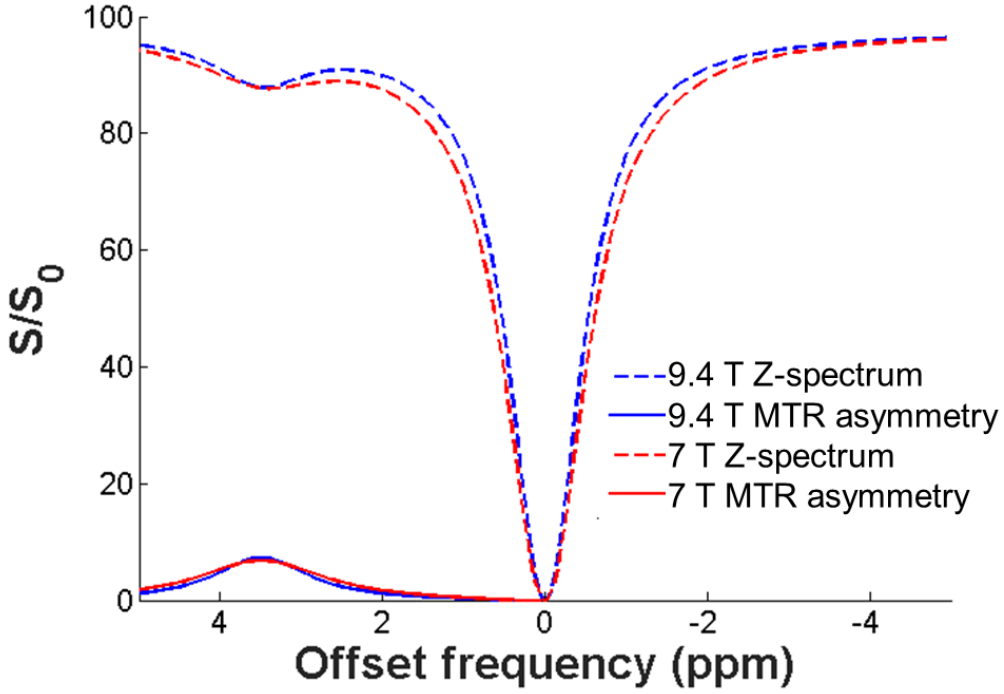


Figure 5.6: Optimal field strength for APT CEST. Relaxation times T_1 and T_2 of the water pool increase and decrease with increased field strength respectively. A broader lineshape for 7 T is observed due to the decreased separation between solute exchange frequency and water frequency. Parameters used are identical to Table 5.3, apart from the increased concentration (100 mM) and exchange rate (k = 50 Hz [219]) to highlight the CEST effect differences between fields.

and the solute pool is reduced to model *in vivo* likely values ($T_{2b} = 0.05$ s). A one pool model is a poor fit for observed data in the literature and my own experiments, since chemical exchange in not accounted for. The two pool simulation models the exchange rate with no MT effect. The three pool model extends the two pool, accounting for a broad MT pool which reduces the available magnetisation, reducing the Z–spectrum as a whole.

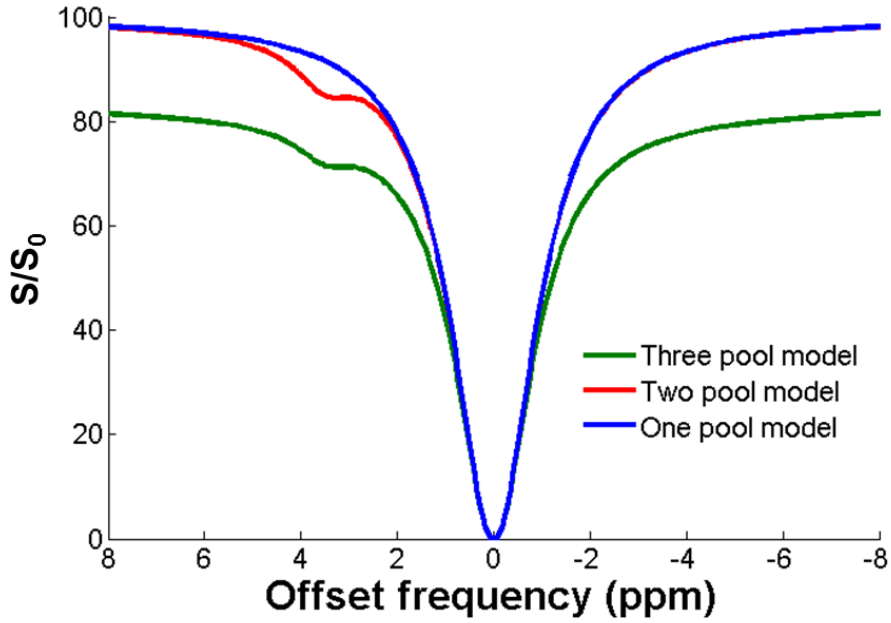


Figure 5.7: Varying number of simulated exchange pools alters Z–spectrum appearance. The three pool model uses a bulk water, MT and solute pool; a two pool model consists of only solute and bulk water pools and the single pool model neglects all chemical exchange, including only bulk water.

5.4.3 Optimal amide proton transfer (APT) parameters

Using the three pool model, the CEST effect for an APT pool is simulated, based on the variation and optimisation of several key model parameters. Fig. 5.8 models the variation in CEST effect with changing B_1 field. The time assumes a saturation time of 14 s, whose respective effect on the CEST contrast is modelled later. The t_{sat} value is based on a fully saturated exchanging pool which is around $5 \times T_1$ of the water pool at 9.4 T. The pulse power shows a maximum peak around 1.5 μT, which rises steeply from 0.5 μT and decreases around 1.8 μT. Between 1 – 2 μT there is little reduction in CEST effect. It is worth noting the value of the predicted CEST effect, which is relatively small (2 to 3 %), due to the slow exchange rate of APT.

The CEST effect was investigated as a function of the saturation time. An increased irradiation at a given frequency will increase the magneti-

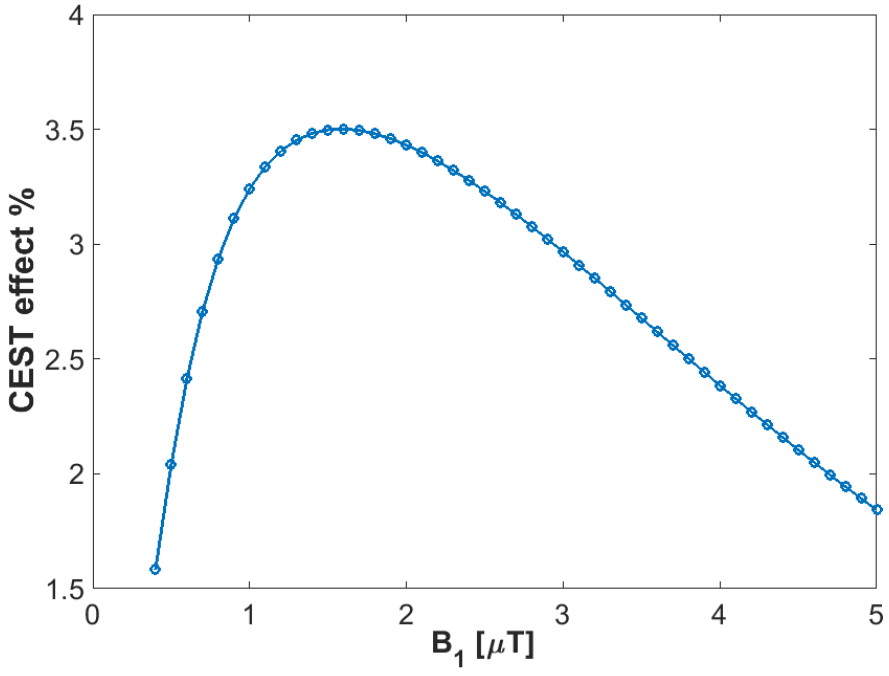


Figure 5.8: CEST effect dependence upon B_1 power. The variation of the CEST effect is plotted over a range of 0.5 – 5 μT, with the maximum effect occurring around 1.5 μT. The CEST effect is insensitive to values around the maximum, dropping off significantly for B_1 less than 1 μT. A gradual reduction in CEST effect is also seen after 2 μT.

sation transfer contrast and hence the CEST effect. This increase levels off in a similar way to T_1 relaxation, which increases back to the equilibrium magnetisation value after excitation. Fig. 5.9 shows the gradual CEST effect increase as the saturation time is increased. Short saturation times do not sufficiently saturate the APT pool and result in a low CEST effect. The CEST effect levels off with longer saturation times (> 5 s) at a value which corresponds to a B_1 value of 1.4 μT in Fig. 5.8.

The saturation effect on the CEST effect is visible when computing the Z–spectra for the APT pool, as shown in Fig. 5.10. Three discrete saturation times are shown, with the resulting Z–spectra and asymmetry curves. The fully saturated time of 15 s produced the most prominent asymmetry curve, as confirmed in Fig. 5.9. The lower saturation times show a markedly reduced asymmetry effect, with a large difference in the CEST effect between 3.5 and 2 s; the non–linearity of the effect of

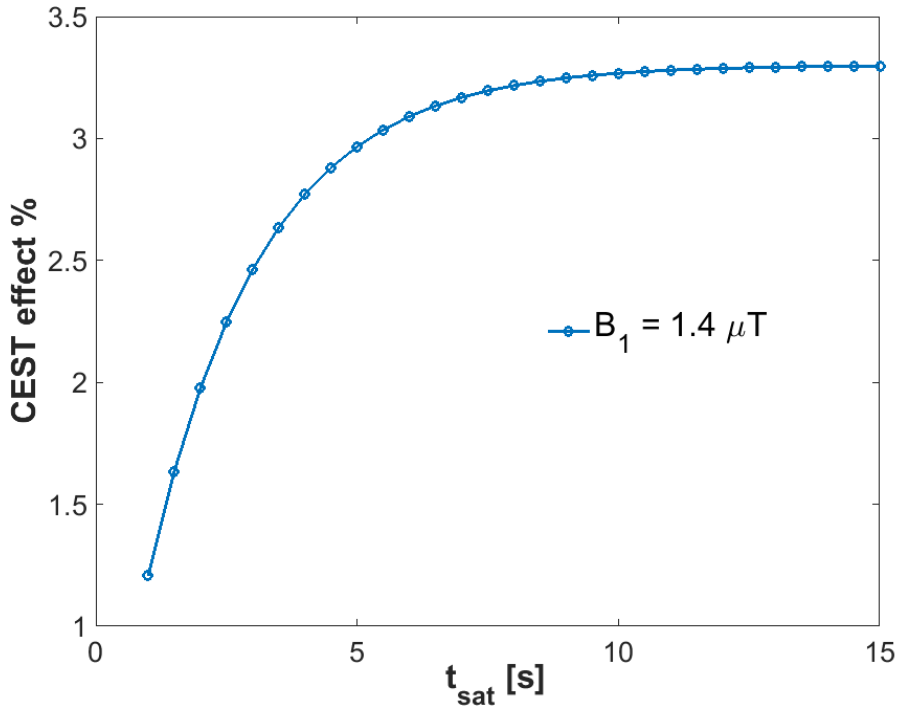


Figure 5.9: Increased pulse saturation duration increases the CEST effect. Based on the optimal B_1 power obtained from Fig. 5.8, the CEST effect increases up to a maximum as the labelling efficiency tends to unity, with increasing saturation time. There is a large difference in the CEST effect arising from saturation times less than 5 s, with marginal % increases above this saturation time.

saturation time on the CEST contrast is clear.

The concentration was also varied in a simulation to investigate the effect of large concentrations on the CEST effect. Shown in Fig. 5.11, a number of concentrations are plotted with the resulting CEST effect for each point. For concentrations on the order of 10^1 mM, a linear regime is observed. As concentrations reach 50 mM and above, a non–linearity is apparent as an increased concentration produces a lower CEST effect than a linear fit would expect. A saturation time of 14 s is used, assuming the solute pool is fully saturated.

The final simulation performed demonstrated the dependence of the CEST effect upon initial parameters. A number of exchange values have been hypothesised in the CEST literature and no particular preference or

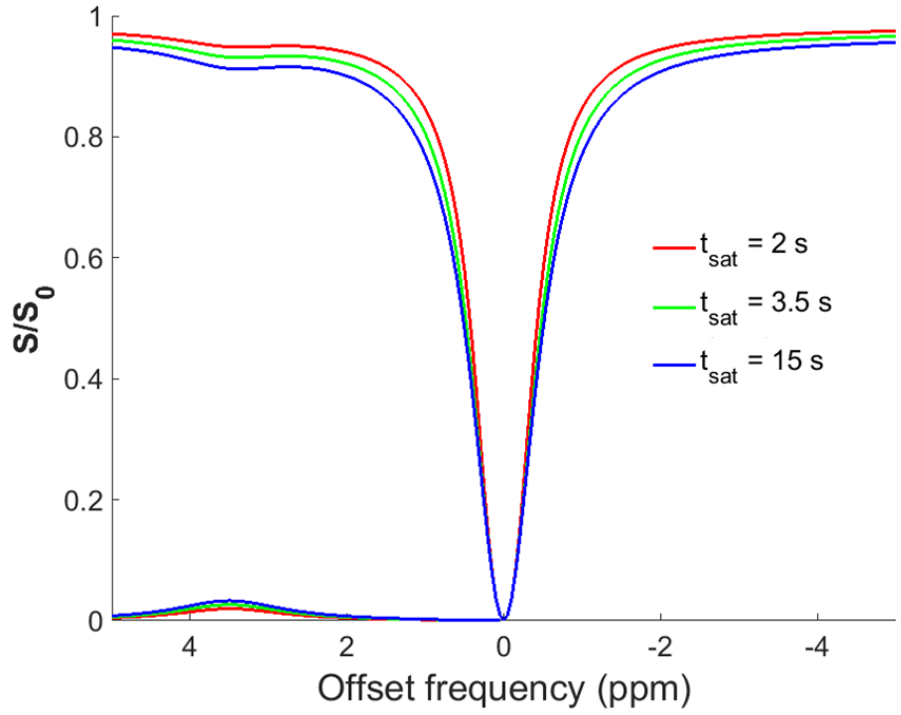


Figure 5.10: Effect of saturation pulse duration on APT Z–spectrum. The Z–spectrum and asymmetry curve for the APT resonance at 3.5 ppm, is plotted for three separate saturation times. The labelling efficiency is saturated at 15 s, resulting in the maximum CEST effect, and with significantly lower CEST effects for lower saturation times.

priority has been demonstrated for a particular value. This is illustrated in Fig. 5.12, where three literature exchange values are simulated with the resulting CEST effect. This parameter has a large effect on the CEST contrast, with an increased exchange rate allowing a higher CEST effect.

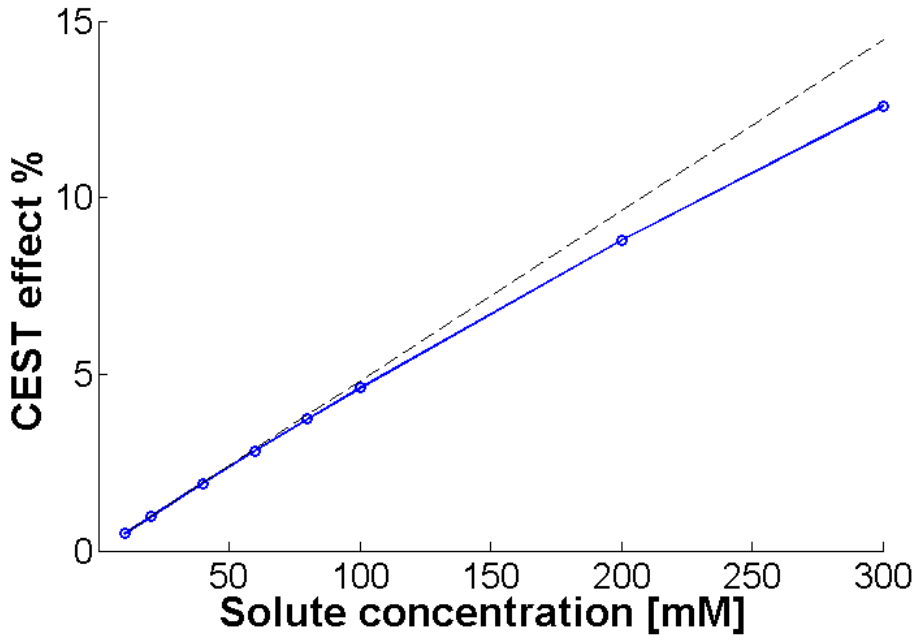


Figure 5.11: CEST effect dependence upon concentration. As the simulated solute concentration (blue circles) is increased, the CEST effect increases linearly up to around 50 mM. Increasing concentration beyond this point produces a drop in the achievable CEST effect below the linear relationship (dotted line) which applied at low concentrations.

5.5 CEST setup optimisation: *in vitro* experiments

5.5.1 Material and methods

Phantom preparation

To validate the effects observed in the CEST simulations, a series of agar phantoms were created using the metabolite creatine as a solute pool for chemical exchange with water. Creatine is commonly used to simulate APT exchange since the amide group on creatine has similar exchange parameters to amide groups expected *in vivo* [249]. The metabolite myo–inositol was used in additional samples, despite a higher exchange rate than APT, for assessing resonances close to the water peaks and potential issues relating to direct saturation overlap.

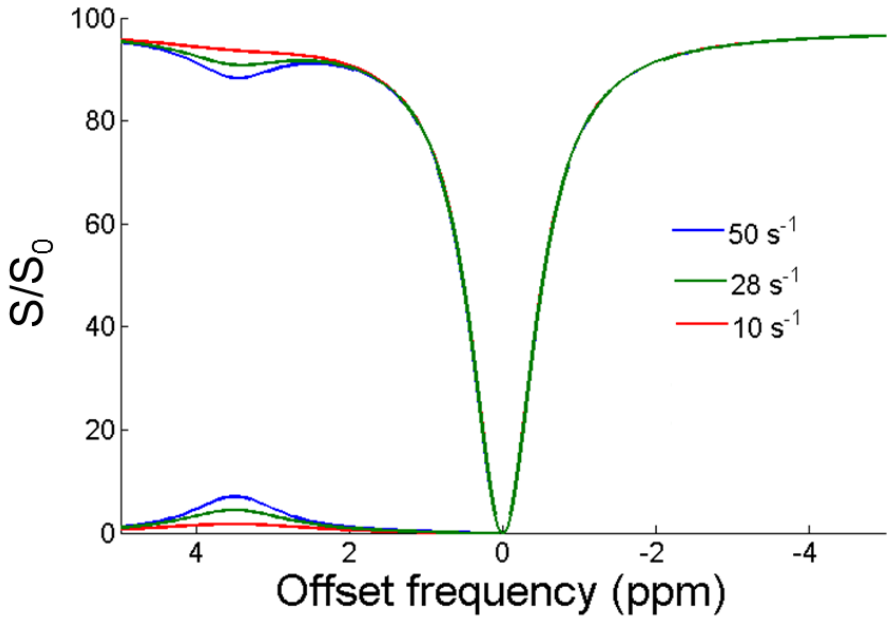


Figure 5.12: Faster exchange rates increase CEST effect. A range of APT exchange rates (from literature, 50 s^{-1} [226], 28 s^{-1} [247] and 10 s^{-1} [248]) are shown with the corresponding effect upon Z–spectra and asymmetry curves for APT CEST at 9.4 T. A CEST effect at 3.5 ppm was found to be 7.2 %, 4.6 % and 1.8 % for the $k = 50$ s^{-1}, $k = 28$ s^{-1} and $k = 10$ s^{-1} rates respectively.

For the Bruker 7 T, three stock solutions containing a volume of 100 mL of phosphate–buffered saline were prepared and 1 g, 2 g and 3 g of agar powder (A7459, AppliChem, Darnstadt, Germany) were added to create 1 %, 2 % and 3 % agar gel solutions respectively. Each solution was heated to boiling point, in order to fully dissolve the agar powder, and was then placed into a water bath heated to 50 °C. Anhydrous creatine (Sigma Aldrich, UK) with a molecular weight (M_r) of $M_r = 131.133$ g/mol was weighed out and then mixed into the stock solutions to give a creatine concentration of 50 mM. This process was repeated for an additional three samples: 1 % agar gel with two different concentrations of creatine (10 mM and 100 mM) to study the effect of metabolite concentration on the CEST effect; 1 % agar without added creatine, to act as a reference standard. 15 mL of each stock solution was poured into plastic cylindrical containers which were then bound to produce a com-

posite phantom. For the purposes of comparison, an additional identical 15 mL container of pure phosphate–buffered saline was attached to the phantom.

An identical preparation procedure was adopted for phantoms to be used on the Varian 9.4 T scanner and 22 mm coil set–up, with the only difference being the tube used; in the Varian case a thinner (10 mm diameter) tube with a 1.5 mL volume was used, rather than a Falcon tube which was used for the Bruker 7 T experiments. Myo–inositol samples were also prepared in an identical method for the Varian with replacement of creatine with myo–inositol.

CEST analysis tool

Previous members of our research group established a CEST analysis software tool (CAT) for Varian CEST data (initially written by Ryan Bendell [250], developed by Dr Maria Yanez Lopez [241] and optimised by Gaelle Ardito [251]). I contributed an original Bruker Matlab code which allowed Bruker data to be processed using the CAT. A brief summary of the sequence of functions performed by the analysis software for both Varian and Bruker data is given below:

1. **Image loading and thresholding of reference image –** All WASSR, reference and CEST array images are loaded in an analyze data format, with noise thresholding applied to all images.

2. **Interpolating and ROI masking –** A spline fitting function is used to interpolate the CEST array and WASSR image intensities over the CEST and WASSR frequency ranges respectively, on a pixel-wise basis. A user defined ROI can be used to select specific regions, over which a single averaged Z–spectrum will be calculated.

3. **CEST and WASSR processing and corrections –** The fitted WASSR data is used to create an absolute map representing B_0. This map is combined with the processed CEST data to correct for variations in the water frequency which affect the Z–spectrum of the CEST data.

4. **Outputs: Z–spectra, MTR asymmetry spectra and CEST maps** – The analysis tool will output a CEST spectrum and asymmetry curves based on the fitting of the acquired raw data. A map providing spatial information on the CEST effect at certain points in a reference image, for a given frequency or interval range, may also be computed.

5.5.2 CEST sequences: Bruker 7 T and Varian 9.4 T

Three sequences were investigated on different scanners to assess the most useful CEST acquisition method for *in vitro* experiments.

Varian CEST sequences

Two sequences were used on the Varian; a gradient echo multi slice (GEMS) sequence and a fast gradient echo (cine) sequence. An identical CEST protocol was used for both scans, the only difference being the CEST array, reference and WASSR sequence, detailed below.

A 9.4 T Varian horizontal bore pre-clinical scanner with Vnmrj 4.0 software (Palo Alto, California) was used for all MR experiments in this study. Phantoms were prepared by attaching two tubes symmetrically on top of each other using tape and placing inside a 22 mm small volume coil (Rapid Biomedical), positioned in the centre of the magnet. Tuning and matching was performed and automatic frequency and gain calibration settings were acquired.

A gradient echo multi slice (GEMS) imaging sequence, "scout_custom", (t_{acq} = 11 s, TE = 5 ms, T_R = 30 ms, MTX = 128 × 128, no. slices = 3, FOV = 30 × 30 mm^2, slice thickness = 2 mm, slice spacing = 2 mm) was used to quickly check the general position of the two tubes. A fast spin echo multi slice (FSEMS) sequence, "fsems_scout", (t_{acq} = 2 m 5, T_R = 2.5 s, TE_{eff} = 12 ms, MTX = 128 × 128, FOV = 20 × 20 mm^2, echo train length (ETL) = 8, no. slices = 10, N_{acq} = 1, slice thickness = 1 mm) with a greater number of slices was then acquired to allow for precise placing of the CEST voxel later on.

A global 3D GE shim was performed using the "ge3dshim_custom" Varian scan (MTX = 128 $\times$ 64 $\times$ 64, FOV = 40 $\times$ 40 mm^2, slice thickness = 40 mm, BW = 100 kHz, T_R = 20 ms, TE = 2 ms). The shimming protocol used first and second order shimming for 1, 2, 3 and 4 ms phase delays.

Next, a localised voxel shim was performed for the chosen CEST voxel, using a point resolved spectroscopy (PRESS) scan voxel. The position of the voxel was determined using the FSEMS "locator" images to choose a voxel away from any air bubbles. The FOV and slice thickness is dependent upon the specific position of the tubes which were normally 20 $\times$ 12 $\times$ 1 mm^3. This volume was then used to perform a local 3–D GE shim in an identical manner to the global shim.

GE Varian sequence

A saturation pulse train of four Gaussian pulses, each of 46 ms duration and 1 μT power, irradiated 41 separate frequencies in a range $\pm$ 4 ppm (or 31 frequencies in a range of $\pm$ 3 ppm) around the water peak with a resolution of one pulse train per 0.2 ppm. The saturation module was coupled with the "gems" sequence which had parameters: excitation pulse angle = 20°, TE = 4 ms, T_R = 202.4 ms, MTX = 64 $\times$ 64, t_{acq} = 11 m 1 s. For CEST array sequence parameters, t_{acq} is the acquisition time for the complete set of scans at various frequencies in the array, rather than an individual measurement.

An identical sequence to the CEST array was acquired for the reference scan but without the frequency selective saturation (t_{acq} = 13 s). A WASSR scan sampling at 18 separate frequencies at 0.0625 ppm intervals between 0.5 ppm and - 0.5 ppm, with a reduced saturation power of 0.1 μT. The sequence used the same parameters as the CEST array, aside from saturation module. The t_{acq} was 3 m 53 s.

Cine Varian sequence

A cine sequence used a continuous wave saturation using a block pulse saturation with t_{sat} = 6 s and B_1 = 1 μT. The acquisition took 41 separate images over a range of $\pm$ 4 ppm. The following parameters were used: T_R = 3.3 s, TE = 1.6 ms, excitation angle = 15°, MTX = 64 $\times$ 64. The reference scan used 18 points at 0.0625 ppm offsets over a range of $\pm$ 0.5

ppm.

FISP Bruker sequence

A FISP CEST protocol was used on the 7 T Bruker to assess the possibility of CEST imaging using that set–up. This sequence was developed using a basic modified FISP sequence with a saturation module, provided by Prof. Mark Pagel [228]. Experiments using 15 mL falcon tube phantoms were performed with a 72 mm transmit and receive volume coil.

A GE tripilot scan was used, acquiring images in the axial, sagittal and coronal directions to assess sample positioning. This scan is based on a FLASH sequence, with the parameters: TE = 6 ms, T_R = 100 ms, t_{acq} = 13 s. A high resolution RARE scan was then used to check for artefacts or possible issues in the axial plane. The RARE scan used the following parameters: RARE factor = 8, TE = 8 ms, TE_{eff} = 33 ms, MTX = 256 $\times$ 256, FOV = 60 $\times$ 60 mm^2, slice thickness = 2 mm, no. slices = 9. An automatic gradient echo field map method was used for shimming with parameters; TE = 1.33 ms (minimum echo time), T_R = 20 ms, FOV = 80 $\times$ 80 $\times$ 80 mm^2, MTX = 64 $\times$ 64 $\times$ 64, comprising of two acquired echo images.

A CEST acquisition sequence in FID mode was chosen for the CEST acquisition. An $\alpha/2$ excitation scheme was used, with a flip angle of $\alpha = 60^\circ$ chosen. Parameters used for all FISP scans were: TE = 1 ms, T_R = 2 ms, slice thickness = 2 mm , MTX = 128 $\times$ 128, FOV = 80 $\times$ 80 mm^2, BW = 60 kHz. Saturation pulses used hard, continuous waves at 1 μT, with a t_{sat} = 6 s and an array between $\pm$ 5 ppm with 41 sampling offsets. WASSR scans sampled 41 points between $\pm$ 1 ppm.

5.5.3 Detecting metabolites using the CEST effect

Bruker 7 T experimental results

The FISP sequence was first investigated on the 7 T Bruker using the composite phantom described in the Methods section of this chapter.

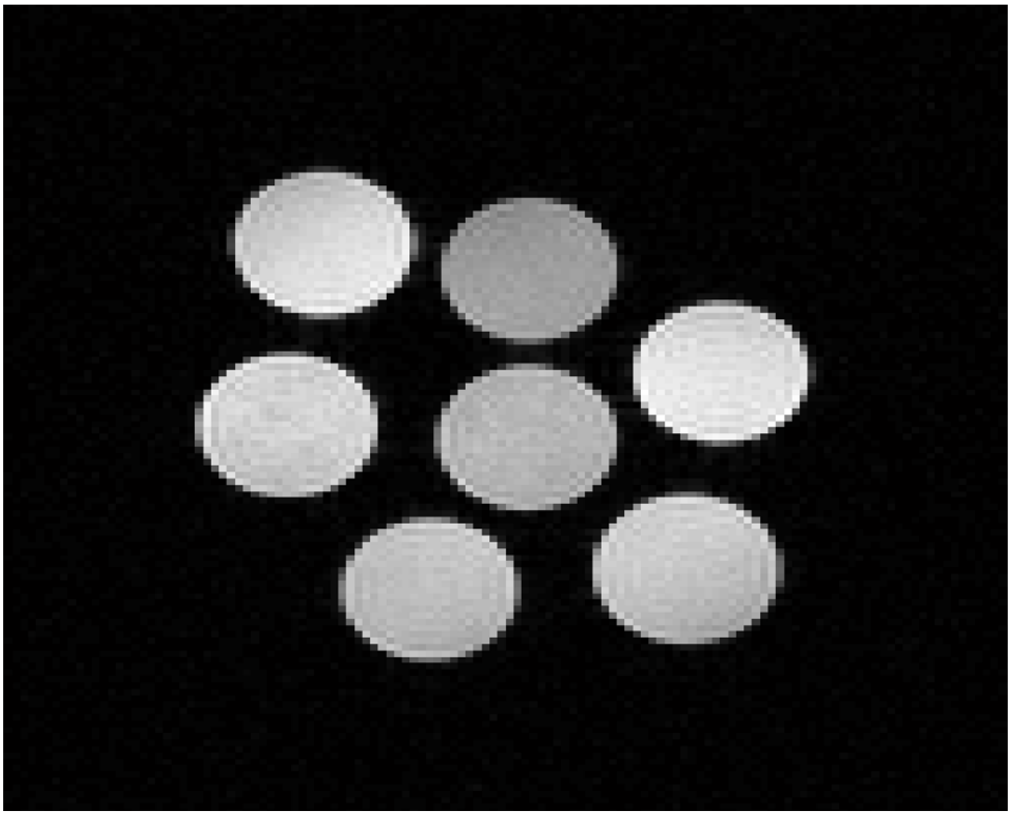


Figure 5.13: *In vitro* phantom experiment at 7 T with volume coil and FISP sequence. A reference FISP image shows a cross–section of the seven tube phantom. 15 mL Falcon tubes were used with varying metabolite and agar concentrations. The contents of the tubes were as follows (clock–wise from top left): 2 % agar, 3 % agar, 10 mM Cr 1 % agar, 50 mM Cr 1 % agar, 100 mM Cr 1 % agar, pure phosphate–buffered saline, 1 % agar.

The CEST–FISP sequence provided to us did not automatically calibrate the pulse power of the saturation pulses, but this could be calculated by converting the reference pulse gain (in dB), calculated from the gain calculation automatically performed during set up, to the desired field strength by changing the flip angle needed. An image from the FISP sequence set–up showing a GE image of the phantom arrangement is given in Fig. 5.13.

A CEST acquisition with the FISP sequence struggled with the large field of view and complete saturation of all the sample frequencies at 0 ppm

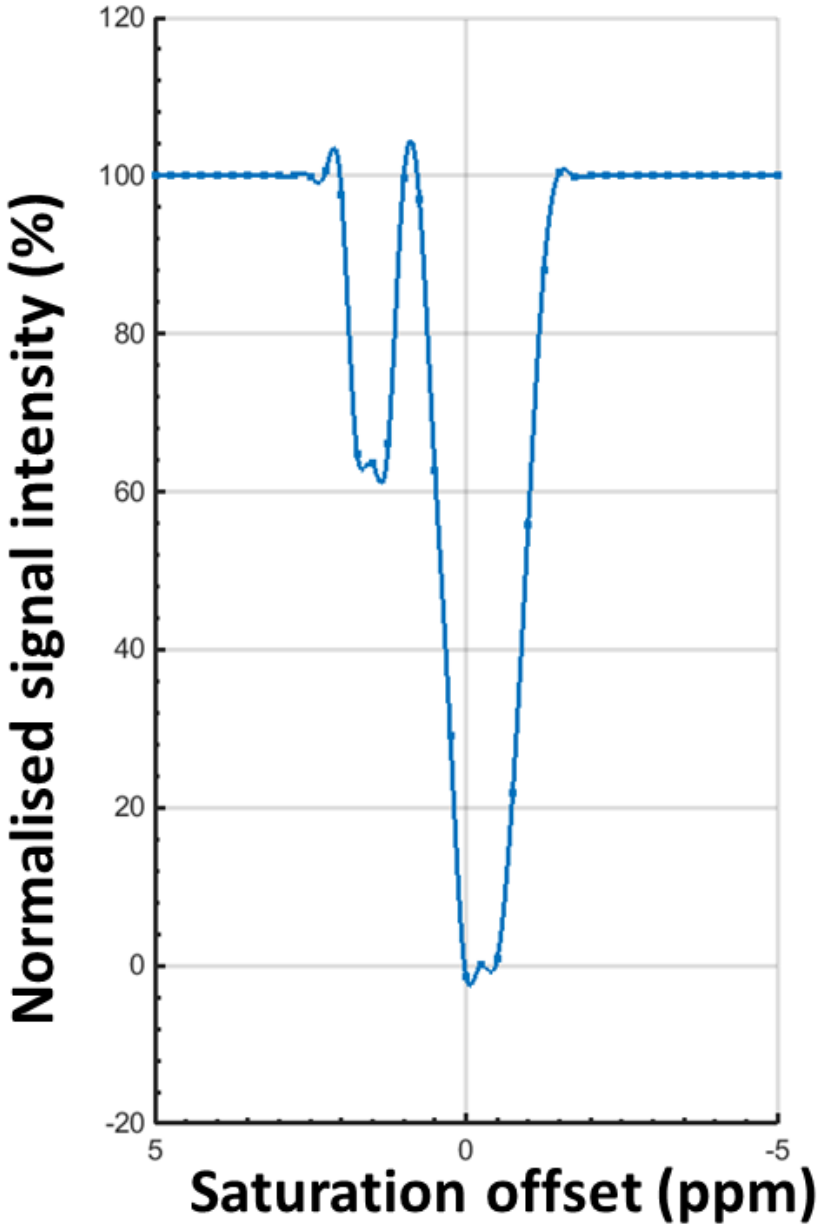


Figure 5.14: Creatine Z–spectrum from FISP 7 T sequence. The resonance around 1.9 ppm is clear, yet there are artefact issues with the spectrum. The WASSR correction has not suitably positioned the spectra around 0 ppm and there is no chemical exchange visible from other regions of the spectra.

was difficult to achieve, due to the large change in B_0 across the sample. A CEST spectrum was acquired but placed regions of interest could not obtain suitable Z–spectra for several samples. A spectra for the 100 mM Cr phantom in 1 % agar could be obtained and the results are shown in

Fig. 5.14. The spectrum shows a Cr peak at 2 ppm with an dip of around 20 %. However, the water peak is not correctly centred around 0 ppm and there is no transfer from other areas of the spectra apart from near 0 ppm and 2 ppm. This would suggest that inhomogeneity of the field has meant that saturation at certain offset frequencies and subsequent chemical exchange has not been possible.

Varian 9.4 T experimental results

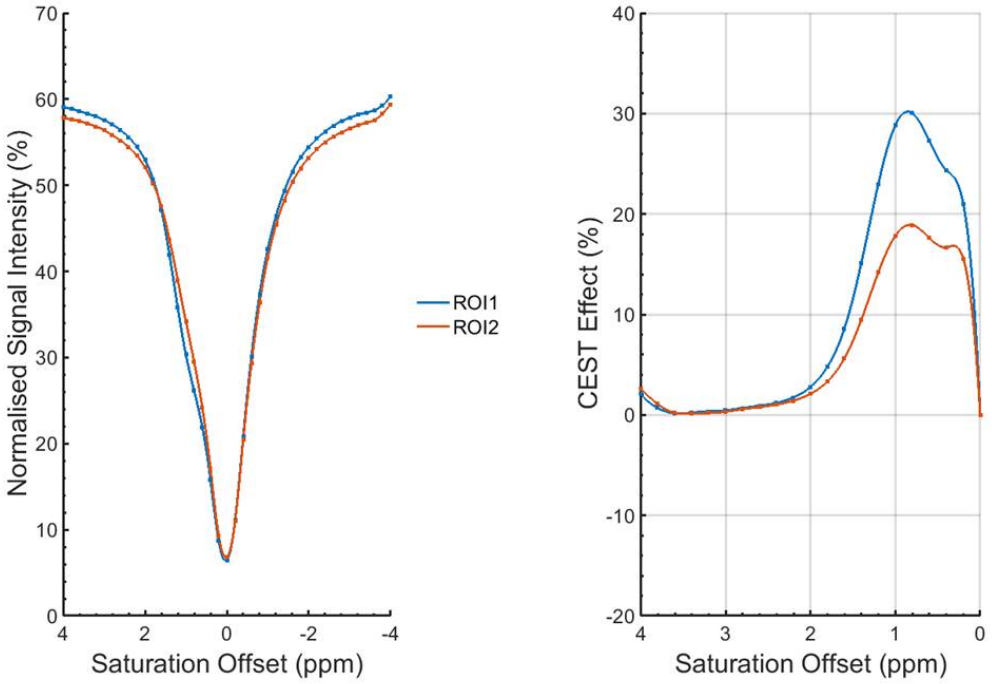


Figure 5.15: Concentration effect on CEST effect for myo-inositol phantoms *in vitro* with GE sequence. Two tubes containing 50 mM and 100 mM of myo–inositol (ROI 2 and ROI 1 respectively) show that an increased metabolite concentration produces an increased CEST effect, with a broad peak visible around 0.9 ppm.

Two myo–inositol phantoms of 50 mM and 100 mM were imaged using the GE CEST sequence to demonstrate the ability to detect changes in metabolite concentrations for exchangeable groups near 0 ppm. The Z–spectra and MTR asymmetry curves are shown in Fig. 5.15. The Z–spectrum shows that a larger myo–inositol concentration produced

a more defined saturation effect in the spectrum, which is confirmed in the asymmetry curves. The non–linearity between the CEST effect and solute concentration also confirms the simulated non–linear effects demonstrated in the previous simulation section.

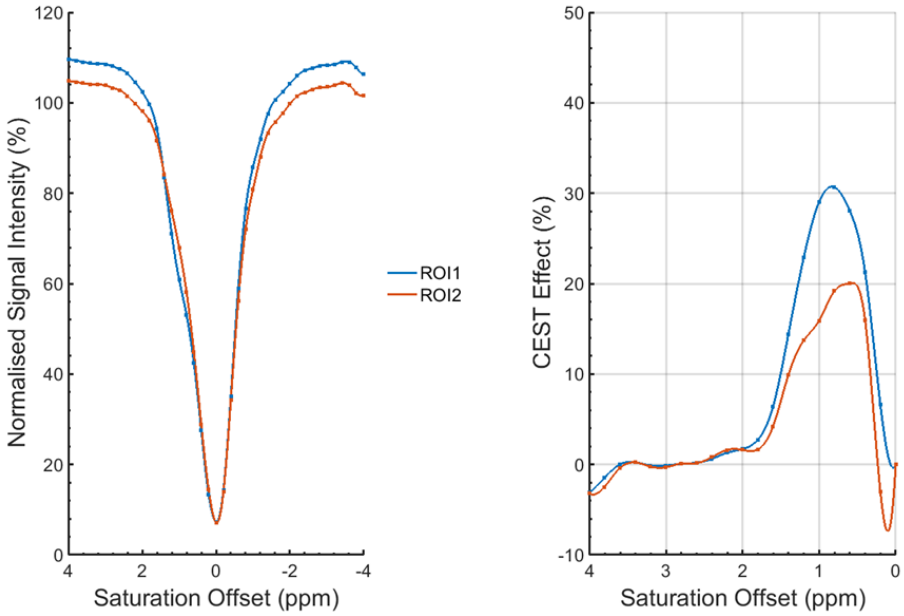


Figure 5.16: Myo-inositol imaging shows similar CEST effect for cine acquisition sequence. The peak CEST effect for both concentrations occurs at a very similar saturation offset and the CEST effect % is very close to the values obtained in Fig. 5.15.

A cine sequence was also used to scan the same myo–inositol phantoms used in the GE scan to compare the reproducibility of the CEST effect (Fig. 5.16). Again, the higher concentration of solute produces a more obvious "dip" in the Z–spectrum and also the asymmetry curve. Importantly the effect sizes of around 30 % and 19 % are very similar to the values found in Fig. 5.15, suggesting the CEST measurement is robust even with different acquisition sequences.
A difference between Fig. 5.16 and Fig. 5.15, is the height of the CEST effect very close to the 0 ppm frequency. The GE scan has a more pronounced CEST effect which is convoluted with the solute resonance around

1 ppm, whereas the cine spectrum is dominated solely by the solute peak. A possible explanation for this is that the GEMS sequence and the cine sequence have different pre–saturation schemes, which result in different saturation profiles.

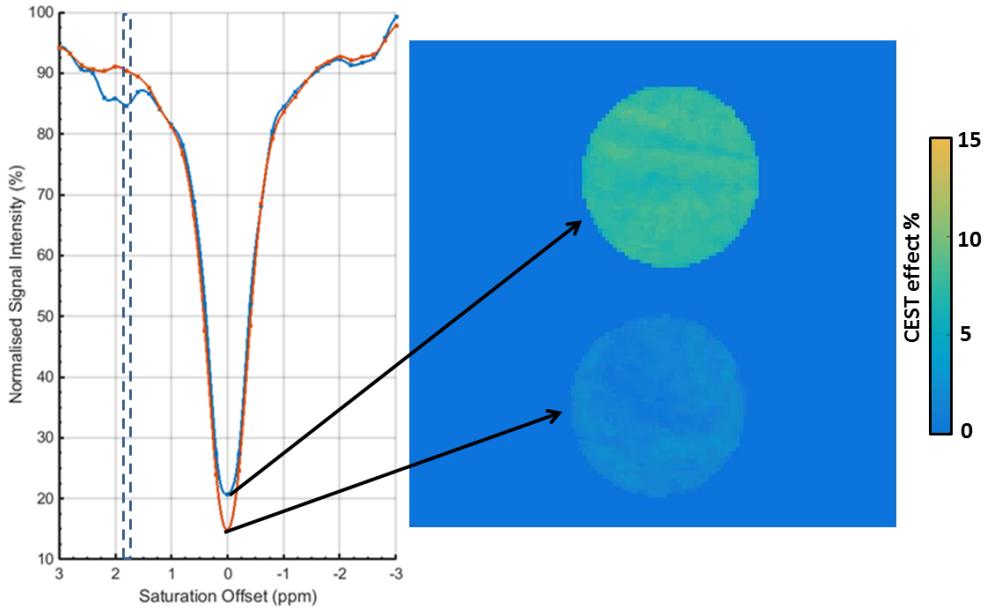


Figure 5.17: CEST image showing detection of Cr metabolite *in vitro* at 1.9 ppm. The two tube Varian set–up using the GEMS sequence shows the ability of the sequence to distinguish solutes exchanging in the slow exchange regime, with negligible CEST effect for the 1 % agar tube (bottom tube) and around a 10 % CEST effect for the 100 mM Cr phantom (top tube). The frequency sampling width is reduced to $\pm$ 3 ppm with the dashed box indicating the CEST at the 1.9 ppm frequency.

To investigate the GEMS CEST sequence's ability to detect amide chemical exchange from a Cr phantom, two tubes containing 100 mM Cr (1 % agar) and pure 1 % agar were scanned. Fig. 5.17 shows the Cr resonance clearly around 2 ppm, with the single frequency (1.9 ppm) image map shown to the right, demonstrating that the CEST effect is homogenous over all over the top tube (Cr sample). The higher CEST effect than those observed in the simulations is partly due to the higher concentration (100 mM instead of 72 mM) and the different T_2 value; as the simulations were provided for the ultimate use in cell experiments in Chapter 6, and the agar T_2 for this creatine sample was not used to

optimise simulations. Nevertheless, the image demonstrates that CEST can provide a technique which gives spatial information regarding the molecular make–up of a sample. The Z–spectrum shows a slight "double dip" in the Cr saturation region, which also appears in the FISP 7 T spectra for the same Cr sample and this is likely due to the Cr sample, rather than multiple resonances. The agar used also contained other compounds such as yeast, used for general bacterial culturing, and this may have combined with the Cr to alter its Z–spectrum profile.

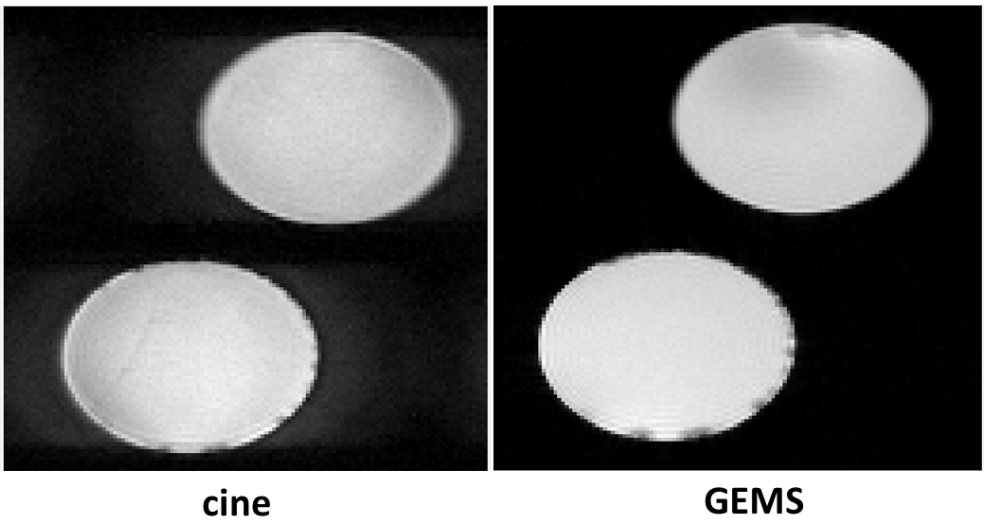


Figure 5.18: Image quality of GEMS and cine for two tube Varian set–up. Two agar phantoms are used for identical scanning using the cine and GEMS reference image as part of individual CEST acquisition protocols. The image quality for the GEMS sequence is better than that of the cine sequence, which has a lower SNR and slight blurring in the read direction.

Finally, the image quality was considered for the cine and GEMS sequence to help assess the most useful CEST acquisition sequence. Fig. 5.18 shows a reference image of both sequences, with apparent superior image quality in the GEMS sequence. Quantitatively, the GEMS sequence has a far higher signal–to–noise ratio (SNR = 291) compared to the cine sequence (SNR = 25), where the signal region is chosen as the area inside the lower tube for each scan and the standard deviation outside the tubes is averaged over ROIs.

5.6 Discussion

Through the simulations and *in vitro* experiments detailed in this chapter, I have been able to inform the set–up for the *in vitro* cell CEST imaging experiments in Chapter 6 and draw conclusions regarding optimal parameters for maximum CEST effect of APT.

The simulations showed that a small CEST effect increase can be expected at higher fields and importantly, the separation between solute and water peak increases with field strength; for APT this is particularly beneficial and hence the optimal field strength appears to be at 9.4 T. Additionally, the FISP sequence investigated at 7 T did not produce robust results to demonstrate that the sequence could be effectively used. A CEST effect was observed for one of the samples in the composite phantom but the Z–spectrum did not show expected saturation over the full frequency range. Shah et al. describe a potential problem with the CEST FISP sequence as the decreased SNR [228], and it is likely that this and the poor WASSR referencing contributed to the poor results. To date, only four publications in the CEST literature have used the CEST FISP sequence ([42, 228, 252, 253]), and further research should be done in order to validate the robustness of this sequence for our set–up.

The simulations also showed that the optimal irradiation strength, B_1, is around 1.4 μT. This value will be taken forward to Chapter 6 for cell experiments, but this is broadly in line with previous APT simulations which state the irradiation power to be around 1 – 3 μT [209].

The sequences used on the Varian scanner both provided results which were in agreement. The cine sequence appeared to have slight blurring in the read direction which could be due to incomplete re–focusing of the crusher gradients used in the acquisition, leading to a decreased image quality. For this reason, the preferred sequence was the GEMS sequence which, despite the longer acquisition time, appeared to provide robust CEST results. The volume coil set–up with two tubes on the Varian worked well and gave a good level of B_0 homogeneity using a suitable shimming routine (typical voxels could be shimmed to less than $\sim$ 20 Hz).

For future *in vitro* cell CEST experiments, it is likely there will be contributing effects at + 3.5 ppm (APT frequency). The APT signal is contributed to by the NH bonds "from multiple unknown amino acids" Van Zijl and colleagues stated [209], with Zhou et al. [226] having previously confirmed the identity of amide protons at 8.3 ^{1}H ppm or 3.5 CEST ppm using a water exchange filter (WEX) method. Simulation of additional effects including NOEs are difficult to simulate and this is a limitation of the work in this chapter. However, determination of optimal parameters are independent of contributing group effects and the simulations described are still important to determine parameters which maximise the CEST effect.

CHAPTER 6

CEST imaging in a cancer cell model and machine learning application

6.1 Outline

This final experimental chapter builds upon the CEST work developed in Chapter 5, using the Varian 9.4 T scanner to investigate chemical exchange signals in a 3–D medulloblastoma cell model. Supervised machine learning based techniques are explained to illustrate the data classification process.

A 3–D cell model experiment is then designed and implemented to obtain *in vitro* CEST data from cancer cells and a control sample, over a frequency of $\pm$ 5 ppm. A support vector machine (SVM) is investigated, basing features on areas of molecular activity in the CEST spectra, to optimise the classification. This analysis was evaluated using a leave–one–out method and comparing discrimination ability with simple quantitative measures in a receiver operating characteristic (ROC) curve. To the best of my knowledge, this is the first application of a SVM approach to CEST data. This chapter provides a means of analysing molecular components in cells for future studies, with the possibility to assess CEST effect changes spatially and correlate with histology or high resolution spectroscopy.

6.2 Introduction

CEST has been successful in recent years in comparing pathological and healthy tissue *in vivo*, and equating differences in Z–spectra with tissue type.

APT CEST

APT CEST has been the most commonly used CEST method for cancer studies. APT has shown signal heterogeneity in high grade gliomas ($n = 12$), with increased APT effects in necrotic and tumour core regions, compared to ordinary white matter [254]. Significantly increased APT signals have been found in prostate tumours compared to benign tissue for confirmed prostate cancer patients [255]. Togao and colleagues [256] further demonstrated that an increased APT effect was found in two separate malignant lung cancer cell lines in a mouse lung cancer model, with a higher APT effect for the more actively proliferating cell line.

An important application of APT CEST has been correlating tumour grade with CEST effect. Significantly increased APT was found in high grade gliomas (stage III or IV), compared to lower grade (stage II) tumour, in a study of 36 histologically confirmed diffuse glioma patients [257]. This confirmed earlier work by Zhou et al. [226] which showed spatial correlation between histology and APT images in a rat 9L tumour model and alluded to the possibility of tumour grading using APT CEST.

Although this simple APT comparison method has also been successful in diverse applications such as stroke [242] (which actually displays a decreased APT effect due to a decreased exchange rate and pH [209]) and multiple sclerosis [258], the molecular source of both amine (AMEX) and amide (APT) contrast is not well understood. Whilst Xu et al. [259] inferred the amine group contributed at 2.75 ppm in human tumours, Togao et al. suggested that the increased CEST effect at 2 ppm in a murine lung cancer model was in fact from the amine groups from the side chains of amino acids [256]. In a CEST rat stroke model study, the amine effect was observed to occur between 2 and 3 ppm and was particularly pronounced at 2.5 ppm in the *in vivo* rat cortex [260].

Molecular decomposition of CEST spectra

Emphasis has typically been placed on differences at a single proton frequency of interest, such as + 3.5 ppm (APT CEST) [227], rather than investigating the chemical and molecular effects on a complete CEST spectrum. Early efforts to quantify molecular effects on Z–spectra focussed on fitting simulated models to acquired CEST Z–spectra. Several studies had assumed a single APT solute pool and used multi–pool models to fit simple *in vitro* Z–spectra [238]. Later work included a Bayesian approach based on *a priori* knowledge of parameters for more accurate fitting [243] and four pool models for PARACEST agents [261].

There is a current trend towards understanding the contributions of several frequencies in a Z–spectrum, and a move to quantify the individual contributions of different solute pools to the spectrum as a whole, acknowledging the convoluted molecular contributions. Zaiss et al. [262] demonstrated accurate modelling of a two pool solute/bulk water exchange system using Lorentzian fitting of peaks. Work by Desmond et al. [263] further sought to decompose the amide, amine and aliphatic peaks in CEST spectra of murine xenografts at 7 T, using Lorentzian line fitting to identify resonances at + 3.5 ppm, 2 ppm and - 3 ppm respectively. It is apparent that these molecular groups produce CEST contributions at certain points in the Z–spectrum, which leads to the consideration of algorithms to assess these spectral "patterns".

Pattern recognition approaches for MRI/S studies

Pattern recognition using machine learning has been used extensively in MRI and MRS, and particularly in cancer applications, as a method of interpreting complex data and identifying meaningful patterns in order to classify new objects or data [264]. In situations where the class ("normal" or "pathological" tissue are examples of classes) is known, approaches focus on classifying new data based on algorithms which have been trained on sample test data. A large multi–centre study in 2006 by Tate et al. [265] examined several features from MRS tumour data to perform pattern recognition analysis and provided an 89 % successful tumour type classification rate for a test case of 91 patients.

Several MR pattern recognition studies have used a support vector machine (SVM) to classify data, where using multiple features can give greater discriminative ability than single measures. Granziera et al. [266] used a SVM analysis with "soft" margins with 7 features, which included magnetisation transfer ratio (MTR) value, to study differences between healthy controls and mild cognitive impairment (MCI) patients. The SVM results showed good test accuracy of 79 % between healthy controls and a subgroup of amnestic MCI patients. Similarly, Iordanescu and colleagues used a SVM to correlate prostate cancer aggressiveness with *ex vivo* MRS [267]; classification of two distinct Gleason score groups was possible with a radial basis function (RBF) classifier. Features were based on fatty acid moiety values from acquired spectra, using a leave–one–out (LOO) method and ROC curves to evaluate their classifiers. Pattern recognition methods are well suited to these examples in which patterns exist in complex data but which are difficult to observe with a single measure or feature.

CEST cell studies

Pattern recognition appears to be a viable option to analyse CEST data, which is inherently complex and has the potential to provide additional information beyond the commonly used single frequency analysis. However, relatively little work has been published regarding CEST imaging specifically *in vitro* of tissue or cells, compared to the large body of published *in vivo* work.

Cell CEST experiments are straightforward to prepare, with several groups using glass capillaries combined in an MR holder as a phantom. Song et al. [268] used this set–up to monitor glycosylated protein expression in tumour cells, using glycogen CEST imaging. The MTR asymmetry values at 1.8 ppm were significantly different between cell lines which overexpressed the proteins and those which did not. Additionally, this work demonstrated the large CEST effect close to 0 ppm which appears to be more commonly observed with cell samples than *in vivo*. This could be due to the presence of many hydroxyl groups from the proteins and metabolites found in cell media. A later cell CEST study also found strong CEST effects at 1.8 ppm, with large effects around 0.9 ppm, for

arginine–rich superpositively charged green fluorescent protein (GFP) cells [269].

CEST experiments with cells have also been shown to be sensitive to particular cell types. An abstract by Chan et al. [270] in 2013 measured the CEST effect at 11.7 T from breast cancer cell lines with different aggressiveness. The study correlated the higher CEST effect in the most aggressive cell line with higher metabolite concentrations using MR spectroscopy. The authors concluded that the combination of metabolites such as myo–inositol, creatine, glutamine and glutamate contributed to the overall CEST signal from the cells.

Aims

In this chapter, the aim is to investigate whether a CEST technique is able to provide biologically relevant information to discriminate between a cancer cell line and control sample, and if a machine learning based approach can be applied to better identify important regions of the resulting Z–CEST spectra. To the best of our knowledge, no study has yet utilized machine learning techniques with CEST data. Based on the CEST literature APT is chosen as a target, which has been shown to be increased in cancer and tumour progression, using the optimised CEST APT parameters from simulations in Chapter 5. Several previously discussed papers have also shown that hydroxyl groups contribute to the CEST effect near 0 ppm, and we expect to see effects in this region which may also help discriminate between samples. These aims are investigated using a designed cell CEST experiment with control and cancer cell samples, to directly compare CEST effects from the cells. Machine learning could potentially allow analysis of the full spectrum rather than individual frequencies of interest.

6.3 Pattern recognition theory

This section aims to act as an introduction to the theory of a SVM model learning approach, demonstrating key steps in the process.

The type of pattern recognition to be performed is a supervised learn-

ing method. Supervised methods rely on the assumption that two clear groups exist in the data and a chosen algorithm must provide an optmised line of separation between the two groups. Unsupervised methods have also been used extensively in MRI, in which no prior assumptions are made and in which algorithms look more at patterns and clustering of data to estimate the number of groups and their distribution in parameter space. The supervised method was considered initially the most appropriate for our research problem in which we wish to compare MR signatures from two distinct samples, using an algorithm to appropriately classify data.

6.3.1 Feature generation and selection

When using machine learning in a classification task such as ours, we are given a specific pattern, which is made up of l features values, to give a unique feature vector, $\boldsymbol{x}$, such that $\boldsymbol{x} = [x(1), x(2), ..., x(l)]^T$, which exists in an l–dimensional real space, R^l.

A feature is the quantitative parameter, for which a given subject or ROI has a value. Features may take the form of a mean intensity or exact relaxation value, or may be a slightly more complicated statistical measure based on a histogram–type distribution; that is to say, a distribution in which the data from a single patient or ROI can be collated and divided into discrete "bins". A number of such distribution based features exist, based on the sample's statistical moment:

$$\mu_i = \frac{E[(x-\mu)^i]}{\sigma^i} \quad . \tag{6.3.1}$$

Here μ_i is the central moment for a distribution where x is the value of interest (greyscale intensity in an image, for example) for i = 1, 2, ..., n. A number of familiar statistical measures are obtained using the central moment distribution, with $i = 1$ being the mean and $i = 2$ is the variance. The skewness, $i = 3$, is a measure of the asymmetric nature of the histogram around the mean and the kurtosis, $i = 4$, is a measure of peak height, relative to a normal distribution.

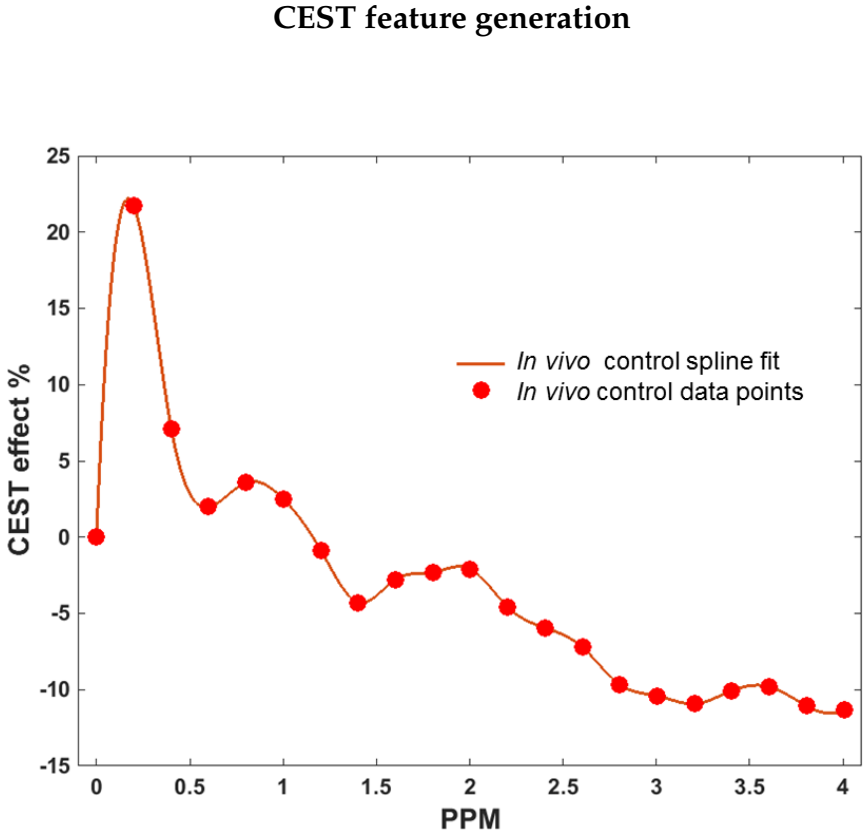


Figure 6.1: Representative CEST MTR asymmetery data for machine learning from *in vivo* data acquired by [241, 271]. The circles represent the raw data, with spline fitting used to extrapolate the CEST effect at ppm values which were not experimentally sampled.

Several cancer MRI studies use texture features in which not only the values of a pixel/voxel are used but their relation and pattern relative to neighbouring voxels is used. This was not used in this study partly due to the lack of heterogeneity in the *in vitro* samples and the fact the CEST is largely susceptible to B_0 inhomogeneities, with current evidence indicating that CEST effect is heavily dependent upon the magnetic field. Previous CEST studies identify the CEST metabolite frequency of interest and normally provide a statistical test at that frequency (or frequency interval) to determine significant differences. Whilst this is a valid method to compare significance of experimental measurements, it is my hypothesis that the complexity of the CEST spectra could yield additional information using machine learning; thus, group classification, rather than a group comparison with hypothesis tests, is the nature of this problem.

In this chapter, analysis is performed by defining features using the MTR asymmetry curves from *in vitro* CEST acquisitions. In Fig. 6.1, an example of an *in vivo* MTR asymmetry curve is shown. This is the typical format of the raw data used in all SVM analysis, where asymmetry curves for two distinct classes are provided with discrete datapoints. The CEST effects at the discrete experimental points are interpolated to give a continous fit over the ppm range. This can then be used to provide features relating to the CEST effect at given frequencies or intervals, as well as using the statistical measures defined above.

Individual feature ranking

Having established a list of possible features, the individual discriminatory power (how good they are at distinguishing whether an asymmetry curve belongs to a given group) is used. It is important to choose the smallest number of features whilst also keeping a good level of discriminatory power, failure to choose appropriate features may lead to poor classification later on.

Fisher discriminant ratio (FDR)

The FDR test can be used to assess the discriminatory power of features, particularly in machine learning of MRI data [272]. It is independent of the underlying data distributions and can rank features based on how well they discriminate between two groups:

$$\text{FDR} = \frac{(m_1 - m_2)^2}{\sigma_1^2 + \sigma_2^2} \quad . \tag{6.3.2}$$

Here the FDR is calculated for each feature, based on all class data values for the specific feature, with m and σ representing the respective mean and standard deviation of the two classes.

Combined feature ranking

Having identified features most likely to be of discriminatory value, it is common to evaluate effective combinations of feature vectors. Specific combination measures used previously in machine learning literature in-

clude divergence measures, Bhattacharyya distance measures and scatter matrix measures [273]. The first two of these are related to Bayesian statistics and assume a known probability density function, thus scatter matrices are chosen as the experimetal combination measure. Different forms of the scatter matrices method exist and subsequent analysis is limited to the measure known as J_1 (using the definition given in [274]), where,

$$J_1 = \frac{trace\{S_m\}}{trace\{S_w\}} \quad . \tag{6.3.3}$$

Here S_w is the within–class scatter matrix, defined as,

$$S_w = \sum_{i=1}^{c} P_i S_i \tag{6.3.4}$$

where S_i is the covariance matrix of class $i = 1, 2, ..., c$ and P_i is the *a priori* probability of the respective class i. The *a priori* probabilities for the two classes in our data sample is the total number of feature vectors divided by the combined total number of feature vectors in each class, thus, the probabilities are both $1/2$. S_b is the between–class scatter matrix, given by,

$$S_b = \sum_{i=1}^{c} P_i (m_i - m_0)(m_i - m_0)^T \tag{6.3.5}$$

with the global mean vector, $m_0 = \sum_{i=1}^{c} P_i m_i$, m_i being the class mean values and T indicates a vector transpose. S_m is obtained from the relation, $S_m = S_w + S_b$. It is apparent that larger values of J_1 will be indicative of smaller within–class variance (small clustering of points) and larger between–class differences (greater distance between the distributions of the two classes), hence optimised J_1 values for feature vectors are preferable.

6.3.2 Classifiers: type, design and evaluation

The aim of the classifier is, as previously stated in the introduction, to correctly classify all input training vectors into the correct groups.

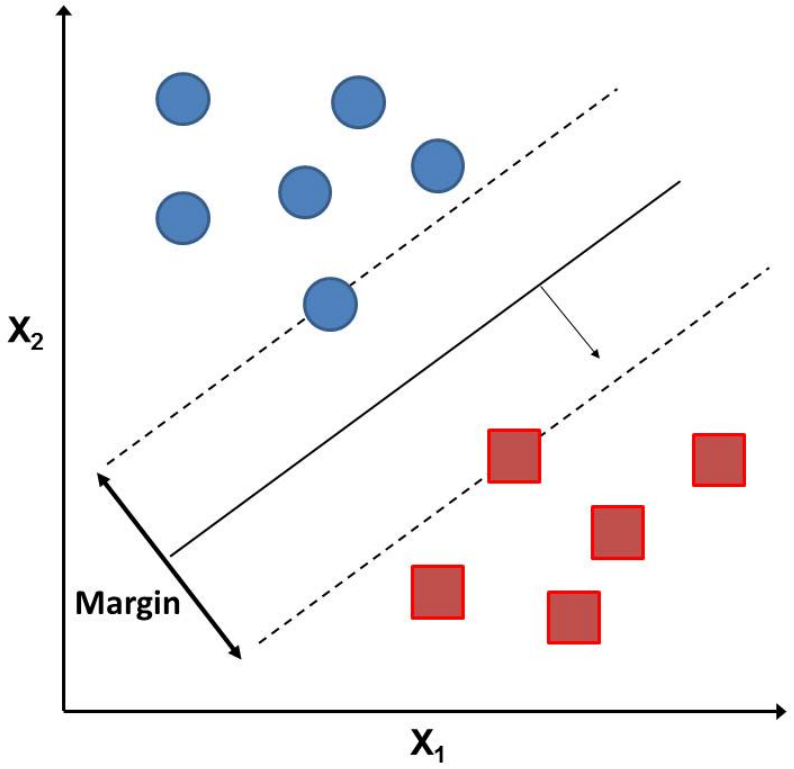


Figure 6.2: SVM illustration: ideal case. The location of the data points for the two groups (blue and red) are defined by the value of the features X_1 and X_2 for each point. The optimal classifier will allow a line to be drawn between the groups, with the maximum margin value achieved.

Support Vector Machine (SVM)

The utility of the SVM classifier is to create a hyperplane, $g(x)$ for correct training vector classification, where the general form of this hyperplane classifier is given below [274]:

$$g(x) = \boldsymbol{w}^T \boldsymbol{x} + w_0 = 0 \tag{6.3.6}$$

where $\boldsymbol{w}$ is the non–zero normal vector to the plane, $\boldsymbol{x}$ is a general vector in feature space and w_0 is a constant. The goal of the SVM is to maximise the margin between data sets, where the margin is defined as the distance between the set of hyperplanes which are characterised by

$$\boldsymbol{w}^T \boldsymbol{x} + w_0 = \pm\, d \quad , \tag{6.3.7}$$

where d is the distance between the hyperplane and supporting vector. The illustration in Fig. 6.2 shows the margin between two groups in the

ideal case.

In more realistic examples there may be overlap between the two groups and we must introduce a soft–margin parameter, such that the misclassification error can formulated as a minimisation task:

$$\text{Minimize} \quad J(w, w_0, \xi) = \frac{1}{2}||w||^2 + C\sum_{i=1}^{N}\xi_i \quad . \tag{6.3.8}$$

Here, ξ_i is the margin error which is a nonzero quantity, and C is a variable parameter used to change the influence of the support vectors involved in the optimisation. Optimisation of this equation is equivalent to a cost function optimisation, subject to the following criteria:

$$w^T x_i + w_0 \geq 1 - \xi_i \quad \text{if} \quad x_i \in \omega_1 \tag{6.3.9}$$

and

$$w^T x_i + w_0 \leq -1 + \xi_i \quad \text{if} \quad x_i \in \omega_2 \tag{6.3.10}$$

for $\xi_i \geq 0$, and where $2/||w||$ is the margin width.

The solution of this is a biased average of the sum of the training points:

$$w = \sum_{i=1}^{N}\lambda_i y_i x_i \quad . \tag{6.3.11}$$

The weighting of each training point is defined by the λ_i coefficient, which is a Lagrange multiplier in the cost function optimization. For points outside the margin, $\lambda = 0$, with all other points contributing to the classifier direction ($\lambda \neq 0$); these points are known as support vectors.

SVM: non–linear classifiers

In many cases, the distribution of the data from two classes is not easily separable with a single straight line (linear classifier), see Fig. 6.3. The approach taken in pattern recognition applications is to define a mapping from the original feature space R^l, defined in section 6.3.1 (2–D in our example case), and map to a new higher–dimensional space, H. This allows the use of functions which can distinguish between classes more

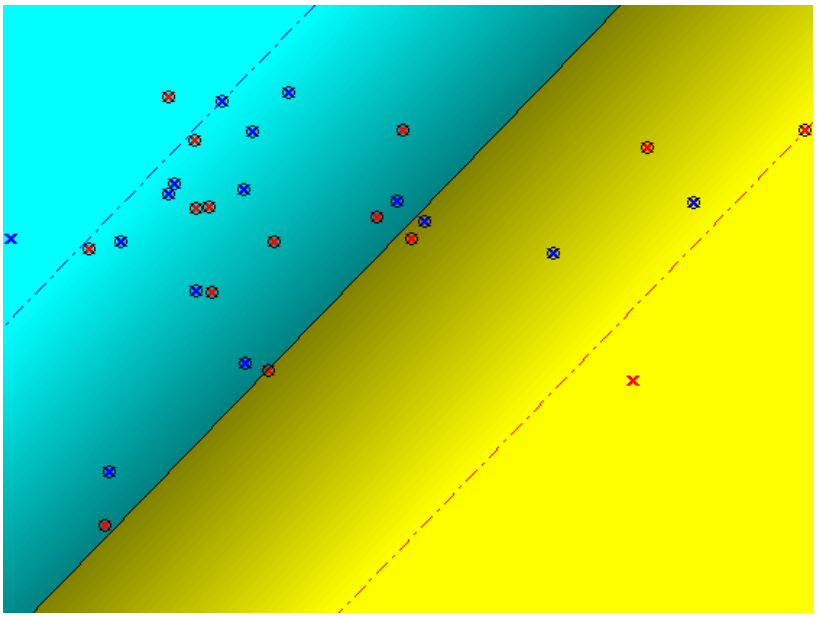


Figure 6.3: The limited utility of linear classifiers for certain classification problems. When two groups are not linearly separable, a linear classifier is poorly suited to the task of group classification. The linear fit shown here will misclassify a large number of points, using generated data for example purposes.

easily using the additional dimensionality. This abstract concept is better understood visually, as in Fig 6.4.

The mapping from the l to the H space requires a mapping function which can be defined for certain functions as the inner product between the images $((\phi(x_1), \phi(x_2))$ of two points x_1, x_2:

$$< ((\phi(x_1), \phi(x_2)) >= k(x_1, x_2) \tag{6.3.12}$$

where $<,>$ is the inner product operator in H and $k(,)$ is the kernel function. For SVM problems, we can replace inner products arising from linear mapping to higher dimensional space with the kernel functions. These are typically polynomial or Gaussian type simple functions, as illustrated below:

Radial basis function (RBF)

$$k(x, y) = \exp\left(- \frac{||x - y||^2}{\sigma^2} \right) \tag{6.3.13}$$

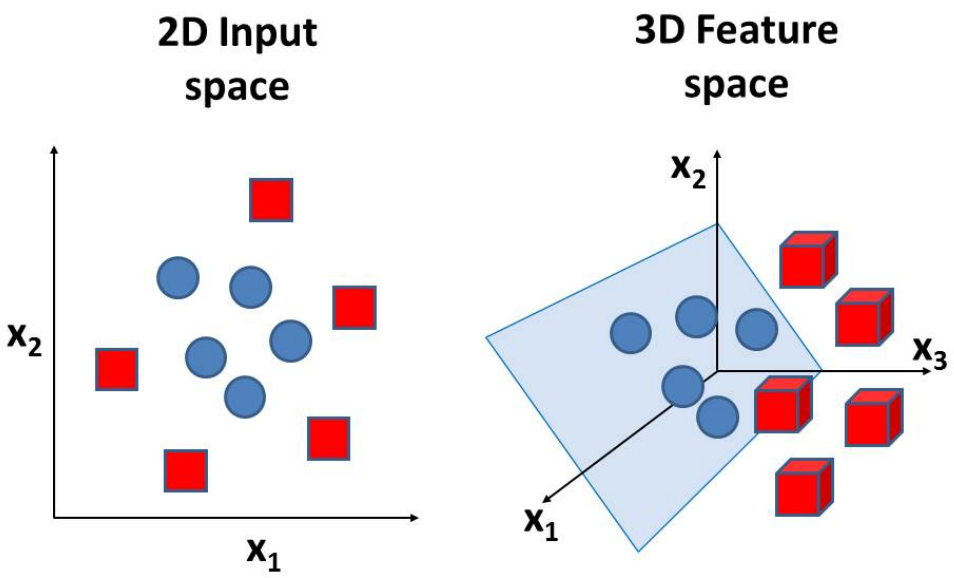


Figure 6.4: Higher dimensional hyperplanes to separate non–linear classification problems. Linear classifiers may not be appropriate in certain problems (left), in which case a higher dimensional hyperplane can act as a non-linear classifier to separate groups (right).

Here σ is a parameter which defines the exponential decay of the function.

Polynomial function

$$k(x, y) = (x^T y + \beta)^n \tag{6.3.14}$$

n and β are parameters defined by the user.

Classifier evaluation: Sensitivity and specificity

To evaluate how good a classifier one has chosen, sensitivity and specificity measures are used [272].

Sensitivity in the context of machine learning is commonly defined as:

$$\text{Sensitivity} = \frac{\text{True positive}}{\text{True positive} \ + \ \text{False negative}} \ . \tag{6.3.15}$$

The specificity measure of a classifier is similarly defined as:

$$\text{Specificity} = \frac{\text{True negative}}{\text{False positive} + \text{True negative}} \quad . \tag{6.3.16}$$

In the two–group scenario the following definitions apply: a true positive (TP) is when a disease sample is correctly identified by the classifier as belonging to the disease group (later in this chapter, this will be a cancer cell sample); a true negative (TN) is when a control sample is correctly identified as belonging to the control group; a false negative (FN) is a disease sample identified as belonging to the control group; and a false positive (FP) is a control sample identified as belonging to a disease sample group. Additionally one can define the test error (Accuracy = 1 - Test error) as:

$$\text{Test error} = \frac{\text{FN} + \text{FP}}{\text{TP} + \text{TN} + \text{FN} + \text{FP}} \quad . \tag{6.3.17}$$

Classifier evaluation: leave–one–out method

Several methods exist which can probe the robustness of classifiers, quantifying their results in terms of sensitivity and specificity measures. These have been demonstrated in the MR literature and have included bootstrap methods [275], holdout methods [276], leave–one–out cross validation (LOOCV) methods [277] and leave–one–out (LOO) methods [278]. For our relatively small sample, a LOO method was chosen as a simple method of classifier evaluation. Other methods require large n for accurate results (holdout method) or do not significantly improve on the LOO method if large classification errors are not involved (bootstrap method [279]).

The LOO method begins by removing one of the data points from the total sample of the two combined groups and calculating the classifier based on the $n - 1$ points. This is repeated with a different data point removed, until all points in the sample have been individually removed and a classifier computed without that point. At each iteration, the removed data point is treated as a test data point and it is recorded whether the point is correctly classified. The total number of false negatives and positives for all iterations are summed and can then be used for sensitivity, specificity and test error calculations.

6.4 Medulloblastoma cell imaging

The main aim of the following experiments were to compare the CEST effects between a cell sample and control sample; in particular, two separate time points in the incubation process (six days and ten days) were analysed. Machine learning is used to aid the process, assigning a number of features to the CEST spectra to extract data which would be otherwise difficult to compare quantitatively.

6.4.1 Tumour cell model

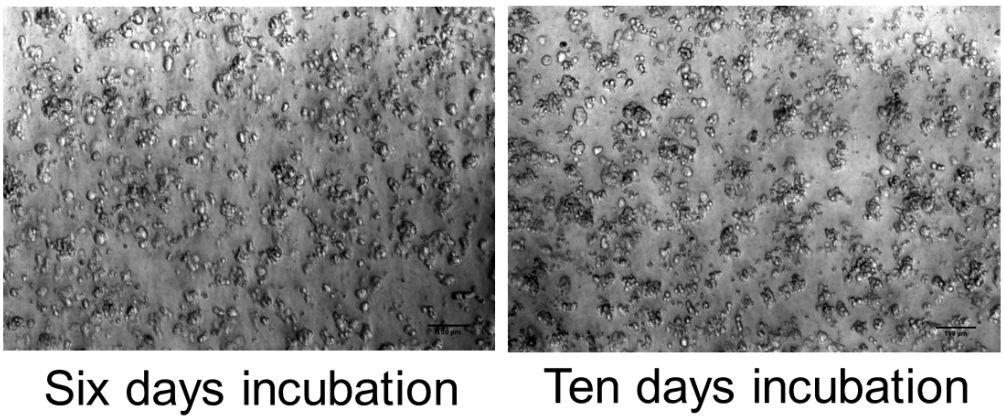


Figure 6.5: Bright–field (x 10) microscope images showing cancer cell aggregates at different incubation time points. Medulloblastoma cells were incubated and removed for bright-field imaging after six and ten days, by Ms Aishah Nasir using a Nikon Eclipse microscope system. In both images the cells can be seen to form aggregates, which are larger in size after ten days incubation compared to six.

The cancer cell models were set up in collaboration with Professor Beth Coyle's research group, with Ms Aishah Nasir responsible for cell preparation and culture, as well as microscope imaging. The cells are grown from the D283 Med cell line, originating from a human epithelial medulloblastoma cell sample [218]. The cells have a doubling time of 52 hours, with three cell populations of adherent, semi–adherent and suspension cells present under normal *in vitro* conditions. A summary of the standard operating procedure (SOP) for the 3–D tumour growth assay (TGA)

followed by Ms Nasir is given as follows:

- Basement membrane extract (BME) is diluted to 6 mg/mL with TGA media (phenol red free RPMI 1640 (Sigma Aldrich, UK) + 1% L–glutamine). The extensive list of contents of the TGA are given on the Sigma Aldrich website. The D283 cells were initially grown in T75 sterile cell culture flasks in serum media DMEM (low glucose, Gibco) with 10 % foetal bovine serum (FBS, Hyclone). These were then trypsinised, centrifuged at 800 rpm for five minutes, suspended in the TGA media and counted using Nikon NIS Elements software. 3.5×10^5 D283 cells were mixed in a solution of 0.5 mL TGA media and 0.5 mL BME and pipetted into a sterile 2 mL imaging tube, temperature controlled at 37 °C using a hot plate. An identical solution without the cells was prepared in the same way to act as a control. Imaging tubes were placed into a humidified cell culture incubator at 37 °C in a 5 % CO_2 atmosphere for 1 hour to allow BME gelling. Tubes were incubated for an additional hour in a PBS induced humid environment. 0.5 mL of TGA media was then added to each tube (final BME conc. = 2 mg/mL). A total of two sample and two control tubes were produced using this standard operating procedure (SOP).

The motivation for choosing the six and ten day timepoints was determined from bright field imaging, which showed a higher degree of cell clustering after ten days of incubation compared to six days (Fig. 6.5).

6.4.2 Methods: experimental and post–processing parameters

The protocol was optimised around the scans necessary to perform a CEST analysis (namely, a reference scan, a series of CEST scans at various frequencies and a WASSR scan to correct for B_0 inhomogeneities).

The scan protocol attempted to minimise the effect between the different environments of the cell culture (37 °C, 5 % CO_2) and the scanner room

($\sim$ 21 °C, standard atmospheric composition). Typical cell counting procedures remove cell samples from incubation for around 30 minutes and I was advised to keep scanning to less than 50 minutes to ensure cell degradation was kept to a minimum.

Testing was performed prior to actual cell experiments to optimise timing from receiving sample tubes to finishing the last scan in the protocol.

Standard experimental protocol

An identical set–up to Chapter 5 CEST experiments (involving "locator" images and global and local shimming protocols) were adopted with identical parameters to the previously detailed experiments. Differences from previous parameters are highlighted below.

CEST array sequence

A saturation pulse train of four Gaussian pulses, each of 46 ms duration and 1.4 μT power, irradiated 51 separate frequencies in a range $\pm$ 5 ppm around the water peak with a resolution of one pulse train per 0.2 ppm.

The saturation module was coupled with the "gems" sequence which had parameters: excitation pulse angle = 20°, TE = 4 ms, T_R = 202.4 ms, MTX = 64 x 64, t_{acq} = 11 m 1 s.

Reference image

An identical sequence to the GEMS CEST array was acquired but without the frequency selective saturation (t_{acq} = 13 s).

WASSR

A WASSR scan sampling at 18 separate frequencies at 0.0625 ppm intervals between 0.5 ppm and - 0.5 ppm, with a reduced saturation power of 0.1 μT. The sequence used the same parameters as the CEST array, aside from saturation module. The t_{acq} was 3 m 53 s.

T_2 spectroscopic scan

The T_2 value of the cell sample was measured at the end of each experiment (the T_2 of the control sample was assumed to remain constant for the six and ten day experiments). The two tubes were removed and the

single cell sample tube was re–positioned in the scanner, with the "locator" images and set–up protocol being repeated. A spectroscopic T_2 scan was then implemented (t_{acq} = 1 – 2 minutes, T_R = 10 s, 4000 real points, 90° calibrated hard pulses, with a six TE array evenly spaced around the T_2 value). The optimised total time for this experimental set–up was around 45 minutes.

SVM analysis for ten day samples

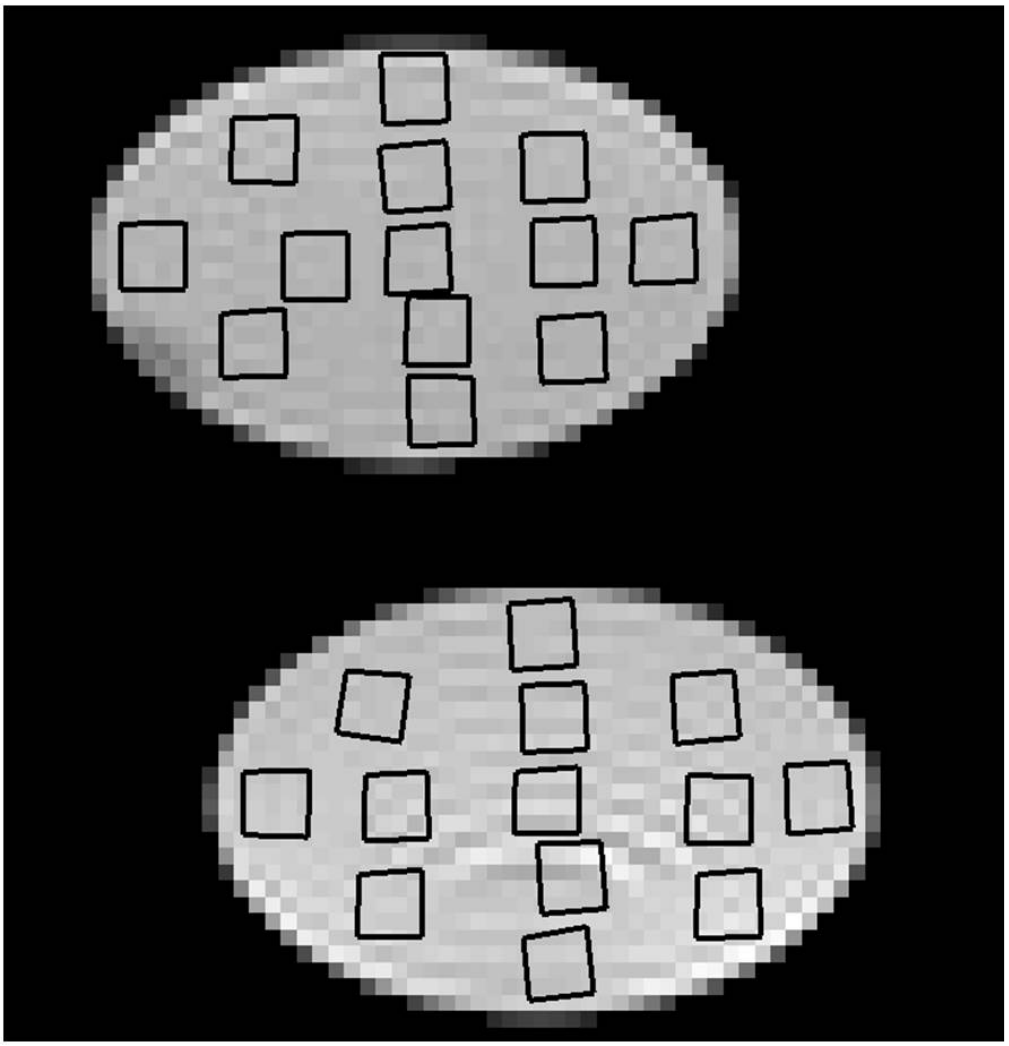


Figure 6.6: Representative positioning of SVM ROIs in a CEST voxel. 13 ROIs are evenly distributed throughout both cell and control samples, each enclosing a 1 mm^3 volume.

A supervised machine learning method was implemented using a SVM algorithm [273] and the raw data provided by the CEST scans described above.

To obtain a number of datasets for SVM analysis, a total of 26 ROIs for both the sample and control were outlined (13 ROIs each), with the asymmetry spectrum calculated for each ROI, with individual volumes of 1 mm^3. The ROIs were placed in an approximately even distribution over the tube volumes in the CEST voxel, see Fig. 6.6. This also allows for investigation of possible significant spatial B_0 differences which could potentially affect CEST results. The resolution in the read and phase encoding directions were different (0.2 mm/pixel and 0.3 mm/pixel respectively), thus, a 1 mm^3 ROI cube has dimensions of ($0.77 \times 1.29 \times 1$) mm^3; this equates to a ROI comprised of around 17 individual pixels.

Each ROI's asymmetry spectrum was extracted and combined to form a complete data set for which to establish classifier features on. Features were decided based on areas of the spectrum highlighted as being of biological interest from the CEST literature, shown in Table. 6.1.

FDR and J_1 tests were applied to rate feature's discriminatory value and to aid choice of principle features (two principle features were chosen). Once chosen, a range of classifiers were used (RBF, linear and polynomial) in conjunction with a SVM algorithm outlined by Theodoridis et al. [273]. A tolerance of 0.001 on all solutions was used for SVM analyses. A LOO method was used to evaluate sensitivity and specificity of classifier solutions, with non–converging analyses being excluded from evaluations.

Finally, ROC curves were computed for two single feature classifiers by plotting histograms of control and cell sample groups and segmenting the range of values into 20 separate bins or threshold values. As the threshold value was varied from the minimum to maximum value, the sensitivity and specificity were calculated at each point, such that a plot of sensitivity vs. 1 - specificity was possible. To plot a ROC curve for the linear SVM classifier, a parametric approach was adopted by varying a constant term in the dividing hyperplane equation, such that a series of parallel hyperplanes bisected the feature space into twenty bins, along a

Feature	Target
Integral 0 – 1 ppm	Integral for hydroxyl resonance (OH)
SF 0.3 ppm	SF for hydroxyl resonance (OH)
SF 0.6 ppm	SF for hydroxyl resonance (OH)
Integral 0.5 – 1.5 ppm	Integral for hydroxyl resonance (OH)
SF 1.9 ppm	SF for amine resonance (NH_2) [280]
Integral 1 – 2 ppm	Integral for amine resonance (NH_2)
SF 2.75 ppm	SF for amine resonance (NH_2). [281]
Integral 2 – 3 ppm	Integral for amine resonance (NH_2)
SF 3.5 ppm	SF for amide resonance (NH) [280]
Integral 3 – 4 ppm	Intergal for amide resonance (NH)
Mean	Statistical measure for MTR asymmetry curve
Variance	Statistical measure for MTR asymmetry curve
Skewness	Statistical measure for MTR asymmetry curve
Kurtosis	Statistical measure for MTR asymmetry curve

Table 6.1: **List of features used in SVM and CEST feature resonance targets.** Integral features refer to the CEST effect integral between two stated frequencies, and a single frequency (SF) feature relates the CEST effect at that particular value. The CEST effect from a given metabolite may have a broad resonance such that an integral measure may be more effective at identifying significant group differences. Statistical measures based on the statistical moments of the data distribution are also used as features.

vector at a tangent to the original linear classifier hyperplane; the constant term's maximum and minimum values allowed thresholding of all of the feature space in an analogous way to the threshold in the single feature histograms. The area under the curve (AUC) was calculated using an in–house Matlab program to compute the histogram of data and measure the area under the curve using a "trapz" function.

6.4.3 CEST results

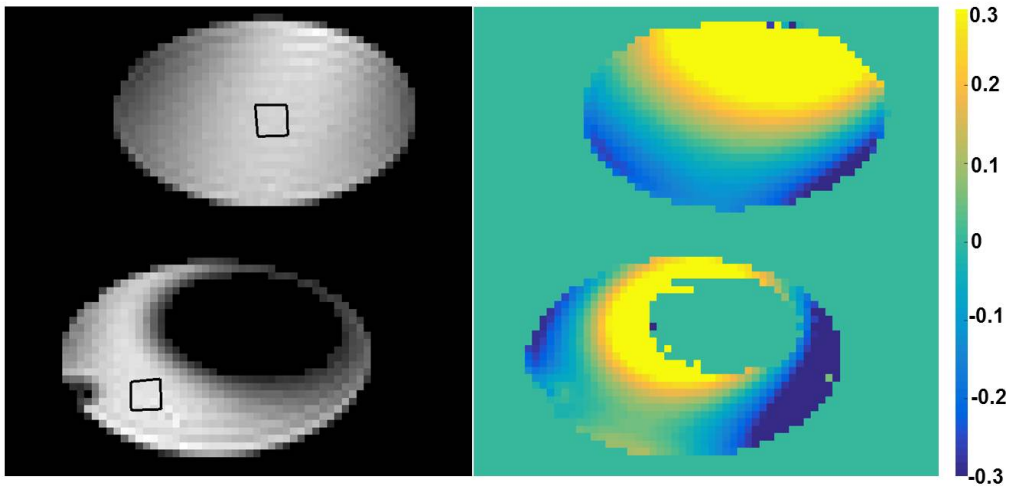


Figure 6.7: Positioning of control and six day cell sample. (**LHS**) A GE reference image shows the location of two ROIs placed in the cell sample (top tube) and the control (bottom tube). A central darkening is present in the control, likely due to a partial volume effect from an air bubble near the sample ROI. (**RHS**) A B_0 map shows the effect of the air bubble, with large variations in B_0 in areas of both the control and cell sample. The scale for the B_0 map is in units of ppm difference from 0 ppm.

A cell sample and control sample were scanned at the six day timepoint using the CEST two tube protocol outlined earlier in this chapter. A CEST voxel ($20 \times 12 \times 1$) mm^3 was chosen to avoid air bubbles, which were not visible in initial "locator" scans. However, during the CEST acquisition it is likely that a bubble may have moved to produce a partial volume effect, visible on images in Fig. 6.7. Due to the timed nature of the experiment, this sample could not be repeated to remove the bubble. The effect of the air bubble is obvious in the B_0 map on the right hand side (RHS) of the figure, showing large differences in B_0 values over the sample; the central bubble is below the thresholded intensity value and is not included in the CEST analysis. A large global FWHM water linewidth for the CEST voxel was measured at 144 Hz.

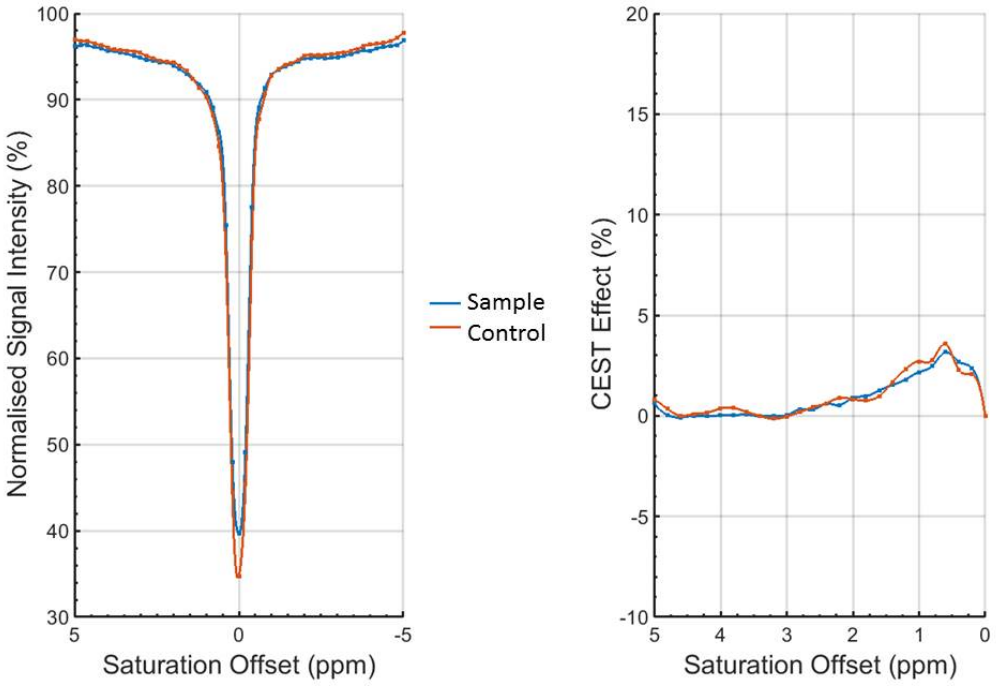


Figure 6.8: CEST spectra for cells after six days incubation. A Z–spectrum is shown **(Left)** over a range $\pm$ 5 ppm for both the control sample without cells and the cell sample removed from incubation for scanning after six days. The corresponding asymmetry spectrums are also shown **(Right)**, with the shape of the control sample being very close to the shape of the cell sample.

However, by judicious placement of a 1 mm^3 ROI in both cell and control samples such that the ROIs are in regions of similar B_0 (variations in ROI less than 0.2 ppm), a CEST spectrum could still be extracted and compared, with Fig 6.8 showing the Z–spectrum and MTR asymmetry plots for the sample and control tubes. The Z–spectrum for both tubes follow a near identical shape and there are no obvious differences (< 1% CEST effect) in the asymmetry curves either.

Ten day incubation cells

After ten days of incubation the second set of samples were removed and the identical CEST scan protocol was applied. There were no obvious susceptibility artefacts present in the CEST voxel (see Fig. 6.9) and a

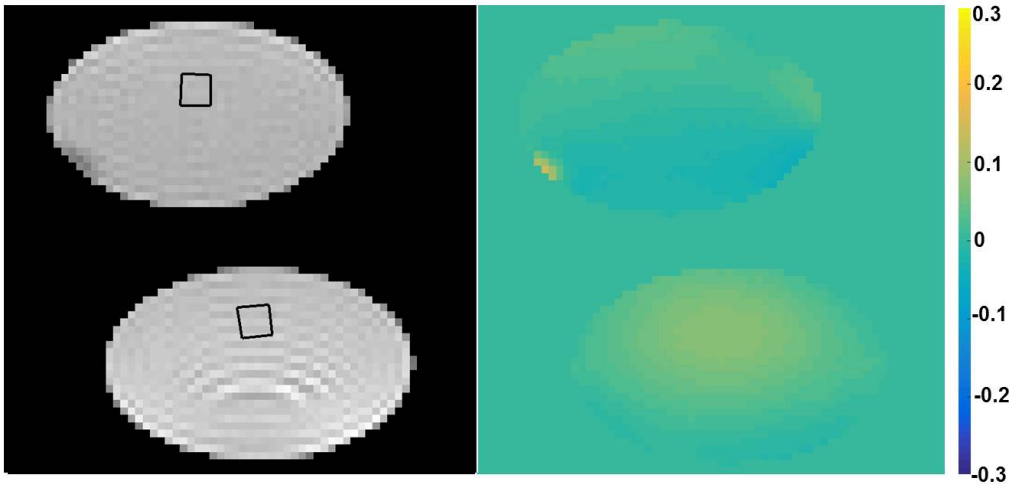


Figure 6.9: Positioning of control and ten day incubated cell sample. (Left) Both tubes are relatively free from artefacts and there is minimal partial volume effects from nearby air bubbles. **(Right)** The B_0 map shows little variation over both tubes, with the ROIs placed in similar field strength areas. Again, the B_0 map has units of ppm difference from 0 ppm.

linewidth of 19.8 Hz was found globally for a CEST voxel volume of (20 $\times$ 12 $\times$ 1) mm^3. Two ROIs were again placed in similar B_0 regions and the Z–spectrum and asymmetry curve were calculated, as shown in Fig. 6.10.

Z–spectra of the ten day incubated cells show differences in shape and position compared to the control sample. Spectral saturation appears to affect both sides of the Z–spectrum (for both control and cell sample), with more pronounced changes for the cell sample. The MTR asymmetry curves show that a large CEST effect occurs near 0 ppm for each sample, with the greatest effect of around 18 % occurring for the control sample. The cell sample showed a noticeable difference at around 2.5 and 3.5 ppm. Compared to the six day sample, the two sample's asymmetry curves are more distinguishable and do not overlap as much as in Fig. 6.8.

Deviation across the control and cell samples were investigated, by computing the MTR asymmetry curves for the ten day samples based on the

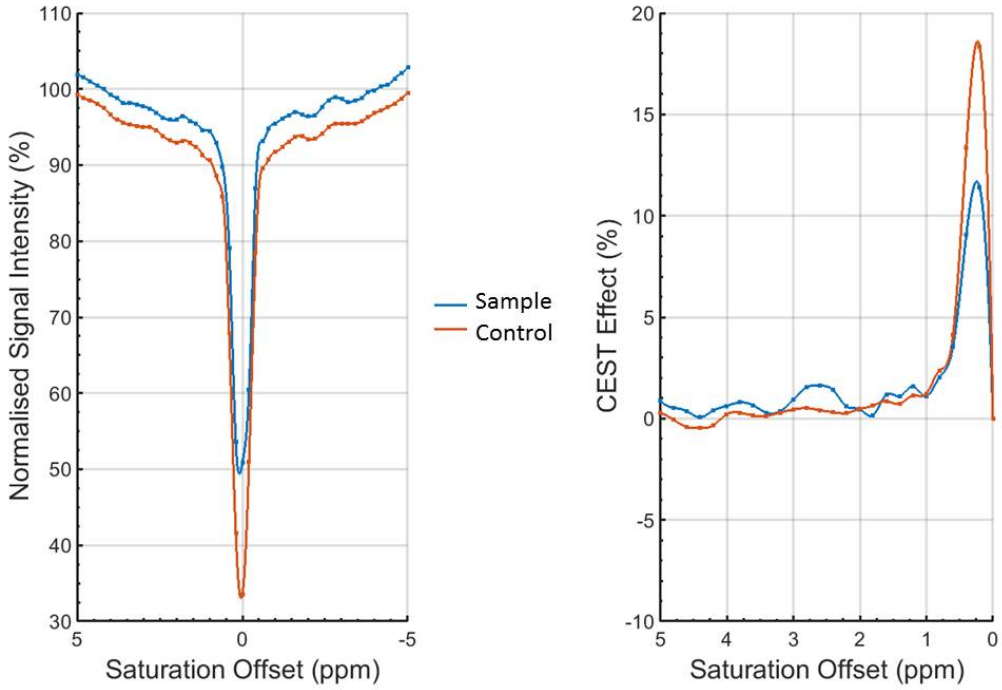


Figure 6.10: CEST spectra for cells after ten days incubation. The Z–spectra of the control and cell sample shown clear differences in shape, **(Left)**, with the control water peak extending to a lower signal intensity than the cell sample. The MTR asymmetry curves produced from the Z–spectra **(Right)** highlight the visible differences between tubes. Areas showing particular differences between the sample and control tubes are the large peak close to 0 ppm and further downfield between 2 and 4 ppm.

mean CEST effect across the 13 ROIs in each sample group used for later SVM analysis. This method allowed the standard deviation at each frequency sampling point to be computed providing a measure of the CEST effect % error. Fig. 6.11 shows the two curves with error bars at each point. Significant parts of the spectrum appear to be around 2 to 3 ppm, at which the error bars do not overlap, as well as less than 1 ppm. The cell sample CEST values are higher consistently between 3 and 5 ppm, but are still within error of the control sample.

The effect of the WASSR correction on the CEST effect was investigated by comparing the output of the CEST analysis tool with and without the

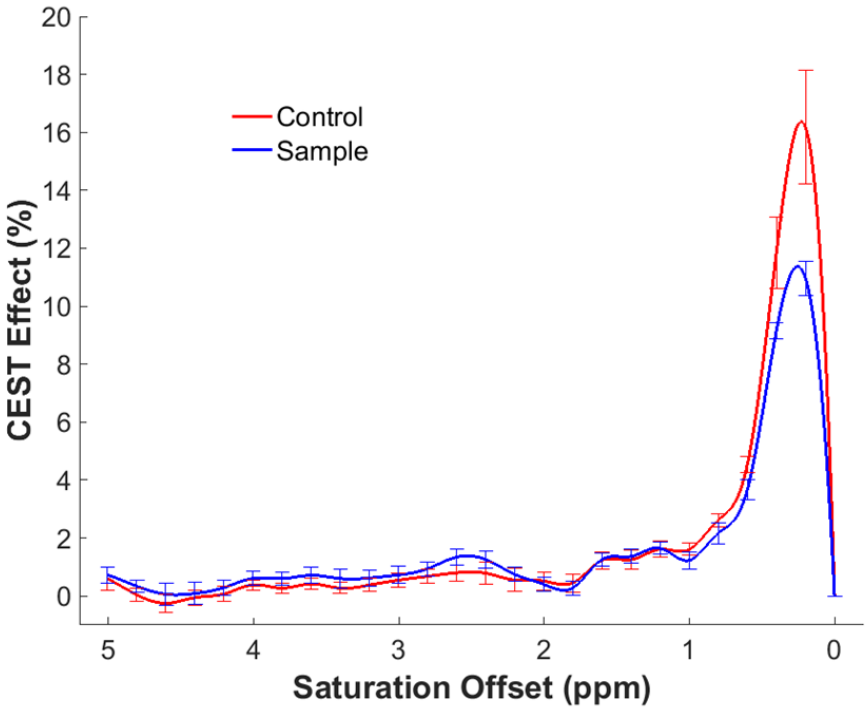


Figure 6.11: Mean CEST spectra of ROIs used for SVM analysis after ten days incubation. The mean CEST effect % value at each offset frequency is computed based on the mean CEST effect of the 13 ROIs distributed around each of the control and cell samples (see Fig. 6.6). The standard deviation of the ROI values is used to provide error bars, with areas in which there is no group overlap being around 2.5 ppm, and less than 1 ppm.

WASSR correction, using two ROIs covering all of the cell and control sample, shown in Fig. 6.12. Small differences in CEST effect are observed > 0.5 ppm between asymmetry curves with and without WASSR correction. Close to 0 ppm, the control sample has a larger CEST effect without the WASSR correction, whilst the cell sample spectrum does not visibly change. The fact that the CEST effect changes significantly close to 0 ppm highlights the importance of the WASSR correction method and is likely due to direct saturation effects which shift the peak away from 0 ppm.

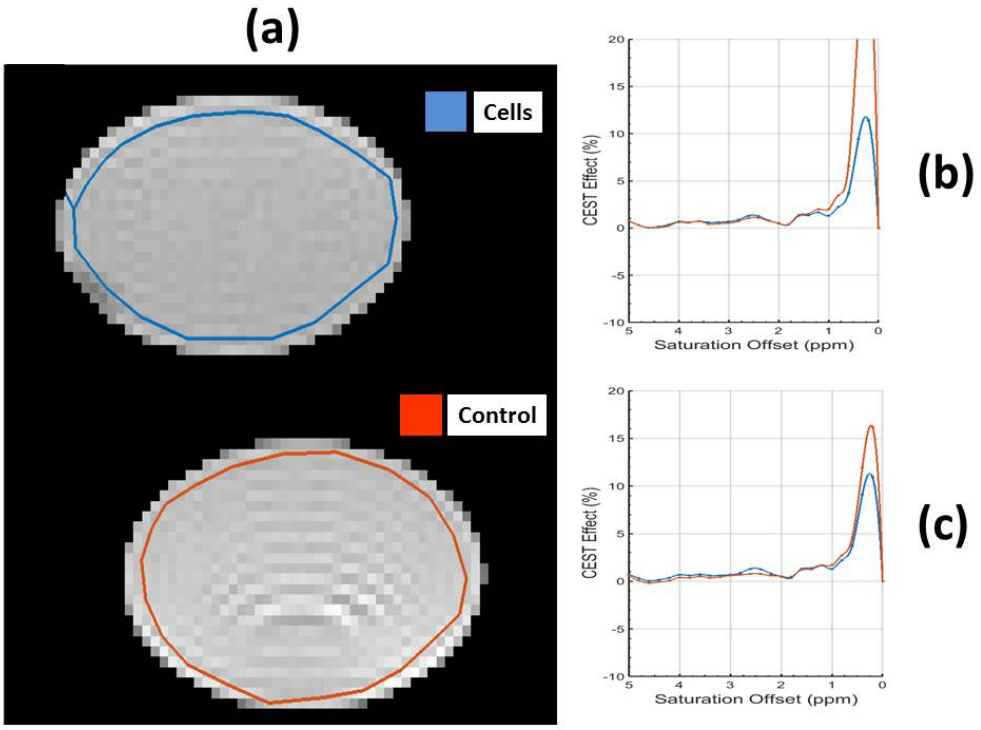


Figure 6.12: Effect of B_0 WASSR correction method on CEST Z–spectra. **(a)** A ROI enclosing all sample volume was chosen for the cell and control samples. **(b)** The resulting MTR asymmetry curves for the samples without WASSR correction applied show an increased CEST effect from the control sample near 0 ppm which is greater than 20 %. **(c)** The MTR asymmetry curves with the WASSR correction applied show a relative decrease in the CEST effect near 0 ppm for the control sample, due to the corrected fitting of the water peak to 0 ppm frequency. The CEST effect for the cell sample remains similar with and without WASSR correction.

T_2 times for samples

The transverse magnetisation relaxation time, T_2, was measured after the CEST protocol for the control and cell samples. T_2 values for the ten day sample were found to be within error of the control values (see Table 6.2). Six day T_2 values were not within error of the control tube, but were close (within 20%) to the control T_2 time.

Sample	T_2 value [ms]
Control cell media	0.27 ± 0.01
Cells after six days incubation	0.22 ± 0.02
Cells after ten days incubation	0.25 ± 0.07

Table 6.2: **Spectroscopic T_2 values for cell experiments.** T_2 values were recorded using MRS, to determine any differences between cell samples and the control sample. The ten day sample was within error of the control sample, with the six day sample differing by 0.05 ms.

6.4.4 SVM applied to CEST data: ten day incubation samples

The MTR asymmetry spectra for each of the 26 ROIs distributed over the CEST voxel (13 for the cell sample and 13 for the control sample) were used in a SVM analysis; features were extracted from the spectra as stated in section 6.4.2.

Feature selection and ranking

The FDR test was used to rank individual features based on their ability to discriminate between spectra belonging to the cell sample or control sample. As is clear in Fig. 6.10, a large CEST effect difference between cell and control groups is found near 0 ppm and the FDR values for features in this region reinforce this observation; FDR values are listed in Table 6.3. The highest ranking value is the integral between 0 and 1 ppm (FDR = 7.5), with the distribution measures of variance and skewness having very poor discrimination ability (FDR = 0). Areas of interest for APT score relatively highly (FDR of integral between 3 and 4 ppm = 1.2) as does the amine resonance region (FDR of integral between 2 and 3 ppm = 1.1). Integral features appear particularly reliable, with the FDR integral value around frequencies of interest having a higher value than FDR single frequency values themselves, in all but one case (the FDR value of 1.9 ppm is higher than the integral value between 1 and 2 ppm,

FDR value	*Feature*
7.4905	Integral 0 – 1 ppm
5.2965	0.3 ppm
4.0466	0.6 ppm
3.7434	Mean
1.2441	Integral 3 – 4 ppm
1.2164	Integral 0.5 – 1.5 ppm
1.0625	Integral 2 – 3 ppm
0.95	2.75 ppm
0.8553	3.5 ppm
0.6763	Kurtosis
0.0526	1.9 ppm
0.0273	Integral 1 – 2 ppm
0	Variance
0	Skewness

Table 6.3: **Discriminatory power of ten day cell CEST features.** The FDR test is used to rank discriminatory features from the CEST asymmetry curves for the "control" and "sample" group types. Features relating to the large peak near 0 ppm rank highly, but the amine (2.75 ppm) and amide (3.5) weighted features also rank highly in terms of ability to distinguish between groups.

but both have very low scores anyway). The utility of integral measures compared to the single frequency in CEST has been previously noted by [228], being particularly useful in PARACEST studies [282].

Individual features were combined to assess the discriminatory power according to the scatter matrix score, J_1, which ranks the best combination of features as well as individual features, according to differences in the mixture scatter and within–class scatter matrices (see section 6.3.1 for the matrices and J_1 mathematical definition). Table 6.4 shows that the highest J_1 scores are found for single features; the highest score was found for the integral between 0 and 1 ppm, validating the same result

Feature	Feature no.	Feature combo.	J_1 value
3.5 ppm	1		
Integral 3 – 4 ppm	2	{ 9 }	57.6280
2.75 ppm	3	{ 2 }	15.5320
Integral 2 – 3 ppm	4	**{ 1 , 2 }**	**15.6229**
1.9 ppm	5	{ 9 , 11}	1.0620
Integral 1 – 2 ppm	6	{ 2 , 7 }	1.0110
0.6 ppm	7	{ 4, 14 }	1.0009
0.3 ppm	8	{ 12, 13 }	1
Integral 0 – 1 ppm	9	{all features}	1.0050
Integral 0.5 – 1.5 ppm	10		
mean	11		
variance	12		
skewness	13		
kurtosis	14		

Table 6.4: **Scatter matrix score, J_1, to assess combined CEST feature ranking.** The left side of the table shows a numbered list of all features used, with the right side showing selected combinations and the corresponding J_1 value.

found with the FDR test. For two features, values which scored 0 in the FDR test score the minimum value of $J_1 = 1$ in this test. Higher FDR ranked features also score highly when combined compared to lower FDR ranked features, for example, feature 9 and 11 score J_1 = 1.0620 whereas feature 2 and 7 score 1.0110 (see Table 6.4). Increasing the number of features used for group discrimination was found to not necessarily provide a large J_1 score, with a low score of $J_1 = 1.005$ calculated for a feature space comprising of all features combined, compared to a two feature score of 1.011 for the integral between 3 and 4 ppm and 0.6 ppm single frequency.

However, care should be taken when interpreting the exact J_1 values, particularly for features which are related such as the integral of 3 and

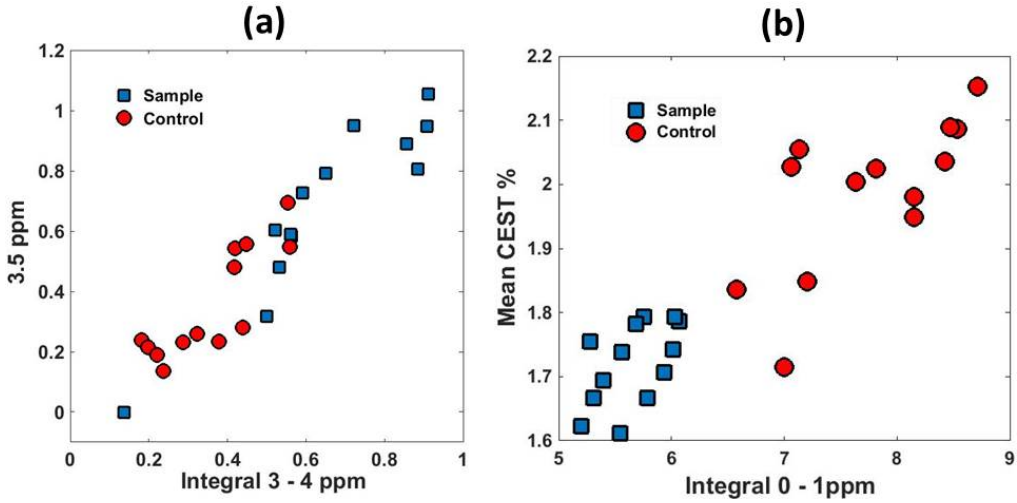


Figure 6.13: Differences in feature space plots with high ranking feature combinations: (a) The integral between 3 and 4 ppm and the single frequency at 3.5 ppm features have a high combined J_1 score with the mean distribution of values for each feature being largely different between the two classes; for example, the control and cell sample values are centred around 0.3 and 0.8 respectively for the 3.5 ppm single frequency feature (a two or three fold difference), hence an larger J_1 score. **(b)** The integral between 0 and 1 ppm and the mean CEST effect features have a relatively lower J_1 score, but visually appear to be easier to separate.

4 ppm and 3.5 ppm single frequency (features 1 and 2, scoring a high J_1 value of 15.6229.). If a high CEST effect is found for one feature, it is likely that the other feature will also exhibit a high CEST effect, since the single frequency values contribute to the integral values based in the same frequency region. This dependence causes the group distributions to become more spread out in feature space, leading to a higher J_1 value. This is well illustrated in Fig 6.13, where the two features' data points are plotted, alongside the combined features of the mean CEST effect and the integral between 0 and 1 ppm.

Fig 6.13 also demonstrates the specific feature value has a large effect on the J_1 score and this should be considered when selecting a classifier method for the feature space. For example, the mean of the two groups in Fig. 6.13(a) are further apart in terms of relative % and thus

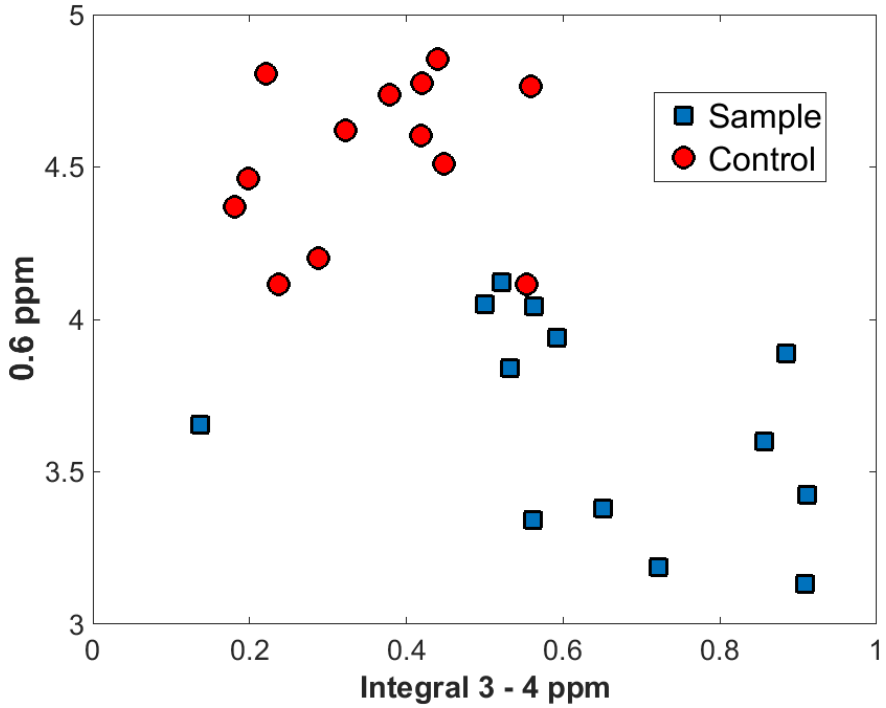


Figure 6.14: SVM raw feature space using two features. From Table. 6.4 and 6.3, the integral between 3 and 4 ppm and the single frequency at 0.6 ppm were chosen as principal features with which to perform SVM classifier analysis.

score a higher J_1 value compared to the distribution in (b), yet this does not guarantee all of the distribution to be easily separable. In fact, it is clear that (b) can be separated by a straight line dividing the sample and control group, whereas in (a), the groups overlap and it is reasonable to assume that a classifier would have a lower discriminatory ability.

I chose two features to form the basis of my SVM analysis, bearing in mind the scores from the FDR and J_1 tests. The features "integral between 3 and 4 ppm" and "0.6 ppm" were chosen since they scored highly particularly in the FDR test, and are related to the 3.5 ppm APT region whose investigation was a goal of this study. These features form the axis of a feature space which is shown in Fig. 6.14.

Although other features scored higher in the FDR test, one should be wary of the physical reason for the large CEST effect near 0 ppm and consider how much can be inferred from the resulting high FDR values

for certain affected features. As will be discussed later in this chapter's discussion and Chapter 7, gradient echo and CEST methods in general suffer from B_0 inhomogeneities, with CEST spectra being particularly susceptible close to 0 ppm. It is difficult to deconvolute the effect of real metabolites and B_0 contributions in the asymmetry curve close to 0 ppm, and therefore I choose to consider features which have been used explicitly in previous CEST studies and ignore features reliant on contributions less than 0.5 ppm; this precludes the use of "Integral of 0 and 1 ppm" and "0.3 ppm". Additionally the mean CEST effect feature is heavily biased by the large CEST effect near 0 ppm and will also not be considered. Excluding these features, the chosen features are the first and second highest ranking FDR features as well as scoring a high "two feature" ranking using J_1.

Classifier selection and evaluation

A range of kernels and associated parameters were investigated as potential classifiers for the groups in my feature space, in particular, a radial basis function (RBF), a linear kernel and a polynomial kernel. Initial evaluation of classifiers assumed all 26 ROIs were training data with which to "train" the classifiers. Feature space plots showing six different classifiers based on the complete sample data sets are shown in Fig. 6.15, with the boundaries between groups and corresponding support vectors clearly shown. The convention when specifying kernel parameters for RBF is RBF(σ) where sigma is a parameter specifying the decay rate of the kernel towards zero. For polynomial kernels, poly(n, β), n and β are user defined parameters for the kernel function of the form $(x^T y + \beta)^n$. Parameters were optimised to reduce the number of misclassified points, with the plotted graphs representing several optimal parameter selections.

The classifier error based on the full training data set was recorded for each classifier as well as the number of support vectors required, as shown in Table 6.5. All classifiers had a predictably low training error since the classifiers were trained using the same data. A maximum number of 5 support vectors were needed for the RBF, linear and polynomial

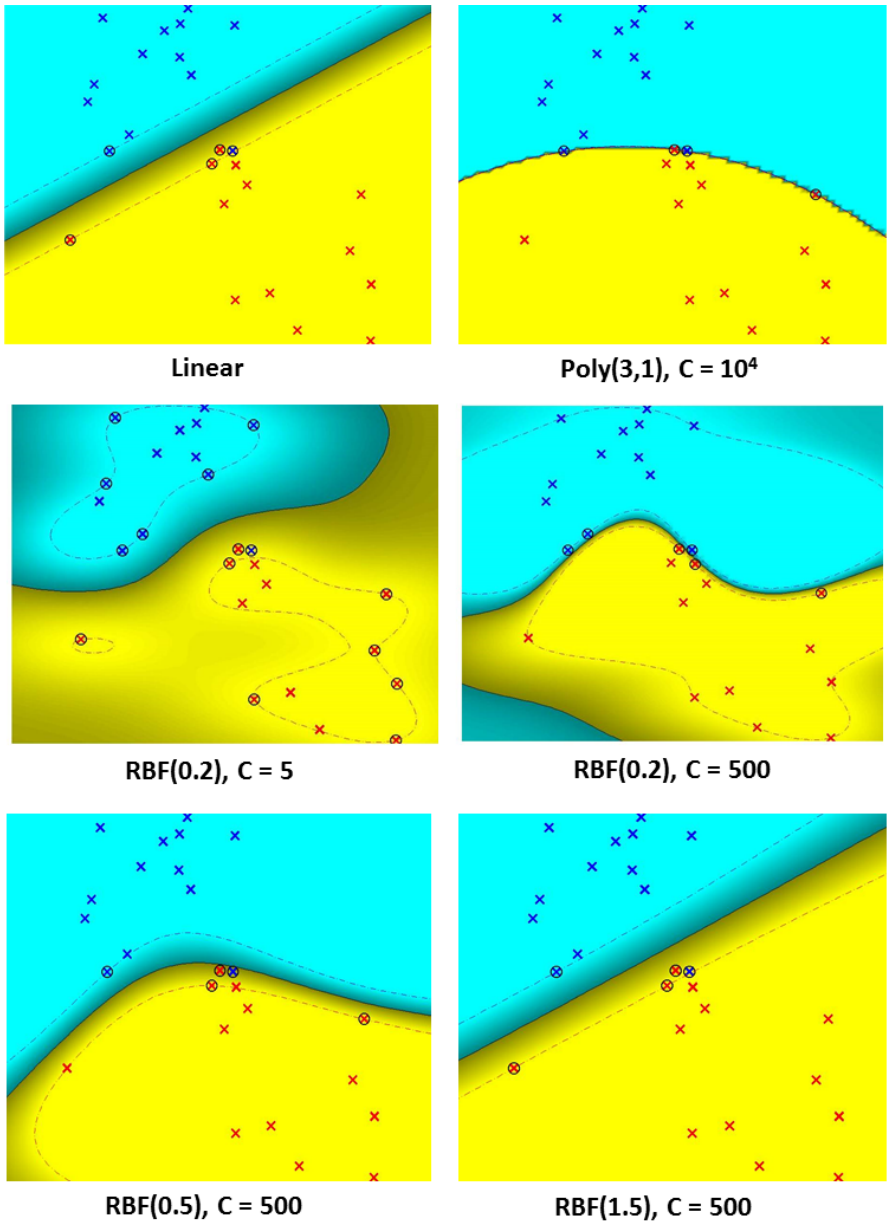


Figure 6.15: SVM feature plots with various kernels. Linear, radial basis function and polynomial kernels are used to provide classifiers which delineate group feature space in varying ways depending on input parameters. The number of support vectors (encircled points) also increases depending on complexity of the margin regions. Red data points indicate the ten day cell sample, blue data points indicate the control medium sample and dotted lines indicate the margins.

classifiers with appropriate parameters; for small σ in RBF kernels, a larger number of support vectors were needed due less stringent margin

SVM parameters	C	Training error	No. support vectors
RBF(0.2)	5	3.85 %	16
RBF(0.2)	500	0 %	13
RBF(0.5)	500	0 %	6
RBF(1.5)	500	3.85 %	5
Poly(3,1)	10×10^4	0 %	4
Linear	100	3.85 %	5

Table 6.5: **Classifier summary for full training data sets.** All 26 ROIs were used when computing the training error, which calculates the total percentage of misclassifications over both groups. All classifiers showed a low training error for all classifiers. The number of support vectors is the minimum number of points needed to construct the margins, with a lower C value requiring a larger number of support vectors particularly for the RBF kernels.

restrictions necessitated by the σ value.

SVM parameters	Sensitivity	Specificity
RBF(0.2, C = 5)	100 %	92.3 %
RBF(0.2, C = 500)	69.2 %	76.9 %
RBF(0.5, C = 500)	75 % *	83.3 % *
RBF(1.5, C = 500)	92.3 %	92.3 % %
Poly(3,1, C = 10^4)	84.6 %	84.6 %
Linear(C = 100)	100 %	92.3 %

Table 6.6: **Classifier evaluation using LOO method.** Specificity and sensitivity values are computed using the LOO method over all 26 sample points. The linear and RBF(1.5) score highly in terms of ability to discriminate between the two groups. * indicates that one of the 13 samples used in LOO process did not converge and was not included in subsequent calculations.

For a more rigorous classifier evaluation, a leave–one–out method (described in the theory section of this chapter) was used to evaluate the classifiers' discriminatory ability, using 25 ROIs as a training set and the "left out" ROI as a test data point, iterating over all 26 ROIs. Misclassifications were quantified in Table 6.6 using the specificity and sensitivity parameters. The best performing RBF kernels used both low σ and C or high σ and C values, with the best RBF classifier being RBF(0.2, C = 5) which showed 100 % sensitivity and 92.3 % specificity. The linear classifier with C = 100 showed identical specificity and sensitivity as the best performing RBF kernel, whilst the optimal polynomial classifiers scored 84.6 % sensitivity and specificity.

A comparision between the SVM linear classifier and the individual features as classifiers was examined using a receiver operating characteristic (ROC) curve (see Fig. 6.16). A linear classifier was chosen as the SVM classifier to compare with, since it had the joint highest specificity and sensitivity values. The area under the curve (AUC) values for the ROC plot were: $AUC_{0.6}$ = 0.99, $AUC_{\int 3-4}$ = 0.87, AUC_{SVM} = 0.99. Both linear SVM and 0.6 ppm SF classifiers showed excellent degrees of sensitivity, with misclassification occurring once and twice respectively over all LOO iterations.

6.5 Discussion

The aim of this study was to investigate the molecular composition of the 3–D cell model with APT CEST, analysing the CEST signal contributions of the cell and control samples with a machine learning approach, to evaluate possible differences between a cell and control sample. Two separate time points in the cell incubation process were imaged with CEST, at six and ten days.

6.5.1 CEST experiment results

The main goal of the CEST acquisitions was to provide MTR asymetry curves to apply the SVM method on, with the aim of classifying data into

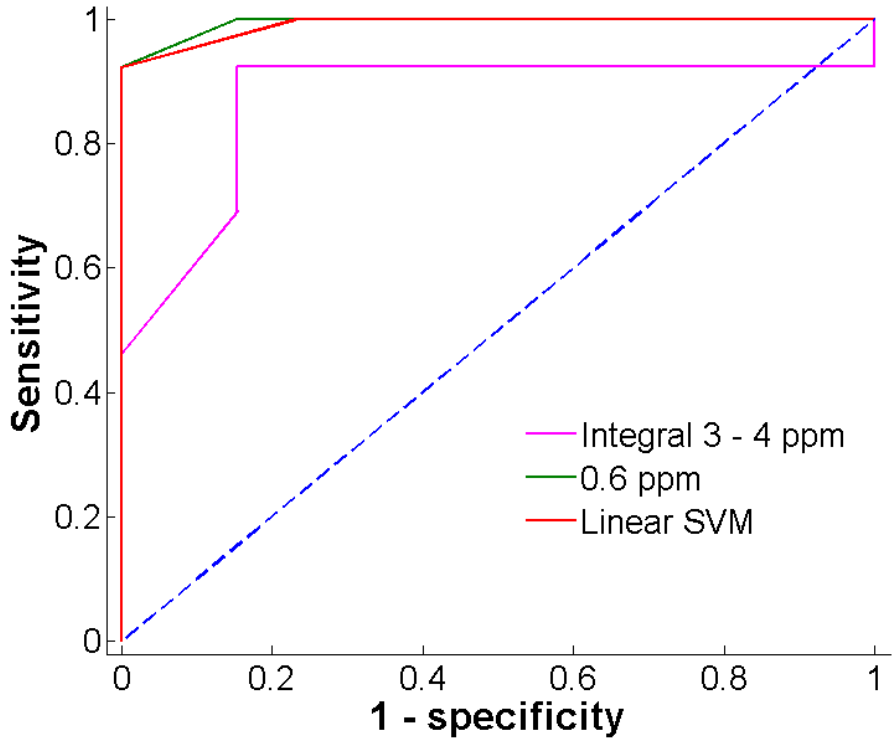


Figure 6.16: Receiver operating characteristic (ROC) curve to evalaute the benefit of combined feature SVM analysis. Sensitivity and specificity values for a range of 20 threshold values for the single feature classifiers, 0.6 ppm value and integral value between 3 and 4 ppm, are compared to the linear classifier computed from the SVM method using an ROC curve. The linear SVM classifier and the 0.6 ppm classifier are comparable in terms of discriminatory power, with the integral classifier being less appropriate to distinguish between groups. AUC values: linear SVM = 0.99, 0.6 ppm SF = 0.99, integral between 3 and 4 ppm = 0.87.

two classes based on features from the whole spectra. Single feature or single frequency group comparisons were not the focus of this work and consequently statistical group difference analyses are not presented. Although our CEST results would imply that there is a difference between the six and ten day time points (spectra in Fig. 6.8 and Fig. 6.10 being clearly different), one should be careful with this conclusion for a number of reasons. Firstly, although the Z–spectra appears the correct shape and size compared to previous CEST results, the level of detail (apparent on both sides of Z–spectra in Fig. 6.10 for both control and cell sample) is

not present, compared to the ten day sample. The lineshapes were measured to be greatly different ($\sim$ 20 Hz compared to $\sim$ 150 Hz) and this is shown by a heterogeneous B_0 map. These differences due to the partial volume air bubble effect would act to reduce the CEST effect; by not allowing optimal frequency excitation this would explain the reduced effect particularly less than 1 ppm for control and cell sample.

However, the asymmetry curves do still show near identical CEST effects at 1.5 ppm which is far enough away from 0 ppm to be less influenced by direct saturation from the water peak. A more accurate conclusion could be drawn from repeating the six day sample and obtaining another CEST spectrum without air bubble issues to confirm this. The T_2 measurements were also important to rule out any large changes which could affect the CEST effect. There are small variations between the T_2 times measured for both the six and ten day cell samples, but importantly the ten day cell sample's T_2 value was within error of the control T_2 value. It is unlikely that the T_2 changes played a large role in the generation of the CEST effects observed.

Another pertinent issue is the confidence in assigning a molecular CEST effect to contributions less than 1 ppm. Direct water saturation of the water peak causes a rapidly changing CEST spectra near 0 ppm and small shifts in the Z–spectra can cause large erroneous MTR asymmetry effects which are not due to the molecular exchanges in the sample [237]. Fig. 6.12 showed the importance of controlling for these effects by using a WASSR correction. A large reduction in the CEST effect was shown for the control sample when the correction was applied. The cell sample's CEST effect less than 1 ppm was not significantly changed by the WASSR correction and there is good evidence in the literature (see Table 5.1) to support a molecular cause for the CEST effect less than 1 ppm. The Van Zijl group showed glycogen contributes at the 0.5 – 1.5 ppm range [222], and more recently lactate contributions at 0.4 ppm in the CEST spectra have been shown to be positively correlated with resonances observed in multiple quantum filtered MRS [283].

Ideally, a large number of separate CEST experiments would have been run with a CEST spectrum being obtained from each sample, thus pro-

viding sufficient n for both statistical CEST and machine learning analysis. However, as previously discussed, the cell sample sizes were limited due to the novel incubation procedure and this approach was not possible. Dividing the sample into significantly smaller quantities to increase the number of possible scans is also limited by the need for a large voxel to provide enough SNR for acquisition, as well as for tuning and matching; this is an issue on the Varian 9.4 T in which the sample size must contain enough ^{1}H to provide sufficient signal, otherwise calibration cannot take place. However, the set–up appeared appropriate for both the CEST imaging and subsequent analysis. B_0 profiles were relatively homogeneous in the absence of air bubbles and this allowed the confident assignment of the CEST effect to molecular exchange rather than field differences. A recent study performed pattern recognition using MRI data and correlated these measures with tumour biopsies taken from the same site and using multiple ROIs, which reinforces the experimental method [284].

6.5.2 SVM analysis results

A supervised SVM method was applied to the CEST data from a ten day incubated cell sample and a control sample, providing a linear group classifier with a high degree of sensitivity and specificity. A range of kernels were investigated as classifiers for the two groups, with a linear classifier (C = 100) providing the best class sensitivity and specificity in a LOO evaluation (sensitivity = 100 %, specificity = 92.3 %). The data showed good separation between data points from the control and cell samples, demonstrated by the high sensitivity and specificity. Indeed, the ROC curve showed an identical AUC for both the linear SVM and the best feature (0.6 ppm single frequency), and a greater AUC than the integral between 3 and 4 ppm feature. With a larger sample size it is very likely that the performance of the SVM for classification will increase, whilst the single feature classifier would decrease as the number of overlapping data points increases.

The linear classifier, depicted in Fig. 6.14, suggests that characteristic Z–

spectra from a medulloblastoma cell sample will tend to have a reduced CEST effect at 0.6 ppm and an increased integral CEST effect between 3 and 4 ppm, compared with a control sample. Several APT CEST studies have observed increased CEST effects in this region for cancer and the classifier results reinforce this observation [226]. The reduction at 0.6 ppm could be explained by the uptake and processing of the proteins and metabolites contributing at that part of the CEST spectrum, which decrease in concentration as the cells grow. Metabolites suggested to contribute at 0.6 ppm in the CEST spectra have included myoinositol [220], known to be present in the cell media control and shown to be essential for malignant cellular growth in tissue culture [285].

6.5.3 Limitations and future work

The presented CEST cell method has demonstrated a protocol for investigating molecular changes in cancer cells lines. Although group differences have been shown to be distinguishable using a machine learning approach, understanding exactly which molecules contribute to the CEST spectra would be beneficial. Due to both the limited number of cell samples and the time pressures on the scanning protocol, investigation in this direction was limited. The impact of this work could be readily extended by including either MS and MRS modalities to quantify molecules in cell samples, and correlating with CEST signals. In particular, this approach would conclusively determine a difference between six and ten day timepoints and highlight the sensitivity of CEST to these molecular changes.

With CEST, the unambiguous assignment of CEST moieties to particular resonant frequencies is difficult; whilst a change at a given ppm frequency is clear, what causes the change may be less so. Important *in vitro* work by Lee and colleagues [286] has demonstrated the CEST spectrum overlap between amide and hydroxyl protons, which convolutes the observed CEST effect. This is also likely to affect *in vivo* CEST studies, where metabolites such as myoinositol, creatine and glucose coexist. One can optimise parameters for a particular metabolite based on the

exchange rate and predicted resonant frequency, but the observed CEST effect may consist of additional metabolite contributions.

Additional problems for APT CEST are contributions from the NOE. The latest CEST literature is still unclear on the origin of the CEST effect at + 3.5 ppm, with the most recent work by Zaiss et al. [287] supporting the theory that NOE effects occur on either side of the water resonance and affect the APT signal [280]. This limits the reliability of assignment of APT contrast to real amide proton transfer effects, due to concomitant NOE contributions. In our work, the influence of the NOE is unclear and further experiments to quantify this effect, with alternative CEST metrics [287], would be beneficial.

A key feature of CEST which differentiates the modality from MRS is that spatial information is obtainable, and signals can be localised to a specific region in a sample. This benefit was not readily utilised in our experiment, in that the samples used were assumed to be fairly homogeneous. A simple extension to the cell experiment would be to prepare a sample which contained a gradient of cell density, and to perform CEST scans on a number of slices of increasing cell density. The CEST effect could then be correlated with cell number and molecular contributions to the CEST effect could be observed more closely. It would also be beneficial to measure the pH in our experiments, by reducing the CEST scan time to allow for a pH measurement. It has been shown that the pH can affect the CEST effect for APT CEST [244], and it would be interesting to compare quantitative pH values to the CEST data.

CHAPTER 7

Discussion

7.1 Summary

The application of new MRI techniques to provide molecular imaging information has been the focus of this work, which utilised both exogenous and endogenous contrast mechanisms to this end.

7.2 Exogenous contrast results

Few fluorine studies consider the factors affecting sensitivity in detail, with the work in Chapter 3 representing a rigorous analysis of ^{19}F MR experimental sensitivity. Indeed, comparison between the detection limits stated for different studies is inherently difficult where the experimental sensitivity of set–ups are different. It is hoped that study of the analytic components in the sensitivity equations will encourage sensor optimisation based on the goal of enhancing sensitivity. Studies typically plot the SNR of various fluorine sensor concentrations to determine minimum detectable limits [126], yet the method in Chapter 3 could reduce the number of experiments needed for sensitivity estimates. Using cheap and easily obtainable reference compounds, detection limits were estimated and extrapolation to new compounds is straightforward.

The development of the novel ^{19}F MMP sensor is one of a small number of enzymatic probes in the literature which is based on a PRE mecha-

nism. The mechanism was able to detect molecular changes after the addition of MMPs, with a 60–fold increase in T_1 times and a two to three–fold decrease in the fluorine lineshape. The detection limit of this probe on a pre–clinical scanner was estimated, using a home–made surface coil. Extrapolation for detection limits of the MMP probe was possible through the theoretical framework described in Chapter 3. The results agreed with the fluorine literature which puts the detection limit $\gtrsim 1$ mM. For our sensor, this limit prevents application to a pre–clinical mouse model, due to the high concentration needed to achieve this limit for a small volume. The fluorine sensor would greatly benefit from an increased number of fluorine atoms per molecule to decrease the minimum concentration required.

7.3 Endogenous contrast results

Few studies in the CEST literature have focussed on purely cell based experiments. In this work, the CEST effect between a control and cancer cell sample was found to have several differences at different sections of the CEST spectrum. By considering several different features in the MTR asymmetry curve, a machine learning approach benefited in its ability to discriminate between the two classes; the discriminative performance of the SVM was better than solely using a single APT measure. The results of the machine learning analysis highlight the potential benefit of considering several contributing CEST frequencies to classify CEST data into groups.

7.4 Future work

The work presented in this thesis has opened a number of potential areas of future research, building on the demonstrated results.

Hyperpolarisation

One possible solution to the problem of sensitivity for fluorine could potentially be found in the field of hyperpolarisation. In theory, flu-

orine nuclei can be hyperpolarised ([288, 289]), however the long T_1 of fluorine, coupled with the signal loss from hyperpolarisation techniques mean ^{19}F hyperpolarised *in vivo* studies are a long way off. A

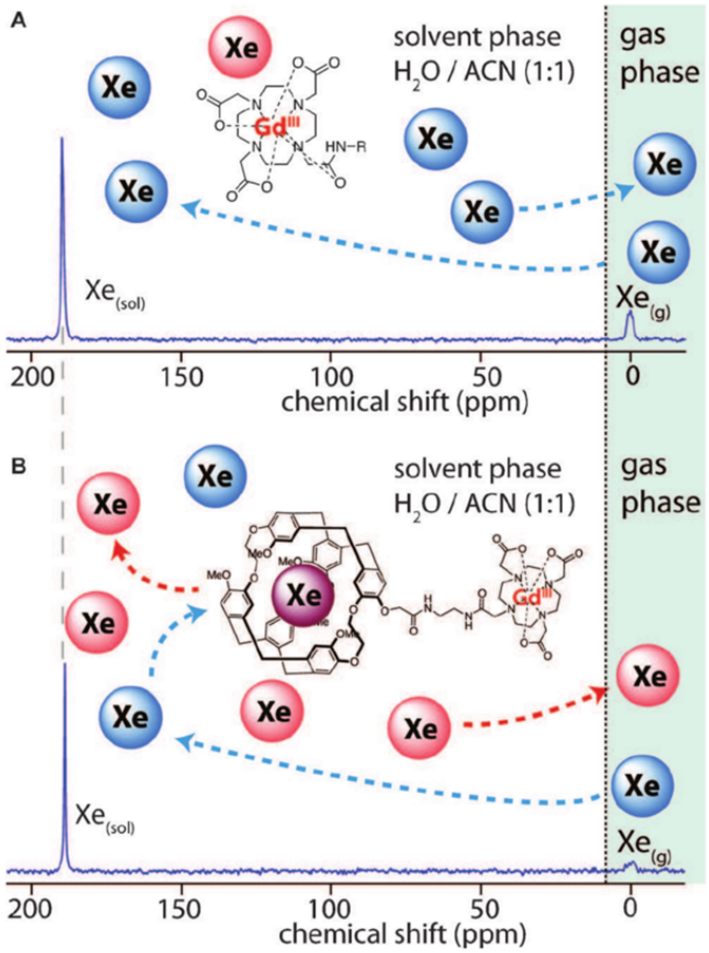


Figure 7.1: Hyperpolarized demonstration of enzymatic probe principle from Zamberlan et al. [290]. **(A)** A solution of gadolinium and xenon produces a small signal in the gas phase of the xenon spectrum. **(B)** When cryptophane is introduced into this solution, the exchanging xenon contributes a broader and flatter signal than in the previous situation. If the proximity of the gadolinium could be increased, for example by a cleavable linker, then a switching between the two situations would be observed.

more promising extension of our sensor is to use the PRE effect and substrate cleavage principle as applied to current hyperpolarised probes,

for whom the sensitivity benefit and application *in vitro* is well established. Such a method has been proposed, in a proof–of–concept work by Zamberlan and colleagues which used cryptophane cages, hyperpolarised xenon and chelated gadolinium to provide a measureable NMR read–out based on the local xenon environment [290]. Exchanging xenon interacts with the cryptophane cage, tethered to the gadolinium, and produces a flattened signal in the gas phase of the xenon spectra; this signal is smaller than a gas phase signal from a solution of gadolinium and xenon, shown in Fig. 7.1. The authors speculate that if an enzymatic substrate could link the cage and gadolinium, upon cleavage a change in the gas phase would occur allowing enzymatic detection.

Fluorine relaxation under paramagnetic influence

To maximise the potential of the MMP fluorine probe, additions such as PEG linkers to increase solubility and more fluorine atoms to increase sensitivity are likely to be required, each of which may change the Gd–^{19}F distance and rotational dynamics. In this work, access to high field T_2 measurements, additional field strengths for relaxometry studies and large quantities of the probes was limited, reducing the need for precise theoretical analysis. However, future theoretical simulations of the PRE effect on the fluorine atoms could prove useful for optimising the probe. This could allow predictions of the reduction in T_1 from the gadolinium depending on the Gd–^{19}F distance, and could be coupled with the theoretical sensitivity model from Chapter 3.

The relaxation enhancement for nuclear spins attached in a ligand bound to a paramagnetic metal ion depends predominantly upon dipole–dipole (DD) interactions between the nuclear and electron spins, and Curie relaxation [291]; compared to gadolinium chelate and water interactions which are dominated by dipole–dipole and scalar coupling interactions. The precise calculations for the MMP probe are complicated, and are not adequately described by the Solomon–Bloembergen–Redfield theory. The situation for a probe, with the fluorine source around 5 Å from the gadolinium chelate has been described by Chalmers et al. [197], giving a quantitative formulae with which to calculate T_1 and T_2 (assuming

other parameters are known):

$$r_1 = \frac{2}{15}\left(\frac{\mu_0}{4\pi}\right)^2 \frac{\gamma_F^2 \mu_{\text{eff}}^2}{r^6}\left(\frac{7\tau_{R+e}}{1+\omega_e^2} + \frac{3\tau_{r+e}}{1+\omega_F}\right) + \frac{2}{5}\left(\frac{\mu_0}{4\pi}\right)^2 \frac{\omega_F^2 \mu_{eff}^4}{(3kT)^2 r^6}\left(\frac{3\tau_{\text{R}}}{1+\omega_F^2\tau_R^2}\right) \tag{7.4.1}$$

$$r_2 = \frac{1}{15}\left(\frac{\mu_0}{4\pi}\right)^2 \frac{\gamma_F^2 \mu_{\text{eff}}^2}{r^6}\left(4\tau_{R+e} + \frac{3\tau_{\text{R}+e}}{1+\omega_e^2\tau_{R+e}^2} + \frac{13\tau_{r+e}}{1+\omega_F^2\tau_{R+e}^2}\right) + \frac{1}{5}\left(\frac{\mu_0}{4\pi}\right)^2 \frac{\omega_F^2 \mu_{eff}^4}{(3k_BT)^2 r^6}\left(4\tau_R + \frac{3\tau_R}{1+\omega_F^2\tau_R^2}\right) \tag{7.4.2}$$

Here τ_{R+e} is the correlation time for the contribution of the electron and nuclear dipole ($\tau_{R+e} = \tau_R^{-1} + T_{1e}^{-1}$), γ_F is the gyromagnetic ratio for the fluorine atom, ω_F is the resonant frequency of fluorine, ω_e is the electron resonant frequency and μ_{eff} is the effective magnetic moment, defined as $\mu_{\text{eff}} = g_e^2 \mu_B^2 S$, where μ_B is Bohr's magneton (μ_B = 9.27 $\times$ 10^{-24} J T^{-1}). To use these equations, one can determine r through measuring the relaxation times at a series of different field strengths and solving for r [198]. Determining r would give more information on the coiling of our probe, and help inform decisions to reduce or increase the protein linker flexibility.

CEST spectral investigations: theoretical models and MRS

The CEST machine learning study would benefit from the introduction of MRS to validate and investigate specific causes on contrast in the *in vitro* spectrum. Several theoretical approaches have attempted to study the APT contrast, since it is unclear what contributes exactly to APT signals *in vivo*, and studies have shown that NOE changes are equally as important to quantify 3.5 ppm changes [259]. Groups have developed amine/amide concentration independent detection (AACID) [281] and APT* [292] methods which look at an extension of the simple MTR asymmetry analysis. For quantifying the NOE, which is known to affect the APT signal,

$$NOE^* = \left(\frac{S(-5.0\text{ppm}) - (-2.0\text{ppm})}{2} - S(-3.5ppm)\right)/S_0 \quad . \tag{7.4.3}$$

The APT signal is given separately,

$$\mathrm{APT}^{*} = \left(\frac{S(3.0\ \mathrm{ppm} + S(4.2\ \mathrm{ppm})}{2} - S(3.6\ \mathrm{ppm}) \right) / S_0 \quad . \qquad (7.4.4)$$

and the two can be used to quantify the effects around 3.5 ppm. Using this method requires a greater sampling of the APT regions of interest to ensure appropriate fitting but could help identify group differences. Validation of the new CEST metric would benefit through use of MRS. Recent publications have correlated MRS and CEST *in vivo* to highlight correlation between pH measurement methods [293]. Using MRS in a cell approach would increase the molecular imaging capability of the CEST technique, identifying exact molecular presence in MRS and assigning molecules to sections of the Z–spectrum.

7.5 Concluding remarks

Two molecular MR imaging methods have been demonstrated to provide useful biochemical information in their application *in vitro*: a fluorine MMP sensor was shown to detect MMP activity; a CEST method used machine learning to classify *in vitro* data in a cancer cell line and control sample. These techniques are not mutually exclusive, with fluorine CEST having been demonstrated previously [294]. A simple theoretical method to determine a fluorine experiment's sensitivity was also presented which could allow future optimisation of ^{19}F MR experiments.

Glossary

1,2,3–D	One,two or three dimensional
5–FC	5–fluorocytosine
5–FU	5–fluorouracil
6FAA	3,5–Bis(trifluoromethyl)benzylamine
Acq.	Acquisition
ADAM	Disintegrin and metalloproteinase
ADAMT	Disintegrin and metalloproteinase with thrombospondin motif
APT	Amide proton transfer
A.U.	Arbitrary units
AUC	Area under the curve
BC	Bloch–McConnell
bSSFP	Balanced steady–state free precession
CA	Contrast agent
CAT	CEST analysis software tool
CD	Cytosine deaminase
CEST	Chemical exchange saturation transfer
CKD	Chronic kidney disease
CSA	Chemical shift anisotropy
CW	Continuous wave
DCE	Dynamic contrast enhanced
DFT	Density functional theory
DOTA	tetra–azacyclo–dodecane–tetra–acetic acid
DS	Direct saturation
DTPA	Diethylene–tetra–amine–penta–acetic acid
ECM	Extracellular matrix

EM	Electromagnetic
ETL	Echo train length
FDR	Fisher Discriminant Ratio
FID	Free induction decay
FISP	Fast imaging with steady–state precession
FLASH	Fast low angle shot
FN	False negative
FOV	Field of view
FP	False positive
FREDOM	Fluorocarbon relaxometry using echo planar imaging for dynamic oxygen mapping
FRET	Föerster resonance exchange transfer
FSEMS	Fast spin echo multi slice
FT	Fourier transform
FWHM	Full width half maximum
GE	Gradient echo
GEMS	Gradient echo multi slice
GRASE	Gradient and spin echo
GSH	Glutathione
GST	Glutathione transferases
HFB	Hexafluorobenzene
IS	Inner sphere
LOO	Leave–one–out
MMP	Matrix metalloproteinase
MMPI	Matrix metalloproteinase inhibitor
MR	Magnetic resonance
MRA	Magnetic resonance angiography
MRI	Magnetic resonance imaging
MRS	Magnetic resonance spectroscopy
MT	Magnetisation transfer
MTR	Magnetisation transfer ratio
MT–MMP	Membrane bound matrix metalloproteinase
NIR	Near–infrared
NMR	Nuclear Magnetic Resonance
NOE	Nuclear overhauser effect

NSF	Nephrogenic systemic fibrosis
OS	Outer sphere
PARACEST	Paramagnetic chemical exchange saturation transfer
PBS	Phosphate buffered solution
PERFECTA	Tetra(perfluorotertbutyl)pentaerythritol
PET	Positron emission tomography
PFC	Perfluorocarbon
PFCE	Perfluorocrown ether
PFD	Perfluorodecalin
PFN	Perfluorononane
PFOB	Perfluorooctylbromide
PRE	Paramagnetic relaxation enhancement
PTR	Pure proton exchange effect
QM	Quantum mechanics
RARE	Rapid imaging with refocussed pulses
RBF	Radial basis function
ROC	Receiver operating characteristic
ROI	Region of interest
R.F.	Radio frequency
SE	Spin echo
SF	Single frequency
SNR	Signal–to–noise ratio
SPIO	Superparamagnetic iron oxide
SVM	Support vector machine
TFA	Trifluoroacetic acid
TIMP	Tissue inhibitor of metalloproteinase
TN	True negative
TMS	Tetramethylsilane
TOF	Time–of–flight
TP	True positive
WASSR	Water shift saturation referencing

References

[1] F. Levin. *An Introduction to Quantum Theory*. Cambridge University Press, 2002.

[2] R. K. Harris, E. D. Becker, S. M. Cabral de Menezes, R. Goodfellow, and P. Granger. NMR nomenclature: nuclear spin properties and conventions for chemical shifts. IUPAC Recommendations 2001. International Union of Pure and Applied Chemistry. Physical Chemistry Division. Commission on Molecular Structure and Spectroscopy. *Magn. Reson. Chem.*, 40(7):489–505, 2002.

[3] S. A. Huettel, A. W. Song, and G. McCarthy. *Functional magnetic resonance imaging*. Sinauer Associates Sunderland, 2004.

[4] Y.-T. Kuo, A. H. Herlihy, P.-W. So, K. K. Bhakoo, and J. D. Bell. In vivo measurements of T1 relaxation times in mouse brain associated with different modes of systemic administration of manganese chloride. *J. Magn. Reson. Imaging*, 21(4):334–339, 2005.

[5] L. Schroeder and C. Faber. *In vivo NMR Imaging: Methods and Protocols*. Humana Press, 2011.

[6] D. W. McRobbie, E. A. Moore, M. J. Graves, and M. R. Prince. *MRI from Picture to Proton*. Cambridge University Press, 2007.

[7] S. Ljunggren. A simple graphical representation of Fourier-based imaging methods. *J Magn. Reson.*, 54(2):338–343, 1983.

[8] S. Aime, M. Fasano, and E. Terreno. Lanthanide(III) chelates for NMR biomedical applications. *Chem. Soc. Rev.*, 27:19–29, 1998.

[9] E. Toth, L. Helm, and A. Merbach. Relaxivity of MRI contrast agents. In *Contrast agents I*, volume 221 of *Topics in current chemistry*, pages 61–101. 2002.

[10] N. Bloembergen, E. M. Purcell, and R. V. Pound. Relaxation Effects in Nuclear Magnetic Resonance Absorption. *Phys. Rev.*, 73:679–712, 1948.

[11] I. Solomon. Relaxation Processes in a System of Two Spins. *Phys. Rev.*, 99:559–565, 1955.

[12] I. Solomon and N. Bloembergen. Nuclear Magnetic Interactions in the HF Molecule. *J. Chem. Phys.*, 25(2):261–266, 1956.

[13] G. Holland, P. Bottomley, and W. Hinshaw. F-19 magnetic-resonance imaging. *J Magn. Reson.*, 28(1):133–136, 1977.

[14] P. Blümler, B. Blümich, R. E. Botto, and E. Fukushima. *Spatially resolved magnetic resonance: methods, materials, medicine, biology, rheology, geology, ecology, hardware*. John Wiley & Sons, 2008.

[15] J. L. Major and T. J. Meade. Bioresponsive, Cell-Penetrating, and Multimeric MR Contrast Agents. *Accounts Chem. Res.*, 42(7):893–903, 2009.

[16] L. M. De León-Rodríguez, A. F. Martins, M. C. Pinho, N. M. Rofsky, and A. D. Sherry. Basic MR relaxation mechanisms and contrast agent design. *J. Magn. Reson. Imaging*, 42(3):545–565, 2015.

[17] D. Artemov, N. Mori, R. Ravi, and Z. M. Bhujwalla. Magnetic Resonance Molecular Imaging of the HER-2/neu Receptor. *Cancer Res.*, 63(11):2723–2727, 2003.

[18] C. Hayes, A. Padhani, and M. Leach. Assessing changes in tumour vascular function using dynamic contrast-enhanced magnetic resonance imaging. *NMR Biomed.*, 15(2):154–163, 2002.

[19] V. Wedeen, R. Meuli, R. Edelman, S. Geller, L. Frank, T. Brady, and B. Rosen. Projective imaging of pulsatile flow with magnetic-resonance. *Science*, 230(4728):946–948, 1985.

[20] G. J. Strijkers, W. J. M. Mulder, G. A. F. van Tilborg, and K. Nicolay. MRI contrast agents: Current status and future perspectives. *Anticancer Agents Med. Chem.*, 7(3):291–305, 2007.

[21] J. S. Mann. Stability of gadolinium complexes in vitro and in vivo. *J. Comput. Assist. Tomogr.*, 17:19–23, 1993.

[22] T. Grobner. Gadolinium–a specific trigger for the development of nephrogenic fibrosing dermopathy and nephrogenic systemic fibrosis? *Nephrol. Dial. Transpl.*, 21(4):1104–1108, 2006.

[23] R. J. McDonald, J. S. McDonald, D. F. Kallmes, M. E. Jentoft, D. L. Murray, K. R. Thielen, E. E. Williamson, and L. J. Eckel. Intracranial Gadolinium Deposition after Contrast-enhanced MR Imaging. *Radiology*, 275(3):772–782, 2015.

[24] United states renal data system, 2014 usrds annual data report: An overview of the epidemiology of kidney disease in the united states, national institutes of health, national institute of diabetes, digestive and kidney diseases, 2014.

[25] E. M. Gale, I. P. Atanasova, F. Blasi, I. Ay, and P. Caravan. A Manganese Alternative to Gadolinium for MRI Contrast. *J. Am. Chem. Soc.*, 137(49):15548–57, 2015.

[26] D. L. Thorek, A. K. Chen, J. Czupryna, and A. Tsourkas. Superparamagnetic Iron Oxide Nanoparticle Probes for Molecular Imaging. *Ann. Biomed. Eng.*, 34(1):23–38, 2006.

[27] C. F. G. C. Geraldes and S. Laurent. Classification and basic properties of contrast agents for magnetic resonance imaging. *Contrast Media Mol. I.*, 4(1):1–23, 2009.

[28] M. G. Harisinghani, J. Barentsz, P. F. Hahn, W. M. Deserno, S. Tabatabaei, C. H. van de Kaa, J. de la Rosette, and R. Weissleder. Noninvasive Detection of Clinically Occult Lymph-Node Metastases in Prostate Cancer. *N. Engl. J. Med.*, 348(25):2491–2499, 2003.

[29] Y.-X. J. Wang, S. M. Hussain, and G. P. Krestin. Superparamagnetic iron oxide contrast agents: physicochemical characteristics

and applications in MR imaging. *Eur. Radiol.*, 11(11):2319–2331, 2001.

[30] R. Weissleder, D. Stark, B. Engelstad, B. Bacon, C. Compton, D. White, P. Jacobs, and J. Lewis. Superparamagnetic iron oxide: pharmacokinetics and toxicity. *Am. J. Roentgenol.*, 152(1):167–173, 1989.

[31] S. C. Berman, C. Galpoththawela, A. A. Gilad, J. W. M. Bulte, and P. Walczak. Long-term MR cell tracking of neural stem cells grafted in immunocompetent versus immunodeficient mice reveals distinct differences in contrast between live and dead cells. *Magn. Reson. Med.*, 65(2):564–574, 2011.

[32] B. Zhou, D. Li, J. Qian, Z. Li, P. Pang, and H. Shan. MR tracking of SPIO-labeled mesenchymal stem cells in rats with liver fibrosis could not monitor the cells accurately. *Contrast Media Mol. I.*, 10 (6):473–480, 2015.

[33] E. J. Van Den Bos, T. Baks, A. D. Moelker, W. Kerver, R.-J. van Geuns, W. J. van der Giessen, D. J. Duncker, and P. A. Wielopolski. Magnetic resonance imaging of haemorrhage within reperfused myocardial infarcts: possible interference with iron oxide-labelled cell tracking? *Eur. Heart J.*, 27(13):1620–1626, 2006.

[34] T. Massoud and S. Gambhir. Molecular imaging in living subjects: seeing fundamental biological processes in a new light. *Genes Dev.*, 17(5):545–580, 2003.

[35] G. Subramanian, M. Adams, J. Venter, and S. Broder. Implications of the human genome for understanding human biology and medicine. *JAMA.*, 286(18):2296–2307, 2001.

[36] R. Moats, S. Fraser, and T. Meade. A ''smart" magnetic resonance imaging agent that reports on specific enzymatic activity. *Angew. Chem. Int. Edit.*, 36(7):726–728, 1997.

[37] A. Louie, M. Huber, E. Ahrens, U. Rothbacher, R. Moats, R. Jacobs, S. Fraser, and T. Meade. In vivo visualization of gene expression

using magnetic resonance imaging. *Nat. Biotechnol.*, 18(3):321–325, 2000.

[38] D. V. Hingorani, B. Yoo, A. S. Bernstein, and M. D. Pagel. Detecting Enzyme Activities with Exogenous MRI Contrast Agents. *Chem-Eur. J.*, 20(32):9840–9850, 2014.

[39] Y.-T. Chang, C.-M. Cheng, Y.-Z. Su, W.-T. Lee, J.-S. Hsu, G.-C. Liu, T.-L. Cheng, and Y.-M. Wang. Synthesis and Characterization of a New Bioactivated Paramagnetic Gadolinium(III) Complex [Gd(DOTA-FPG)(H2O)] for Tracing Gene Expression. *Bioconjug. Chem.*, 18(6):1716–1727, 2007.

[40] C.-Y. Cao, Y.-Y. Shen, J.-D. Wang, L. Li, and G.-L. Liang. Controlled intracellular self-assembly of gadolinium nanoparticles as smart molecular MR contrast agents. *Sci. Rep.*, 3, 2013.

[41] S. Zhang, P. Winter, K. Wu, and A. Sherry. A novel europium(III)-based MRI contrast agent. *J. Am. Chem. Soc.*, 123(7):1517–1518, 2001.

[42] B. Yoo, V. R. Sheth, C. M. Howison, M. J. K. Douglas, C. T. Pineda, E. A. Maine, A. F. Baker, and M. D. Pagel. Detection of In Vivo Enzyme Activity with CatalyCEST MRI. *Magn. Reson. Med.*, 71(3): 1221–1230, 2014.

[43] D. V. Hingorani, E. A. Randtke, and M. D. Pagel. A CatalyCEST MRI Contrast Agent That Detects the Enzyme-Catalyzed Creation of a Covalent Bond. *J. Am. Chem. Soc.*, 135(17):6396–6398, 2013.

[44] Y. Li, V. R. Sheth, G. Liu, and M. D. Pagel. A self-calibrating PARACEST MRI contrast agent that detects esterase enzyme activity. *Contrast Media Mol. I.*, 6(4):219–228, 2011.

[45] L. Schroeder, T. J. Lowery, C. Hilty, D. E. Wemmer, and A. Pines. Molecular imaging using a targeted magnetic resonance hyperpolarized biosensor. *Science*, 314(5798):446–449, 2006.

[46] A. Louie. MRI Biosensors: A Short Primer. *J. Magn. Reson. Imaging*, 38(3):530–539, 2013.

[47] J. L. Major, R. M. Boiteau, and T. J. Meade. Mechanisms of ZnII-Activated Magnetic Resonance Imaging Agents. *Inorg. Chem.*, 47 (22):10788–10795, 2008.

[48] I. Mamedov, S. Canals, J. Henig, M. Beyerlein, Y. Murayama, H. A. Mayer, N. K. Logothetis, and G. Angelovski. In Vivo Characterization of a Smart MRI Agent That Displays an Inverse Response to Calcium Concentration. *ACS Chem. Neurosci.*, 1(12):819–828, 2010.

[49] G. B. Giovenzana, R. Negri, G. A. Rolla, and L. Tei. Gd-Aminoethyl-DO3A Complexes: A Novel Class of pH-Sensitive MRI Contrast Agents. *Eur. J. Inorg. Chem.*, (12, SI):2035–2039, 2012.

[50] S. Aime, F. Fedeli, A. Sanino, and E. Terreno. A R2/R1 Ratiometric Procedure for a Concentration-Independent, pH-Responsive, Gd(III)-Based MRI Agent. *J. Am. Chem. Soc.*, 128(35):11326–11327, 2006.

[51] B. Sitharaman, R. D. Bolskar, I. Rusakova, , and L. J. Wilson. Gd@C60[C(COOH)2]10 and Gd@C60(OH)x:Nanoscale Aggregation Studies of Two Metallofullerene MRI Contrast Agents in Aqueous Solution. *Nano Lett.*, 4(12):2373–2378, 2004.

[52] E. Tóth, R. D. Bolskar, A. Borel, G. González, L. Helm, A. E. Merbach, B. Sitharaman, and L. J. Wilson. Water-Soluble Gadofullerenes: Toward High-Relaxivity, pH-Responsive MRI Contrast Agents. *J. Am. Chem. Soc.*, 127(2):799–805, 2005.

[53] J. W. M. Bulte. In Vivo MRI Cell Tracking: Clinical Studies. *Am. J. Roentgenol.*, 193(2):314–325, 2009.

[54] I. J. M. de Vries, W. J. Lesterhuis, J. O. Barentsz, P. Verdijk, J. H. van Krieken, O. C. Boerman, W. J. G. Oyen, J. J. Bonenkamp, J. B. Boezeman, G. J. Adema, J. W. M. Bulte, T. W. J. Scheenen, C. J. A. Punt, A. Heerschap, and C. G. Figdor. Magnetic resonance tracking of dendritic cells in melanoma patients for monitoring of cellular therapy. *Nat. Biotechnol.*, 23(11):1407–1413, 2005.

[55] J. Zhu, L. Zhou, and F. XingWu. Tracking Neural Stem Cells in Patients with Brain Trauma. *N. Engl. J. Med.*, 355(22):2376–2378, 2006.

[56] R. Mason, P. Antich, E. Babcock, J. Gerbereich, and R. Nunnally. Perfluorocarbon imaging in vivo – A F-19 MRI study in tumor–bearing mice. *Magn. Reson. Imaging*, 7(5):475–485, 1989.

[57] T. Hahn, S. Kozerke, W. Schwizer, M. Fried, P. Boesiger, and A. Steingoetter. 19F MR Imaging Golden Angle-based Capsule Tracking for Intestinal Transit and Catheter Tracking: Initial in Vivo Experience. *Radiology*, 265(3):917–925, 2012.

[58] W. Wolf, C. Presant, and V. Waluch. F-19-MRS studies of fluorinated drugs in humans. *Adv. Drug Delivery Rev.*, 41(1):55–74, 2000.

[59] D. G. Reid and P. S. Murphy. Fluorine magnetic resonance in vivo: A powerful tool in the study of drug distribution and metabolism. *Drug Discov. Today*, 13(11–12):473 – 480, 2008.

[60] S. Mizukami, R. Takikawa, F. Sugihara, Y. Hori, H. Tochio, M. Walchli, M. Shirakawa, and K. Kikuchi. Paramagnetic relaxation-based F-19 MRI probe to detect protease activity. *J. Am. Chem. Soc.*, 130(3):794–795, 2008.

[61] V. Catanzaro, C. V. Gringeri, V. Menchise, S. Padovan, C. Boffa, W. Dastrù, L. Chaabane, G. Digilio, and S. Aime. A R2p/R1p Ratiometric Procedure to Assess Matrix Metalloproteinase-2 Activity by Magnetic Resonance Imaging. *Angew. Chem. Int. Edit.*, 52(14): 3926–3930, 2013.

[62] J.-X. Yu, R. R. Hallac, S. Chiguru, and R. P. Mason. New frontiers and developing applications in 19F NMR. *Prog. Nucl. Magn. Reson. Spectrosc.*, 70(0):25–49, 2013.

[63] M. Higuchi, N. Iwata, Y. Matsuba, K. Sato, K. Sasamoto, and T. Saido. F-19 and H-1 MRI detection of amyloid beta plaques in vivo. *Nat. Neurosci.*, 8(4):527–533, 2005.

[64] M. Ito, A. Shibata, J. Zhang, M. Hiroshima, Y. Sako, Y. Nakano, K. Kojima-Aikawa, B. Mannervik, S. Shuto, Y. Ito, R. Morgenstern, and H. Abe. Universal Caging Group for the in-Cell Detection of Glutathione Transferase Applied to 19F NMR and Bioluminogenic Probes. *Chembiochem.*, 13(10):1428–1432, 2012.

[65] Y. Yuan, H. Sun, S. Ge, M. Wang, H. Zhao, L. Wang, L. An, J. Zhang, H. Zhang, B. Hu, J. Wang, and G. Liang. Controlled Intracellular Self-Assembly and Disassembly of 19F Nanoparticles for MR Imaging of Caspase 3/7 in Zebrafish. *ACS Nano.*, 9(1):761–768, 2015.

[66] Y. Takaoka, T. Sakamoto, S. Tsukiji, M. Narazaki, T. Matsuda, H. Tochio, M. Shirakawa, and I. Hamachi. Self-assembling nanoprobes that display off/on F-19 nuclear magnetic resonance signals for protein detection and imaging. *Nat. Chem.*, 1(7):557–561, 2009.

[67] H. Matsushita, S. Mizukami, Y. Mori, F. Sugihara, M. Shirakawa, Y. Yoshioka, and K. Kikuchi. F-19 MRI Monitoring of Gene Expression in Living Cells through Cell-Surface beta-Lactamase Activity. *Chembiochem.*, 13(11):1579–1583, 2012.

[68] S. Mizukami, H. Matsushita, R. Takikawa, F. Sugihara, M. Shirakawa, and K. Kikuchi. F-19 MRI detection of beta-galactosidase activity for imaging of gene expression. *Chem. Sci.*, 2(6):1151–1155, 2011.

[69] J. Yu, L. Liu, V. D. Kodibagkar, W. Cui, and R. P. Mason. Synthesis and evaluation of novel enhanced gene reporter molecules: detection of beta-galactosidase activity using 19F NMR of trifluoromethylated aryl beta-D-galactopyranosides . *Bioorg. Med. Chem.*, 14(2):326–333, 2006.

[70] J.-X. Yu, V. D. Kodibagkar, R. R. Hallac, L. Liu, and R. P. Mason. Dual F-19/H-1 MR Gene Reporter Molecules for in Vivo Detection of beta-Galactosidase. *Bioconjug. Chem.*, 23(3):596–603, 2012.

[71] L. D. Stegman, A. Rehemtulla, B. Beattie, E. Kievit, T. S. Lawrence, R. G. Blasberg, J. G. Tjuvajev, and B. D. Ross. Noninvasive quantitation of cytosine deaminase transgene expression in human tumor xenografts with in vivo magnetic resonance spectroscopy. *Proc. Natl. Acad. Sci. U. S. A.*, 96(17):9821–9826, 1999.

[72] A. Keliris, I. Mamedov, G. E. Hagberg, N. K. Logothetis, K. Scheffler, and J. Engelmann. A smart 19F and 1H MRI probe with self-immolative linker as a versatile tool for detection of enzymes. *Contrast Media Mol. I.*, 7(5):478–483, 2012.

[73] X. Yue, Z. Wang, L. Zhu, Y. Wang, C. Qian, Y. Ma, D. O. Kiesewetter, G. Niu, and X. Chen. Novel F-19 Activatable Probe for the Detection of Matrix Metalloprotease-2 Activity by MRI/MRS. *Mol. Pharm.*, 11(11):4208–4217, 2014.

[74] J. M. Brown. Tumor hypoxia in cancer therapy. In *Oxygen Biology and Hypoxia*, volume 435 of *Methods in Enzymology*, pages 295 – 321. Academic Press, 2007.

[75] R. Reid, C. Koch, M. Castro, J. Lunt, E. Treieber, D. Boisvert, and P. Allen. The influence of oxygenation on the F-19 spin-latice relaxation rates of fluosol-DA (artificial blood). *Phys. Med. Biol.*, 30 (7):677–686, 1985.

[76] B. D. Spiess. Perfluorocarbon emulsions as a promising technology: a review of tissue and vascular gas dynamics. *J. Appl. Physiol.*, 106(4):1444–1452, 2009.

[77] I. Tirotta, A. Mastropietro, C. Cordiglieri, L. Gazzera, F. Baggi, G. Baselli, M. G. Bruzzone, I. Zucca, G. Cavallo, G. Terraneo, F. B. Bombelli, P. Metrangolo, and G. Resnati. A Superfluorinated Molecular Probe for Highly Sensitive in Vivo(19)F-MRI. *J. Am. Chem. Soc.*, 136(24):8524–8527, 2014.

[78] J. Chen, G. M. Lanza, and S. A. Wickline. Quantitative Magnetic Resonance Fluorine Imaging: Today and tomorrow. *Wiley Interdiscip. Rev. Nanomed. Nanobiotechnol.*, 2(4):431–440, 2010.

[79] B. F. Jordan, G. O. Cron, and B. Gallez. Rapid monitoring of oxygenation by 19F magnetic resonance imaging: Simultaneous comparison with fluorescence quenching. *Magn. Reson. Med.*, 61(3): 634–638, 2009.

[80] R. A. Carano, A. L. Ross, J. Ross, S. P. Williams, H. Koeppen, R. H. Schwall, and N. Van Bruggen. Quantification of tumor tissue populations by multispectral analysis. *Magn. Reson. Med.*, 51(3):542–551, 2004.

[81] S. Hunjan, D. Zhao, A. Constantinescu, E. W. Hahn, P. P. Antich, and R. P. Mason. Tumor oximetry: demonstration of an enhanced dynamic mapping procedure using fluorine-19 echo planar magnetic resonance imaging in the Dunning prostate R3327-AT1 rat tumor . *Int. J. Radiat. Oncol.*, 49(4):1097 – 1108, 2001.

[82] Y. Shi, J. Oeh, J. Eastham-Anderson, S. Yee, D. Finkle, F. V. P. Jr, J. Ross, M. Hedehus, N. van Bruggen, R. Venook, S. Ross, D. Sampath, and R. A. Carano. Mapping In Vivo Tumor Oxygenation within Viable Tumor by 19F-MRI and Multispectral Analysis. *Neoplasia*, 15(11):1241 – IN1, 2013.

[83] C. P. Lee, G. S. Payne, A. Oregioni, R. Ruddle, S. Tan, F. I. Raynaud, D. Eaton, M. J. Campbell, K. Cross, G. Halbert, M. Tracy, J. McNamara, B. Seddon, M. O. Leach, P. Workman, and I. Judson. A phase I study of the nitroimidazole hypoxia marker SR4554 using 19F magnetic resonance spectroscopy. *Br. J. Cancer*, 101(11): 1860–1868, 2009.

[84] E. Aboagye, A. Lewis, A. Johnson, P. Workman, M. Tracy, and I. Huxham. The novel fluorinated 2-nitroimidazole hypoxia probe SR-4554: reductive metabolism and semiquantitative localisation in human ovarian cancer multicellular spheroids as measured by electron energy loss spectroscopic analysis. *Br. J. Cancer*, 72(2):312–318, 1995.

[85] E. Aboagye, R. Maxwell, A. Kelson, M. Tracy, A. Lewis, M. Graham, M. Horsman, J. Griffiths, and P. Workman. Preclinical Eval-

uation of the Fluorinated 2-Nitroimidazole N-(2-hydroxy-3,3,3-trifluoropropyl)-2-(2-nitro-1-imidazolyl) Acetamide (SR-4554) as a Probe for the Measurement of Tumor Hypoxia. *Cancer Res.*, 57(15): 3314–3318, 1997.

[86] B. M. Seddon, G. S. Payne, L. Simmons, R. Ruddle, R. Grimshaw, S. Tan, A. Turner, F. Raynaud, G. Halbert, M. O. Leach, I. Judson, and P. Workman. A Phase I Study of SR-4554 via Intravenous Administration for Noninvasive Investigation of Tumor Hypoxia by Magnetic Resonance Spectroscopy in Patients with Malignancy. *Clin. Cancer Res.*, 9(14):5101–5112, 2003.

[87] M. Oishi, S. Sumitani, and Y. Nagasaki. On-off regulation of F-19 magnetic resonance signals based on pH-Sensitive PEGylated nanogels for potential tumor-specific smart F-19 MRI probes. *Bioconjug. Chem.*, 18(5):1379–1382, 2007.

[88] C. Deutsch and J. Taylor. Intracellular pH as measured by 19F NMR. *Ann. NY. Acad.Sci.*, 508:33–47, 1987.

[89] M. G. Vander Heiden, L. C. Cantley, and C. B. Thompson. Understanding the Warburg Effect: The Metabolic Requirements of Cell Proliferation. *Science*, 324(5930):1029–1033, 2009.

[90] J. Taylor and C. Deutsch. Fluorinated alpha-methylamino acids as 19F {NMR} indicators of intracellular pH. *Biophys. J.*, 43(3):261 – 267, 1983.

[91] C. Deutsch, J. Taylor, and D. Wilson. Regulation of intracellular pH by human peripheral blood lymphocytes as measured by 19F NMR. *Proc. Natl. Acad. Sci. U. S. A.*, 79(24):7944–7948, 1982.

[92] R. Mason. Transmembrane pH gradients in vivo: measurements using fluorinated vitamin B6 derivatives. *Curr. Med. Chem.*, 6(6): 481–499, 1999.

[93] X. Huang, G. Huang, S. Zhang, K. Sagiyama, O. Togao, X. Ma, Y. Wang, Y. Li, T. C. Soesbe, B. D. Sumer, M. Takahashi, A. D. Sherry, and J. Gao. Multi-Chromatic pH-Activatable 19F-MRI

Nanoprobes with Binary ON/OFF pH Transitions and Chemical-Shift Barcodes. *Angew. Chem. Int. Edit.*, 52(31):8074–8078, 2013.

[94] G. Smith, R. Hesketh, J. Metcalfe, J. Feeney, and P. Morris. Intracellular calcium measurements by F-19 NMR fluorine-labelled chelators. *Proc. Natl. Acad. Sci. U. S. A.*, 80(23):7178–7182, 1983.

[95] T. Sakamoto, H. Hayakawa, and K. Fujimoto. Development of a Potassium Ion Sensor for 19-F Magnetic Resonance Chemical Shift Imaging Based on Fluorine-labeled Thrombin Aptamer. *Chem. Lett.*, 40(7):720–721, 2011.

[96] G. A. Smith, H. L. Kirschenlohr, J. C. Metcalfe, and S. D. Clarke. A new 19F NMR indicator for intracellular sodium. *J. Chem. Soc., Perkin Trans. 2*, pages 1205–1209, 1993.

[97] J. Benters, U. Flögel, T. Schäfer, D. Leibfritz, S. Hechtenberg, and D. Beyersmann. Study of the interactions of cadmium and zinc ions with cellular calcium homoeostasis using 19F-NMR spectroscopy. *Biochem. J.*, 322(Pt 3):793–799, 1997.

[98] Z.-X. Jiang, Y. Feng, and Y. B. Yu. Fluorinated paramagnetic chelates as potential multi-chromic F-19 tracer agents. *Chem. Commun.*, 47(25):7233–7235, 2011.

[99] P. Harvey, I. Kuprov, and D. Parker. Lanthanide Complexes as Paramagnetic Probes for 19F Magnetic Resonance. *Eur. J. Inorg. Chem.*, (12, SI):2015–2022, 2012.

[100] P. Harvey, K. H. Chalmers, E. De Luca, A. Mishra, and D. Parker. Paramagnetic 19F Chemical Shift Probes that Respond Selectively to Calcium or Citrate Levels and Signal Ester Hydrolysis. *Chem-Eur J*, 18(28):8748–8757, 2012.

[101] P. Kadjane, C. Platas-Iglesias, P. Boehm-Sturm, V. Truffault, G. E. Hagberg, M. Hoehn, N. K. Logothetis, and G. Angelovski. Dual-Frequency Calcium-Responsive MRI Agents. *Chem-Eur. J.*, 20(24): 7351–7362, 2014.

[102] F. Bonetto, M. Srinivas, A. Heerschap, R. Mailliard, E. T. Ahrens, C. G. Figdor, and I. J. M. de Vries. A novel (19)F agent for detection and quantification of human dendritic cells using magnetic resonance imaging. *Int. J. Cancer*, 129(2):365–373, 2011.

[103] P. Boehm-Sturm, L. Mengler, S. Wecker, M. Hoehn, and T. Kallur. In Vivo Tracking of Human Neural Stem Cells with F-19 Magnetic Resonance Imaging. *PLoS One*, 6(12), 2011.

[104] E. Ahrens, R. Flores, H. Xu, and P. Morel. In vivo imaging platform for tracking immunotherapeutic cells. *Nat. Biotechnol.*, 23(8):983–987, 2005.

[105] E. T. Ahrens and J. Zhong. In vivo MRI cell tracking using perfluorocarbon probes and fluorine-19 detection. *NMR Biomed.*, 26(7, SI): 860–871, 2013.

[106] K. C. Partlow, J. Chen, J. A. Brant, A. M. Neubauer, T. E. Meyerrose, M. H. Creer, J. A. Nolta, S. D. Caruthers, G. M. Lanza, and S. A. Wickline. F-19 magnetic resonance imaging for stem/progenitor cell tracking with multiple unique perfluorocarbon nanobeacons. *FASEB J.*, 21(8):1647–1654, 2007.

[107] M. Srinivas, P. Boehm-Sturm, C. G. Figdor, I. J. de Vries, and M. Hoehn. Labeling cells for in vivo tracking using F-19 MRI. *Biomaterials*, 33(34):8830–8840, 2012.

[108] A. Tennstaedt, A. Mastropietro, M. Nelles, A. Beyrau, and M. Hoehn. In Vivo Fate Imaging of Intracerebral Stem Cell Grafts in Mouse Brain. *PLoS One*, 10(12):e0144262, 2015.

[109] E. Bible, F. Dell'Acqua, B. Solanky, A. Balducci, P. M. Crapo, S. F. Badylak, E. T. Ahrens, and M. Modo. Non-invasive imaging of transplanted human neural stem cells and ECM scaffold remodeling in the stroke-damaged rat brain by 19F- and diffusion-MRI. *Biomaterials*, 33(10):2858–2871, 2012.

[110] J. Ruiz-Cabello, P. Walczak, D. A. Kedziorek, V. P. Chacko, A. H. Schmieder, S. A. Wickline, G. M. Lanza, and J. W. M. Bulte. In Vivo

"Hot Spot" MR Imaging of Neural Stem Cells Using Fluorinated Nanoparticles. *Magn. Reson. Med.*, 60(6):1506–1511, 2008.

[111] J. M. Gaudet, E. J. Ribot, Y. Chen, K. M. Gilbert, and P. J. Foster. Tracking the Fate of Stem Cell Implants with Fluorine-19 MRI. *PLoS One*, 10(3), 2015.

[112] E. T. Ahrens, B. M. Helfer, C. F. O'Hanlon, and C. Schirda. Clinical cell therapy imaging using a perfluorocarbon tracer and fluorine-19 MRI. *Magn. Reson. Med.*, 72(6):1696–1701, 2014.

[113] J. M. Janjic and E. T. Ahrens. Fluorine-containing nanoemulsions for MRI cell tracking. *Wiley Interdiscip. Rev. Nanomed. Nanobiotechnol.*, 1(5):492–501, 2009.

[114] D. J. Smith, E. S. Kornbrust, and T. A. Lane. Phagocytosis of A Fluorescently Labeled Perflubron Emulsion By A Human Monocyte Cell-line. *Artif. Cells Blood Substit. Immbol. Biotechnol.*, 22(4): 1215–1221, 1994.

[115] G. Weise, T. Basse-Luesebrink, C. Wessig, P. Jakob, and G. Stoll. In vivo imaging of inflammation in the peripheral nervous system by 19F MRI. *Exp. Neurol.*, 229(2):494–501, 2011.

[116] U. Floegel, Z. Ding, H. Hardung, S. Jander, G. Reichmann, C. Jacoby, R. Schubert, and J. Schrader. In vivo monitoring of inflammation after cardiac and cerebral ischemia by fluorine magnetic resonance imaging. *Circulation*, 118(2):140–148, 2008.

[117] D. K. Kadayakkara, S. Ranganathan, W.-B. Young, and E. T. Ahrens. Assaying macrophage activity in a murine model of inflammatory bowel disease using fluorine-19 MRI. *Lab. Invest.*, 92 (4):636–645, 2012.

[118] B. Ebner, P. Behm, C. Jacoby, S. Burghoff, B. A. French, J. Schrader, and U. Flögel. Early Assessment of Pulmonary Inflammation by 19F MRI In Vivo. *Circ. Cardiovasc. Imaging*, 3(2):202–210, 2010.

[119] U. Noeth, S. Morrissey, R. Deichmann, S. Jung, H. Adolf, A. Haase, and J. Lutz. Perfluoro-15-Crown-5-Ether Labelled Macrophages in

Adoptive Transfer Experimental Allergic Encephalomyelitis. *Artif. Cells Blood Substit. Immbol. Biotechnol.*, 25(3):243–254, 1997.

[120] J. Zhong, K. Narsinh, P. A. Morel, H. Xu, and E. T. Ahrens. In vivo Quantification of Inflammation in Experimental Autoimmune Encephalomyelitis Rats Using Fluorine-19 Magnetic Resonance Imaging Reveals Immune Cell Recruitment outside the Nervous System. *PLoS One*, 10(10):e0140238, 10 2015.

[121] T. Hertlein, V. Sturm, S. Kircher, T. Basse-Lüsebrink, D. Haddad, K. Ohlsen, and P. Jakob. Visualization of Abscess Formation in a Murine Thigh Infection Model of Staphylococcus aureus by 19F-Magnetic Resonance Imaging (MRI). *PLoS One*, 6(3):e18246, 03 2011.

[122] T. K. Hitchens, Q. Ye, D. F. Eytan, J. M. Janjic, E. T. Ahrens, and C. Ho. 19F MRI detection of acute allograft rejection with in vivo perfluorocarbon labeling of immune cells. *Magn. Reson. Med.*, 65 (4):1144–1153, 2011.

[123] U. Floegel, S. Su, I. Kreideweiß, Z. Ding, L. Galbarz, J. Fu, C. Jacoby, O. Witzke, and J. Schrader. Noninvasive Detection of Graft Rejection by In Vivo 19F MRI in the Early Stage. *Am. J. Transplant.*, 11(2):235–244, 2011.

[124] J. Ruiz-Cabello, B. P. Barnett, P. A. Bottomley, and J. W. M. Bulte. Fluorine (F-19) MRS and MRI in biomedicine. *NMR Biomed.*, 24(2): 114–129, 2011.

[125] M. Srinivas, P. A. Morel, L. A. Ernst, D. H. Laidlaw, and E. T. Ahrens. Fluorine-19 MRI for visualization and quantification of cell migration in a diabetes model. *Magn. Reson. Med.*, 58(4):725–734, 2007.

[126] J. Miroslaw, W. Guan, X. Jiadi, P. Monica, M. Gokhuldass, B.-S. Amnon, B. Monika, A. H. Joanna Wojtkiewicz, and, W. Maksymowicz, J. W. Bulte, D. Kraitchman, , and P. Walczak. Hot-spot 19F imaging of stem cell transplantation into the intrathecal space

in a large animal model. In *ISMRM. Intl Soc Mag Reson Med, Milan, Italy*, page 474, 2014.

[127] D. Hoult and R. Richards. Signal–to–noise ratio the nuclear magnetic resonance experiment. *J Magn. Reson.*, 24(1):71–85, 1976.

[128] D. Hoult and P. C. Lauterbur. The sensitivity of the zeugmatographic experiment involving human samples. *J Magn. Reson.*, 34 (2):425–433, 1979.

[129] W. A. Edelstein, G. H. Glover, C. J. Hardy, and R. W. Redington. The intrinsic signal-to-noise ratio in NMR imaging. *Magn. Reson. Med.*, 3(4):604–618, 1986.

[130] G. Kruger and G. Glover. Physiological noise in oxygenation-sensitive magnetic resonance imaging. *Magn. Reson. Med.*, 46(4): 631–637, 2001.

[131] H. Qiao, X. Zhang, X.-H. Zhu, F. Du, and W. Chen. In vivo 31P MRS of human brain at high/ultrahigh fields: a quantitative comparison of NMR detection sensitivity and spectral resolution between 4 T and 7 T. *Magn. Reson. Imaging*, 24(10):1281 – 1286, 2006.

[132] S. S. Hidalgo, S. E. Solis, K. Ocegueda, and A. O. Rodriguez. Theoretical signal-to-noise ratio of a slotted surface coil for magnetic resonance imaging with experimental validation. *J. Appl. Phys.*, 112(3), 2012.

[133] R. Kreis, T. Ernst, and B. Ross. Absolute Quantitation of Water and Metabolites in the Human Brain. II. Metabolite Concentrations. *J. Magn. Reson. Ser. B.*, 102(1):9 – 19, 1993.

[134] N. R. Bolo, Y. Hode, J.-F. Nedelec, E. Laine, G. Wagner, and J.-P. Macher. Brain Pharmacokinetics and Tissue Distribution In Vivo of Fluvoxamine and Fluoxetine by Fluorine Magnetic Resonance Spectroscopy. *Neuropsychopharmacol.*, 23(4):428–438, 2000.

[135] A. Abragam. *Principles of Nuclear Magnetism (International Series of Monographs on Physics)*. Oxford University Press, USA, reprint edition, 1983.

[136] R. Ernst, G. Bodenhausen, and A. Wokaun. *Principles of Nuclear Magnetic Resonance in One and Two Dimensions*. International series of monographs on chemistry. Clarendon Press, 1990.

[137] J. A. Nordmeyer-Massner, N. De Zanche, and K. P. Pruessmann. Noise figure characterization of preamplifiers at NMR frequencies. *J. Magn. Reson.*, 210(1):7–15, 2011.

[138] J. Granwehr. Multiplicative or t(1) noise in NMR spectroscopy. *Appl. Magn. Reson.*, 32(1-2):113–156, 2007.

[139] H. Gudbjartsson and S. Patz. The rician distribution of noisy MRI data. *Magn. Reson. Med.*, 34(6):910–914, 1995.

[140] A. Haase. Snapshot FLASH MRI - applications to T1, T2 and chemical-shift imaging. *Magn. Reson. Med.*, 13(1):77–89, 1990.

[141] K. Stupic, Z. Cleveland, G. Pavlovskaya, and T. Meersmann. Quadrupolar relaxation of hyperpolarized krypton-83 as a probe for surfaces. *Solid State Nucl. Magn. Reson.*, 29(1-3):79–84, 2006.

[142] C. Jacoby, S. Temme, F. Mayenfels, N. Benoit, M. P. Krafft, R. Schubert, J. Schrader, and U. Floegel. Probing different perfluorocarbons for in vivo inflammation imaging by F-19 MRI: image reconstruction, biological half-lives and sensitivity. *NMR Biomed.*, 27(3): 261–271, 2014.

[143] H. Mo, J. Harwood, S. Zhang, Y. Xue, R. Santini, and D. Raftery. R: A quantitative measure of NMR signal receiving efficiency. *J Magn. Reson.*, 200(2):239–244, 2009.

[144] H. Mo, J. S. Harwood, and D. Raftery. Receiver gain function: the actual NMR receiver gain. *Magn. Reson. Chem.*, 48(3):235–238, 2010.

[145] H. Amiri, M. Srinivas, A. Veltien, M. van Uden, I. de Vries, and A. Heerschap. Cell tracking using 19F magnetic resonance imaging: Technical aspects and challenges towards clinical applications. *Eur. Radiol.*, 25(3):726–735, 2015.

[146] H.-S. Lee, D.-C. Woo, K.-H. Min, Y.-K. Kim, H.-K. Lee, and B.-Y. Choe. Development of a solenoid RF coil for animal imexperiment 3 T high-magnetic-field MRI. *Scanning*, 30(5):419–425, 2008.

[147] J. Libove and J. Singer. Resolution and signal-to-noise relationships in NMR imaging in the human-body. *J. Phys. E.*, 13(1):38–44, 1980.

[148] F. D. Doty, G. Entzminger, J. Kulkarni, K. Pamarthy, and J. P. Staab. Radio frequency coil technology for small-animal MRI. *NMR Biomed.*, 20(3):304–325, 2007.

[149] L. Mignion, J. Magat, O. Schakman, E. Marbaix, B. Gallez, and B. F. Jordan. Hexafluorobenzene in comparison with perfluoro-15-crown-5-ether for repeated monitoring of oxygenation using 19F MRI in a mouse model. *Magn. Reson. Med.*, 69(1):248–254, 2013.

[150] C. Giraudeau, J. Flament, B. Marty, F. Boumezbeur, S. Mériaux, C. Robic, M. Port, N. Tsapis, E. Fattal, E. Giacomini, F. Lethimonnier, D. Le Bihan, and J. Valette. A new paradigm for high-sensitivity 19F magnetic resonance imaging of perfluorooctylbromide. *Magn. Reson. Med.*, 63(4):1119–1124, 2010.

[151] M. J. Goette, G. M. Lanza, S. D. Caruthers, and S. A. Wickline. Improved quantitative 19F MR molecular imaging with flip angle calibration and B1-mapping compensation. *J. Magn. Reson. Imaging*, 42(2):488–494, 2015.

[152] M. B. Kok, A. de Vries, D. Abdurrachim, J. J. Prompers, H. Grüll, K. Nicolay, and G. J. Strijkers. Quantitative 1H MRI, 19F MRI, and 19F MRS of cell-internalized perfluorocarbon paramagnetic nanoparticles. *Contrast Media Mol. I.*, 6(1):19–27, 2011.

[153] A. Kimura, M. Narazaki, Y. Kanazawa, and H. Fujiwara. 19F Magnetic resonance imaging of perfluorooctanoic acid encapsulated in liposome for biodistribution measurement . *Magn. Reson. Imaging*, 22(6):855–860, 2004.

[154] R. Weissleder and U. Mahmood. Molecular imaging. *Radiology*, 219(2):316–333, 2001.

[155] R. Roy, J. Yang, and M. A. Moses. Matrix Metalloproteinases As Novel Biomarkers and Potential Therapeutic Targets in Human Cancer. *J. Clin. Oncol.*, 27(31):5287–5297, 2009.

[156] J. A. Madri and D. Graesser. Cell migration in the immune system: the evolving inter-related roles of adhesion molecules and proteinases. *Dev. Immunol.*, 7(2-4):103–16, 2000.

[157] C. Bremer, S. Bredow, U. Mahmood, R. Weissleder, and C. Tung. Optical imaging of matrix metalloproteinase-2 activity in tumors: Feasibility study in a mouse model. *Radiology*, 221(2):523–529, 2001.

[158] B. K. Giersing, M. T. Rae, M. CarballidoBrea, R. A. Williamson, and P. J. Blower. Synthesis and Characterization of 111In-DTPA-N-TIMP-2: A Radiopharmaceutical for Imaging Matrix Metalloproteinase Expression. *Bioconjug. Chem.*, 12(6):964–971, 2001.

[159] N. Matusiak, A. van Waarde, R. Bischoff, R. Oltenfreiter, C. van de Wiele, R. A. Dierckx, and P. H. Elsinga. Probes for Non-invasive Matrix Metalloproteinase-targeted Imaging with PET and SPECT. *Curr. Pharm. Des.*, 19(25):4647–4672, 2013.

[160] J. Krupa. *Design and synthesis of MRI ligand for in vivo imaging of protease activity activity*. PhD thesis, University of Nottingham, 2015.

[161] B. Alberts, A. Johnson, J. Lewis, M. Raff, K. Roberts, and P. Walter. *Cell junctions, cell adhesion, and the extracellular matrix*. Garland Science, 2002.

[162] G. A. Limb, K. Matter, G. Murphy, A. D. Cambrey, P. N. Bishop, G. E. Morris, and P. T. Khaw. Matrix Metalloproteinase-1 Associates with Intracellular Organelles and Confers Resistance to Lamin A/C Degradation during Apoptosis. *Am. J. Pathol.*, 166(5): 1555–1563, 2005.

[163] J. Kwan, C. Schulze, W. Wang, H. Leon, M. Sariahmetoglu, M. Sung, J. Sawicka, D. Sims, G. Sawicki, and R. Schulz. Matrix metalloproteinase-2 (MMP-2) is present in the nucleus of cardiac myocytes and is capable of cleaving poly (ADP-ribose) polymerase (PARP) in vitro. *FASEB J.*, 18(2):690+, 2004.

[164] W. G. Stetler-Stevenson. Tissue Inhibitors of Metalloproteinases in Cell Signaling: Metalloproteinase-Independent Biological Activities. *science signaling*, 1(27), 2008.

[165] M. Egeblad and Z. Werb. New functions for the matrix metalloproteinases in cancer progression. *Nat. Rev. Cancer*, 2(3):161–174, 2002.

[166] K. Kessenbrock, V. Plaks, and Z. Werb. Matrix Metalloproteinases: Regulators of the Tumor Microenvironment. *Cell*, 141(1):52–67, 2010.

[167] C. Gialeli, A. D. Theocharis, and N. K. Karamanos. Roles of matrix metalloproteinases in cancer progression and their pharmacological targeting. *FEBS J.*, 278(1):16–27, 2011.

[168] T. Szarvas, T. Jäger, M. Becker, S. Tschirdewahn, C. Niedworok, I. Kovalszky, H. Rübben, S. Ergün, and F. vom Dorp. Validation of Circulating MMP-7 Level as an Independent Prognostic Marker of Poor Survival in Urinary Bladder Cancer. *Pathol. Oncol. Res.*, 17(2): 325–332, 2011.

[169] Z. Fu, S. Xu, Y. Xu, J. Ma, J. Li, and P. Xu. The Expression of Tumor-Derived and Stromal-Derived Matrix Metalloproteinase 2 Predicted Prognosis of Ovarian Cancer. *Int. J. Gynecol. Cancer*, 25 (3):356–362, 2015.

[170] K. Wolf, Y. I. Wu, Y. Liu, J. Geiger, E. Tam, C. Overall, M. S. Stack, and P. Friedl. Multi-step pericellular proteolysis controls the transition from individual to collective cancer cell invasion. *Nat. Cell Biol.*, 9(8):893–904, 2007.

[171] G. Bergers and L. E. Benjamin. Tumorigenesis and the angiogenic switch. *Nat. Rev. Cancer*, 3(6):401–410, 2003.

[172] G. Bergers, R. Brekken, G. McMahon, T. Vu, T. Itoh, K. Tamaki, K. Tanzawa, P. Thorpe, S. Itohara, Z. Werb, and D. Hanahan. Matrix metalloproteinase-9 triggers the angiogenic switch during carcinogenesis. *Nat. Cell Biol.*, 2(10):737–744, 2000.

[173] H. Zheng, H. Takahashi, Y. Murai, Z. Cui, K. Nomoto, H. Niwa, K. Tsuneyama, and Y. Takano. Expressions of MMP-2, MMP-9 and VEGF are closely linked to growth, invasion, metastasis and angiogenesis of gastric carcinoma. *Anticancer Res.*, 26(5):3579–3583, 2006.

[174] N. Mitsiades, W.-h. Yu, V. Poulaki, M. Tsokos, and I. Stamenkovic. Matrix Metalloproteinase-7-mediated Cleavage of Fas Ligand Protects Tumor Cells from Chemotherapeutic Drug Cytotoxicity. *Cancer Res.*, 61(2):577–581, 2001.

[175] H. Crawford, C. Scoggins, M. Washington, L. Matrisian, and S. Leach. Matrix metalloproteinase-7 is expressed by pancreatic cancer precursors and regulates acinar-to-ductal metaplasia in exocrine pancreas. *J. Clin. Invest.*, 109(11):1437–1444, 2002.

[176] B. Sheu, S. Hsu, H. No, H. Tien, S. Huang, and R. Lin. A novel role of metalloproteinase in cancer-mediated immunosuppression. *Cancer Res.*, 61(1):237–242, 2001.

[177] H. Kataoka, H. Uchino, T. Iwamura, M. Seiki, K. Nabeshima, and M. Koono. Enhanced tumor growth and invasiveness in vivo by a carboxyl-terminal fragment of alpha 1-proteinase inhibitor generated by matrix metalloproteinases - A possible modulatory role in natural killer cytotoxicity. *Am. J. Pathol.*, 154(2):457–468, 1999.

[178] M. Lepage, W. Dow, M. Melchior, Y. You, B. Fingleton, C. Quarles, C. Pepin, J. Gore, L. Matrisian, and J. McIntyre. Noninvasive detection of matrix metalloproteinase activity in vivo using a novel MRI contrast agent with a solubility switch. *Mol. Imaging*, 6:393–403, 2007.

[179] R. Lebel, B. Jastrzebska, H. Therriault, M.-M. Cournoyer, J. O. McIntyre, E. Escher, W. Neugebauer, B. Paquette, and M. Lepage. Novel solubility-switchable MRI agent allows the noninvasive detection of matrix metalloproteinase-2 activity in vivo in a mouse model. *Magn. Reson. Med.*, 60(5):1056–1065, 2008.

[180] E. Schellenberger, F. Rudloff, C. Warmuth, M. Taupitz, B. Hamm, and J. Schnorr. Protease-Specific Nanosensors for Magnetic Resonance Imaging. *Bioconjug. Chem.*, 19(12):2440–2445, 2008.

[181] K. Matsuo, R. Kamada, K. Mizusawa, H. Imai, Y. Takayama, M. Narazaki, T. Matsuda, Y. Takaoka, and I. Hamachi. Specific Detection and Imaging of Enzyme Activity by Signal-Amplifiable Self-Assembling 19F MRI Probes. *Chem-Eur. J.*, 19(38):12875–12883, 2013.

[182] D. W. Piston and G.-J. Kremers. Fluorescent protein FRET: the good, the bad and the ugly. *Trends Biochem. Sci.*, 32(9):407 – 414, 2007.

[183] T. Foerster. Transfer Mechanisms of Electronic Excitation Energy. *Radiat. Res. Suppl.*, 2:326–339, 1960.

[184] J. Yang, Z. Zhang, J. Lin, J. Lu, B. feng Liu, S. Zeng, and Q. Luo. Detection of MMP activity in living cells by a genetically encoded surface-displayed FRET sensor. *BBA-Mol. Cell Res.*, 1773(3):400–407, 2007.

[185] M. Stawarski, I. Rutkowska-Wlodarczyk, A. Zeug, M. Bijata, H. Madej, L. Kaczmarek, and J. Wlodarczyk. Genetically encoded FRET-based biosensor for imaging MMP-9 activity. *Biomaterials*, 35 (5):1402 – 1410, 2014.

[186] C. Bremer, C.-H. Tung, and R. Weissleder. In vivo molecular target assessment of matrix metalloproteinase inhibition. *Nat. Med.*, 7(6): 743–748, 2001.

[187] J. McIntyre, B. Fingleton, K. Wells, D. Piston, C. Lynch, S. Gautam, and L. Matrisian. Development of a novel fluorogenic proteolytic

beacon for in vivo detection and imaging of tumour-associated matrix metalloproteinase-7 activity. *Biochem. J.*, 377(3):617–628, 2004.

[188] P. Miller, N. Long, R. Vilar, and A. Gee. Synthesis of 11C, 18F, 15O, and 13N Radiolabels for Positron Emission Tomography. *Angew. Chem. Int. Edit.*, 47(47):8998–9033, 2008.

[189] S. Furumoto, K. Takashima, K. Kubota, T. Ido, R. Iwata, and H. Fukuda. Tumor detection using 18F-labeled matrix metalloproteinase-2 inhibitor. *Nucl. Med. Biol.*, 30(2):119–125, 2003.

[190] Q.-H. Zheng, X. Fei, T. R. DeGrado, J.-Q. Wang, K. L. Stone, T. D. Martinez, D. J. Gay, W. L. Baity, B. H. Mock, B. E. Glick-Wilson, M. L. Sullivan, K. D. Miller, G. W. Sledge, and G. D. Hutchins. Synthesis, biodistribution and micro-PET imaging of a potential cancer biomarker carbon-11 labeled MMP inhibitor (2R)-2-[[4-(6-fluorohex-1-ynyl)phenyl]sulfonylamino]-3-methylbutyric acid [11C]methyl ester. *Nucl. Med. Biol.*, 30(7):753–760, 2003.

[191] N. Kondo, T. Temma, J. Deguchi, K. Sano, M. Ono, and H. Saji. Development of PEGylated peptide probes conjugated with F-18-labeled BODIPY for PET/optical imaging of MT1-MMP activity. *J. Controlled Release*, 220(A):476–483, 2015.

[192] C. Knight, F. Willenbrock, and G. Murphy. A novel coumarin-labelled peptide for sensitive continuous assays of the matrix metalloproteinases. *FEBS Lett.*, 296(3):263–266, 1992.

[193] S. Netzel-Arnett, S. K. Mallya, H. Nagase, H. Birkedal-Hansen, and H. E. V. Wart. Continuously recording fluorescent assays optimized for five human matrix metalloproteinases. *Anal. Biochem.*, 195(1):86 – 92, 1991.

[194] A. R. Welch, C. M. Holman, M. F. Browner, M. R. Gehring, C.-C. Kan, and H. E. V. Wart. Purification of Human Matrilysin Produced inEscherichia coliand Characterization Using a New Opti-

mized Fluorogenic Peptide Substrate. *Arch. Biochem. Biophys.*, 324 (1):59–64, 1995.

[195] J. Cha, M. Pedersen, and D. Auld. Metal and pH dependence of heptapeptide catalysis by human matrilysin. *Biochemistry*, 35(49): 15831–15838, 1996.

[196] S. Mizukami, R. Takikawa, F. Sugihara, M. Shirakawa, and K. Kikuchi. Dual-Function Probe to Detect Protease Activity for Fluorescence Measurement and F-19 MRI. *Angew. Chem. Int. Edit.*, 48(20):3641–3643, 2009.

[197] K. H. Chalmers, E. De Luca, N. H. M. Hogg, A. M. Kenwright, I. Kuprov, D. Parker, M. Botta, J. I. Wilson, and A. M. Blamire. Design Principles and Theory of Paramagnetic Fluorine-Labelled Lanthanide Complexes as Probes for F-19 Magnetic Resonance: A Proof-of-Concept Study. *Chem-Eur. J.*, 16(1):134–148, 2010.

[198] P. K. Senanayake, N. J. Rogers, K.-L. N. A. Finney, P. Harvey, A. M. Funk, J. I. Wilson, D. O'Hogain, R. Maxwell, D. Parker, and A. M. Blamire. A new paramagnetically shifted imaging probe for MRI. *Magn. Reson. Med.*, 2016. DOI: 10.1002/mrm.26185.

[199] F. Schmid, C. HÃűltke, D. Parker, and C. Faber. Boosting 19F MRI-SNR efficient detection of paramagnetic contrast agents using ultrafast sequences. *Magn. Reson. Med.*, 69(4):1056–1062, 2013.

[200] J. Hennig, A. Nauerth, and H. Friedburg. RARE imaging: A fast imaging method for clinical MR. *Magn. Reson. Med.*, 3(6):823–833, 1986.

[201] H. Schlemmer, M. Becker, P. Bachert, A. Dietz, V. Rudat, B. Vanselow, P. Wollensack, I. Zuna, M. Knopp, H. Weidauer, F. Wannenmacher, and G. van Kaick. Alterations of intratumoral pharmacokinetics of 5-fluorouracil in head and neck carcinoma during simultaneous radiochemotherapy. *Cancer Res.*, 59(10):2363–2369, 1999.

[202] Y. Takaoka, K. Kiminami, K. Mizusawa, K. Matsuo, M. Narazaki, T. Matsuda, and I. Hamachi. Systematic Study of Protein Detection Mechanism of Self-Assembling 19F NMR/MRI Nanoprobes toward Rational Design and Improved Sensitivity. *J. Am. Chem. Soc.*, 133(30):11725–11731, 2011.

[203] W. Yu, Y. Yang, S. Bo, Y. Li, S. Chen, Z. Yang, X. Zheng, Z.-X. Jiang, and X. Zhou. Design and Synthesis of Fluorinated Dendrimers for Sensitive 19F MRI. *J. Org. Chem.*, 80(9):4443–4449, 2015.

[204] K. H. Chalmers, M. Botta, and D. Parker. Strategies to enhance signal intensity with paramagnetic fluorine-labelled lanthanide complexes as probes for F-19 magnetic resonance. *Dalton Trans.*, 40(4): 904–913, 2011.

[205] M. Weiger, K. P. Pruessmann, and F. Hennel. MRI with Zero Echo Time: Hard versus Sweep Pulse Excitation. *Magn. Reson. Med.*, 66 (2):379–389, 2011.

[206] M. Lustig, D. Donoho, and J. M. Pauly. Sparse MRI: The application of compressed sensing for rapid MR imaging. *Magn. Reson. Med.*, 58(6):1182–1195, 2007.

[207] T. Kampf, A. Fischer, T. C. Basse-Lüsebrink, G. Ladewig, F. Breuer, G. Stoll, P. M. Jakob, and W. R. Bauer. Application of compressed sensing to in vivo 3D F-19 CSI. *J Magn. Reson.*, 207(2):262–273, 2010.

[208] J. Zhong, P. H. Mills, T. K. Hitchens, and E. T. Ahrens. Accelerated fluorine-19 MRI cell tracking using compressed sensing. *Magn. Reson. Med.*, 69(6):1683–1690, 2013.

[209] P. C. M. van Zijl and N. N. Yadav. Chemical exchange saturation transfer (CEST): What is in a name and what isn't? *Magn. Reson. Med.*, 65(4):927–948, 2011.

[210] K. Ward, A. Aletras, and R. Balaban. A New Class of Contrast Agents for MRI Based on Proton Chemical Exchange Dependent Saturation Transfer (CEST). *J Magn. Reson.*, 143(1):79–87, 2000.

[211] V. Guivel-Scharen, T. Sinnwell, S. Wolff, and R. Balaban. Detection of Proton Chemical Exchange between Metabolites and Water in Biological Tissues . *J Magn. Reson.*, 133(1):36–45, 1998.

[212] G. Liu, X. Song, K. W. Y. Chan, and M. T. McMahon. Nuts and bolts of chemical exchange saturation transfer MRI. *NMR Biomed.*, 26(7):810–828, 2013.

[213] M. T. McMahon, A. A. Gilad, J. Zhou, P. Z. Sun, J. W. M. Bulte, and P. C. M. van Zijl. Quantifying exchange rates in chemical exchange saturation transfer agents using the saturation time and saturation power dependencies of the magnetization transfer effect on the magnetic resonance imaging signal (QUEST and QUESP): Ph calibration for poly-L-lysine and a starburst dendrimer. *Magn. Reson. Med.*, 55(4):836–847, 2006.

[214] M. Zaiß and P. Bachert. Chemical exchange saturation transfer (CEST) and MR Z -spectroscopy in vivo : a review of theoretical approaches and methods. *Phys. Med. Biol.*, 58(22):R221, 2013.

[215] A. W. Overhauser. Polarization of Nuclei in Metals. *Phys. Rev.*, 92: 411–415, 1953.

[216] J. Lu, J. Zhou, C. Cai, S. Cai, and Z. Chen. Observation of true and pseudo NOE signals using CEST-MRI and CEST-MRS sequences with and without lipid suppression. *Magn. Reson. Med.*, 73(4): 1615–1622, 2015.

[217] C. K. Jones, A. Huang, J. Xu, R. A. Edden, M. Schär, J. Hua, N. Oskolkov, D. Zacà, J. Zhou, M. T. McMahon, J. J. Pillai, and P. C. van Zijl. Nuclear Overhauser enhancement (NOE) imaging in the human brain at 7 T . *Neuroimage*, 77:114 – 124, 2013.

[218] P. D. Johnson and A. G. Redfield. Pulsed FT-NMR double resonance studies of yeast tRNAPhe: specific nuclear Overhauser effects and reinterpretation of low temperature relaxation data. *Nucleic Acids Res.*, 5(10):3913–3928, 1978.

[219] Z. Zu, V. A. Janve, J. Xu, M. D. Does, J. C. Gore, and D. F. Gochberg. A new method for detecting exchanging amide protons using chemical exchange rotation transfer. *Magn. Reson. Med.*, 69(3):637–647, 2013.

[220] M. Haris, K. Cai, A. Singh, H. Hariharan, and R. Reddy. In vivo mapping of brain myo-inositol. *Neuroimage*, 54(3):2079–2085, 2011.

[221] W. Ling, R. R. Regatte, G. Navon, and A. Jerschow. Assessment of glycosaminoglycan concentration in vivo by chemical exchange-dependent saturation transfer (gagCEST). *P. Natl. Acad. Sci. USA.*, 105(7):2266–2270, 2008.

[222] P. C. M. van Zijl, C. K. Jones, J. Ren, C. R. Malloy, and A. D. Sherry. MRI detection of glycogen in vivo by using chemical exchange saturation transfer imaging (glycoCEST). *Proc. Natl. Acad. Sci. U. S. A.*, 104(11):4359–4364, 2007.

[223] R. Wu, C.-M. Liu, P. K. Liu, and P. Z. Sun. Improved measurement of labile proton concentration-weighted chemical exchange rate (k(ws)) with experimental factor-compensated and T(1)-normalized quantitative chemical exchange saturation transfer (CEST) MRI. *Contrast Media Mol. I.*, 7(4):384–389, 2012.

[224] X. Zong, P. Wang, S.-G. Kim, and T. Jin. Sensitivity and Source of Amine-Proton Exchange and Amide-Proton Transfer Magnetic Resonance Imaging in Cerebral Ischemia. *Magn. Reson. Med.*, 71 (1):118–132, 2014.

[225] K. Cai, M. Haris, A. Singh, F. Kogan, J. H. Greenberg, H. Hariharan, J. A. Detre, and R. Reddy. Magnetic resonance imaging of glutamate. *Nat. Med.*, 18(2):302–306, 2012.

[226] J. Zhou, B. Lal, D. A. Wilson, J. Laterra, and P. C. van Zijl. Amide proton transfer (APT) contrast for imaging of brain tumors. *Magn. Reson. Med.*, 50(6):1120–1126, 2003.

[227] C. K. Jones, M. J. Schlosser, P. C. van Zijl, M. G. Pomper, X. Golay, and J. Zhou. Amide proton transfer imaging of human brain tumors at 3T. *Magn. Reson. Med.*, 56(3):585–592, 2006.

[228] T. Shah, L. Lu, K. M. Dell, M. D. Pagel, M. A. Griswold, and C. A. Flask. CEST-FISP: A novel technique for rapid chemical exchange saturation transfer MRI at 7 T. *Magn. Reson. Med.*, 65(2):432–437, 2011.

[229] G. Liu, M. M. Ali, B. Yoo, M. A. Griswold, J. A. Tkach, and M. D. Pagel. PARACEST MRI with improved temporal resolution. *Magn. Reson. Med.*, 61(2):399–408, 2009.

[230] H. Zhu, C. K. Jones, P. C. M. van Zijl, P. B. Barker, and J. Zhou. Fast 3D chemical exchange saturation transfer (CEST) imaging of the human brain. *Magn. Reson. Med.*, 64(3):638–644, 2010.

[231] A. Pumphrey, Z. Yang, S. Ye, D. K. Powell, S. Thalman, D. S. Watt, A. Abdel-Latif, J. Unrine, K. Thompson, B. Fornwalt, G. Ferrauto, and M. Vandsburger. Advanced cardiac chemical exchange saturation transfer (cardioCEST) MRI for in vivo cell tracking and metabolic imaging. *NMR Biomed.*, 29(1):74–83, 2016.

[232] K. Scheffler and S. Lehnhardt. Principles and applications of balanced SSFP techniques. *Eur. Radiol.*, 13(11):2409–2418, 2003.

[233] B. Schmitt, M. Zaiß, J. Zhou, and P. Bachert. Optimization of pulse train presaturation for CEST imaging in clinical scanners. *Magn. Reson. Med.*, 65(6):1620–1629, 2011.

[234] S.-M. Huang, M.-L. Jan, H.-C. Liang, C.-H. Chang, Y.-C. Wu, S.-Y. Tsai, and F.-N. Wang. Investigation of Readout RF Pulse Impact on the Chemical Exchange Saturation Transfer Spectrum. *Sci. Rep.*, 5: 15062, 2015.

[235] Z. Zu, K. Li, V. A. Janve, M. D. Does, and D. F. Gochberg. Optimizing Pulsed-Chemical Exchange Saturation Transfer (CEST) Imaging Sequences. *Magn. Reson. Med.*, 66(4):1100–1108, 2011.

[236] Y. Tee, A. Khrapitchev, N. Sibson, S. Payne, and M. Chappell. Evaluating the use of a continuous approximation for model-based quantification of pulsed chemical exchange saturation transfer (CEST) . *J Magn. Reson.*, 222:88–95, 2012.

[237] M. Kim, J. Gillen, B. A. Landman, J. Zhou, and P. C. van Zijl. Water saturation shift referencing (WASSR) for chemical exchange saturation transfer (CEST) experiments. *Magn. Reson. Med.*, 61(6):1441–1450, 2009.

[238] D. E. Woessner, S. Zhang, M. E. Merritt, and A. D. Sherry. Numerical solution of the Bloch equations provides insights into the optimum design of PARACEST agents for MRI. *Magn. Reson. Med.*, 53(4):790–799, 2005.

[239] P. Z. Sun, E. Wang, J. S. Cheung, X. Zhang, T. Benner, and A. G. Sorensen. Simulation and optimization of pulsed radio frequency irradiation scheme for chemical exchange saturation transfer (CEST) MRI-demonstration of pH-weighted pulsed-amide proton CEST MRI in an animal model of acute cerebral ischemia. *Magn. Reson. Med.*, 66(4):1042–1048, 2011.

[240] K. Murase and N. Tanki. Numerical solutions to the time-dependent Bloch equations revisited. *Magn. Reson. Imaging*, 29(1): 126–131, 2011.

[241] M. Yanez-Lopez. *Detecting neuroinflammation with molecular MRI*. PhD thesis, University of Nottingham, 2015.

[242] P. Z. Sun, C. T. Farrar, and A. G. Sorensen. Correction for artifacts induced by B0 and B1 field inhomogeneities in pH-sensitive chemical exchange saturation transfer (CEST) imaging. *Magn. Reson. Med.*, 58(6):1207–1215, 2007.

[243] M. A. Chappell, M. J. Donahue, Y. K. Tee, A. A. Khrapitchev, N. R. Sibson, P. Jezzard, and S. J. Payne. Quantitative Bayesian model-based analysis of amide proton transfer MRI. *Magn. Reson. Med.*, 70(2):556–567, 2013.

[244] J. Zhou, J. Payen, D. Wilson, R. Traystman, and P. van Zijl. Using the amide proton signals of intracellular proteins and peptides to detect pH effects in MRI. *Nat. Med.*, 9(8):1085–1090, 2003.

[245] J. Zhou, D. A. Wilson, P. Z. Sun, J. A. Klaus, and P. C. van Zijl. Quantitative description of proton exchange processes between water and endogenous and exogenous agents for WEX, CEST, and APT experiments. *Magn. Reson. Med.*, 51(5):945–952, 2004.

[246] A. N. Dula, B. E. Dewey, L. R. Arlinghaus, J. M. Williams, D. Klomp, T. E. Yankeelov, and S. Smith. Optimization of 7-T Chemical Exchange Saturation Transfer Parameters for Validation of Glycosaminoglycan and Amide Proton Transfer of Fibroglandular Breast Tissue. *Radiology*, 275(1):255–261, 2015.

[247] C. K. Jones, D. Polders, J. Hua, H. Zhu, H. J. Hoogduin, J. Zhou, P. Luijten, and P. C. van Zijl. In Vivo 3D Whole-Brain Pulsed Steady State Chemical Exchange Saturation Transfer at 7T. *Magn. Reson. Med.*, 67(6):1579–1589, 2011.

[248] V. Roeloffs, C. Meyer, P. Bachert, and M. Zaiss. Towards quantification of pulsed spinlock and CEST at clinical MR scanners: an analytical interleaved saturation-relaxation (ISAR) approach. *NMR Biomed.*, 28(1):40–53, 2015.

[249] Z. Zu, V. A. Janve, K. Li, M. D. Does, J. C. Gore, and D. F. Gochberg. Multi-angle ratiometric approach to measure chemical exchange in amide proton transfer imaging. *Magn. Reson. Med.*, 68(3):711–719, 2012.

[250] R. Bendell. Molecular MRI using chemical exchange saturation transfer (CEST). Master's thesis, School of Medicine, University of Nottingham, 2011.

[251] G. Ardito. Second year internship for the Ecole Centrale Lyon: A matlab tool for CEST Imaging. Technical report, School of Medicine, University of Nottingham, 2013.

[252] V. R. Sheth, Y. Li, L. Q. Chen, C. M. Howison, C. A. Flask, and M. D. Pagel. Measuring in vivo tumor pHe with CEST-FISP MRI. *Magn. Reson. Med.*, 67(3):760–768, 2012.

[253] L. Q. Chen, C. M. Howison, J. J. Jeffery, I. F. Robey, P. H. Kuo, and M. D. Pagel. Evaluations of Extracellular pH within In Vivo Tumors Using acidoCEST MRI. *Magn. Reson. Med.*, 72(5):1408–1417, 2014.

[254] Z. Wen, S. Hu, F. Huang, X. Wang, L. Guo, X. Quan, S. Wang, and J. Zhou. MR imaging of high-grade brain tumors using endogenous protein and peptide-based contrast. *Neuroimage*, 51(2):616–622, 2010.

[255] G. Jia, R. Abaza, J. D. Williams, D. L. Zynger, J. Zhou, Z. K. Shah, M. Patel, S. Sammet, L. Wei, R. R. Bahnson, and M. V. Knopp. Amide proton transfer MR imaging of prostate cancer: A preliminary study. *J. Magn. Reson. Imaging*, 33(3):647–654, 2011.

[256] O. Togao, C. W. Kessinger, G. Huang, T. C. Soesbe, K. Sagiyama, I. Dimitrov, A. D. Sherry, J. Gao, and M. Takahashi. Characterization of Lung Cancer by Amide Proton Transfer (APT) Imaging: An In Vivo Study in an Orthotopic Mouse Model. *PLoS One*, 8(10), 2013.

[257] O. Togao, T. Yoshiura, J. Keupp, A. Hiwatashi, K. Yamashita, K. Kikuchi, Y. Suzuki, S. O. Suzuki, T. Iwaki, N. Hata, M. Mizoguchi, K. Yoshimoto, K. Sagiyama, M. Takahashi, and H. Honda. Amide proton transfer imaging of adult diffuse gliomas: correlation with histopathological grades. *Neuro-oncol.*, 16(3):441–448, 2014.

[258] A. Dula, R. Dortch, B. Landman, J. Gore, and S. Smith. Application of chemical exchange saturation transfer (CEST) imaging to examine amide proton transfer (APT) in the spinal cord at 3T. In *Proceedings of the 19th Annual Meeting of ISMRM, Montreal*, page 407, 2011.

[259] J. Xu, M. Zaiss, Z. Zu, H. Li, J. Xie, D. F. Gochberg, P. Bachert, and J. C. Gore. On the origins of chemical exchange saturation transfer (CEST) contrast in tumors at 9.4 T. *NMR Biomed.*, 27(4):406–416, 2014.

[260] T. Jin, P. Wang, X. Zong, and S.-G. Kim. Magnetic resonance imaging of the Amine–Proton EXchange (APEX) dependent contrast. *Neuroimage*, 59(2):1218 – 1227, 2012.

[261] A. X. Li, R. H. Hudson, J. W. Barrett, C. K. Jones, S. H. Pasternak, and R. Bartha. Four-pool modeling of proton exchange processes in biological systems in the presence of MRI-paramagnetic chemical exchange saturation transfer (PARACEST) agents. *Magn. Reson. Med.*, 60(5):1197–1206, 2008.

[262] M. Zaiß, B. Schmitt, and P. Bachert. Quantitative separation of CEST effect from magnetization transfer and spillover effects by Lorentzian-line-fit analysis of z-spectra. *J Magn. Reson.*, 211(2):149–155, 2011.

[263] K. L. Desmond, F. Moosvi, and G. J. Stanisz. Mapping of amide, amine, and aliphatic peaks in the CEST spectra of murine xenografts at 7 T. *Magn. Reson. Med.*, 71(5):1841–1853, 2014.

[264] W. El Deredy. Pattern recognition approaches in biomedical and clinical magnetic resonance spectroscopy: A review. *NMR Biomed.*, 10(3):99–124, 1997.

[265] A. R. Tate, J. Underwood, D. Acosta, M. Julia-Sapé, C. Majós, A. Moreno-Torres, F. A. Howe, M. van der Graaf, V. Lefournier, M. M. Murphy, A. Loosemore, C. Ladroue, P. Wesseling, J. Luc Bosson, M. E. Cabañas, A. W. Simonetti, W. Gajewicz, J. Calvar, A. Capdevila, P. R. Wilkins, B. Bell, C. Rémy, A. Heerschap, D. Watson, J. R. Griffiths, and C. Arús. Development of a decision support system for diagnosis and grading of brain tumours using in vivo magnetic resonance single voxel spectra. *NMR Biomed.*, 19 (4):411–434, 2006.

[266] C. Granziera, A. Daducci, A. Donati, G. Bonnier, D. Romascano, A. Roche, M. B. Cuadra, D. Schmitter, S. Klöppel, R. Meuli, A. von Gunten, and G. Krueger. A multi-contrast MRI study of microstructural brain damage in patients with mild cognitive impairment. *Neuroimage Clin.*, 8:631–639, 2015.

[267] G. Iordanescu, C. Brendler, S. E. Crawford, A. M. Wyrwicz, P. N. Venkatasubramanian, and J. A. Doll. MRS measured fatty acid composition of periprostatic adipose tissue correlates with pathological measures of prostate cancer aggressiveness. *J. Magn. Reson. Imaging*, 42(3):651–657, 2015.

[268] X. Song, R. D. Airan, D. R. Arifin, A. Bar-Shir, D. K. Kadayakkara, G. Liu, A. A. Gilad, P. C. M. van Zijl, M. T. McMahon, and J. W. M. Bulte. Label-free in vivo molecular imaging of underglycosylated mucin-1 expression in tumour cells. *Nat. Commun.*, 6:6719, 2015.

[269] A. Bar-Shir, Y. Liang, K. W. Y. Chan, A. A. Gilad, and J. W. M. Bulte. Supercharged green fluorescent proteins as bimodal reporter genes for CEST MRI and optical imaging. *Chem. Commun.*, 51:4869–4871, 2015.

[270] K. W. Y. Chan. Chemical Exchange Saturation Transfer (CEST)-MRS reveals metabolite levels for monitoring the aggressiveness of breast cancer cells. In *World molecular imaging congress proceedings*, 2013.

[271] M.-C. Pardon, M. Y. Lopez, D. Yuchun, M. Marjanska, M. Prior, C. Brignell, S. Parhizkar, A. Agostini, L. Bai, D. P. Auer, and H. M. Faas. Magnetic Resonance Spectroscopy discriminates the response to microglial stimulation of wild type and Alzheimer's disease models. *Sci. Rep.*, 6:19880, 2016.

[272] C. Salvatore, A. Cerasa, I. Castiglioni, F. Gallivanone, A. Augimeri, M. Lopez, G. Arabia, M. Morelli, M. Gilardi, and A. Quattrone. Machine learning on brain MRI data for differential diagnosis of Parkinson's disease and Progressive Supranuclear Palsy. *J. Neurosci. Methods*, 222:230 – 237, 2014.

[273] S. Theodoridis, A. Pikrakis, K. Koutroumbas, and D. Cavouras. *Introduction to Pattern Recognition: A Matlab Approach*. Academic Press, 2010.

[274] S. Theodoridis and K. Koutroumbas. Pattern recognition. 2003.

[275] D. Greenstein, J. D. Malley, B. Weisinger, L. Clasen, and N. Gogtay. Using Multivariate Machine Learning Methods and Structural MRI to Classify Childhood Onset Schizophrenia and Healthy Controls. *Front. Psychiatry*, 3:53–, 2012.

[276] M. C. Lee and S. J. Nelson. Supervised pattern recognition for the prediction of contrast-enhancement appearance in brain tumors from multivariate magnetic resonance imaging and spectroscopy. *Artif. Intell. Med.*, 43(1):61–74, 2008.

[277] C. Davatzikos, D. Shen, R. Gur, X. Wu, D. Liu, Y. Fan, P. Hughett, B. Turetsky, R. Gur, and P. MD. Whole-brain morphometric study of schizophrenia revealing a spatially complex set of focal abnormalities., 2005.

[278] W. Yang, R. L. Lui, J.-H. Gao, T. F. Chan, S.-T. Yau, R. A. Sperling, and X. Huang. Independent component analysis-based classification of Alzheimer's MRI data. *J. Alzheimers Dis.*, 24(4):775–783, 2011.

[279] S. J. Raudys and A. K. Jain. Small Sample Size Effects in Statistical Pattern Recognition: Recommendations for Practitioners. *IEEE Trans. Pattern Anal. Mach. Intell.*, 13(3):252–264, 1991.

[280] M. Zaiß, J. Windschuh, D. Paech, J.-E. Meissner, S. Burth, B. Schmitt, P. Kickingereder, B. Wiestler, W. Wick, M. Bendszus, H.-P. Schlemmer, M. E. Ladd, P. Bachert, and A. Radbruch. Relaxation-compensated CEST-MRI of the human brain at 7 T: Unbiased insight into NOE and amide signal changes in human glioblastoma. *Neuroimage*, 112:180–188, 2015.

[281] N. McVicar, A. X. Li, D. F. Goncalves, M. Bellyou, S. O. Meakin, M. A. Prado, and R. Bartha. Quantitative tissue pH measurement

during cerebral ischemia using amine and amide concentration-independent detection (AACID) with MRI. *J. Cereb. Blood Flow Metab.*, 34(4):690–698, 2014.

[282] E. Terreno, J. Stancanello, D. Longo, D. D. Castelli, L. Milone, H. M. H. F. Sanders, M. B. Kok, F. Uggeri, and S. Aime. Methods for an improved detection of the MRI-CEST effect. *Contrast Media Mol. I.*, 4(5):237–247, 2009.

[283] C. DeBrosse, R. P. R. Nanga, P. Bagga, K. Nath, M. Haris, F. Marincola, M. D. Schnall, H. Hariharan, and R. Reddy. Lactate Chemical Exchange Saturation Transfer (LATEST) Imaging in vivo: A Biomarker for LDH Activity. *Sci. Rep.*, 6:19517, 2016.

[284] L. S. Hu, S. Ning, J. M. Eschbacher, N. Gaw, A. C. Dueck, K. A. Smith, P. Nakaji, J. Plasencia, S. Ranjbar, S. J. Price, N. Tran, J. Loftus, R. Jenkins, B. P. O'Neill, W. Elmquist, L. C. Baxter, F. Gao, D. Frakes, J. P. Karis, C. Zwart, K. R. Swanson, J. Sarkaria, T. Wu, J. R. Mitchell, and J. Li. Multi-Parametric MRI and Texture Analysis to Visualize Spatial Histologic Heterogeneity and Tumor Extent in Glioblastoma. *PLoS One*, 10(11):1–14, 2015.

[285] H. Eagle, V. I. Oyama, M. Levy, and A. Freeman. Myo-Inositol as an Essential Growth Factor for Normal and Malignant Human Cells in Tissue Culture. *Science*, 123(3202):845–847, 1956.

[286] J.-S. Lee, D. Xia, A. Jerschow, and R. R. Regatte. In vitro study of endogenous CEST agents at 3 T and 7 T. *Contrast Media Mol. I.*, 11 (1):4–14, 2016.

[287] M. Zaiß, J. Windschuh, S. Goerke, D. Paech, J.-E. Meissner, S. Burth, P. Kickingereder, W. Wick, M. Bendszus, H.-P. Schlemmer, M. E. Ladd, P. Bachert, and A. Radbruch. Downfield-NOE-suppressed amide-CEST-MRI at 7 Tesla provides a unique contrast in human glioblastoma. *Magn. Reson. Med.*, 2016. DOI: 10.1002/mrm.26100.

[288] M. Plaumann, U. Bommerich, T. Trantzschel, D. Lego, S. Dillenberger, G. Sauer, J. Bargon, G. Buntkowsky, and J. Bernarding.

Parahydrogen-Induced Polarization Transfer to 19F in Perfluorocarbons for 19F NMR Spectroscopy and MRI. *Chem-Eur. J.*, 19(20): 6334–6339, 2013.

[289] Y. Lee, H. Zeng, S. Ruedisser, A. D. Gossert, and C. Hilty. Nuclear Magnetic Resonance of Hyperpolarized Fluorine for Characterization of Protein-Ligand Interactions. *J. Am. Chem. Soc.*, 134(42): 17448–17451, 2012.

[290] F. Zamberlan, C. Lesbats, N. J. Rogers, J. L. Krupa, G. E. Pavlovskaya, N. R. Thomas, H. M. Faas, and T. Meersmann. Molecular Sensing with Hyperpolarized 129Xe Using Switchable Chemical Exchange Relaxation Transfer. *Chem. Phys. Chem.*, 16(11): 2294–2298, 2015.

[291] E. Belorizky, P. H. Fries, L. Helm, J. Kowalewski, D. Kruk, R. R. Sharp, and P.-O. Westlund. Comparison of different methods for calculating the paramagnetic relaxation enhancement of nuclear spins as a function of the magnetic field. *J. Chem. Phys.*, 128(5): 052315, 2008.

[292] T. Jin, P. Wang, X. Zong, and S.-G. Kim. MR imaging of the amide-proton transfer effect and the pH-insensitive nuclear overhauser effect at 9.4 T. *Magn. Reson. Med.*, 69(3):760–770, 2013.

[293] D. Coman, Y. Huang, J. U. Rao, H. M. De Feyter, D. L. Rothman, C. Juchem, and F. Hyder. Imaging the intratumoral-peritumoral extracellular pH gradient of gliomas. *NMR Biomed.*, 29(3):309–319, 2016.

[294] S. Langereis, J. Keupp, J. L. J. van Velthoven, I. H. C. de Roos, D. Burdinski, J. A. Pikkemaat, and H. Grüll. A Temperature-Sensitive Liposomal 1H CEST and 19F Contrast Agent for MR Image-Guided Drug Delivery. *J. Am. Chem. Soc.*, 131(4):1380–1381, 2009.